CRANFIELD UNIVERSITY

Anastasios Danezis

Heat transfer modelling, optimisation and monitoring of flashlamp-assisted automated tape placement

School of Aerospace, Transport and Manufacturing

Composites and Advanced Materials Centre

Engineering Doctorate (EngD) in Composites Manufacture

Academic Years: 2018 – 2022

Supervisor: Dr Alex Skordos
Industrial Supervisor: Dr David Williams
January 2023

CRANFIELD UNIVERSITY

Anastasios Danezis

Heat transfer modelling, optimisation and monitoring of flashlamp-assisted automated tape placement

School of Aerospace, Transport and Manufacturing

Composites and Advanced Materials Centre

Engineering Doctorate (EngD) in Composites Manufacture

Academic Years: 2018 – 2022

Supervisor: Dr Alex Skordos
Industrial Supervisor: Dr David Williams
January 2023

Abstract

This study aims to develop tools for the design, optimisation and control of automated tape placement (ATP) that integrates flashlamp heating. A thermo-optical simulation of ATP is developed, combining a 2D finite element model of the heat conduction with 3D ray tracing analysis. The methodology is validated against measurements acquired during ATP trials of AS4 carbon/PEEK composites, presenting deviations up to 20°C. Flashlamp operation at low frequency and long pulses (25 Hz /4.75 ms) results in up to 150°C higher irradiation temperatures and increased thermal penetration depth, 100 over 50 μm, compared to high frequency and short pulses (100 Hz/1.1 ms) or continuous operation. Consolidation temperatures under the roller are identical for pulsing scenarios of equivalent average power, including continuous operation. To increase computational efficiency, an 1D simulation of ATP is put forward comprising distinct models representing the tow, deposited material, and consolidated stack with transfer of temperature information to ensure field continuity. The 1D solution requires only 1-2% of the computational effort of the 2D model with a minor trade-off in accuracy, up to 14°C. Based on the efficient 1D solution, an optimisation scheme of ATP is developed by integrating models of material degradation, interfacial bonding and a Genetic Algorithm. The optimisation scheme identifies the Pareto front of the multi-objective problem accurately in 25% of the computational effort required for an exhaustive search. Strong trade-offs exist between bonding, thermal degradation and productivity, limiting the average bonding value in the stack to 0.35 before matrix degradation exceeds the 1% threshold typically set for aerospace applications. A monitoring strategy for ATP of thermoplastic prepregs is proposed combining 1D analytical solutions and temperature data acquired on the tool side of the deposited material, allowing estimation of nip point temperatures in real time. The method integrates an inverse solution to determine the heater power input from temperature data and enhance the nip point estimation accuracy. The monitoring scheme presents good accuracy for a wide range of velocities, substrate thickness and tooling materials, with an average error of 15°C even in the presence of significant measurement noise.

Keywords: Tape placement; Thermoplastic composites; Simulation; Heat transfer; Multi-objective optimisation; Process Monitoring; Inverse solution; Pulsed heating.

«...Λογής ταξίδια μ' έχουν τρικυμίσει

μ' είδαν τόποι, μου ανοίξανε ναοί

και τέχνες με περπάτησαν και η φύση»

Κωστής Παλαμάς

Acknowledgements

I would like to express my deepest gratitude to my academic supervisor Dr Alex Skordos for his technical and moral support, mentoring and unlimited effort to improve this work. He always pushed me to step outside my comfort zone, pursue excellence and grow as a researcher and individual. I'm also thankful to Mr Jim Hurley and Dr David Ayre for the technical assistance during experimental activities at Cranfield University. Special thanks to Prof Ivana K. Partridge, Prof Janice Barton, Mrs Maria Aviles and Mrs Kathleen Swales for their support with my integration, interest in my mental health and help with administrative topics. Finally, I wish to thank the EngD cohort for the support and moments of joy during our activities.

This endeavour would not have been possible without Heraeus Noblelight (HNL), and especially my industrial supervisor Dr David Williams. He has demonstrated continuous care and attention towards my integration into the research team at HNL, advising on my professional development and on how the impact of this work can be maximised at a company and industry level. I would like to extend my sincere thanks to Mr Martin Brown for his technical contribution on the experimental work at HNL, as well as all those I met there during these four years.

Words cannot express my gratitude to my parents, Evangelia and Loukas, for their continuous support in every chapter of my life, and inspiration to pursue the education and career path of my dreams.

I'm also thankful to my friend Artemis for his constant support and encouragement. I am very grateful to Konstantina for her endless patience and moral support.

I would like to acknowledge the support of Prof. Ralf Schledjewski and Mrs Neha Yadav at the University of Leoben, Austria for offering the experimental facilities and human resources for the model validation studies. Discussions with Professor Jay I. Frankel of New Mexico State University on the inverse problems are also gratefully acknowledged.

This work is supported by the Engineering and Physical Sciences Research Council (EPSRC) through the Industrial Doctorate Centre (IDC) in Composites Manufacture [EP/ EP/L015102/1] and sponsored by Heraeus Noblelight Ltd (Cambridge, UK).

Contents

List of Figures

List of Tables

List of Equations

Nomenclature

A_i	Arrhenius pre-exponential factor for degradation kinetics
A_v	Arrhenius pre-exponential factor for viscosity model
A_w	Arrhenius pre-exponential factor for welding time model
a_o	Geometrical factor for tape roughness
a_x	Composite longitudinal thermal diffusivity
a_y	Composite transverse thermal diffusivity
$\hat{a}$	Arc length of tow-roller curved region
B	Roller contact patch length
$\boldsymbol{b}(\boldsymbol{x})$	Constrains vector
C	Ambient zone length
c	Composite degree of degradation
c_f	Carbon fibre conversion
c_m	Matrix conversion
c_p	Composite specific heat capacity
$c_p{}'$	Tool specific heat capacity

$\bar{c}$	Experimentally measured conversion
D	Pulsed source duty cycle
D_b	Degree of bonding
D_h	Degree of healing
D_{ic}	Degree of intimate contact
$\overline{D_b}$	Average degree of bonding in the stack
d	Fractal dimension
d_p	Ply thickness
d_s	Deposited material thickness
d_{st}	Deposited material and tow total thickness
d_t	Thermal penetration depth
d_{tool}	Tool thickness
E_c	Effective compaction modulus
E_v	Parameter for viscosity model
E_w	Parameter for welding time model

E_i	Activation energy for degradation kinetics
$\bar{E}_i$	Average irradiance over material surface exposed to radiation
e	Heater conversion factor from electrical to optical output
F	Flashlamp system frequency
F_o	Fourier number
f	Fractal scaling factor
$\boldsymbol{f}(\boldsymbol{x})$	Objective function vector
G	Empirical parameter
g	Scaling factor for roller pressure distribution
h	Surface heat transfer coefficient
h_g	Hot gas torch heat transfer coefficient
h_o	Recess of the first-generation asperity
h_r	Distance from roller centre to tool surface
$\boldsymbol{K}$	Composite thermal conductivity tensor
k_{air}	Thermal conductivity of air

k_x	Composite longitudinal thermal conductivity
k_y	Composite through-thickness thermal conductivity
$k_y{}'$	Tool through-thickness thermal conductivity
L	Irradiation zone length
L_o	Total length of the cantor set
L_s	Irradiation zone length on deposited material
L_t	Irradiation zone length on incoming tow
l	Characteristic length
$\mathrm{m}_i, \mathrm{n}_i$	Fitting parameters for degradation kinetics
$\boldsymbol{n}$	Surface vector
o	Fitting parameter of extended Schott equation
P	Instantaneous power during pulse
p	Pulse duration
P_{app}	Applied temperature at bond interface
Pe	Peclet number

P_{rec}	Equivalent power of rectangular pulses
Pr	Prandtl number
$\bar{P}$	Flashlamp system average power
q	Prescribed heat flux
q_{conv}	Losses due to convection
q_o	Peak heat flux value
q_{roller}	Heat losses to the roller
q_s	Heat flux on deposited material surface
q_{se}	Heat flux for the semi-infinite approximation
q_t	Heat flux on incoming tow surface
q_{tool}	Heat losses to the tool
$\dot{q}$	Heat rate of latent heat due to material transformations
$\dot{q}_{conv}$	Heat losses per unit volume due to convection
$\dot{q}_{eff}$	Heat rate per unit volume across the path of the tape
$\dot{q}_i$	Heat rate per unit volume due to irradiation

$\dot{q}_{tool}$	Power losses per unit volume to the tool
$\overline{\dot{q}_{conv}}$	Average power losses per unit volume due to convection
$\overline{\dot{q}_{eff}}$	Average volumetric heat rate across the path of the tape
$\overline{\dot{q}_{\iota}}$	Average heat rate per unit volume due to irradiation
$\overline{\dot{q}_{tool}}$	Average power losses per unit volume to the tool
R	Gas constant
Re_x	Reynolds number of the air flow
R_c	Thermal contact resistance
$\boldsymbol{r}$	Spatial vector
r_o	Roller inner diameter
r	Roller diameter
S	Total heat transfer domain
S_1	Prescribed temperature boundary
S_2	Prescribed heat flux boundary
S_3	Convection boundary

S_4	Insulating boundary
S_5	Combined heat flux-convection boundary
S_{ij}	Interface boundary of i and j materials
T	Temperature
T_b	Tool surface temperature
T_{gas}	Gas torch temperature
T_m	Measured temperature
T_n	Nip point temperature
T_o	Initial analysis temperature
T_{ref}	Reference temperature for welding time model
T_{sur}	Element surface temperature
T_∞	Temperature of fluid at convective boundary
T_n^o	Nip point temperature for the finite body approximation
T_n^∞	Nip point temperature for the semi-infinite approximation
$\overline{T_1}$	Average temperature at the start of irradiation zone

$\overline{T_2}$	Average temperature at the start of nip point section
t	Time
t_m	Timing of peak heat flux value
t_o	Timing of irradiation zone entry
t_w	Welding time
t_∞	Nip point timing
U	Factor for incident irradiance
$\boldsymbol{u}$	Velocity vector
u_x	Material velocity across x-axis
u_y	Material velocity across y-axis
v	Irradiation zone width
w_f	Fibre mass fraction
w_o	Initial sample weight in TGA testing
w_t	Sample weight at time t in TGA testing
w'	Final sample weight in TGA testing

$\boldsymbol{x}$	Design variables vector
Z	Scaling factor for heater power

Greek symbols

α, β	Fitting parameters for heater power curve
ε	Coefficient of extinction
η	Refractive index
η'	Complex refractive index
μ	Polymer viscosity
μ	Mean of normal distribution
λ	Wavelength
ρ	Composite density
ρ'	Tool material density
σ	Standard deviation of normal distribution
τ	Final bonding time
$\varphi(c)$	Kinetics model function
ω	Pulse angular frequency

List of Abbreviations

AFP	Automated fibre placement
AI	Artificial Intelligence
ANOVA	Analysis of variance
ATP	Automated tape placement
BDRF	Bidirectional reflectance distribution function
CF	Carbon Fibre
DCB	Double cantilever beam
DMA	Dynamic mechanical analysis
DoE	Design of experiments
DSC	Differential scanning calorimetry
ELS	End-loaded split
FE	Finite element
FD	Finite differences
FTIR	Fourier transform infrared spectroscopy
FW	Filament winding

GA	Genetic algorithm
GF	Glass fibre
GRA	Grey relational analysis
ILSS	Interlaminar shear strength
ISD	Interlaminar shear device
LED	Light-emitting diodes
NIR	Near-infrared
PA6	Polyamide-6
PE	Polyethylene
PEEK	Polyether-ether-ketone
PEI	Polyethylenimine
PES	Poly(ether-sulfone)
PET	Polyethylene terephthalate
PP	Polypropylene
RSM	Surface response method

SBS	Short beam strength
TGA	Thermogravimetric analysis
VCSEL	Vertical-cavity surface-emitting laser
VSG	Virtual sample generation
XRD	X-ray Powder Diffraction

1. Introduction

1.1 Motivation

Achieving Net Zero necessitates the decarbonisation of the transport sector which can be achieved through innovative propulsion technologies, environmentally friendly materials, and efficient production methods. Lightweighting is also a key aspect directly influencing vehicle fuel consumption and therefore emissions. For years, composite materials have been seen as an enabler of lightweight structures due to their exceptional strength-to-weight ratio compared to metals. As a result, the utilisation of composites in aerospace applications has been increasing exponentially in the last 50 years, as shown in Figure 1.1 [1]. The state-of-the-art Airbus A350 is the world's first commercial aircraft with fuselage and wings made predominately from composites, exceeding 50% of their total weight. The A350 is 20 t lighter than the previous generation thanks to the extensive use of advanced materials and innovative designs, delivering 25% less fuel burn and CO_2 emissions per seat [2].

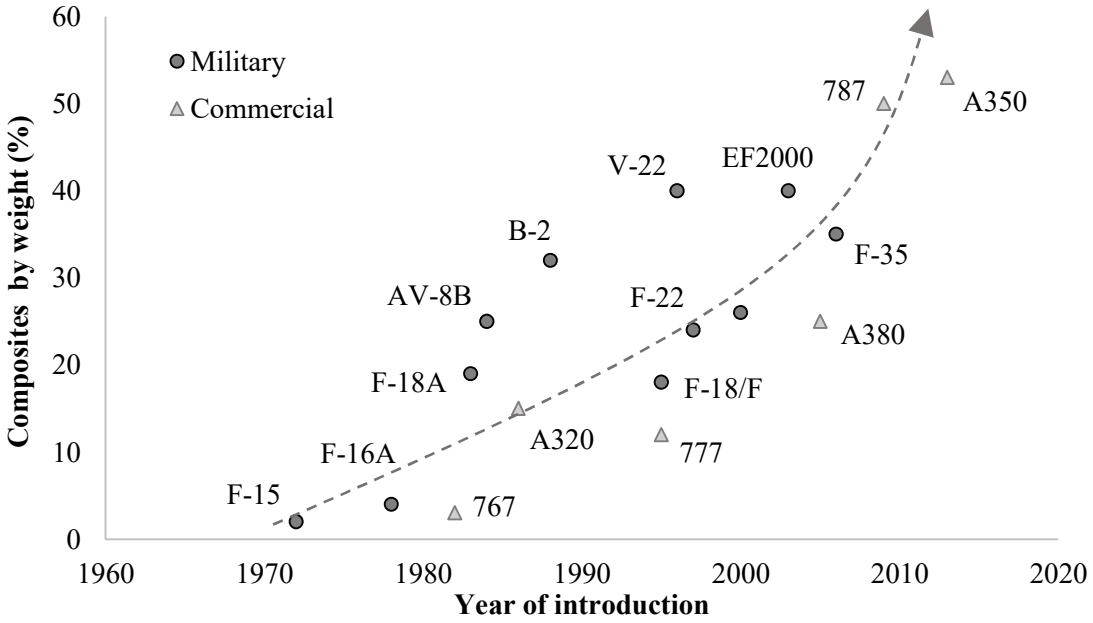

Figure 1.1 Composites content in military and commercial aircrafts in recent years. Adapted with permission from [1].

Despite the breakthrough of composites in the aerospace sector, the number of in-service commercial aircrafts utilising composites at high levels remains low compared to the total market. Airbus only recently delivered the 500th aircraft of the A350 family since its

launch in 2014 [3], whilst its contender in the battle of composites utilisation - the Boeing 787 Dreamliner - has reached only double this figure [4]. These rates appear insufficient when considering the market outlook of both major OEMs, forecasting the need for almost 40,000 new aircrafts by 2040 [5, 6]. This corresponds to the production of 100-200 aircrafts per month, which is significantly higher than what is common today. While increasing production rates has been hindered by a combination of factors such as supply chain issues and financial barriers for both OEMs and airlines, the strong utilisation of composites is believed to have introduced new challenges in the production process. This is attributed to the increased cost of raw materials as well as the complex multi-stage manufacturing methods of composites. Full automation could enable the production of high-quality components at fast rates for the next generation aircrafts to meet the increasing market demand and reduce the costs involved.

The ambitious production targets could be reached through the automated fibre and tape placement (AFP/ATP) manufacturing methods, which utilise robotic equipment to achieve robust, repeatable, fully automated production of large composite components. This method has gained significant industrial and research interest in recent years [7, 8], especially with the use of thermoplastic matrix composites. AFP/ATP processing of thermoplastic composites opens the way for the production of aircraft parts in a single-step process, mitigating the time-consuming and costly autoclave cycles required for thermosetting composites. Out-of-autoclave processing is key for aerospace considering the large dimensions of aircraft parts and the associated challenges in terms of autoclave size and energy needed for the curing stage. In addition, thermoplastic composites enable the efficient assembly of aircraft structures through induction welding and overmoulding, reducing or eliminating the need for fasteners. However, the uptake of this technology has not been achieved yet due to the challenges of achieving quality on par with conventional processing at competitive production rates, as a result of the complex interdependencies introduced by the dynamic process character. AFP of thermosetting composites has been utilised to produce aircraft components, as shown in Figure 1.2 for the fuselage of the 787 Dreamliner, but automated deposition of thermoplastic composites at this level is still a target. Further advancements on the process design and optimisation, monitoring techniques, and industrial equipment fronts are necessary to enable the wide adoption of these automated methods in aerospace.

Figure 1.2 Manufacture of monolithic fuselage section for the 787 Dreamliner with AFP on a rotating mandrel. Reproduced with permission from CompositesWorld [9].

AFP/ATP processing of high-performance thermoplastic composites requires elevated temperatures above the matrix melting point, which commonly lies within the 250-350°C temperature range for aerospace-grade polymers. These temperature levels challenge productivity necessitating a heating technology capable of delivering high power at very short timings. Fast response is also critical for effective temperature control during deposition speed changes around complex geometrical features. A recent addition to the available heating solutions for AFP/ATP applications are flashlamp-based systems. In contrast to established lasers and IR heaters, flashlamps feature a pulsed operation delivering high-energy pulses of several milliseconds periodically on the target surface. The wide parameters space in conjunction with the fast response promise advanced process tailoring and on-line control capabilities. Despite being as powerful as lasers, flashlamp systems require less stringent safety measures and have lower capital costs. Especially with respect to health and safety, flashlamp systems can operate without the protection requirements closely linked to use of heating lasers. This is reflected both in lower costs of operation as well as in greater flexibility in setting operating systems in different environments directly integrated with other stages of processing. To make use of these potential advantages, a thorough understanding of the effect of pulsing conditions

on the temperature field is necessary, whilst establishing the process design and monitoring workflow is imperative. Previous research on AFP/ATP has advanced towards these frontiers for conventional heating technologies, but adoption from the industry has been low due to increased complexity and effort required for analysis and detailed understanding of process intricacies. Development of computation tools suitable for industrial applications can facilitate the integration of flashlamp systems into production lines, as well as mitigate the experimental design campaigns which are time consuming and costly, hindering the overall competitiveness of AFP/ATP against other processes.

1.2 Aim and objectives

The overall aim of this study is the development of tools for the design, optimisation and control of ATP processes that integrate flashlamp-based energy sources. To accomplish significant progress towards this aim, the following objectives are addressed:

- Investigation of the effect of pulsed heating on the temperature field throughout the ATP process and identification of differences in behaviour over continuous heating.
- Development of a methodology for design and optimisation of flashlamp-assisted ATP of thermoplastic composites and demonstration of its application.
- Validation of the design tools based on instrumented manufacture of composites using ATP methods.
- Simplification of modelling tools to minimise computational effort and provide fast estimations suitable for optimisation purposes.
- Investigation of interdependencies and trade-offs involved in the flashlamp-assisted ATP concerning processing conditions and resulting part quality in terms of bond strength and thermal degradation.
- Development of on-line monitoring for ATP utilising remote temperature data, and methods for the determination of flashlamp energy input on the tape surface.

1.3 Road map

The present thesis is organised in 10 chapters. Chapter 2 summarises the state of the art on heat transfer modelling, optimisation and monitoring of continuous deposition processes such as ATP/AFP and filament winding. Chapter 3 details the experimental

methods used, including the characterisation of flashlamp systems, instrumented ATP trials and Thermogravimetric analysis (TGA). Chapter 3 also details the materials utilised and their thermal properties, as well as the numerical methods for process simulation and multi-objective optimisation. Chapter 4 presents the development of a 2D thermal-optical simulation for the flashlamp-assisted ATP process and its validation. Chapter 5 details the development of a simplified and efficient numerical solution of the heat conduction problem based on the decomposition of the domain into distinct one dimensional through-thickness models. Chapter 6 focuses on the multi-objective optimisation of ATP integrating the 1D heat transfer simulation with interlaminar bonding and thermal degradation constitutive models and a Genetic Algorithm (GA) to obtain process parameters that result in a favourable process duration and product quality. Chapter 7 describes the development of an in-process monitoring scheme of the nip point temperatures reached during ATP processing, by combining analytical heat transfer solutions and monitoring data from the lower surface of the deposited material based on an inverse solution. Chapter 8 presents an overall discussion of the findings of this work including overall impact and limitations. Chapters 9 and 10 summarise the main conclusions of the study and recommendations for further development.

2. Literature review

2.1 Introduction

This chapter presents the state of the art on heat transfer modelling, optimisation and monitoring applied to the ATP and AFP manufacturing methods. Studies on the filament winding (FW) process, which shares similar principles and therefore analysis, are included to provide a comprehensive review. The critical role of the developed temperature field on the final part quality has motivated the development of numerous heat transfer models. The approaches in terms of domain dimensions, boundary conditions, implementation, and numerical methods are discussed. Significant modelling and experimental efforts have been made to uncover the role of process parameters on the final part quality and tailor these to achieve optimised outcomes. On the other hand, the process complexity has necessitated the development of monitoring schemes which can provide useful information during processing, allowing the identification of changes in conditions and defects in real time.

2.2 Heat transfer modelling of AFP/ATP/FW

The AFP/ATP and FW are advanced manufacturing methods which deploy robotic equipment to deposit fibre-reinforced composite tapes onto a tool or mandrel and build the part in an additive fashion. A schematic of laser-assisted FW is given in Figure 2.1 [10]. Similarly to AFP/ATP, a heating source is used to heat the new layer and the already deposited material before they come into contact underneath a compaction roller.

Experimental design of the AFP/ATP and FW processes can be time-consuming due to the number of process variables influencing the process. Extensive experimental campaigns can be prohibitive given the high costs associated with aerospace-grade materials and the operation of advanced robotic equipment. Temperature measurements on the material surface can be obtained with thermal imaging for design purposes; however, the material is out of sight underneath the compaction roller and for the remaining processing cycle, during which temperature influences the final quality to a great extent. Embedding temperature sensors in, or in contact with, the moving material is possible for research/development purposes but not in a production environment. Large multi-layered parts are typically produced requiring a high number of sensors which interfere with the final component, whilst their setup slows down productivity. To address

these challenges, process design based on heat transfer modelling has received significant attention in recent years [11, 12]. Important aspects and results of existing methodologies are discussed in the next sections.

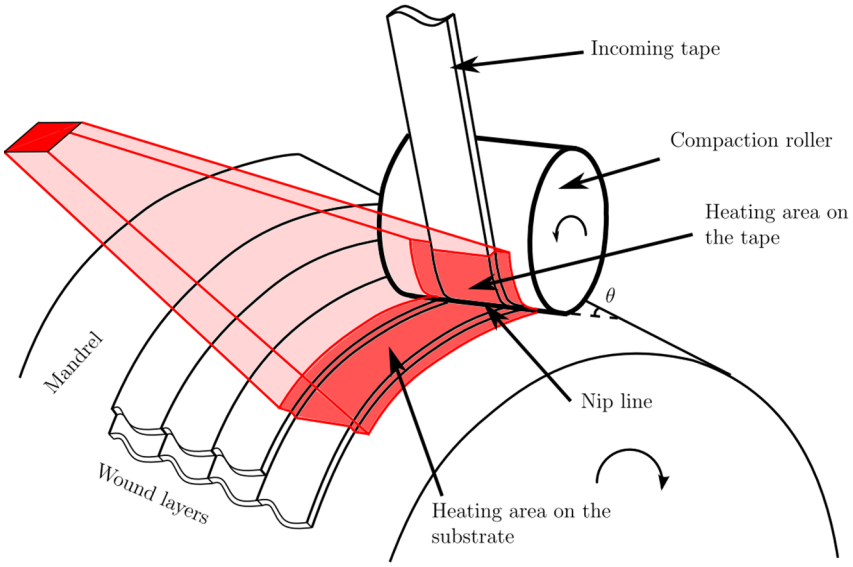

Figure 2.1 Schematic of the laser-assisted FW process. Reproduced with permission from [10].

2.2.1 Governing equations and assumptions

The AFP/ATP and FW processes are highly transient with the heat conduction problem in three dimensions expressed by the general energy balance [13]:

$$\rho c_p \left(\frac{\partial T}{\partial t}\right) = \dot{q} + \nabla \cdot \boldsymbol{K} \nabla T \tag{2.1}$$

where ρ is the density of the composite, c_p the specific heat capacity, $\boldsymbol{K}$ the thermal conductivity tensor and T is the temperature.

The term $\dot{q}$ corresponds to the latent heat as a result of matrix chemical transformations or physical transitions. In the case of thermoplastic matrices, heat is released and absorbed during crystallisation and melting, respectively. These effects have been included in the analysis through crystallisation and melting models, which enable the estimation of the amount released/absorbed according to the material temperature and history [13-15]. However, their influence on the heat transfer is typically assumed to be negligible given the low crystallinity levels during in-situ consolidation and the polymer constituting only 30-35% of tape mass [16-19]. For thermosetting materials, $\dot{q}$ corresponds to the energy

released due to the curing reaction. These exothermic effects have a strong influence on the temperature field and can be included by coupling the heat transfer model with cure kinetics models [20-22]; however, they can be omitted if curing is not expected to progress significantly at the temperatures attained and/or for the short time window of the placement [23-25]. Nevertheless, the validity of this assumption depends on the temperatures reached and the type of thermosetting system.

Table 2.1 Influence of modelling approaches and assumptions on computation time and accuracy for ATP.

Approach/ Assumption	Computation time	Accuracy
Full 3D problem (reference)	–	–
Negligible latent heat	↓	–
Uniform heating across material width (2D)	↓↓	↓
Negligible heat conduction in placement direction (2D)	↓↓	↓
Domain decomposition to 1D models	↓↓↓	↓↓
Roller at fixed temperature/ convective boundary (1D)	↓↓↓	↓↓↓
Analytical solution (1D)	↓↓↓↓	↓↓↓↓

The 3D heat transfer problem has been addressed for both the AFP/ATP [16-17, 23- 24] and FW [18-20, 26-31] methods. Three-dimensional modelling offers a comprehensive description of the complex heat transfer phenomena [20]. However, the substantial computational effort renders these methodologies not suitable for optimisation purposes and iterative schemes, where a high number of solutions is needed. An overview of the main simplifications typically applied are summarised in Table 2.1, presenting the expected effect on computation time and accuracy. The domain is typically simplified to 2D assuming the deposited material and tape are heated uniformly across the width and

the losses through the tape edges are negligible due to the small thickness compared to other dimensions, as well as the high tape length to width ratio [32-63]. Further simplifications can be applied by considering the ratio of the energy transfer due to material advection to energy transfer due to heat conduction, expressed by the non-dimensionless Peclet number. For the AFP/ATP and FW processes, the Peclet number can be calculated as [36]:

$$Pe = \frac{u_x\, l}{a_x} \tag{2.2}$$

where a_x denotes the thermal diffusivity of the composite in the longitudinal direction, u_x is the placement/ winding rate, and l is a characteristic length of deposited tape.

The high values of Peclet number under typical AFP/ATP and FW conditions indicate that the thermal field in the placement/winding direction is strongly governed by material advection, whereas the contribution of heat conduction in this direction is negligible [36, 37]. Low velocities during the first moments of the process can result in Peclet numbers lower than unity. However, this condition is true for a short period compared to the duration of the process. Applying these assumptions, the two-dimensional form of Eq. (2.1), assuming the material thickness is in the y direction, can be simplified to:

$$\rho c_p \left(\frac{\partial T}{\partial t}\right) = \frac{\partial}{\partial y}\left(k_y \frac{\partial T}{\partial y}\right) \tag{2.3}$$

One-dimensional simulation of AFP/ATP and FW based on Eq. (2.3) has been proposed [64, 65], in some cases by decomposing the domain into district 1D models representing the different composite parts and process stages [66-72], as shown in Figure 2.2. The temperatures of the deposited material and tow heating are transferred as initial values to a 1D model which represents the final stack. However, the heat exchange between the composite and compaction roller is simplified to a fixed temperature boundary [69-70], which introduces discontinuities in the profiles near the stack surface, or to a convective boundary of assumed heat transfer coefficient [66-68, 71-72]. In both approaches, the effect of the roller on the temperature field is oversimplified, especially for processes utilising rollers made from low conductivity materials. Strong temperature gradients are developed close to the roller-tow interface necessitating a more accurate description of the effects involved. In other simplified approaches, the through-thickness temperature

distribution of the tape has been assumed to be uniform whilst the heat exchange between the roller, deposited material and mandrel has been modelled as 1D in the radial direction [73]. In addition, the representation of the AFP/ATP process as three bodies of uniform temperature exchanging heat has led to simplified finite differences models [74, 75]. Nevertheless, such methodologies are intended for integration into feedback control systems, providing fast solutions but limited information for comprehensive design.

Three dimensional heat conduction in FW has been simplified by combining submodels with different domains. The domain of the incoming tow has been reduced to 2D or 1D whilst maintaining a three-dimensional representation of the deposited material [19, 27-29]. The 3D deposited material-mandrel assembly has been decomposed to multiple adjacent material slices across the width [10], or through-thickness models along the placement path [30], as shown in Figure 2.3, assuming negligible heat conduction across the width or in-plane direction, respectively. In some cases, the consolidation zone has not been part of the domain limiting predictions to the heating stage of the process [19, 28]. The temperature distribution near the nip point during winding has been captured by a transient thermal model coupled with a 2D steady state model to extend predictions at component level [27]. The local model predictions function as input to the global model in every solution iteration [27].

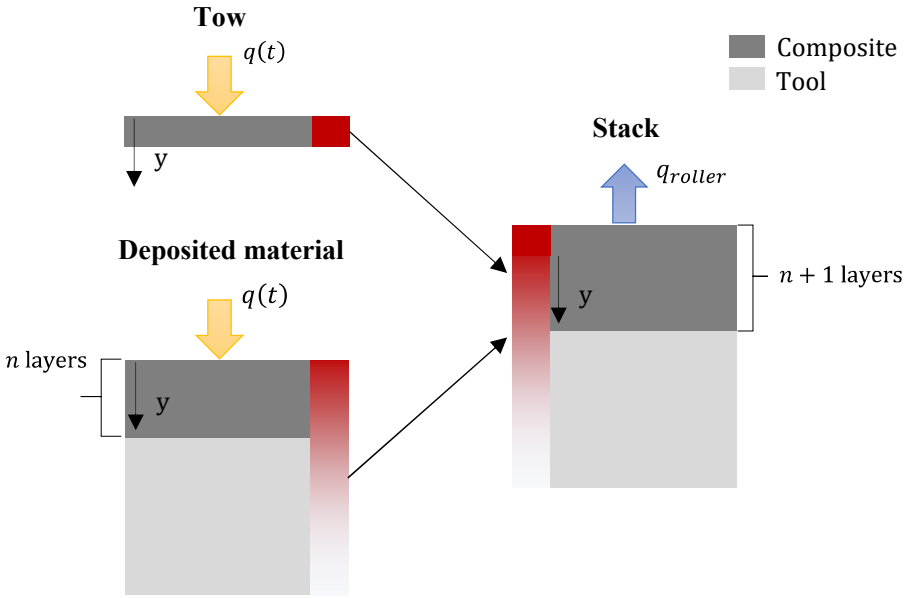

Figure 2.2 Schematic of the decomposition to 1D through-thickness models corresponding to the different composite parts and the necessary transfer of temperature information.

Eq. (2.3) has facilitated the development of analytical models for fast approximations. Existing analytical solutions of a semi-infinite body under prescribed surface heat flux have been adapted to AFP/ATP and FW processes [76-79], assuming the deposited material is partially heated through its thickness, has constant thermophysical properties and uniform initial temperature. In addition, uniform heat flux on the tapes and simplified heat exchange between the composite and the roller are part of the assumptions. A solution corresponding to finite body heating has been developed and combined with the semi-infinite solution as indicated by the dimensionless Fourier number [76] to address the substantial bulk heating at low thicknesses and/or longer heating times. In addition, the heater power, velocity and resulting nip point temperature have been correlated through semi-empirical approaches based on the aforementioned semi-infinite solution [80]. A linear relationship between the nip point temperature and heater power has been assumed to facilitate fitting to experimental data [80]. The limitations of the semi-infinite assumption have been acknowledged, and application of the semi-empirical scheme has been limited to high thickness parts [80].

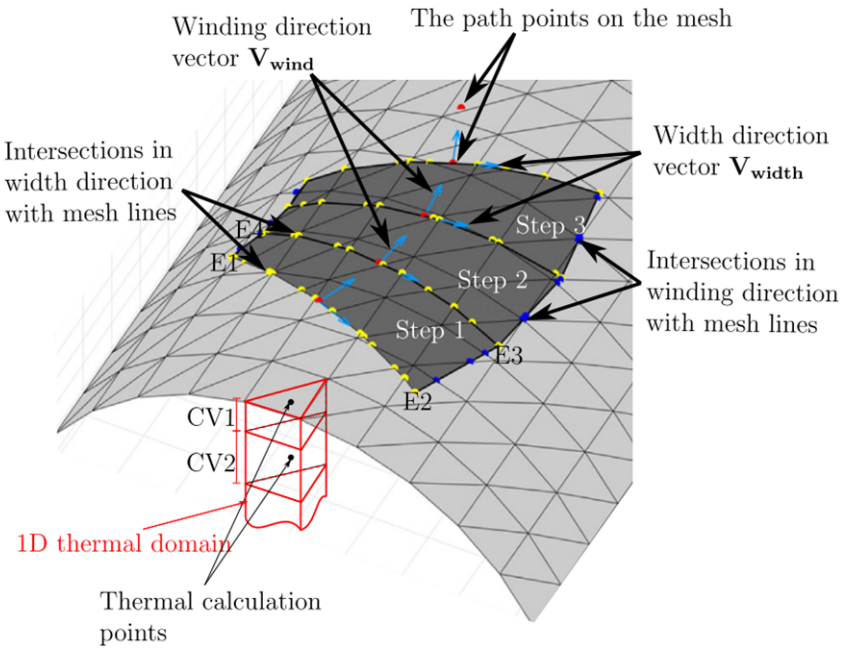

Figure 2.3 Schematic of the kinematics during FW and the decomposition of 3D space into 1D through-thickness models along the winding path. Reproduced with permission from [30].

The finite element (FE) [20, 24, 34, 43, 55, 63] and finite differences (FD) [23, 26, 49, 56, 65, 75] methods have been deployed for solving the boundary value problem in

AFP/ATP and FW processes. The Proper Generalized Decomposition technique has also been applied [17, 45].

2.2.2 Material deposition

The additive nature of the AFP/ATP and FW methods necessitates a modelling strategy to account for the material addition over time. Analyses based on Eqs. (2.1) and (2.3) use a Lagrangian reference system mounted on tool [48-63], where every material point is assigned coordinates that do not vary with time. Simulating the addition of new material and movement of the heating source requires constant adjustment of the boundary conditions. To simplify modelling, the deposition has been assumed to be instantaneous [34], or the tow has been excluded from the analysis, essentially transforming the problem to that of a moving heat source over a stationary surface [23-24]. However, such approaches do not allow the detailed description of the heat exchange effects between the incoming tow and the deposited material. Material addition has also been simulated by progressively activating elements at each iteration step according to the processing rate deploying a birth-death strategy [20, 54, 78], as illustrated in Figure 2.4. The elements are part of the analysis prior to their activation but feature null properties so that they do not influence the temperature field.

A common approach that simplifies the modelling of material deposition involves solution using a coordinate system mounted on the moving placement head [32-47]. Material is advected across an Eulerian analysis frame with a velocity opposite to the placement direction. This is achieved mathematically by introducing additional velocity terms to Eq. (2.1). In the general transient case, the energy balance in a Eulerian frame is expressed as follows:

$$\rho c_p \left(\frac{\partial T}{\partial t} + \boldsymbol{u}^{\boldsymbol{T}} \nabla T \right) = \dot{q} + \nabla \cdot \boldsymbol{K} \nabla T \tag{2.4}$$

where $\boldsymbol{u}$ is the velocity vector of the material with the involved terms corresponding to heat transport due to material advection. Applying the assumptions of Eq. (2.3) to Eq. (2.4) yields:

$$\rho c_p \left(\frac{\partial T}{\partial t} + u_x \frac{\partial T}{\partial x} \right) = \frac{\partial}{\partial y} \left(k_y \frac{\partial T}{\partial y} \right) \tag{2.5}$$

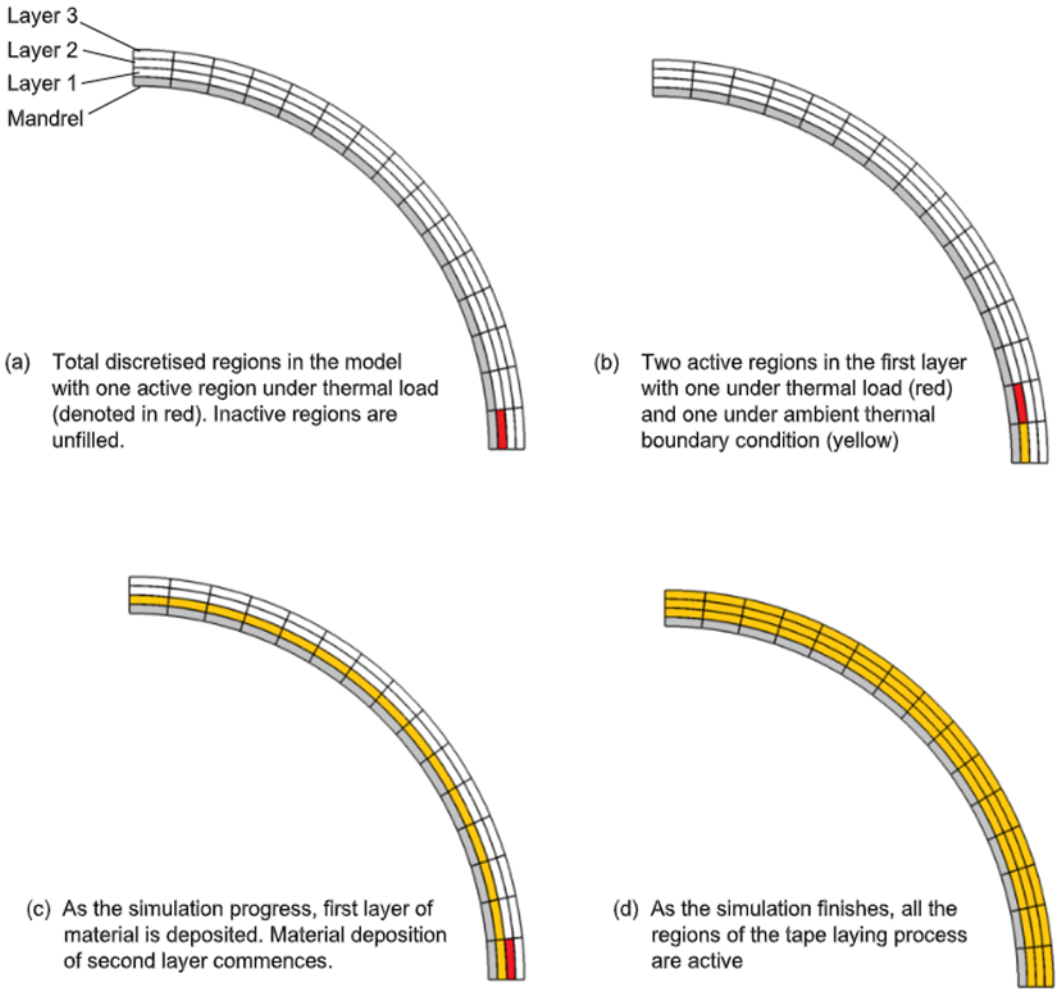

Figure 2.4 Simulation of material deposition using the birth and death technique. Reproduced with permission from [11].

The smaller domain of the Eulerian approach provides efficient solutions in the vicinity of the nip point at the expense of analysing the temperature evolution outside this analysis frame. The analysis follows the deposition head, solving the boundary problem for a narrow time window spanning typically from the irradiation zone start to some point outside the roller contact patch. However, the temperature and material state are not computed outside the narrow analysis frame, necessitating assumptions for the initial conditions at the frame entry points. This imposes challenges when material transformations are considered, which normally progress throughout the process, requiring computation over the full temperature history. Solving for a large enough geometry to capture these effects impacts computational times severely. As a result, the Lagrangian approach has been the preferred method when considering material transformations [20, 52].

2.2.3 Thermal boundary conditions

The boundary conditions in the AFP/ATP and FW processes are complex and in the case of a Lagrangian analysis constantly evolving to emulate the material addition and heating source movement. Boundary conditions apply to the free surfaces of the different bodies, whilst additional interfacial conditions can also apply to the interfaces between composite layers and the composite-roller interface depending on the modelling approach.

A typical 2D heat transfer model of AFP/ATP based on a Eulerian system is presented in Figure 2.5. The compaction roller is typically omitted and the heat exchange with the composite in contact is described as a convective [15, 21, 42, 71] or fixed temperature boundary [69-70]. However, such an approach oversimplifies the heat transfer, especially when low-conductivity rollers are involved. Deformable rollers have been modelled as full [13, 55] or geometrically reduced bodies [16, 39-41, 49] which interact with the composite through conduction. The roller material and deformed shape have a major effect on prediction accuracy due to the influence on contact times with the composite [40]. Water-cooled rollers have been examined and modelled by assigning a constant temperature at the inner roller boundary (S_8) [13, 49].

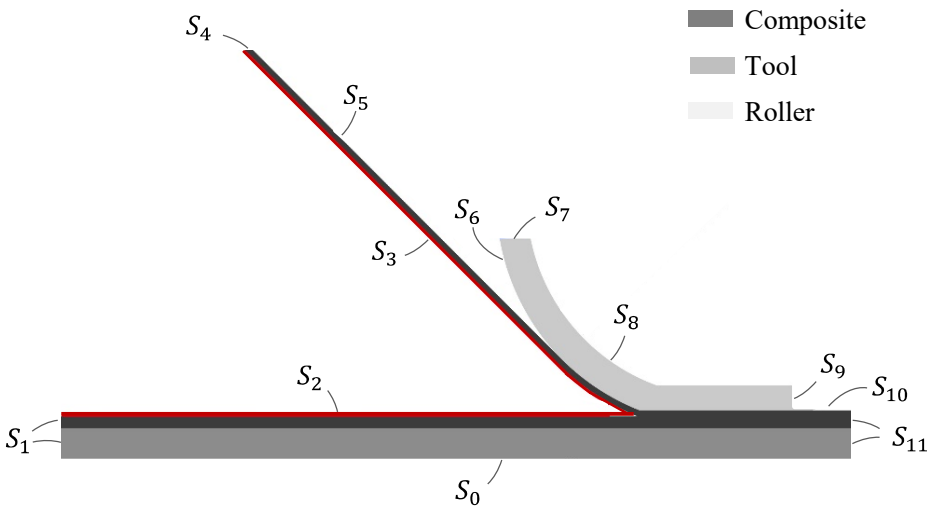

Figure 2.5 Schematic of boundaries for a thermal model of AFP/ATP on a Eulerian system.

The initial temperature of all bodies at t=0 s is typically set equal to ambient. The outer surfaces of the composite (S_5, S_{10}), the roller (S_6), and the tool (S_0) are subjected to free convection to ambient conditions, expressed as:

$$k_y \frac{\partial T}{\partial t} = h(T - T_\infty) \tag{2.6}$$

where h denotes the convective heat transfer coefficient, which is typically set constant and equal for all surfaces, and T_∞ the ambient temperature.

The exit of the roller (S_9) and laminate-tool (S_{11}) are typically assumed to be insulated in the direction normal to the boundary, translated to a time derivative form due to the Eulerian coordinate system:

$$k_x \frac{\partial T}{\partial t} = 0 \tag{2.7}$$

The heat input $q(x)$ acts on the deposited material and tow surfaces, S_2 and S_3 respectively. For IR and laser heating, a boundary of prescribed heat flux is applied on the composites surface:

$$k_y \frac{\partial T}{\partial t} = q(x) \tag{2.8}$$

Hot gas torch heating is commonly modelled as a convective boundary of heat transfer coefficient h_g and gas temperature T_{gas}:

$$k_y \frac{\partial T}{\partial t} = -h_g(T - T_{gas}) \tag{2.9}$$

An additional set of boundary conditions is set for Eulerian analyses to address the fact that computation of temperature is not performed outside the narrow analysis frame. The temperature across the material entry boundaries (S_1, S_4) is typically fixed to a uniform value equal to ambient. The value can be adjusted accordingly when the composite is preheated. An initial temperature above ambient has been assigned to the roller entry (S_7) to account for the increased temperature under continuous processing [16, 39]. A simple relationship can be used to correlate the roller entry (S_7) and exit (S_9) temperatures to estimate its cooling during rotation outside the frame, applying a cooling factor estimated through thermal imaging [49].

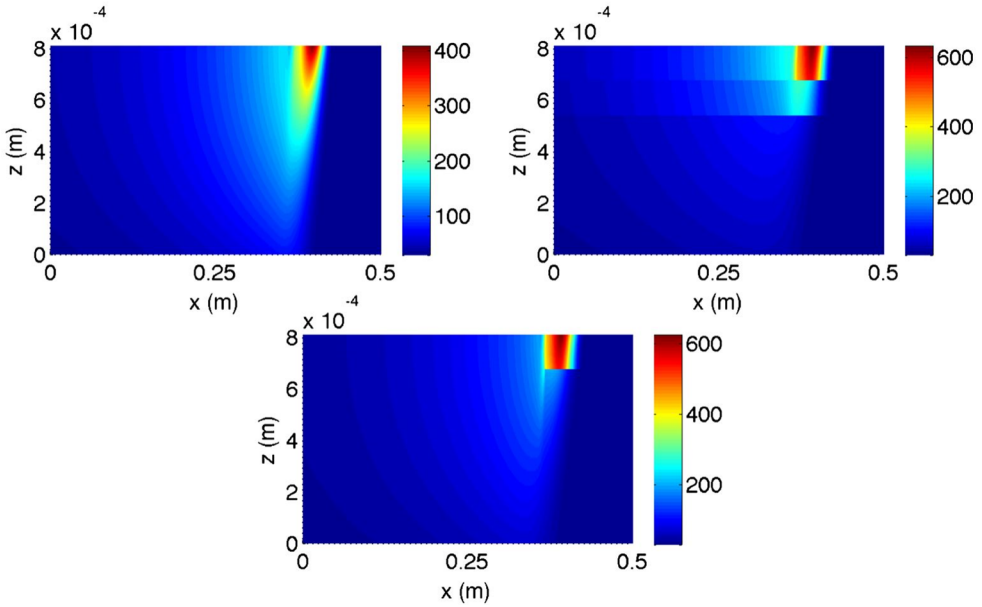

Figure 2.6 Effect of interlayer contact resistances on the through-thickness temperature field (z-direction). Top left: negligible resistances; top right: constant value; bottom: evolving with temperature-time. Reproduced with permission from [45].

Thermal contact resistances can have a strong influence on the heat transfer in ATP/AFP and FW processes. Interlaminar thermal resistance is highly dependent on the surface roughness and the degree of intimate contact developed between adjacent layers [81]. The presence of thermal resistance causes temperature discontinuities, acting as barriers to the through-thickness heat diffusion, as shown in Figure 2.6 [45]. Higher temperatures are developed near the stack surface as a result. However, these effects are typically assumed to be negligible [39, 53, 67]. A constant thermal resistance has been introduced between layers and at the composite-roller interface [17, 24, 37, 39, 45, 49], incorporated in models by defining the heat flux between two bodies or plies as:

$$q_{ij}(x,t) = \frac{1}{R_c(x)}\left(T_i(x,t) - T_j(x,t)\right) \tag{2.10}$$

where $R_c(x)$ is the thermal resistance, and T_i and T_j the temperatures of the corresponding bodies or layers.

In some cases, interlaminar resistance has been determined as a function of the degree of intimate contact during processing [37, 42], based on a relationship derived in [81]:

$$R_c\ (D_{ic}) = D_{ic}(t=0)\ a_o \left(\frac{1}{k_y {D_{ic}}^2} + \frac{1 - D_{ic}}{k_{air}\ D_{ic}} \right) \tag{2.11}$$

where D_{ic} denotes the degree of intimate contact between adjacent layers, a_o a geometrical factor characterising the tape surface roughness, and k_{air} the thermal conductivity of air.

2.2.4 Incorporation of heating sources

Heat transfer analysis has been performed for ATP/AFP and FW processes involving a variety of heating systems. Early work on thermoplastics focused on hot gas torches which can achieve high temperature at low capital cost. Hot air torches have been examined [54, 63, 78, 79]; however, nitrogen-based torches are preferred to suppress the material oxidation at elevated temperatures [18, 38, 61]. Near-Infrared (NIR) lasers are the latest development of CO_2 and Nd: YANG technologies which have been utilised for composites processing. This type of laser has become the preferred option for high temperature applications due to its increased efficiency, fast response, and high-intensity focused beams [40]. Advances in the Vertical Cavity Surface-Emitting Laser (VCSEL) technology have allowed the development of modules with power outputs on par with NIR lasers. Modules featuring multiple VCSEL chips can produce varying power distributions by controlling the power of each chip individually [82-84]. Ultrasonic heating has been studied extensively for the welding of thermoplastics [85-88], but only few studies have addressed AFP/ATP applications [57, 62, 77]. A recent addition to the available options for high-temperature materials are Xenon flashlamp heating systems, which deliver short high-energy pulses to heat up the target surface [89]. The semi-empirical scheme developed for modelling lasers in [80] has been applied to flashlamp heating [90], treating the source as continuous and therefore neglecting the effects introduced by the pulsed operation. Regarding low temperature applications, IR heaters have been studied extensively for thermosetting composites. Heaters based on light-emitting diodes (LED) has also been examined featuring improved response over IR heating, as well as the capability of tailoring the output radiation by controlling each of the LED arrays individually [23].

In the case of gas torch heating, the heat transfer coefficient and gas temperature involved in the convective boundary expressed by Eq. (2.9) are typically considered constant and

uniform, estimated empirically [47, 50, 58, 61] or experimentally by minimising the error between thermal model predictions and temperature measurements using an iterative procedure [20, 31, 55]. However, calibrating against experimental data can yield invalid results if regularisation is not used for the inverse problem. In addition, the calculated coefficient compensates for any inaccuracies introduced due to modelling assumptions and material properties uncertainties. The distribution of the heat transfer coefficient on the tape has been assumed to be three-dimensional determined by four parameters, which have been estimated by fitting thermal modelling results to temperature sensor readings inside the laminate [31]. Jet impingement theory has been employed to predict the heat transfer coefficient in the cavity formed by the tow and deposited material, simplifying it as a 2D corner geometry [14]. A more advanced methodology of combined 3D flow and 2D heat conduction analysis has been developed to determine the spatial distribution of the coefficient across the ATP cavity [38]. The coefficient is highly nonuniform, presenting significantly higher values near the nip point [38].

For IR heating, the heat flux term in Eq. (2.8) is typically estimated based on radiative heat transfer phenomena between two black body surfaces [21, 25, 73]. Similar methods have been applied for LED heaters [23]. The purely geometric quantity of view factor has been introduced to account for the relative orientation of two surfaces, the heater and deposited material in this case. The view factor is independent of material properties. The distribution of irradiance on the composite has been assumed to be uniform, simplifying the view factor analysis [52]. However, the spatial distribution has been estimated across the deposited material by discretising its surface into a grid and performing view factor analysis for each finite area [23-25]. The IR heater has been treated as a point source due to its small size compared to the process tool [24]; however, its dimensions have been considered in other analyses when a comparison to tape width makes the assumption of point source challenging to adhere to [25]. A comprehensive model of IR heater has been developed which accounts for the geometric characteristics and materials of the unit components as well as the relevant heat transfer and optical interactions [73].

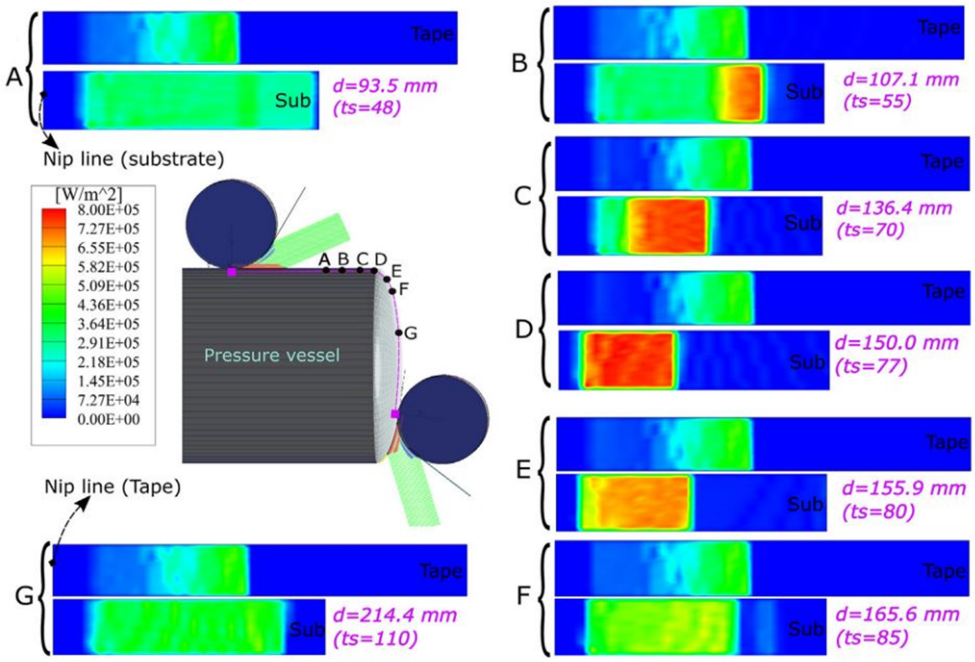

Figure 2.7 Ray tracing predictions of absorbed laser power by the deposited material and tow at different locations across a pressure vessel dome. Reproduced with permission from [28].

The need for accurate representation of thermal boundary conditions has motivated the development of optical models for laser heating. The heat flux distribution on the tapes has been assumed to be uniform, idealising the surfaces as black bodies with total or partial light absorption [15, 34, 39, 41]. Analytical models have been developed assuming first-order specular reflections [49, 91]. More advanced 2D and 3D optical models have been developed based on ray tracing to determine the spatial irradiance on the tapes and subsequently use it as an input to heat transfer models [10, 28, 36, 40, 51]. The ray tracing models describe the interaction of the incoming laser beam with the ATP cavity considering the roller-tow complex geometry and material behaviour. The incoming laser beam has been assumed to be collimated or top-hat divergent [19, 27, 40], or having a two-dimensional super-Gaussian distribution [42]. The reflection from the composite tape has been assumed to be specular [36], or non-specular using either micro-half cylinders on the tape surface [40] or a bidirectional reflectance distribution function (BRDF) based on microfacet theory [91]. Ray tracing modelling has primarily addressed the deposition on flat surfaces but methodologies for curved components have been put forward targeting pressure vessel applications [27-28], as shown in Figure 2.7.

The energy delivered by IR heaters, LED and lasers sources has been primarily modelled as a heat flux acting on the tape surface. The radiation transmittance through carbon fibre composites has been found negligible in the 1-5 μm wavelength range based on modelling and experimental results [92-93]. A model of the radiative transfer through a high-density fibrous medium has been combined with spectrometer measurements [33, 92]. The optical depth has been estimated to be orders of magnitude lower than the ply thickness indicating that the incoming radiation is fully absorbed near the tape surface [92]. In addition, the transmittance of AS4/PEEK tapes has been measured to be below 0.1% in the 500-2000 nm range [93]. The absorption behaviour of carbon fibre composites has been studied using an optical model describing the interaction of incoming laser radiation and fibre-matrix microstructure [94]. The absorptivity of the composite is improved at micro level compared to homogeneous material due to the multiple reflections taking place between adjacent fibres near the surface [94]. Characterisation of the reflectivity of carbon-reinforced composites has revealed a strong dependence on angle of incidence and fibre orientation [92-96], as shown in Figure 2.8. The influence of material temperature has been found to be weak in the 20-450°C range [96], but material state in terms of crystallinity has a strong influence [93]. Radiation transmittance in glass-reinforced composites has been found to be substantial [33]. This effect has been included in heat transfer modelling by introducing volumetric heating as a result of the absorbed energy at deeper material levels [21, 33].

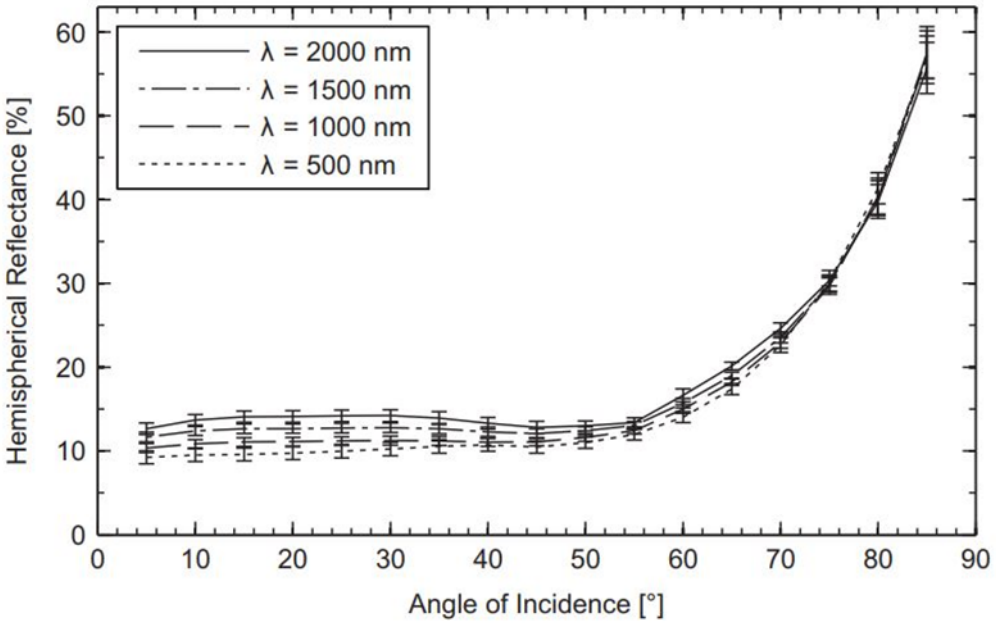

Figure 2.8 The reflectance of AS4/PEEK according to the angle of incidence at various wavelengths. Reproduced with permission from [93].

2.2.5 Material and thermal properties

The heat transfer analysis of AFP/ATP and FW has focused primarily on thermoplastic-based composites, with fewer works on thermosetting matrix materials [20, 23, 52]. Poly(ether-ether-ketone) reinforced with continuous carbon fibres (CF/PEEK) [17, 32, 40, 60, 69] has received significant attention due to its excellent combination of strength, toughness, temperature, and chemical resistance making it ideal for aerospace applications. Lower temperature carbon-reinforced thermoplastics have been studied including polypropylene (CF/PP) [18], polyamide-6 (CF/PA6) [28, 73], polyethylenimine (CF/PEI) [46], poly(ether-sulfone) (CF/PES) [49], polyethylene terephthalate (CF/PET) [77] as well as bindered dry fibre materials [80]. A hybrid material consisting of CF/PEEK tapes and amorphous PEI films has also been modelled [42]. Models for processing glass-reinforced systems have been developed, specifically the composites based on polypropylene (GF/PP) [57, 65, 77] and polyethylene (GF/PE) as matrix [19].

Composites processed with AFP/ATP and FW are highly anisotropic. The thermal conductivity of the composite in the fibre direction is typically an order of magnitude higher than the value in the width and thickness directions. In addition, density, heat capacity and thermal conductivity are temperature dependent. Although the temperature

sensitivity of density can be assumed negligible, a 100% increase of heat capacity and transverse conductivity has been measured for CF/PEEK in the 25- 400°C temperature range [36]. As a result, the thorough characterisation of material properties is crucial for accuracy, considering the wide temperature window of these processes, from ambient up to 600°C. However, characterisation campaigns are challenging and time-consuming, and therefore representative constant properties are typically selected, which also simplifies the analysis. Nonlinear analyses using temperature dependent thermal properties with a linear or nonlinear dependence on temperature have been conducted [31, 36, 39, 73, 78]. Representative values and approaches are summarised in Table 2.2.

Table 2.2 Representative approaches to material thermal properties. [a] Values in the 0-400°C with increments of 50°C, value reported at 200°C; [b] linear relationship in the 25- 300°C range.

Source	Material	c_p (J/kg/K)	k_y (W/m/K)	k_x (W/m/K)	ρ (kg/m^3)
[39]	CF/PEEK	1300 [a]	0.7 [a]	5.9 [a]	1575 [a]
[41]	CF/PEEK	886 - 1803 [b]	0.813 - 1.188 [b]	5.542 - 9.36 [b]	1540
[28]	CF/PA6	1600	5	0.45	1450
[18]	CF/PP	$969.3 + 5.024\,T$ $-0.009794\,T^2$	0.41	0.55	1640
[24]	CF/3900-2 (epoxy)	$2.84610^{-3}\,T + 1.197$	$1.01\times10^{-3}\,T$ +0.44	$1.44\times10^{-4}\,T$ +20.42	1278

2.2.6 Data-driven modelling

In addition to physics-based approaches, heat transfer analysis based on surrogate [97] and neural network models [98-102] has been performed. These approaches utilise a large data set for training which has been generated by a high number of physics-based simulations [97, 100, 101] or experiments [98-99]. Methodologies have combined offline simulations and on-line temperature measurements to increase training effectiveness [102]. Design of experiments (DoE) has been employed to investigate the effect of

process parameters on temperature whilst keeping the effort of data set creation at minimum [97]. Overall, these approaches provide fast computations and can be employed for on-line process control [98, 102]. However, the training data correspond to a specific process ATP/AFP configuration narrowing the application of these in terms of part geometry, heat source characteristics and involved materials. For instance, studies have primarily focused on placement across straight paths and under constant velocities. Deviations from the original data set conditions necessitate a new round of simulations/ experiments.

2.2.7 Influence of process variables

The number of variables affecting the temperatures inside the AFP/ATP and FW processes is high. The influence of major variables on the nip point temperature, which is typically used for process design, are summarised in Table 2.3. Nip point temperature decreases with the placement/winding velocity in a nonlinear way due to the shorter heating timings [36]. In contrast, temperature increases with the heater input as a higher amount of energy is delivered in the proximity of the nip point [36, 61]. The heater input is adjusted differently depending on the heater technology. The energy input from hot gas torches is controlled by the gas temperature and velocity/flow [14, 47, 61, 64, 68], whilst the power of laser sources is defined explicitly. The laser position and tilt angle with respect to the material surface influences the incident energy on the tow and deposited material, and therefore the temperatures developed [30, 43, 66, 97]. Combined thermal-optical modelling is required to elucidate the effect of these changes on the temperatures. The input from IR and LED heaters is also set explicitly and affected by the heater position [23, 25]; however, LED heaters offer increased capability through the control of each LED array power value [23]. The power of flashlamp systems is a product of the operating frequency and pulse duration [89]; however, only the effect of average power has been examined treating the source as continuous [90]. Preheating of the composite and of the tool results in higher nip point temperatures, whereas high conductivity tooling and rollers have the opposite effect due to the increased heat losses away from the laminate. Several other parameters affect temperatures including the roller deformation [10, 39, 43, 68], mandrel radius/curvature [19, 26] and winding angle [19, 65]. The influence of these depends on the configuration examined. Overall, nip point temperatures change monotonically with the major process variables. However, this is

not the case for all parts of the temperature field which are critical for the numerous material reactions involved. As a consequence, the selection of optimal parameters is challenging, as discussed in section 2.3.

Table 2.3 Influence of major process variables on the nip point temperature.

Parameter	Heating technology	Influenced by	Nip point temperature
Processing rate ↑	-	-	↓
Heater input ↑	Hot gas torches	Gas temperature Gas flow rate	↑
	Lasers	Power Spot size Position/tilt angle	↑
	IR, LED heaters	Power Position	↑
	Flashlamp systems	Pulse duration Frequency	↑
Composites Preheating ↑	-	-	↑
Tool temperature ↑	-	-	↑
Tool/ roller conductivity ↑	-	-	↓

2.2.8 Integrated process simulation

Heat transfer modelling is only the first step towards the design of the AFP/ATP and FW manufacturing methods. The thermal models discussed are typically coupled with material constitutive models to elucidate the influence of process variables on product quality. A typical framework is presented in Figure 2.9. The thermal model provides predictions of temperature for given process conditions, feeding bond strength [46, 61, 68, 103-107], crystallisation kinetics [14, 34, 53, 61, 107], material degradation kinetics [34, 61, 107], residual stresses [54, 65, 107, 108-110], and void dynamics [61, 67, 70, 107, 111-112] models to estimate relevant quality metrics. For thermosetting matrix

composites, heat transfer models are coupled with cure kinetics models [22, 52]. Process simulation has also been conducted based on neural networks which have been trained by a high number of physics-based simulations [100-101] or experiments [98]. Training has been achieved combining modelling and experimental practices [102]; however, the experimental input has been limited to temperature readings in the irradiation zone. Data-driven approaches yield fast solutions crucial for process design and optimisation in a viable timeframe for industrial applications. However, generating a large dataset for training can be time-consuming whilst application is limited to the process configuration the simulations/experiments have been conducted for. On the other hand, physics-based process models require significant computational effort to perform a high number of simulations required for optimisation purposes.

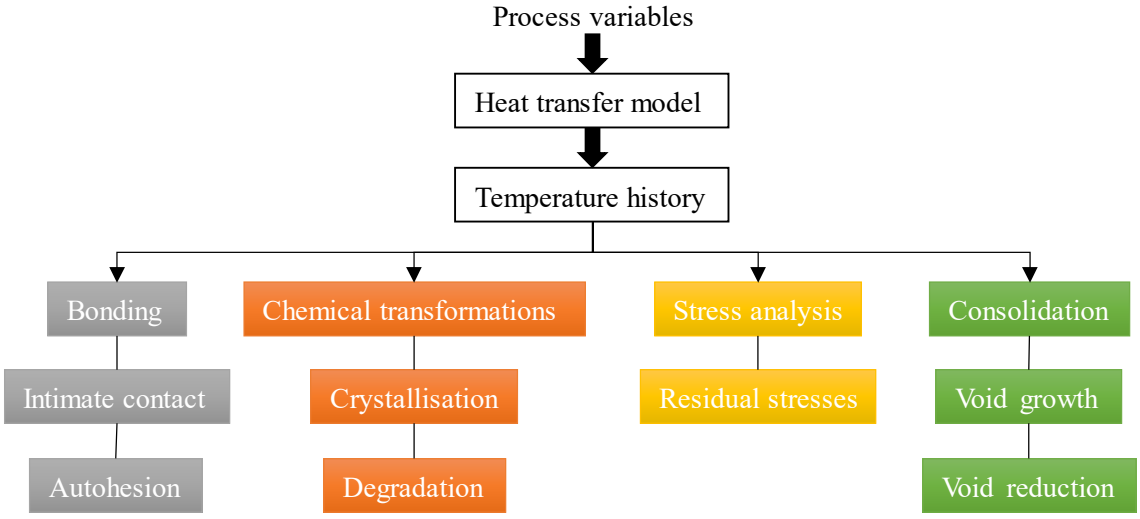

Figure 2.9 Schematic of typical process modelling framework for AFP/ATP and FW.

2.3 Optimisation of ATP/AFP/FW

The selection of process parameters is critical for the manufacture of composites with ATP/AFP and FW. The quality of thermoplastic composites is highly dependent on the temperature history with the optimal processing window being narrow: insufficient heating can lead to partial consolidation and void formation whereas overheating can trigger decomposition effects, damage the polymer, and impede bond development. Effects such as crystallinity, residual stresses and void formation complicate the identification of optimal parameters even further. Out-of-autoclave processing of thermoplastic composites typically yields laminates of inferior mechanical properties,

higher void content and lower crystallinity levels than autoclave or hot press processing [113-122]. Controlled cooling with a heated tooling during the manufacture or post-manufacture autoclave treatment can improve properties significantly [118, 120]. The optimisation of ATP/AFP and FW is challenging considering the number and complexity of the effects involved, as well as the trade-off between quality and productivity. Experimental and modelling efforts for the optimisation of ATP/AFP and FW processes are discussed here, focusing on thermoplastic composites.

2.3.1 Estimation of process window based on temperature thresholds

Processing windows for the AFP/ATP and FW processes have been proposed based on temperatures thresholds of key material reactions or transformations [14-15, 26, 41, 46, 92, 123]. The optimal window is typically restricted within a lower and upper bound, corresponding to polymer melting point and expected thermal decomposition threshold, respectively. Parametric studies have allowed the identification of parameter combinations that yield temperatures within the desirable temperature range. An example of such approach is shown in Figure 2.10. The process map correlates the power and position of the laser source with respect to the nip point to yield maximum bond strength, which requires material melting (above 343°C), and minimum degradation simplified as an upper threshold of 450°C. Such approaches can act as a starting point towards process optimisation. However, the influence of temperature on material reactions is far more complex so that process design based on single temperature values cannot ensure optimised outcomes. For instance, the upper degradation bound has been typically set in the 450-550°C range for the AS4/PEEK, which corresponds to Thermogravimetric Analysis (TGA) results for significantly slower heating rates than those developed in AFP/ATP and FW. The material can potentially withstand higher temperatures for shorter exposure times. On the other hand, interlaminar strength development is a highly time-dependent process, and therefore achieving melting temperatures does not ensure desired outcomes. Interlaminar bond development has also been found to progress even below melting temperatures when the material is in amorphous state [124].

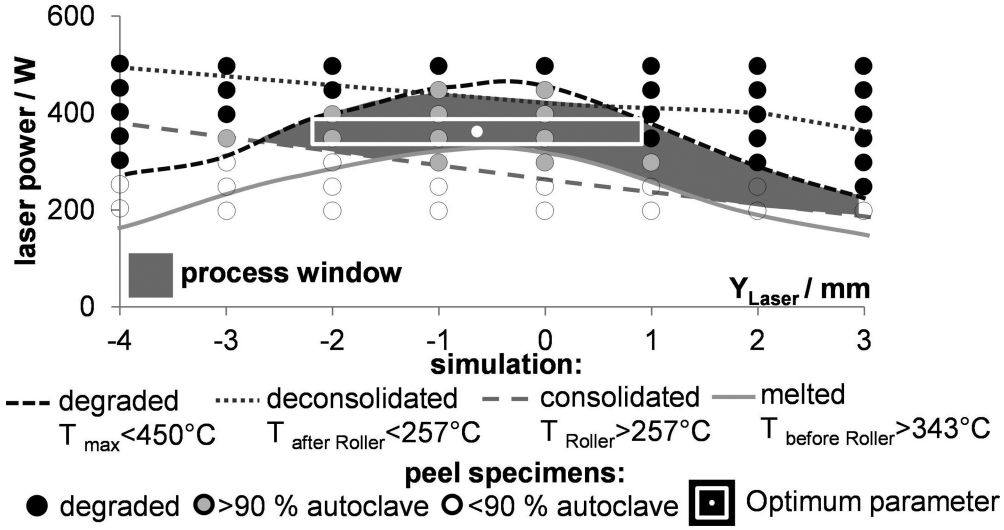

Figure 2.10 Process map of laser power-position achieving maximum bond strength and minimum degradation, simplified as different temperature thresholds. Reproduced with permission from [41].

2.3.2 Optimisation of temperature using optical-thermal analysis

Variations in nip point temperature caused by geometry complexity involved in FW has been addressed by combining optical and thermal analyses [28, 125]. The heater power required for achieving constant nip point temperature across curved geometries, such as the dome part of a pressure vessel, have been determined using an optimisation framework based on a Genetic Algorithm [28]. The nip point temperature during hoop and helical winding has also been tailored through the adjustment of the spatial power distribution on the material [125], enabled by the VCSEL technology. The incident heat flux has been adjusted through an iterative scheme to ensure desired nip point temperature during hoop and helical winding [125]. The nip point temperature achieved after the optimisation of heat source output presents significantly lower variations, as seen in Figure 2.11. However, the controllability of the VCSEL source is only moderate; the heat flux profiles have been scaled almost linearly to compensate for heat accumulation in the stack and mandrel during consecutive placements, indicating that the outcome depends mainly on the power level. To enable fast solutions for such iterative schemes, the nip point temperature is typically calculated at each solution step as the average of two distinct models representing the heating of deposited material and tow [28, 125]. As a result, transient effects taking place in the consolidation phase are assumed negligible.

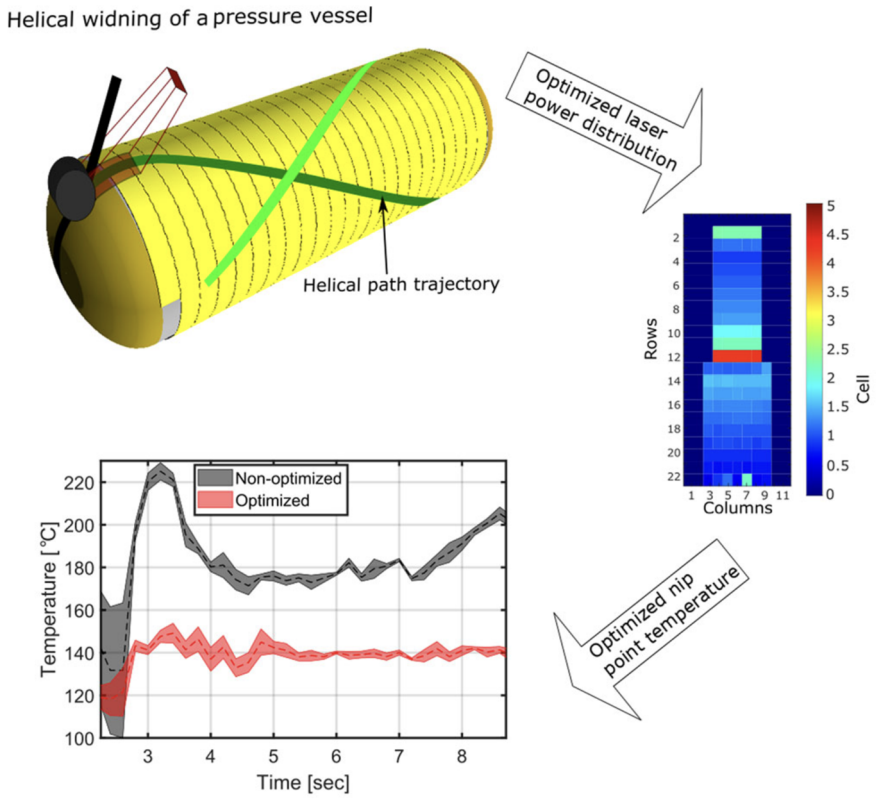

Figure 2.11 Optimisation of the VCSEL source irradiance output to ensure constant nip point temperature during helical winding of a pressure vessel. Reproduced with permission [125].

The irradiation temperatures have been optimised utilising the capabilities of VCSEL sources [82-84], using finite element [83-84] and analytical solutions [82]. To derive an analytical solution, the problem has been simplified to that of a moving tape underneath an emitting VCSEL source, assuming constant thermal properties and significant heat accumulation in the tape (finite body heating). The benefits of controlling the heat zone temperatures through VCSEL heating distributions have been demonstrated by testing the effect of surface profiles on the composite short beam strength [84]. A step change temperature profile has been found to result in the highest strength, attributed to the higher thermal penetration depth in the material, whilst a two-stepped heating profile can provide a good balance between strength and overall source power [84], as shown in Figure 2.12. However, an inverse determination of the surface temperatures, and thus heat flux distributions which achieve the desired quality has not been performed. The potential of improved outcomes has been limited to the examination of pre-defined surface temperature profiles [82-84]. An iterative scheme based on temperature predictions

obtained by the Proper Generalised Decomposition method for a simplified version of the ATP process has been utilised to optimise laser power during velocity changes [126].

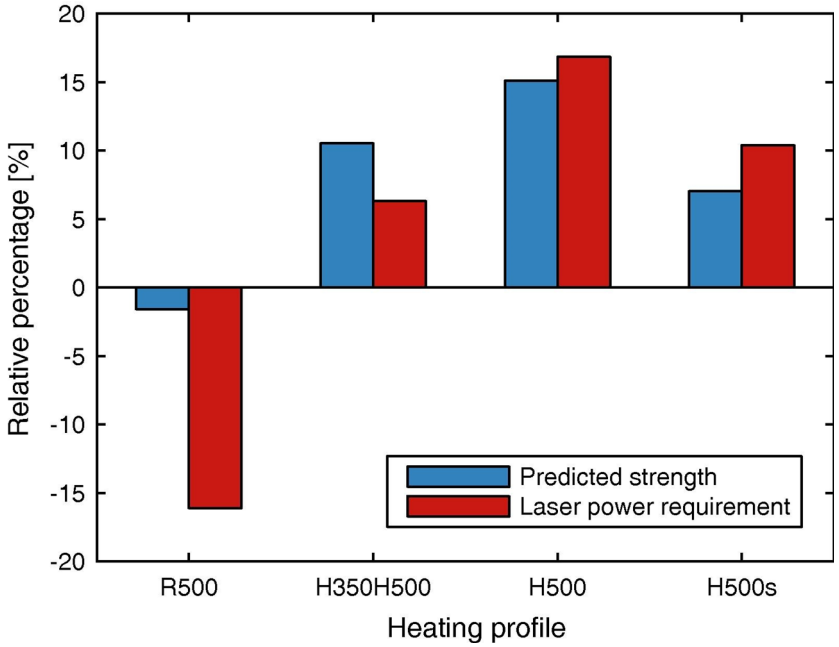

Figure 2.12 Comparison of different VCSEL surface profiles in terms of bond strength achieved and power utilised. Reproduced with permission from [84].

2.3.3 Online tailoring of temperature

Methodologies for the online control of nip point temperatures during the AFP/ATP and FW processes have been proposed, combining temperature feedback from the process with simplified heat transfer models [74-76] or neural networks [98]. Closed-loop control based on temperature measurements on the backside of the tape has been outlined but its development has not been carried out [76]. The application of the method has been limited to conditions which yield significant heat accumulation inside the tape [76]. Nip point temperature feedback using thermal imaging has also been proposed [98, 127]. Nevertheless, the actual nip point is out of sight under the compaction roller. Adjusting the process parameters according to measurements in the vicinity of the nip point location can result in significant errors. Rapid temperature changes occur at this region due to roller shadowing and the abrupt heat exchange when tow and deposited material come into contact [39]. Furthermore, the viewing angle varies with the robot head movements, influencing the effective surface emissivity which acts as a calibration value for such measurements, or limiting it completely across convex geometries.

2.3.4 Numerical optimisation based on process models

Process modelling of AFP/ATP and FW process has offered an in-depth understanding of the role of design variables on part quality. However, the selection of optimal parameters is challenging given the number of involved phenomena, outlined in Figure 2.9. Objectives typically include the maximisation of bond strength and production throughput, and the minimisation of residual stresses, thermal degradation, and void content. These effects present complex relationships with temperature and pressure, therefore with the process variables. The identification of a single set of parameters which satisfies all quality and productivity objectives is in most cases not possible. The interlaminar strength development is facilitated by prolonged heating and compaction, which effectively deteriorates productivity and can trigger thermal decomposition. On the other hand, fast processing results in high cooling rates which impede the crystallisation process. Such dependencies necessitate optimisation to determine the variables sets which offer the best compromise among the different conflicting objectives. However, existing methodologies have limited the optimisation to a single objective, with any additional ones being included as constrains [61, 104, 107]. Parameter sets resulting in objective values outside these constrains are eliminated during the iterative procedure, which effectively narrows down the search for optimal parameters. Objectives related to bonding quality and void content have been integrated into a single cost function [101], as shown in Figure 2.13. The Nelder-Mead and the Levenberg-Marcqart algorithms have been utilised to solve the minimisation/maximisation problem [104, 107], whilst exhaustive searches have also been conducted [61]. The latter approach can be highly inefficient and time consuming considering the high number of parameters and broad range of values. Combinations of parameters leading to desired quality have been identified, and selection has been narrowed down based on the highest processing rate [101]. Overall, a strong trade-off between degree of bonding and velocity exists. Multi-objective optimisation has been performed for autoclave curing of thermosetting composites [128] but not for the AFP/ATP or FW manufacturing methods.

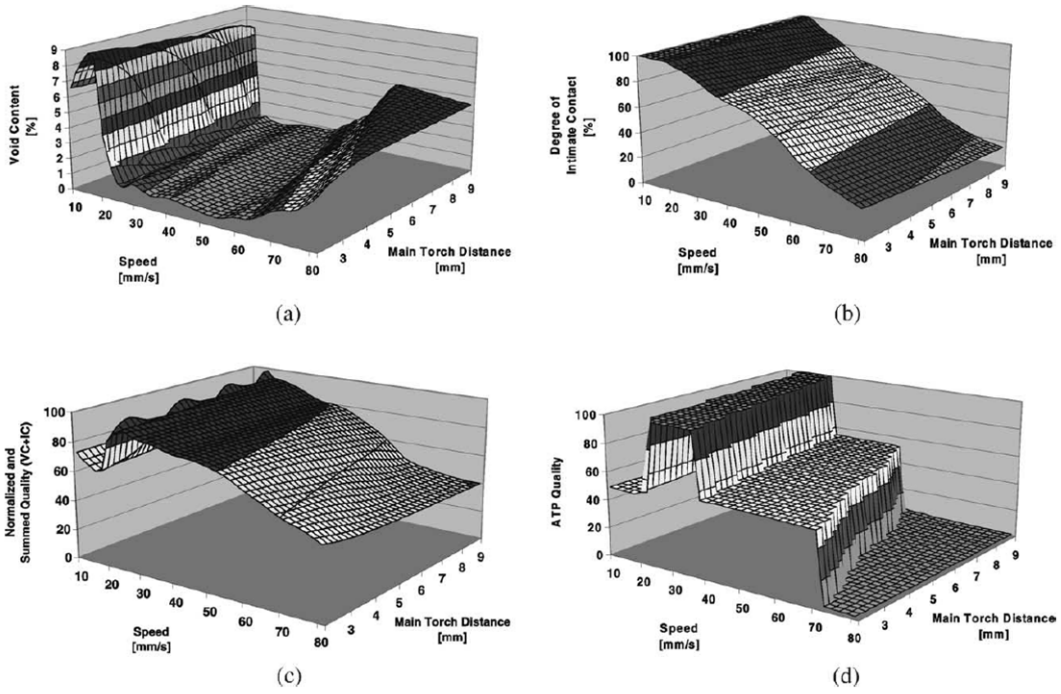

Figure 2.13 Model outputs and evaluation of single objective cost function (ATP Quality) combining void content and bond quality calculations. Reproduced with permission [101].

2.3.5 Experimental investigations and optimisation techniques

The influence of process parameters on the produced part quality has been investigated through mechanical and physical testing [113-122, 129-160]. The interlaminar shear strength (ILSS) of laminates fabricated with AFP/ATP and FW has been measured with the short beam strength (SBS) method [46, 69, 113, 118, 129, 141, 155]. The interlaminar fracture toughness in Model I has been measured using the double cantilever beam method (DCB) [114-116], whilst for Mode II the end-loaded split (ELS) technique has been deployed [71]. The single lap shear [114, 146] and wedge peel tests [113, 131, 140] have been proposed as alternatives to the time-consuming SBS and DCB tests. However, the wedge peel testing can only act as a comparative technique due to certain difficulties associated with high friction between the layers and the wedge. As a result, the mandrel peel technique has been chosen to quantify the interfacial fracture toughness [132-133]. The interlaminar shear device (ISD) has also been utilised as an alternative to SBS [117]. Mechanical testing conducted also includes tension [120], compression [118, 120], three-point bending [77, 113], in-plane shear [121], unnotched pendulum impact [115] and open hole compression [113, 144] testing. Bond quality has been approximated using non-destructive ultrasonic methods [130, 149]. The crystallinity levels of specimens have

been measured using differential scanning calorimetry (DSC) [115, 120, 131, 137, 147], Fourier transform infrared spectroscopy (FTIR) [137] and X-ray powder diffraction (XRD) [108]. Dynamic mechanical analysis (DMA) [116] and TGA [118] have also been deployed in relevant studies. The void content of samples has been determined with a variety of techniques including 2D microscopy, weight measurements, the immersion or displacement method, matrix acid digestion, C-scanning, 2D microscopy and 3D X-ray tomography [70, 113, 118, 122, 130, 142, 145]. Surface roughness measurements have been performed to assess the effect of different repass treatments to the laminate surface quality [136, 144]. Nano-indentation testing has been performed on cross sections of laminates fabricated in autoclave and with AFP/ATP methods to determine the differences in modulus and hardness.

Optimisation of AFP/ATP and FW processes based on experimental methods is a time-consuming and costly procedure due to the wide parameters space. Efficient planning of the experimental campaign is crucial to minimise the effort needed. For this purpose, experimental optimisation has been achieved by deploying the DoE and Taguchi methods [150-154]. Three to four process variables are typically selected with these fractional factorial design methods, each acquiring three potential values (levels). The combinations to be tested are determined by orthogonal arrays. The results are analysed with statistical methods which indicate how each factor influences the examined objective, whilst analysis of variance (ANOVA) is used to quantify the contribution of each factor. Optimisation has been limited to a single objective which has simplified the selection of the optimal variables among those tested. However, Taguchi results have been combined with grey relational analysis (GRA) and surface respond methods (RSM) for the optimisation of the sample tensile strength and induced residual stresses [154]. Virtual sample generation (VSG) have been employed to expand the experimental data set for training of neural networks [155-157]. Surrogate models based on experimental results [158], as well as approaches based on the surface response method [159-160] have been reported. A typical response surface of a quality aspect against two major process variables generated by experimental testing is shown in Figure 2.14. Overall, these methodologies rely on a small number of data points which can lead to inaccuracies since the uncertainties of experimental practices are not addressed. Furthermore, application is

restricted within the initially tested parameters range, whilst conclusions and regression models correspond to a specific process configuration and material system.

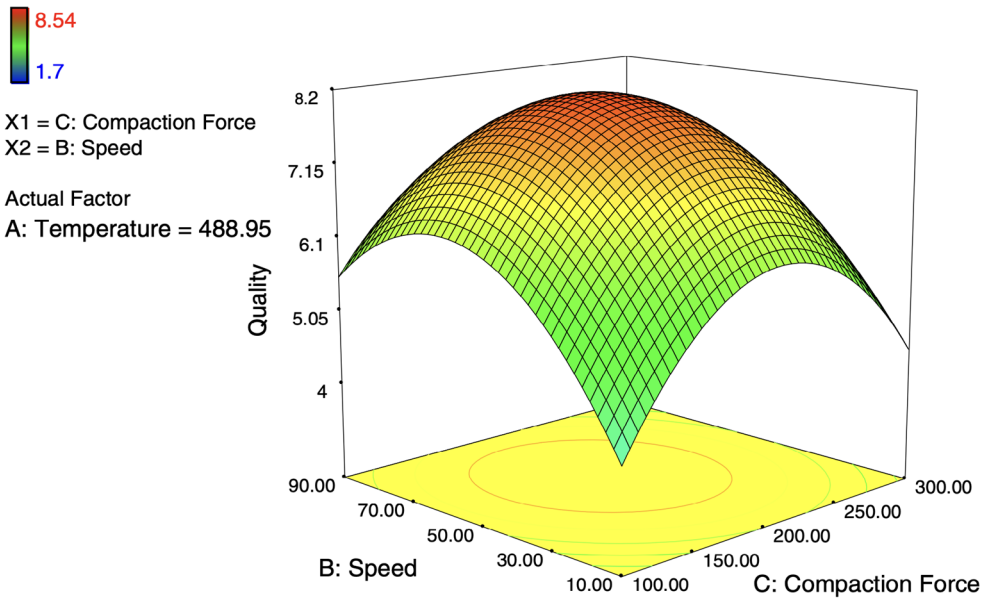

Figure 2.14 Response surface of a quality related aspect against two major process variables. Reproduced with permission from [159].

2.4 Monitoring of ATP/AFP/FW manufacture

The use of predictive simulation for the design and optimisation of AFP/ATP and FW, discussed in sections 2.2 and 2.3, yields results which correspond to ideal process conditions and material properties. Deviations from the conditions the process design corresponds to can lead to temperatures outside the narrow optimal window, and therefore hinder the process outcome. On the other hand, equipment inaccuracies can introduce major defects in the layup, such as gaps and overlaps between adjacent placement paths. Producing high-quality parts with AFP/ATP and FW necessitates in-process monitoring to incorporate variations in conditions and materials behaviour in process and quality control. The state-of-art on monitoring of these manufacturing methods is discussed here.

2.4.1 Detection of placement/winding defects

The identification of placement/winding defects during AFP/ATP and FW processing has been achieved with a variety of techniques [161]. Online detection of placement defects and foreign objects has been performed based on thermography [162-168]. A thermal imaging device is typically mounted on the moving placement head to capture the temperature distribution on the composite surface. Localised disruptions of the

temperature field in the form of significantly colder or hotter areas are identified as defects, as shown in Figure 2.15 [162]. However, setting the threshold for translating temperature deviations to defects is challenging due to the wide temperature range in these processes and the transient effects involved. This necessitates establishing the link between process variables and temperature readings [166]. Furthermore, monitoring of defects with thermal imaging is only possible on the laminate surface. Defects at deeper levels can be identified using optical fibre Bragg grating sensors [169]. In this case, the defects are detected as changes in the reflected spectrum of Bragg grating sensors embedded in the layup. For similar purposes, the relationship between void content and stress wave propagation has been investigated experimentally by mounting strain gages in the proximity of the deposition region [170]. Wave attenuation increases with void content due to the scattering of energy and stress concentrations around defects [170]. However, the use of these sensor-based strategies in an industrial environment is challenging, since the utilisation for large multilayer components necessitates a high number of sensors.

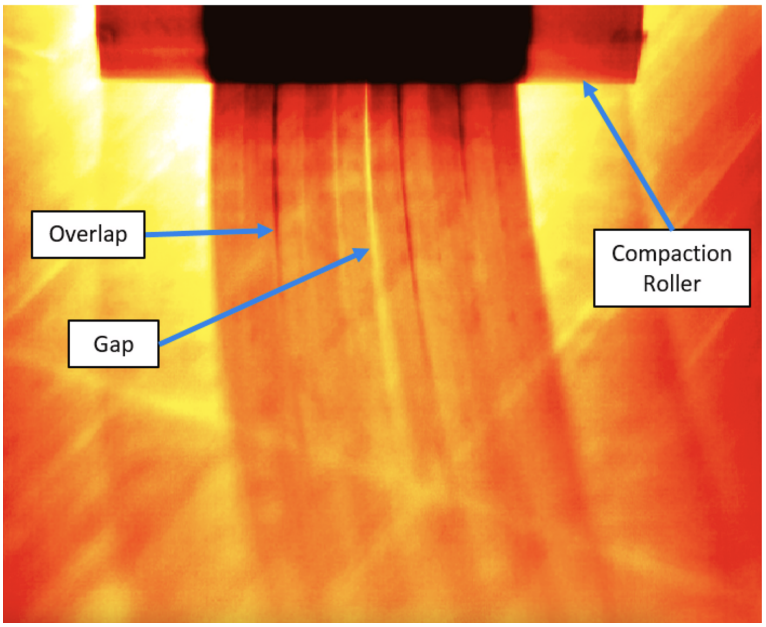

Figure 2.15 Identification of placement defects using thermal imaging. Reproduced with permission from [162].

Strain and deformation measurements have been conducted during AFP/ATP processing by utilising digital image correlation techniques [171]. However, carbon fibre composites have a black colour which challenges the application of these strategies. Applying a

random pattern of points using paint has been typically adopted for offline inspection. Tapes have been treated with specialised high-temperature paints to enable the application of these techniques during AFP/ATP [171]. As an alternative, a digital projection method has been proposed [173] which is adequate for assessing gaps and overlaps, but it cannot yield strain measurements since the pattern is not applied to the component surface. Placement accuracy has been evaluated through laser scanners and laser-vision systems [172-173]. On-line placement path correction based on the detection of tape edges using a laser sensor has also been performed [173].

2.4.2 Temperatures monitoring

Monitoring of temperatures in AFP/ATP and FW is essential to ensure conditions are within the optimal window and to enable the control of process variables to compensate for variations. Thermal image devices mounted on the moving placement head and miniature thermocouples embedded in the layup are typically deployed for monitoring temperatures. Optical fibre Bragg grating sensors have also been utilised [174]. Thermal imaging offers continuous remote measurements on the surface of the tape and deposited material. However, the monitoring and control capabilities are limited to irradiation temperatures. The nip point and bonding zone are out of sight under the compaction roller, with the temperature history across these regions having a critical role in material reactions and transformations. Furthermore, the viewing angle varies with the robot head movements and can be limited over convex geometries. On the other hand, embedding sensors in, or in contact with, the moving material is possible in experimental setups, but not in a production environment due to the additive nature of these processes.

Utilisation of thermal measurements in conjunction with simplified models and inverse methods can yield useful information for the process parameters and their influence on the product. Such methodologies have been put forward for the curing of thermosetting composites manufacture [175-176], but not for AFP/ATP or FW primarily due to the challenges of acquiring accurate temperature measurements on the material as it is processed. A closed-loop control system combining pyrometer readings on the tow back surface and approximate process model has been outlined [76]. The method works under finite body heating, whilst monitoring under strong temperature gradients across the tape thickness is not possible.

2.5 Research gap

As discussed in sections 2.2 and 2.3, heat transfer and optimisation methodologies have been developed for AFP/ATP and FW processes which utilise hot gas, IR or laser heating. Unlike established heating systems, flashlamps feature a pulsed operation which can introduce additional capabilities over continuous heating since the selection of operating frequency and pulse duration determines the delivery of energy to the materials. To unravel these effects, a thorough understanding of the influence of pulsing parameters on the temperature field and part quality must be established. Efforts in this direction in an AFP/ATP and FW environment have not been reported. A semi-empirical heat transfer model based on experimental estimates of the steady-state nip-point temperature has been utilised to analyse the process [90]. Nevertheless, the scheme has been originally developed for laser heating and thus the pulsed source has been treated as continuous, limiting the investigation significantly.

Computation time of model-based optimisation is critical to yield results in a feasible timescale and render methodologies suitable for industrial application. As discussed in section 2.2, simplified heat transfer models are typically preferred for integration into process models to enable faster solutions. However, existing approaches involve major assumptions on aspects regarding the roller implementation, temperature-dependent material properties and non-homogeneous irradiance distribution on the tapes. An approach of decomposing the domain to 1D subdomains has been put forward; however, the effects of contact between the composite and the roller and its dynamic character have not been considered [66-72]. An 1D methodology which accounts for these effects, as well as being applicable to flashlamp heating, is necessary to act as the heat transfer model for use in iterative schemes such as optimisation frameworks, inverse solutions, training of AI approaches and stochastic simulation.

Numerical optimisation developed for AFP/ATP and FW has been limited to a single objective introducing other desired targets as constrains [104]. Such approaches can yield optimised results concerning the examined objective but the trade-offs and interdependencies between the different variables and material phenomena are not elucidated. This often necessitates further decision-making since there is not a single set of parameters that satisfies all conflicting objectives. Multi-objective optimisation can

uncover these effects; however, such frameworks have not been developed for AFP/ATP or FW processes. In addition, existing schemes utilise an exhaustive search which can be highly inefficient, or algorithms which are prone to converging to local minima. The use of GA could provide an improved description of the objectives space due to the integration of crossover and mutation functions, which are designed to extent the investigation away from identified optima. Finally, proposed methodologies do not incorporate process models describing flashlamp heating, and therefore cannot optimise the flashlamp frequency and pulse duration to reach improved outcomes potentially unlocked by this type of heating.

As discussed in section 2.4, monitoring of temperatures in AFP/ATP and FW has been typically carried out using thermal imaging or sensors embedded in the layup. However, methodologies utilising thermal measurements in combination with process models and inverse methods have not been developed for AFP/ATP or FW processing. The concept of a closed-loop control system combining thermal imaging measurements on the tow back surface and an approximate process model has been outlined but its development has not been carried out [76]. Establishing a method for in-process estimation of the temperature and process conditions, such as the heater input, at critical locations inside AFP/ATP and FW is a fundamental step in exploiting its automation potential while meeting product quality requirements.

3. Methodology

3.1 Introduction

This chapter covers the general methodological approaches followed in this work. The characterisation of flashlamp systems and instrumented ATP manufacturing trials conducted for the validation of the modelling studies are detailed. The principles of heat transfer modelling and the finite element method utilised for solving the boundary value problem of ATP are also described. The ray tracing technique employed for addressing the optical simulation of the process is introduced. The materials and their constitutive models are reported, as well as the testing for thermal degradation modelling. The method for the multi-objective optimisation of ATP is also presented.

3.2 Materials

The composite material studied in this work is the APC-2 system produced by the Solvay Group [177]. The composite consists of thermoplastic poly(ether-ether-ketone) matrix reinforced with continuous AS4 carbon fibres, commonly referred as AS4/PEEK. This tape has been widely used in automated processing due to its excellent combination of high strength, toughness, temperature and chemical resistance making it ideal for aerospace applications. The polymer is semi-crystalline with a glass transition temperature of 140°C and a melting point of approximately 340°C. The material was supplied in a form of 25 mm wide unidirectional tapes for manufacturing trials and characterisation, featuring a nominal 60% fibre volume fraction.

Aluminium tooling and deformable elastomeric rollers were included in the experimental and modelling studies as part of the ATP equipment employed for the manufacturing of AS4/PEEK composites. The roller was produced by MBK MaschinenBau Kieler [178]. Aluminium and quartz glass parts were also involved in the optical modelling of the flashlamp system head.

3.3 Process trials

Instrumented ATP manufacturing process trials were carried out for the validation of modelling work. A typical ATP configuration is illustrated in Figure 3.1. The basic principle of processing thermoplastic composites with ATP is the sequential deposition of material layers by a moving robotic head onto a tool, in order to build the part in an additive fashion. During the placement, an energy source heats the new layer and the already deposited part moments before they come in contact underneath a compaction roller. Melting temperatures are achieved which in conjunction with the pressure applied under the compaction roller facilitate the bonding between the composite layers.

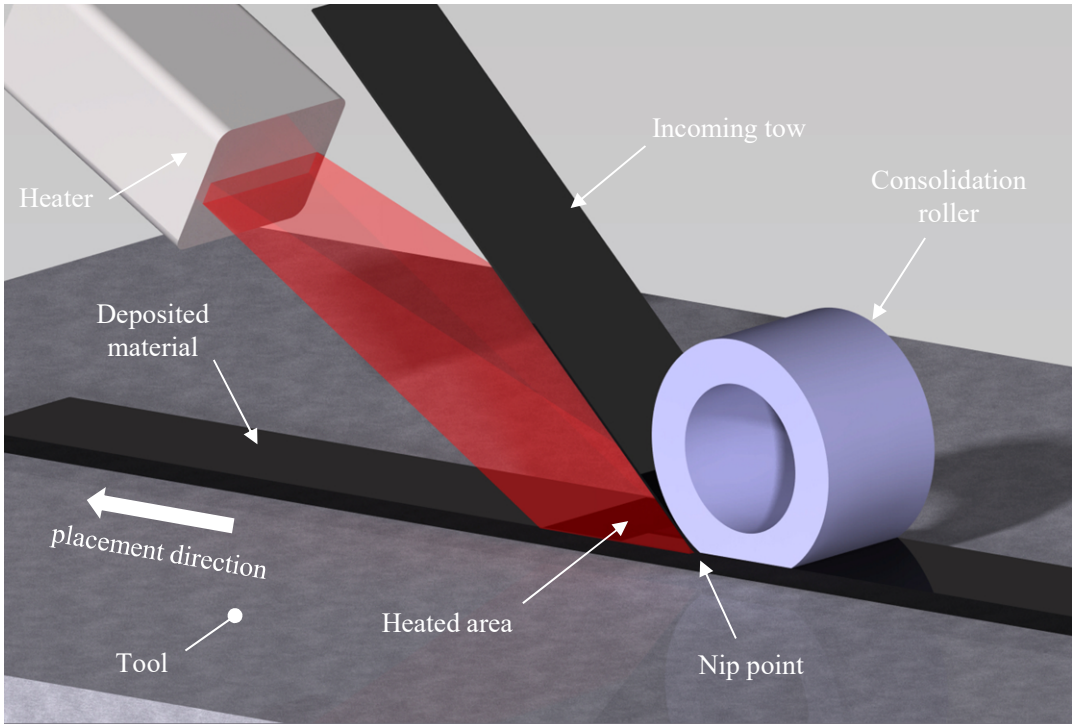

Figure 3.1 Schematic of typical ATP processing.

The humm3® system by Heraeus Noblelight [179] was utilised as heating source during the manufacturing ATP trials of this work. This technology converts electrical energy stored in a capacitor into a high intensity light flash. It produces light by passing electricity through ionized Xenon gas at high pressure in a quartz glass tube, producing short-duration energy pulses when triggered under high voltage. The system can deliver single pulses or a sequence of desired frequency, offering a greater flexibility and opportunities for tailoring compared to existing continuous sources such as lasers and IR heaters. These advantages in combination with the fast response to operation changes,

equivalent to lasers but superior to IR heaters, increase the potential for advanced process design and on-line control. Despite being as powerful as lasers, flashlamp systems do not require strict safety measures around the manufacturing area during processing. In terms of cost, flashlamp systems are placed in the middle ground between IR lamps and laser systems, with the latter usually being associated with high acquisition and operation expenses.

A typical humm3® system head is shown in Figure 3.2. The Xenon flashlamp is located inside the head housing submerged in a water-filled chamber for cooling purposes. The housing features reflective interior surfaces to redirect the light emitted by the flashlamp towards the head opening, where a solid quartz part takes over the task of delivering the light to the desired location (Figure 3.2a). The quartz light guide can be engineered to adjust the irradiation area size and energy distribution. In ATP applications, the system head is typically mounted near the cavity formed by the deposited material and tow, with the quartz block being few millimetres away from the tapes surface (Figure 3.2b).

(a) (b)

Figure 3.2 humm3® heating system: (a) head design; (b) operating position inside the ATP process. Reproduced with permission from Heraeus Noblelight Ltd.

3.3.1 Flashlamp system characterisation

The humm3® system utilised in the manufacturing trials of this study features a Xenon flashlamp capable of delivering 4.4 kW of average electrical power. The system delivers single pulses with their duration been adjusted when in pulse train mode according to the operating frequency so that the system power is not exceeded. The system average power for given pulsing conditions can be calculated as the root mean square power of the waveform:

$$\bar{P} = \sqrt{F \int_0^{\frac{1}{F}} P(t)^2 \, dt} \tag{3.1}$$

where F is the pulsing frequency and P the instantaneous system power at time t.

The system average power is not determined explicitly by the user but is a product of frequency, pulse duration and driving voltage. The latter varies during pulse delivery as a result of gas transformation into plasma and the power supply capacitors charging /discharging rapidly under continuous operation. Therefore, the instantaneous power during a pulse is a system characteristic which depends on the lamp design/size, gas pressure/mixture and power supply architecture/efficiency.

The power curve during pulsing of the humm3® system was characterised in order to enable accurate power control during the manufacturing trials of this work. A high-voltage differential probe TA044 by Pico Technology [180] was connected in parallel to the lamp connection points, whilst a TA167 current probe [181] was used to measure the current across the head connection power lines. The signals of instantaneous voltage and current were captured by a Tektronix MDO3024 [182] oscilloscope at a sampling rate of 2500 Hz in triggering mode. The signals were multiplied to calculate the power drawn by the system. The source was left pulsing for 10 s before measurements were conducted to ensure the measured values correspond to nominal steady state operation. Figure 3.3a presents the instantaneous power during pulses of different duration at 140 V, whilst Figure 3.3b depicts the effect of driving voltage to pulse power for 4 ms pulses. Overall, the system power during a pulse is an order of magnitude higher than the average value specified. The short duration of the pulses relatively to the period results in a lower average value over a given time period, equivalent to continuous sources. This ratio is known as the pulse source duty cycle (D):

$$D = p\,F \tag{3.2}$$

where p is the duration of the energy pulses.

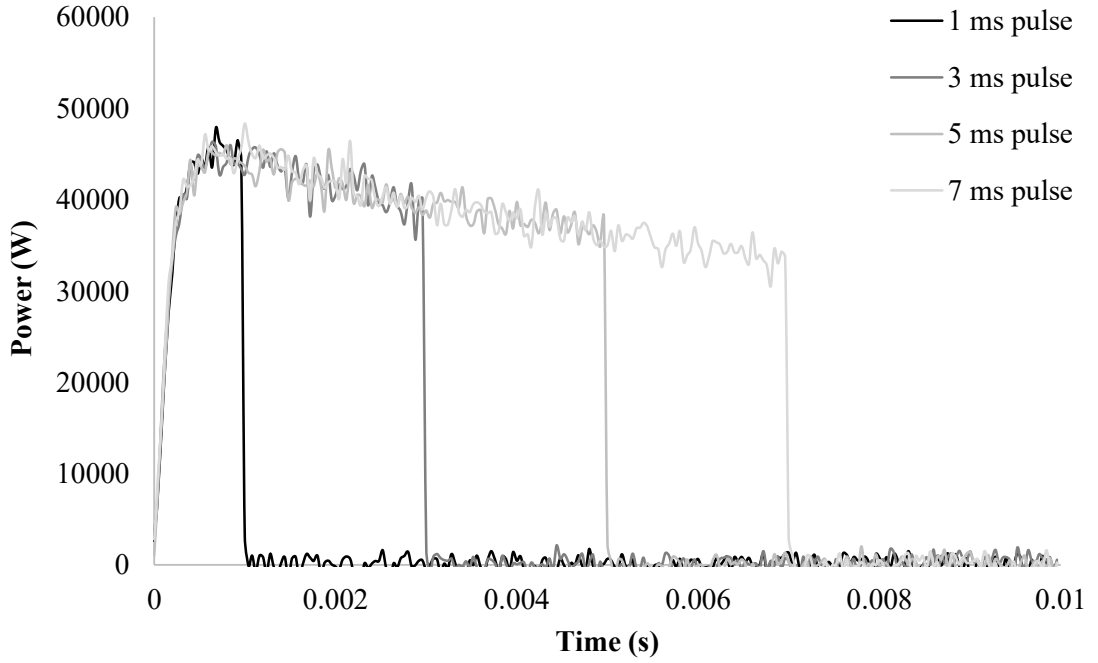

(a)

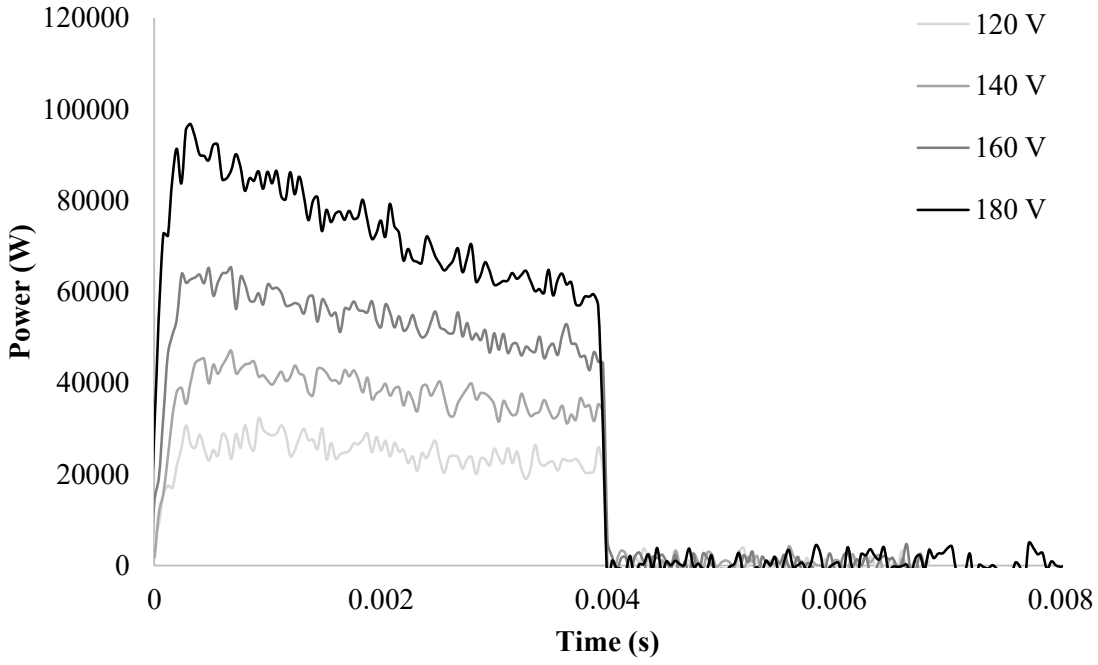

(b)

Figure 3.3 Power measurements on the humm3® flashlamp system of this study: (a) different pulse durations at 140 V; (b) 4 ms pulses at different driving voltage.

The power curve features an initial response phase in which power increases rapidly until a nearly horizontal value is reached (Figure 3.3). A non-linear drop of power follows before the power is switched off by the power supply to create pulses of the desired duration. Pulses of different duration follow equivalent initial responses and power drop

phases (Figure 3.3a). On the other hand, voltage shifts the pulse power curve to higher/ lower values (Figure 3.3b), adjusting the possible combinations of frequency and pulse duration according to the system capability (Eq. (3.1)).

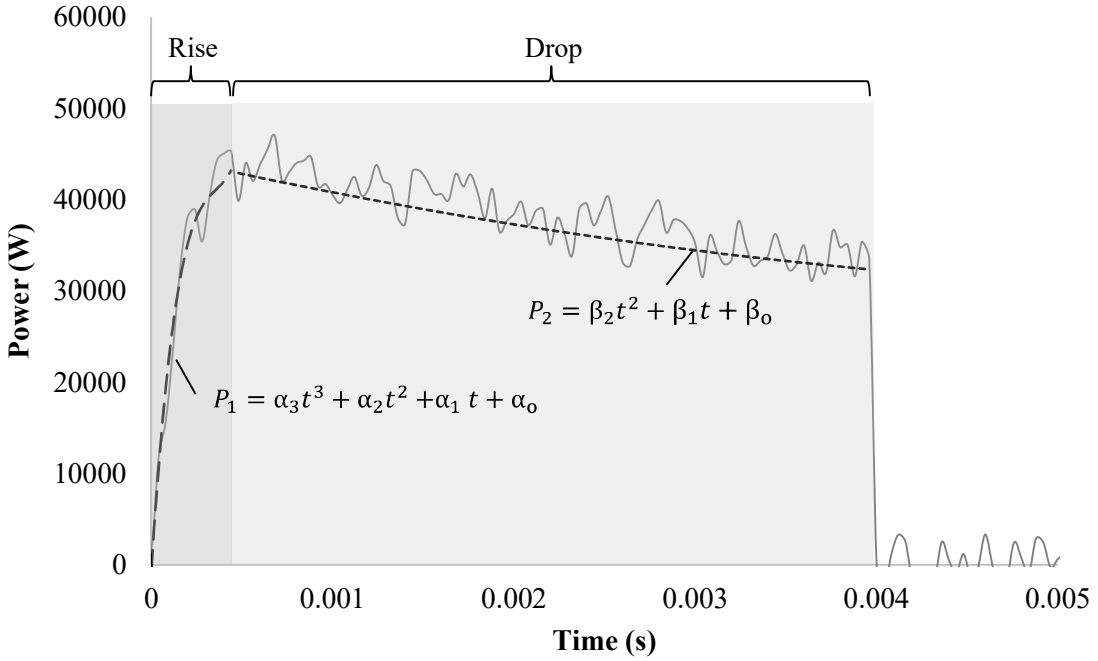

Figure 3.4 Polynomial fitting of pulse power curve. 4 ms pulse at 140 V.

The instantaneous pulse power of a flashlamp system is influenced by the voltage but not the operating frequency or pulse duration (Figure 3.3). Polynomial equations were fit to the power curve data to develop an expression representing the evolution of power during the pulse. The power curve was segmented in two parts describing the initial rise and subsequent power drop stages with a single equation each, as shown in Figure 3.4. Third- and second-degree polynomials were found sufficient to describe these pulse phases. Coefficient of determination (R^2) values of 0.98 and 0.95 were achieved respectively. The parameters of this fitting are reported in Table 3.1 for the 140 V case. The resulting expressions are a function of time. As a result, the system average power can be calculated by Eq. (3.1) for a given pulse duration and frequency without conducting additional measurements, which can be useful for controlling the system output during the manufacture.

Table 3.1 Fitting parameters at 140 V for the polynomial representation illustrated in Figure 3.4.

Stage	Parameter (W/ms)	Value	R^2
Rise $0 \leq t \leq 0.44$ ms	α_3	7.74×10^{14}	0.98
	α_2	-8.22×10^{11}	
	α_1	3.12×10^{8}	
	α_o	-5.4×10^{2}	
Drop $0.44 \leq t \leq 4$ ms	β_2	3.4×10^{8}	0.95
	β_1	-4.57×10^{6}	
	β_o	4.5×10^{4}	

For heat transfer modelling purposes, the pulse shape is simplified to rectangular which allows the description of instantaneous power during the pulse event with a single power value, as shown in Figure 3.5. Eq. (3.1) is reduced to:

$$\bar{P} = p\ F\ P_{rec} \tag{3.3}$$

where P_{rec} is the constant power value which results to equal area, thus average power, with that calculated based on the polynomial fitting and Eq. (3.1):

$$P_{rec} = \frac{1}{p}\int_0^p P(t)dt \tag{3.4}$$

The value of P_{rec} was calculated to be approximately 39 kW for 4 ms pulses and 140 V operation, as shown in Figure 3.5.

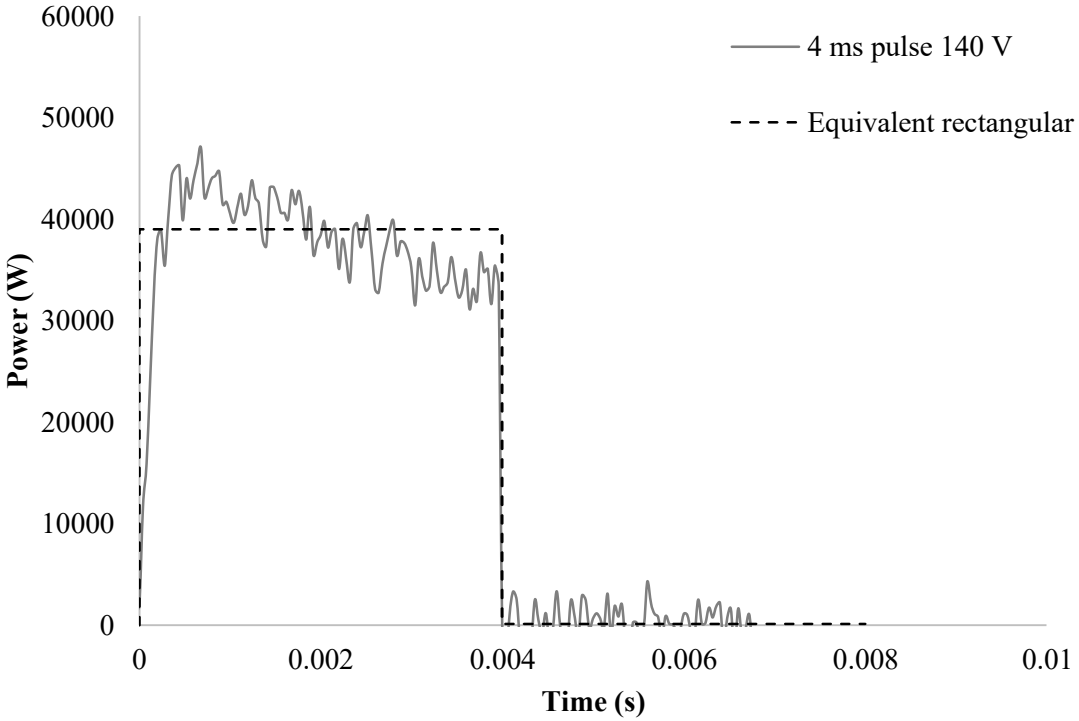

Figure 3.5 Representation of flashlamp system pulses as rectangular.

3.3.2 ATP manufacturing trials

Manufacturing trials of AS4/PEEK composites were performed at the University of Leoben, Austria to validate model predictions. The in-house developed robot cell used featured an ATP head capable of placing 1-inch wide composite tapes on an aluminium tool. The setup is presented in [163]. The incoming tape is fed at an angle of 45° whilst the roller has a diameter of 50 mm. The compaction force was set at 200 N which resulted in an approximately 14 mm long roller contact patch. The humm3® flashlamp system studied in section 3.3.1 was employed as the heating source during these trials. The light guide featured a double asymmetric design with chamfered edges at an angle of 20°. The light guide edges were positioned 5 mm away from the substrate and incoming material.

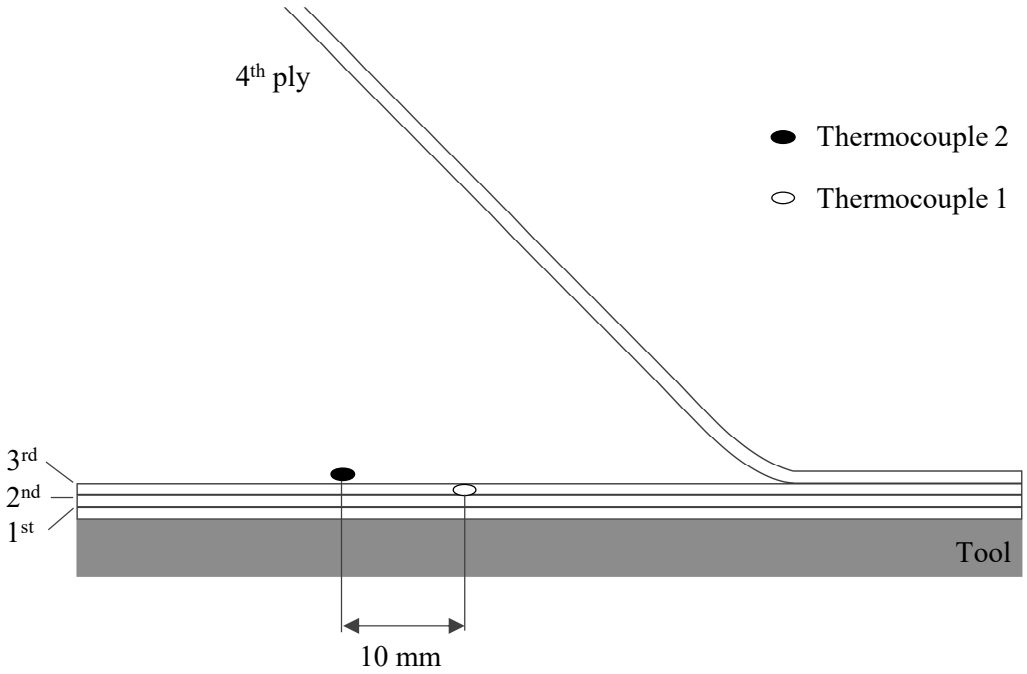

Figure 3.6 Schematic of the temperature measurements acquired during the 4th layer placement in ATP manufacturing trials.

Four-ply 25 mm wide AS4/PEEK specimens were fabricated by operating the flashlamp system at 25, 50 and 100 Hz and 140 V. The pulse duration was compensated following the procedure described in section 3.3.1 to utilise the system power (4.4 kW). The pulse duration was set at 4.75 ms, 2.25 ms and 1.1 ms respectively. The processing rate was selected at 50 mm/s for all trials. Temperature profiles on the deposited material surface and one ply below were acquired using 75 μm diameter K-type thermocouples during the deposition of the 4th ply, as shown in Figure 3.6. The thermocouples were placed in the centre of the deposited material and 10 mm apart to minimise their effect on the thermal field and local thickness. An Omega Engineering OM-DAQ-USB-2401 [183] acquisition module was used with a sampling frequency of 150 Hz to capture the temperature data.

3.4 Heat transfer modelling

3.4.1 Boundary value problem

The governing energy balance expressing the heat transfer in the ATP on a Eulerian frame of reference is:

$$\rho c_p \left(\frac{\partial T(\boldsymbol{r},t)}{\partial t} + \boldsymbol{u}^{\boldsymbol{T}} \nabla T(\boldsymbol{r},t) \right) = \dot{q} + \nabla \cdot \boldsymbol{K} \nabla T(\boldsymbol{r},t) \tag{3.5}$$

where ρ is the density of the composite, c_p the specific heat capacity, $\boldsymbol{K}$ the thermal conductivity tensor, T the temperature, $\boldsymbol{r}$ the spatial vector, $\boldsymbol{u}$ the velocity vector, t the time and $\dot{q}$ the heat rate absorbed or released due to material transformations.

Three types of boundary conditions can be applied in the general case [184]:

I. Prescribed temperature:

$$T(\boldsymbol{r},t) = \tilde{T}(\boldsymbol{r},t), \ \boldsymbol{r} \in S_1 \tag{3.6}$$

II. Prescribed heat flux

$$\boldsymbol{n} \cdot \boldsymbol{K} \nabla T(\boldsymbol{r},t) = q(\boldsymbol{r},t), \ \boldsymbol{r} \in S_2 \tag{3.7}$$

III. Convection

$$\boldsymbol{n} \cdot \boldsymbol{K} \nabla T(\boldsymbol{r},t) = h\,(T(\boldsymbol{r},t) - T_\infty), \ \boldsymbol{r} \in S_3 \tag{3.8}$$

where

$$S_1 \cup S_2 \cup S_3 = S \tag{3.9}$$

with S denoting the whole domain boundary, and S_1, S_2, S_3 the boundaries at which the prescribed temperature, prescribed heat flux and convection conditions are applied respectively. $\boldsymbol{n}$ is a surface vector, h the surface heat transfer coefficient and T_∞ the temperature of the air at the convective boundary.

An initial temperature distribution is required for the transient solution:

$$T(\boldsymbol{r},0) = T_o(\boldsymbol{r}) \tag{3.10}$$

In the ATP process, heat conduction takes place between different materials and thus an additional set of interfacial conditions is needed at interfaces to ensure temperature and heat flux continuity:

$$T_i(\boldsymbol{r}, t) = T_j(\boldsymbol{r}, t), \ \boldsymbol{r} \in S_{ij} \tag{3.11}$$

$$\boldsymbol{n} \cdot \boldsymbol{K_i} \nabla T_i(\boldsymbol{r}, t) = \boldsymbol{n} \cdot \boldsymbol{K_j} \nabla T_j(\boldsymbol{r}, t), \quad \boldsymbol{r} \in S_{ij} \tag{3.12}$$

where i and j denote the two different material domains and S_{ij} their interface.

3.4.2 Finite element modelling strategy

The Finite Element (FE) solver Ansys APDL 2021 R1 [185] was utilised to provide a numerical solution to the heat transfer problem expressed by Eqs. (3.5) - (3.12). Two-dimensional and one-dimensional models of the ATP process were developed. The 2D models were meshed with PLANE55 elements which feature four in-plane nodes, each node corresponding to a single temperature degree of freedom [186]. The 1D models in this work were meshed with the LINK33 element which is uniaxial with two nodes having a temperature degree of freedom each. In LINK33 elements, the heat conduction takes place in the element longitudinal direction.

The heat transport by material advection part of Eq. (3.5) was modelled in the 2D analyses by activating the mass transport capability available for the PLANE55 element in Ansys, via the KEYOPT (8) option [186]. The element coordinate system is aligned with the material motion across the whole domain and thus the velocity vector of each element is simplified as $\boldsymbol{u} = [u_x]$. The velocity of every element in the analysis is set equal to the processing rate of the ATP processes. However, it is adjusted for elements across curved regions according to the distance between the element centre of mass and the rotation centre, in order to result in a common angular velocity as part of the same rotating body. The velocity can be assigned and modified during the model creation as well as during the analysis to simulate varying processing rates.

For the activation of mass transport effects, the FE solver imposes limitations on the mesh size to diminish the possibility of solution oscillations and lack of convergence [186-187]. This ensures the Peclet number of each element is lower than unity:

$$Pe = \frac{u_x\, l}{a_x} \tag{3.13}$$

where a_x denotes the thermal diffusivity of the composite in the longitudinal direction and l is a characteristic length, equal to the element size in the direction of movement in this case.

The restriction represented by Eq. (3.13) couples the mesh grid size to the velocities modelled, leading to especially high number of elements for fast processing rates and low conductivity materials, such as the composite and elastomeric roller. Specifically, the element size for the AS4/PEEK composite in the direction of the movement should be kept lower than 10 μm at 100 mm/s. Similar requirements have been reported in previous studies which used this element type [39]. ATP processing rates can be well above this value making the 2D simulation under this restriction highly inefficient. The heat conduction in the composite in the moving direction has been found to be negligible compared to the heat transport due to material advection [36], manifested as high values of Peclet number. This also applies to the elastomeric roller of this study, given the similar velocities but even lower thermal diffusivity (section 3.6.1). This observation allows the use of artificially increased thermal conductivities in the direction of placement, as long as the values maintain the Peclet number at high levels, and thus do not influence the heat transfer. For a deposition rate of 50 mm/s and thermal diffusivity in the 1-10×10^{-6} m^2/s range, the Peclet number is in the order of 10^3 for characteristic length as short as the roller diameter. As a result, the thermal conductivity of the composite and roller in the longitudinal direction (section 3.6.1) was artificially increased by a factor of 10 in the 2D analyses. This results in Peclet number values in the order of 10^2 and keeps solution times within acceptable limits due to the use of a coarser mesh. As a result, a single mesh grid was created for all 2D analyses regardless of the processing rate simulated.

The mesh size in the thickness direction for both the 1D and 2D models of this work was determined based on convergence studies and the expected penetration depth of the heat wave delivered by a pulsing source, estimated as [188-189]:

$$d_t = \sqrt{\frac{2a_y}{\omega}} \tag{3.14}$$

where ω is the pulse angular frequency and a_y the transverse thermal diffusivity of the composite. The heat flux applied on the composites surface, necessitated an element size of 10 μm. However, refining a thin slice near the material surface was found to be sufficient to reach convergence if the thickness of this zone exceeds the thermal penetration depth of the incident pulses calculated by Eq. (3.14). Outside this region, the periodic temperature variations become negligible, and the temperature distribution can be captured accurately by a coarser mesh with element thickness of 10-200 μm. The 2D mesh grid in the vicinity of the process nip point is shown in Figure 3.7.

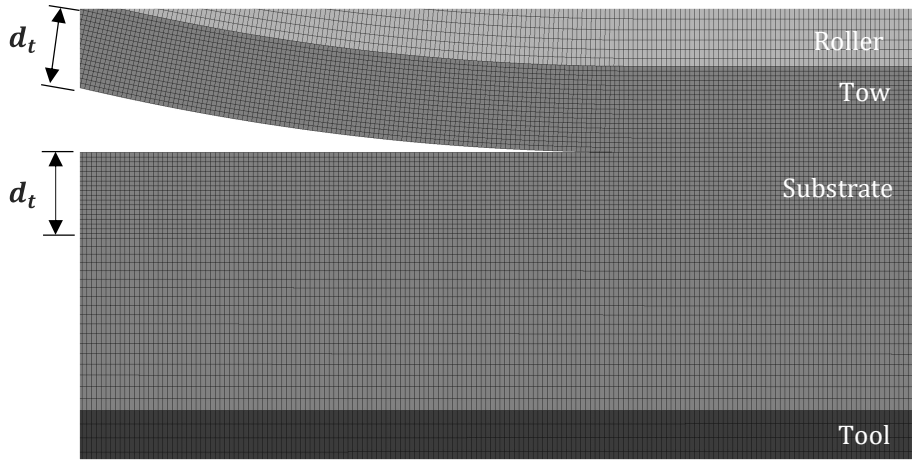

Figure 3.7 Mesh of the substrate, tow and roller near the nip point. The composite features refined zones which exceed the thermal penetration depth (d_t).

The simulation in both 1D and 2D models was discretised into a finite number of load steps governed by the flashlamp frequency, processing speed and desired resolution of results. These load steps have a short enough duration to model the individual pulses delivered by the source. Since the energy pulses are modelled as a rectangular waveform in the FE models (section 3.3.1), a minimum of two load steps per period is needed: one covering the duration of the pulse event and one the remaining period time. The use of two load steps per pulsing period results in the fastest computation for a given processing scenario; however, capturing the non-linear heating/cooling curves accurately in the pulse timescale requires additional calculation points. The number of load steps per period is adjusted throughout this work according to the desired balance between resolution and computational effort. In all cases, the time increments within each load step are adjusted by the software to achieve convergence, until the square root of the sum of the squares

(SRSS) of the residual vector is lower than the SSRR of the 0.1% of applied fluxes or lower than 10^{-9} [186].

3.5 Optical modelling

A 3D optical model of the ATP process was developed and solved using the ray tracing method implemented in TracePro LC 7.5.3 [190]. The ATP configuration and flashlamp system modelled correspond to those used in the manufacturing trials, described in section 3.3.2. The model, which is presented in Figure 3.8, comprises the cavity formed by the composite deposited material and incoming material as well as critical components for the system optical output: the flashlamp tube, the water-filled cooling chamber, the quartz light guide and the reflective housing. The composite tapes have a width of 25 mm. The flashlamp head is mounted inside the ATP cavity with the light guide edges being 5 mm away from each tape, as in the manufacturing trials.

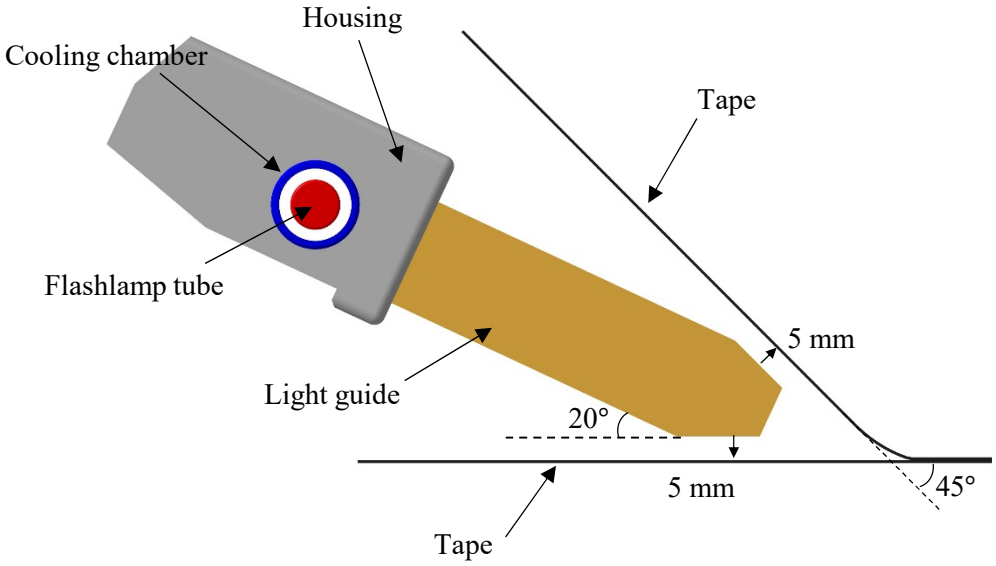

Figure 3.8 Schematic of the flashlamp ATP configuration modelled using ray tracing.

The composite tapes were modelled as specular surfaces described by Fresnel equations with an angular dependence corresponding to a refractive index of 1.95, which yields good agreement with experimental results [93]. The transmittance of AS4/PEEK tapes has been found to be below 0.1 % over the 500-2000 nm wavelength range, whilst PEEK is highly absorptive over the 200-500 nm range [93]. Therefore, the material transmittance is considered negligible across the flashlamp spectrum which lies in the 200-1000 nm range [95]. The relationship between the angle of incidence and reflectance

is plotted in Figure 3.9. Measurements have indicated a weak dependence on wavelength with only 2% changes in reflectivity for the AS4/PEEK in the range of 500-1000 nm [93]. Since transmittance is negligible, the tape absorptance is the complement of reflectance (Figure 3.9).

The models and properties of the rest of the materials are summarised in Table 3.2. The refractive index (η) of quartz glass was calculated using the extended Schott equation in TracePro [190], as a function of ray wavelength (λ):

$$\eta(\lambda)^2 = o_1\lambda^8 + o_2\lambda^6 + o_3\lambda^4 + o_4\lambda^2 + o_5 + o_6\frac{1}{\lambda^2} + o_7\frac{1}{\lambda^4} + o_8\frac{1}{\lambda^6} + o_9\frac{1}{\lambda^8} + o_{10}\frac{1}{\lambda^{10}} \quad (3.15)$$

Fitting parameters (o_i) for representative fused silica material were available in the TracePro database. They are reported in Table 3.3 for wavelengths in the 0.2-3 μm range.

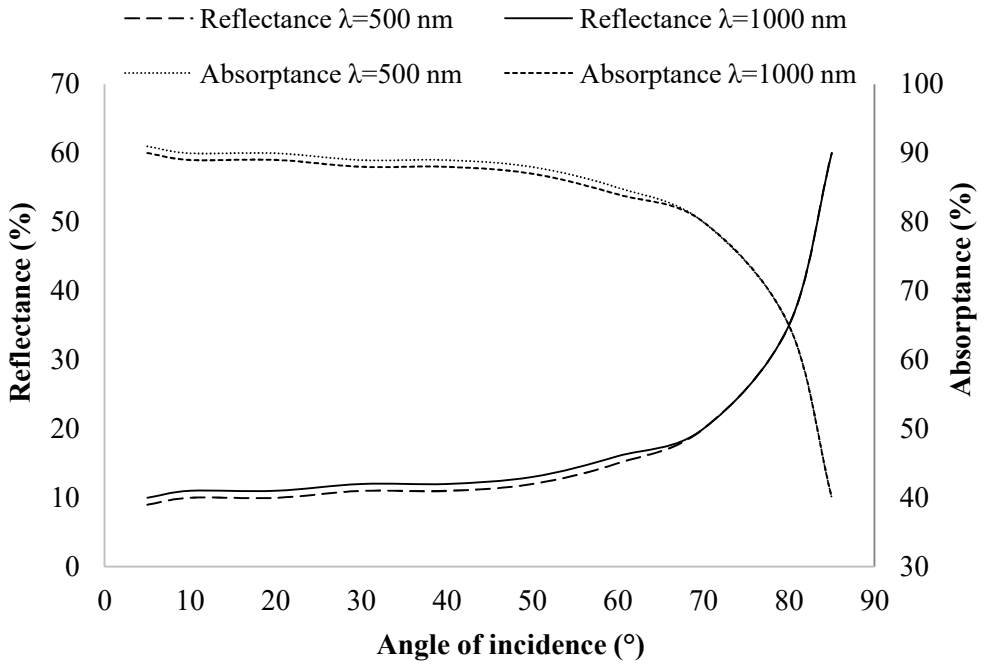

Figure 3.9 Angular dependence of AS4/PEEK properties for 500 and 1000 nm wavelengths [93]. Angle is relatively to the surface normal vector.

Table 3.2 Models and properties used in the optical model.

Material	Model/Assumptions	Input properties	Source
AS4/PEEK	Partially absorbing surface with specular reflections	Absorptance Reflectance	[93]
Quartz (Fused silica)	Extended Schott equation	Refractive index	TracePro Database [190]
Water	Complex refractive index by Beer-Lambert Law	Refractive index Extinction coefficients	[191]
Aluminium	Partially absorbing surface with specular reflections	Absorptance Reflectance	[192]

Table 3.3 Fitting parameters for the extended Schott equation (Eq. (3.15)) for the fused silica [190], corresponding to wavelengths in μm.

Parameter	Value	Units
o_1	-1.08791×10^{-7}	μm^{-8}
o_2	1.17826×10^{-6}	μm^{-6}
o_3	-1.05663×10^{-4}	μm^{-4}
o_4	-9.15974×10^{-3}	μm^{-2}
o_5	2.10418	-
α_6	8.71518×10^{-3}	μm^{2}
o_7	1.05600×10^{-4}	μm^{4}
α_8	-9.50819×10^{-7}	μm^{6}
o_9	1.25383×10^{-7}	μm^{8}
o_{10}	-1.90524×10^{-9}	μm^{10}

The aluminium parts of the head housing were modelled as partially absorbing surfaces with specular reflections. The reflectance as a function of wavelength, and therefore absorptance if transmission is assumed to be negligible, was taken by [192] and plotted in Figure 3.10.

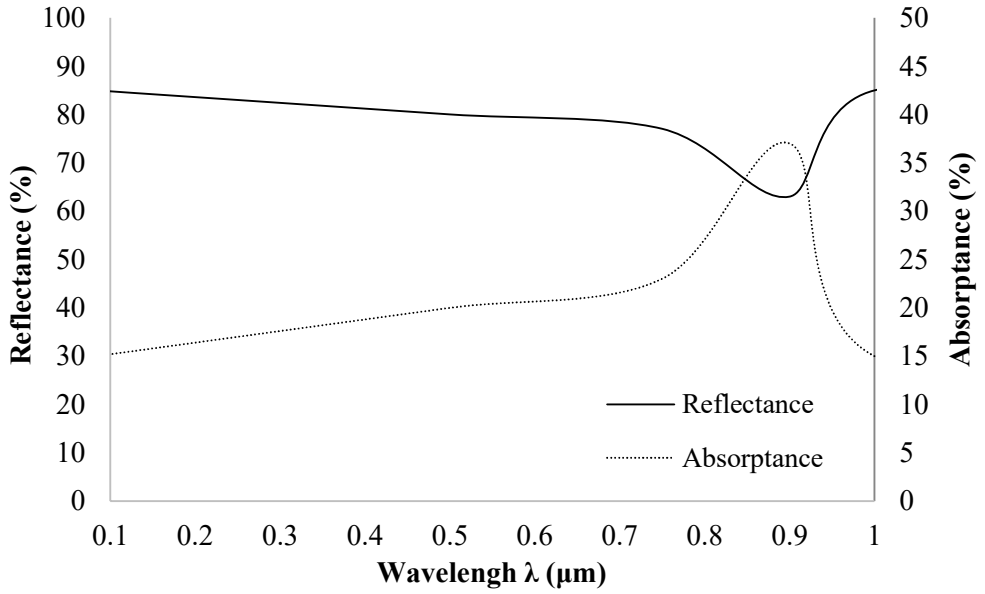

Figure 3.10 Wavelength dependence of aluminium reflectance and absorptance [192].

The water film located between the flashlamp tube and cooling chamber interior surface (Figure 3.8) was modelled based on the Beer-Lambert Law featuring a complex refractive index (η'):

$$\eta' = \eta - i\,\varepsilon \tag{3.16}$$

where ε is the imaginary part of the complex refractive index which indicates the amount of attenuation for the electromagnetic wave propagation though the water medium, also known as extinction coefficient. The real and imaginary parts of the complex refractive index adopted from [191] are detailed in Table 3.4 as a function of ray wavelength.

The model provides the irradiance distributions on the tow and deposited material of a single irradiation event. The pulsed operation is modelled in the heat transfer model by scaling this solution at appropriate timings to produce pulse trains of specific duration and frequency, as detailed in sections 3.4.2 and 4.2.

Table 3.4 Optical constants for water [191].

Wavelength (μm)	$\eta(\lambda)$	$\varepsilon(\lambda)$	Wavelength (μm)	$\eta(\lambda)$	$\varepsilon(\lambda)$
0.2	1.396	1.1×10^{-7}	0.625	1.322	1.39×10^{-8}
0.225	1.373	4.9×10^{-8}	0.65	1.331	1.64×10^{-8}
0.25	1.362	3.35×10^{-8}	0.675	1.331	2.23×10^{-8}
0.275	1.354	2.35×10^{-8}	0.7	1.331	3.35×10^{-8}
0.3	1.349	1.6×10^{-8}	0.725	1.33	9.15×10^{-8}
0.325	1.346	1.08×10^{-8}	0.75	1.33	1.56×10^{-7}
0.35	1.343	6.5×10^{-9}	0.775	1.33	1.48×10^{-7}
0.375	1.341	3.5×10^{-9}	0.8	1.329	1.25×10^{-7}
0.4	1.339	1.86×10^{-9}	0.825	1.329	1.82×10^{-7}
0.425	1.338	1.3×10^{-9}	0.85	1.329	2.93×10^{-7}
0.45	1.337	1.02×10^{-9}	0.875	1.328	3.91×10^{-7}
0.475	1.336	9.35×10^{-10}	0.9	1.328	4.86×10^{-7}
0.5	1.335	1×10^{-9}	0.925	1.328	1.06×10^{-6}
0.525	1.334	1.32×10^{-9}	0.95	1.328	2.93×10^{-6}
0.55	1.333	1.96×10^{-9}	0.975	1.327	3.48×10^{-6}
0.575	1.333	3.6×10^{-9}	1	1.327	2.89×10^{-6}
0.6	1.332	1.09×10^{-8}			

3.6 Material properties and constitutive models

3.6.1 Thermal properties

The thermal properties for the AS4/PEEK used in this study are detailed in Table 3.5. The longitudinal and transverse conductivity have been determined based on inverse heat transfer methods up to 200°C [193], as well heat pulse methods up to 400°C [36]. The latter measurements were performed by two independent laboratories and the values were averaged. The uncertainty is lower than ±10% for a given temperature value [36]. The two data sets have been compared and found to be in good agreement in the 50-200°C range [193]. For this study, representative values were selected in the 50-400°C range.

The volumetric heat capacity of the AS4/PEEK material has been estimated using inverse methods [193] and Differential Scanning Calorimetry [36]. Similarly, the two data sets are in good correlation in the 50-200°C range [193]. The specific heat capacity was calculated from the volumetric values and the temperature-dependent density of AS4/PEEK reported in [194]. All properties were extrapolated to obtain values at ambient temperature (25°C).

Representative constant thermal properties were assumed for the elastomeric roller and aluminium tool for use in the modelling work throughout this study. These are also reported in Table 3.5. Similar values have been utilised in previous studies [40].

Table 3.5 Material thermal properties.

Material/Temperature	**Specific heat capacity (J/K/kg)**	**Transverse conductivity (W/m/K)**	**Longitudinal conductivity (W/m/K)**	**Density (kg/m^3)**
AS4/PEEK	[36, 193]	[36, 193]	[36, 193]	[194]
25°C	800	0.38	3.5	1601
50°C	930	0.44	4.6	1598
100°C	1040	0.51	5.1	1593
150°C	1260	0.57	5.9	1593
200°C	1300	0.64	6	1586
250°C	1400	0.70	6.1	1575
300°C	1550	0.76	6.7	1563
350°C	1650	0.68	6.8	1537
400°C	1700	0.65	7	1524
Elastomeric roller	1255	0.25	0.25	1250
Aluminium tool	950	237	237	2700

3.6.2 Bonding strength development

Processing thermoplastics-based composites with ATP relies on the mechanism of fusion bonding, which is facilitated under conditions of high temperature and pressure. Elevated temperatures lower the viscosity of the polymer which in combination with the acting pressure cause the deformation of surface asperities, effectively improving the contact between the layers (intimate contact). This first step is essential since the tapes typically present surface roughness which limits the effective contact area. Under high temperatures and sufficient intimate contact, the interdiffusion of polymer chains across the bond interface is promoted, a process known as healing or autohesion, with the bond between the two parts being a result of substantial entanglement of polymer chains.

In this study, the bonding strength development of AS4/PEEK tapes has been modelled based on experimentally validated models available in the literature. The surface of AS4/PEEK tapes has been modelled as a Cantor set fractal surface with the deformation being described through a squeeze flow model [195-196]. The degree of intimate contact between two surfaces (D_{ic}) can be calculated as follows:

$$D_{ic}{}^{(n)} = \frac{1}{\mathrm{f}^n}\left[\frac{5}{4}\left(\frac{h_o}{L_o}\right)^2 \mathrm{f}^{\frac{2n\mathrm{d}}{2-\mathrm{d}}+n+4}\frac{}{(\mathrm{f}+1)^2}\int_{t_{(n+1)}}^{t}\frac{P_{app}}{\mu(T)}dt + 1\right]^{1/5} \tag{3.17}$$

where n is the number of asperities generation, d the fractal dimension, f the fractal scaling factor, L_o the total length of the cantor set, h_o the recess of the first-generation asperity, P_{app} the applied pressure, and $\mu(T)$ the temperature-dependent viscosity of the matrix. t_{n+1} and t_n are start and end times of consolidation of the $n(th)$ generation asperities respectively. The intimate contact development is calculated from the highest generation of asperities down to the first. A maximum of 15 generations were assumed here which has been found sufficient in previous studies [196]. The geometric parameters for the Cantor set model have been measured for AS4/PEEK tapes using profilometry [105], reported in Table 3.6.

The temperature-dependent viscosity of PEEK can be estimated by an Arrhenius type relation:

$$\mu(T) = A_v \exp\left(\frac{E_v}{T(K)}\right) \tag{3.18}$$

where A_v and E_v are obtained by fitting to experimental data. Values for the AS4/PEEK are adopted from [69] and reported in Table 3.6.

The degree of healing (D_h) for general non-isothermal conditions has been modelled by [195, 197]:

$$D_h = \left[\int_o^t \frac{1}{t_w(T)} dt\right]^{1/4} \tag{3.19}$$

and t_w is the welding time of the PEEK matrix which can be expressed by:

$$t_w(T) = A_w \exp\left(\frac{E_w}{R}\left(\frac{1}{T} - \frac{1}{T_{ref}}\right)\right) \tag{3.20}$$

where R is the universal gas constant (8.314 J/mol/K), T_{ref} a reference temperature and A_w, E_w empirical parameters obtained by fitting to experimental data. Values for the AS4/PEEK are adopted from [68] and reported in Table 3.6.

The healing model adopted here has been used to represent the highly non-isothermal conditions of ATP previously [107, 124]. The majority of studies utilising healing models have assumed that fusion progresses only above the polymer melting point, around 343°C for PEEK. This ensures that the material is in amorphous state and the crystallised regions do not impede the inter-diffusion of chains [198]. However, this approach has led to significant underestimation of strength against lap shear tests for processing speeds in the 100-300 mm/s range [123]. A better correlation can be achieved when the fusion threshold is set at the glass transition temperature (143°C) [124]. This behaviour was attributed to the extreme cooling rates during the consolidation stage in ATP and the fact that the crystallisation process occurs in a longer timeframe than the intimate contact and healing evolution, especially at high speeds. In this study, the calculation of healing is carried out down to the glass transition temperature of the polymer.

The interlaminar bond strength is a product of the intimate contact and autohesion. For every formation of intimate contact, a healing process takes place until the final bonding time τ with the degree of healing denoted as $D_h(\tau - t)$. The degree of bonding (D_b) has been approximated as [195]:

$$D_b(\tau) = D_{ic}(0)\, D_h(\tau) + \int_o^\tau D_h(\tau - t)\frac{dD_{ic}}{dt}dt \tag{3.21}$$

where $D_{ic}(0)$ is the initial degree of intimate contact.

In this study, the development of intimate contact and autohesion during ATP are estimated independently based on the thermal model predictions and assumed pressure distribution underneath the compaction roller (section 6.4.1). The degree of bonding is then calculated based on the degree of intimate contact and degree of healing (Eq. (3.21)). The corresponding expressions are computed numerically in MATLAB in the multi-objective optimisation scheme presented in section 6.4. Time increments of 0.001 s were found adequate to achieve convergence for all three models. Regardless the time discretisation of the heat transfer model, the temperature profiles are linearly interpolated to this uniform time interval.

Table 3.6 Modelling parameters.

Model	Parameter	Value	Source
Welding time	A_w	0.1 s	[69]
	E_w	57300 J/mol	[69]
	T_{ref}	400°C	[69]
Viscosity	A_v	132.95 N s/ m^2	[69]
	E_v	2969 K	[69]
Cantor set	d	1.30	[105]
	f	1.44	[105]
	h_o/L_o	0.050	[196]

3.6.3 Thermal degradation kinetics

The suppression of thermal decomposition is crucial during the ATP of thermoplastic composites, which requires temperatures in the 320-400°C range to initiate processing. The substantial energy losses to the tool and environment necessitate the development of

higher temperature during the irradiation stage. Localised temperatures up to 700°C are often developed on the tape surface [39]. Such elevated temperatures can cause the decomposition of the polymer matrix despite the short irradiation times [199-200], which deteriorates the tape surface quality. Consolidation is negatively affected due to the increase of matrix viscosity as a result of matrix crosslinking [105, 201]. Therefore, it is essential to define the process temperature window in order to eliminate these effects.

The thermal decomposition of pure PEEK and carbon-reinforced composites expressed as polymer weight loss has been investigated based on reaction kinetics [202-205]. The conversion rate of the reaction has been expressed as:

$$\frac{dc_m}{dt} = A\, e^{\left(\frac{-E}{RT}\right)} \varphi(c) \tag{3.22}$$

where A is an Arrhenius pre-exponential factor, E the activation energy, c_m the matrix degree of degradation and $\varphi(c)$ the expression of the kinetics model.

This kinetics equation is capable of describing a single reaction mechanism. Up to three reaction stages have been identified for the degradation of PEEK in air [200]. In the case of multiple reaction stages, each one following Eq. (3.22), the total conversion rate is:

$$\frac{dc_m}{dt} = \left.\frac{dc_m}{dt}\right|_1 + \left.\frac{dc_m}{dt}\right|_2 + \left.\frac{dc_m}{dt}\right|_3 \tag{3.23}$$

where $\left.\frac{dc_m}{dt}\right|_i$ corresponds to the conversion rate of each reaction stage.

In the general case, an autocatalytic mechanism has been considered in the kinetics model [200]:

$$\varphi(c) = c^{\mathrm{n}}\,(1-c)^{\mathrm{m}} \tag{3.24}$$

where m and n are fitting parameters.

Combining Eqs. (3.22) - (3.24) yields:

$$\begin{aligned}\frac{dc_m}{dt} = {} & A_1\, e^{\left(\frac{-E_1}{RT}\right)} {c_m}^{\mathrm{n}_1}\,(1-c_m)^{\mathrm{m}_1} + A_2\, e^{\left(\frac{-E_2}{RT}\right)} {c_m}^{\mathrm{n}_2}\,(1-c_m)^{\mathrm{m}_2} \\ & + A_3\, e^{\left(\frac{-E_3}{RT}\right)} {c_m}^{\mathrm{n}_3}\,(1-c_m)^{\mathrm{m}_3}\end{aligned} \tag{3.25}$$

Every degradation stage is determined by a set of kinetic parameters (A_i, E_i, n_i, m_i).

In this study, an additional degradation stage is considered which corresponds to the thermal decomposition of the fibres and carbon by-products, occurring in an oxidative atmosphere and therefore under realistic ATP conditions. The reaction can be described by Eqs. (3.22) and (3.24):

$$\frac{dc_f}{dt} = A_f\, e^{\left(\frac{-E_4}{RT}\right)}\, {c_f}^{\mathrm{n_f}}\, (1 - c_f)^{\,\mathrm{m_f}} \tag{3.26}$$

where c_f denotes the conversion of fibres. The total conversion of the composite tape, or degree of degradation, is then calculated as:

$$c = c_m(1 - w_f) + \, w_f * c_f \tag{3.27}$$

where w_f is the weight fraction of the fibres in the tape.

The parameters required for defining the kinetics model of the AS4/PEEK material were derived using Thermogravimetric Analysis (TGA) and fitting to the experimental results. The composite degree of degradation during an experiment is calculated based on the sample weight at time t (w_t), initial sample weight (w_o), and final weight (w'):

$$c = \frac{w_o - w_t}{w_o - w'} \tag{3.28}$$

The fitting aims to identify the optimal set of kinetic parameters which minimises the error between the kinetics model predictions and experimental data:

$$\left[A_i,\ E_i,\ n_i,\ m_i,\ w_{f\,k}\right] = argmin \sum\nolimits_k \sum\nolimits_j \left[c\left(D_i,\ E_i,\ n_i,\ m_i,\ t_j\right) - \overline{c(t_j)}\right] \tag{3.29}$$

where $i \in (1, 2, 3, 4) \subset \mathbb{N}$ denotes the reaction stage number. The summation is performed over all conversion values $(\bar{c})$ measured at times t_j and during k experiments. The fibre weight fraction $\left(w_f\right)$ is considered as an additional fitting parameter for each experiment, since the fibre content of the sample tested can deviate from the nominal value of 0.6 (section 3.2). This parameter was allowed values in the 0.6-0.7 range which corresponds approximately to ±0.05 uncertainty in fibre volume fraction, for polymer and fibre density equal to 1300 kg/m^3 and 1800 kg/m^3 respectively. The fitting was performed using an Evolutionary Algorithm available in the Solver of Microsoft Excel [206].

TGA tests were conducted using a TGA Q550 from TA Instruments [207]. The equipment was calibrated to ensure furnace temperature accuracy employing the Curie temperature

of certified reference materials. The kit supplied by PerkinElmer included Alumel, Perkalloy, Nickel and Iron reference samples allowing temperature calibration at 154, 355, 596 and 770°C respectively. These calibration points spread evenly across the temperature range expected during the tests. The equipment was calibrated for each heating rate tested.

Dynamic tests were carried out at heating rates of 2, 5, 10, 20 and 50°C/min. At the start of these tests, the furnace temperature was left to equilibrate at 50°C for 10 mins. The furnace temperature was then increased up to 1000°C at the examined heating rate. In addition, isothermal experiments were performed at 530, 550, 570, 590 and 610°C. For these tests, the furnace temperature jumped rapidly from 50°C up to the desired temperature and remained constant until the sample decomposition is completed. Both types of experiments were performed in air with a flow rate of 60 L/min. Samples of AS4/PEEK composite tape weighting 8-10 mg were cut and placed in the furnace on platinum TGA pans.

3.7 Multi-objective optimisation

Composites manufacture requires the optimisation of processing conditions in order to accomplish desired part characteristics and quality, as well as competitive production rates. However, the complex physics involved cause complex trade-offs between the desired outcomes, making challenging the identification of optimal process parameters which satisfy all objectives simultaneously. The interlaminar strength development, as discussed in section 3.6.2, requires high temperatures and adequate time to facilitate fusion bonding, and as a result slow ATP speeds and/or high heater power for a given configuration. However, these conditions lead to poor production rates whilst they can also trigger material decomposition (section 3.6.3). Therefore, there is a strong trade-off among interlaminar strength, production rate and the elimination of decomposition effects. An additional layer of complexity is introduced with the use of flashlamp sources. The heater power output is a product of the frequency and pulse duration, unlike continuous sources which are controlled by a single power variable. Besides the overall power output, the selection of these determines the energy delivery to the material in means of irradiation timings and repetition. Multi-objective optimisation can reveal these interdependencies and provide sets of optimal processing conditions.

A multi-objective optimisation problem involves $n \in \mathbb{N}$ design variables, $k \in \mathbb{N}$ objective functions and $m \in \mathbb{N}$ constraints. The method links a design variables vector $\boldsymbol{x} = \left(x_1, x_{2,} \ldots, x_n\right)^T$ to an objective function vector $\boldsymbol{f}(\boldsymbol{x})$=$(f_1(x),\ f_2(x) \ldots, f_k(x))^T$ so that:

$$f: x \in X \subset \mathbb{R}^n \rightarrow f(x) \in Y \subset \mathbb{R}^k \tag{3.30}$$

under the conditions of a constrain vector:

$$\boldsymbol{b}(\boldsymbol{x}) = \left(b_1(\boldsymbol{x}), b_2(\boldsymbol{x}). \ldots, b_m(\boldsymbol{x})\right)^T \in B \subset \mathbb{R}^m \tag{3.31}$$

where $\mathbb{R}^n$, $\mathbb{R}^k$, $\mathbb{R}^m$ are the design variable, objective function and constrain vector spaces respectively.

The optimisation problem aims to minimise each i-th component of the objective function so that for every $i \in (1, 2, \ldots, k) \subset \mathbb{N}$ and $j \in (1, 2, \ldots, m) \subset \mathbb{N}$ [207]:

$$\begin{cases} \min f_i(\boldsymbol{x}) \\ b_j(\boldsymbol{x}) = 0 \text{ or } b_j(\boldsymbol{x}) \neq 0 \end{cases} \tag{3.32}$$

Similar expressions are utilised for maximisation or mixed optimisation problems [208].

The objective function is optimised when none of the f_i components can be improved further without compromising at least another component. A design variable vector $\boldsymbol{x}'$ is non dominated by another vector $\boldsymbol{x}$ if all objective functions corresponding to $\boldsymbol{x}'$ are better simultaneously, or at least one is not worse:

$$\forall\ i \in (1, 2, \ldots, k) \subset \mathbb{N} : f_i(\boldsymbol{x}') \leq f_i(\boldsymbol{x}) \tag{3.33}$$

$$\exists\ i \in (1, 2, \ldots, k) \subset \mathbb{N}: f_i(\boldsymbol{x}') < f_i(\boldsymbol{x}) \tag{3.34}$$

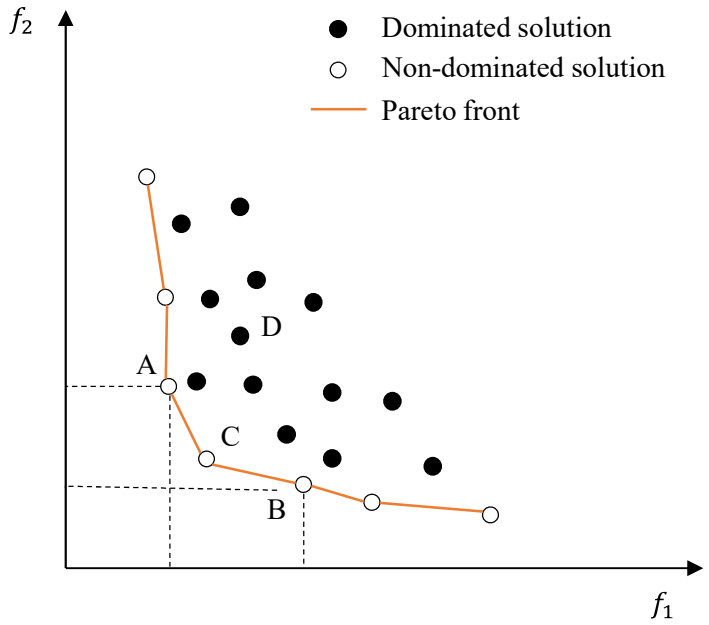

Figure 3.11 Illustrative Pareto front of a two-dimensional objectives space.

The design variable vectors satisfying Eqs. (3.33) and (3.34) correspond to the Pareto-optimal objective function vector, or Pareto-optimal front, offering the most efficient trade-off among the objectives in conflict. This is illustrated in Figure 3.11. Point D is dominated by A, B and C and therefore it does not lie in the Pareto front. Points A, B and C are not strictly dominated by any other, and hence they are both part of the Pareto front. A and B solutions are equivalent in terms of problem optimisation, requiring decision making to identify the desirable trade-off for a given application. However, Pareto solutions located at the corner region, such as Point C in Figure 3.11, offer a balanced trade-off.

4. Thermal-optical modelling of the flashlamp-assisted ATP

4.1 Introduction

This chapter presents the development of a predictive 2D simulation of flashlamp-assisted ATP. The heat transfer problem is solved using the finite element model described in section 3.4.2, whilst the thermal boundary conditions on the tapes are determined by a 3D optical model based on ray tracing, as detailed in section 3.5. The simulation results are compared against temperature measurements acquired during ATP manufacturing trials (section 3.3.2) for different pulsing conditions and depth in the laminate. Parametric modelling studies are carried out to investigate the influence of the pulsed operation and processing rate on the thermal field in the process.

4.2 2D heat transfer model of ATP

A finite element model of the flashlamp-assisted ATP was developed based on the two-dimensional form of Eq. (3.5), with a Eulerian reference of frame mounted on the moving placement robotic head:

$$\rho c_p \left(\frac{\partial T}{\partial t} + u_x \frac{\partial T}{\partial x} + u_y \frac{\partial T}{\partial y}\right) = \dot{q} + \frac{\partial}{\partial x}\left(k_x \frac{\partial T}{\partial x}\right) + \frac{\partial}{\partial y}\left(k_y \frac{\partial T}{\partial y}\right) \tag{4.1}$$

where k_x and k_y denote the longitudinal and transverse thermal conductivities of the composite whilst u_x and u_y the corresponding components of the velocity vector.

Following previous studies [36], the latent heat term ($\dot{q}$) due to material transformations of the thermoplastic matrix can be considered negligible when compared to the high amount of energy provided by the heating source and the energy transfer by the rapid material advection. Specifically, the latent heat of PEEK is 130 kJ/kg for the 100% crystalline polymer, or 7.2×10^4 kJ/m^3 for ρ=1600 kg/m^3 and w_f =0.65. The energy absorbed/released can be up to 72 J for a 0.0002 m thin tape with an area of 0.005 m^2. This is two orders of magnitude lower than the heater input over equal area which exceeds 1×10^3 J for typical heat flux of 5×10^5 W/m^2 and irradiation times as short as 0.5 s. Taking this into account and aligning the material motion with the local x-coordinate leads to:

$$\rho c_p \left(\frac{\partial T}{\partial t} + u_x \frac{\partial T}{\partial x}\right) = \frac{\partial}{\partial x}\left(k_x \frac{\partial T}{\partial x}\right) + \frac{\partial}{\partial y}\left(k_y \frac{\partial T}{\partial y}\right) \tag{4.2}$$

The 2D model geometry is illustrated in Figure 4.1. The model describes the composite deposited material and tow, the deformed elastomeric roller and the aluminium tool. The feed angle of the incoming tow, the roller diameter (r) and the deformation length (B) correspond to the configuration used in experimental trials detailed in section 3.3.2. The substrate comprises three AS4/PEEK 0.18 mm (d_p) thick layers, whilst the thickness of the roller and the tool have been reduced to 2 mm to decrease the number of elements in the analysis but without affecting the solution. The thermal properties used are detailed in section 3.6.1.

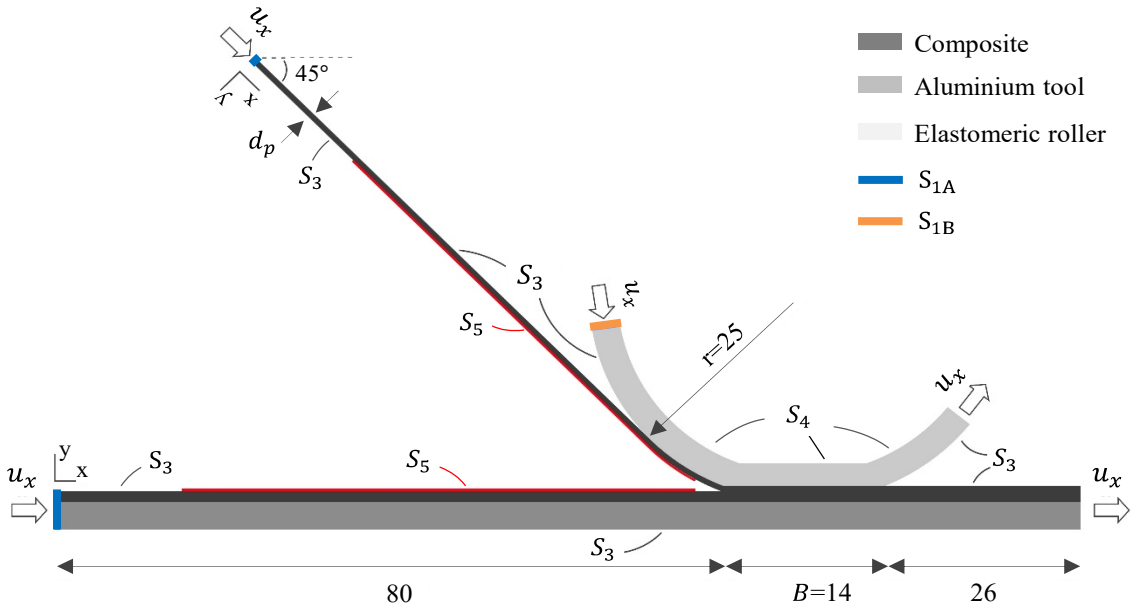

Figure 4.1 Materials, geometry, dimensions and regions of boundary conditions of the 2D heat transfer model. Lengths are in mm.

The boundary conditions applied in the model are presented in Figure 4.1. A prescribed temperature (S_{1A}) of 25°C is assigned to the nodes at the entry edges of the composite and tool. This temperature value can be adjusted accordingly if a heated tool is used. For the elastomeric roller entry nodes (S_{1B}), the value is set at 50°C to account for the residual roller heating during continuous processing. The impact of this condition on the predicted nip-point temperature has been found to be weak [39].

The boundaries denoted as S_3 are subjected to air convection. The condition is given by Eq. (3.8) for a two-dimensional domain and element coordinate system aligned with the x-axis:

$$k_y \frac{\partial T}{\partial y} = h(T_{sur} - T_\infty) \tag{4.3}$$

where T_{sur} denotes the element surface temperature. The average convection coefficient across these boundaries corresponds to forced convection due to laminar flow [209]:

$$h = \frac{k_{air}}{l} 0.664\, Re_x^{\frac{1}{2}}\, Pr^{\frac{1}{3}} \tag{4.4}$$

where Re_x is the Reynolds number of the air flow corresponding to the velocity of the tapes, and Pr and k_{air} are the Prandtl number and thermal conductivity of air respectively. A length scale (l) of 0.05 m is used for the model. The properties of air are calculated for the average value of ambient (T_∞) and element surface temperature (T_{sur}) in every time step during the solution.

A combined boundary of irradiation and convection is applied to the S_5 boundaries, which according to Eqs. (3.7) and (3.8) is:

$$k_y \frac{\partial T}{\partial y} = q\,(x,t) - h(T_{sur} - T_\infty) \tag{4.5}$$

The length of these boundaries on the deposited material and tow surface is equal to the span of the irradiance distributions predicted by the optical model. Outside this length, the surfaces are subjected to air convection (S_3) expressed by Eq. (4.3).

The pulsed operation is simulated by periodically activating the heat flux term $q(x,t)$ in Eq. (4.5) as dictated by the frequency and pulse duration of the flashlamp system. The heat flux value applied is determined by the system power output (section 3.3.1) and ray tracing predictions presented in section 4.3.

The roller inner boundaries, denoted as S_4, are modelled as insulated which according to Eq. (3.7) is expressed in local coordinates as:

$$k_y \frac{\partial T}{\partial y} = 0 \tag{4.6}$$

The geometry was meshed with PLANE55 elements following the procedure described in section 3.4.2. The penetration depth was calculated by Eq. (3.14) in the 40-80 μm range for frequencies of 25-100 Hz and AS4/PEEK transverse thermal diffusivity (section 3.6.1). The material longitudinal thermal conductivity was artificially increased by a

factor of 10, as described in section 3.4.2. A thickness of 180 μm for the fine mesh zone was used across the substrate and incoming material in all simulations, which exceeds the maximum expected penetration depth by a factor of two. The rest of the deposited material, roller and tool were represented by a coarser mesh leading to a mesh grid of approximately 400,000 elements.

The analysis goes through a transient phase before all node temperatures reach a periodic steady state. This is accomplished at a simulation time equal to the geometry length divided by velocity, about 2 s at 50 mm/s and 50 Hz in this case. This translates to about 1 hour of computational time on a 4-core PC (i7-4790), with two load steps per period.

4.3 Ray tracing predictions

The predicted irradiance on the ATP cavity by the optical model described in section 3.5 is illustrated in Figure 4.2, as a result of a single irradiation. The values correspond to a total of 4.4 kW average electrical power delivered by the incident rays. The area of maximum irradiance values is located approximately 20-30 mm away from the nip point for both the deposited material and tow, due to the position of the chamfered edges of the light guide. A high number of rays escape at these edges which reinforces the importance of including the light guide geometry in the optical model. Few rays reach deeper into the cavity due to its tapered shape, with the irradiance dropping to zero at the nip point.

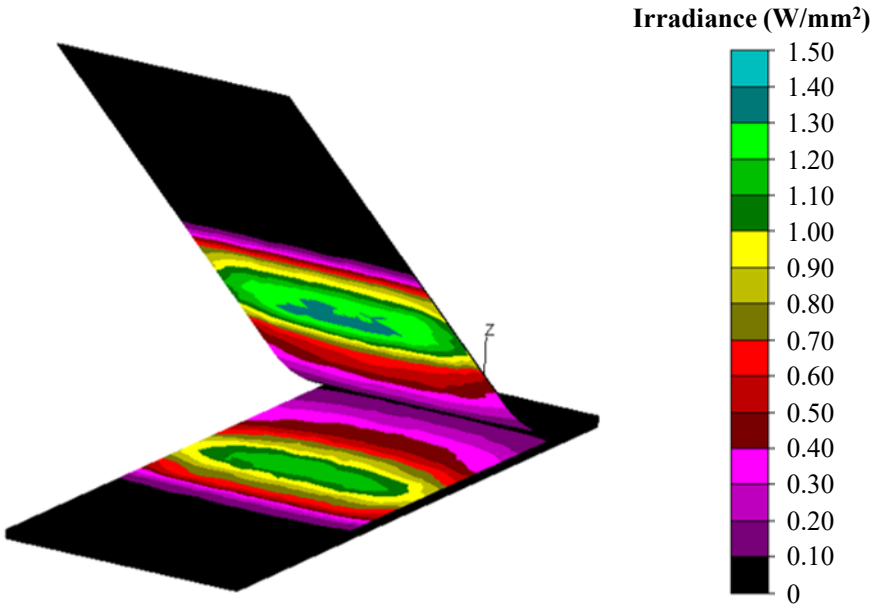

Figure 4.2 Irradiance predicted by the optical model in the ATP cavity as a result of single irradiation event. The values correspond to system average power of 4.4 kW.

The 3D spatial distributions estimated by the model (Figure 4.2) are reduced to a single profile to accommodate the 2D domain of the heat transfer model. The result is an average of five profiles around the central line of the tape. The Savitzky-Golay filter available in MATLAB [210-211] is utilised to smooth the 2D profile and eliminate outliers caused by the statistical nature of the solution. The distribution is then scaled linearly based on the acting power during pulses (section 3.3.1) and system electrical to optical energy conversion. The heat transfer model describes individual rectangular pulses of constant pulse power calculated by Eq. (3.4). As a result, the irradiance profile which corresponds to 4.4 kW is scaled up to match the power during individual pulses, calculated at 39 kW in section 3.3.1. This value is used for all the operations examined here. If the flashlamp is modelled macroscopically as a continuous source, the average value is used and such scaling is not required. In all cases, a conversion factor from electrical to optical output equal to 0.5 is assumed, which is typical for Xenon-filled flashlamps [212-213]. Energy losses due to the light attenuation throughout the different media are incorporated in the ray tracing predictions. The profiles applied on the 2D model are presented in Figure 4.3, before and after the application of the Savitzky-Golay filter.

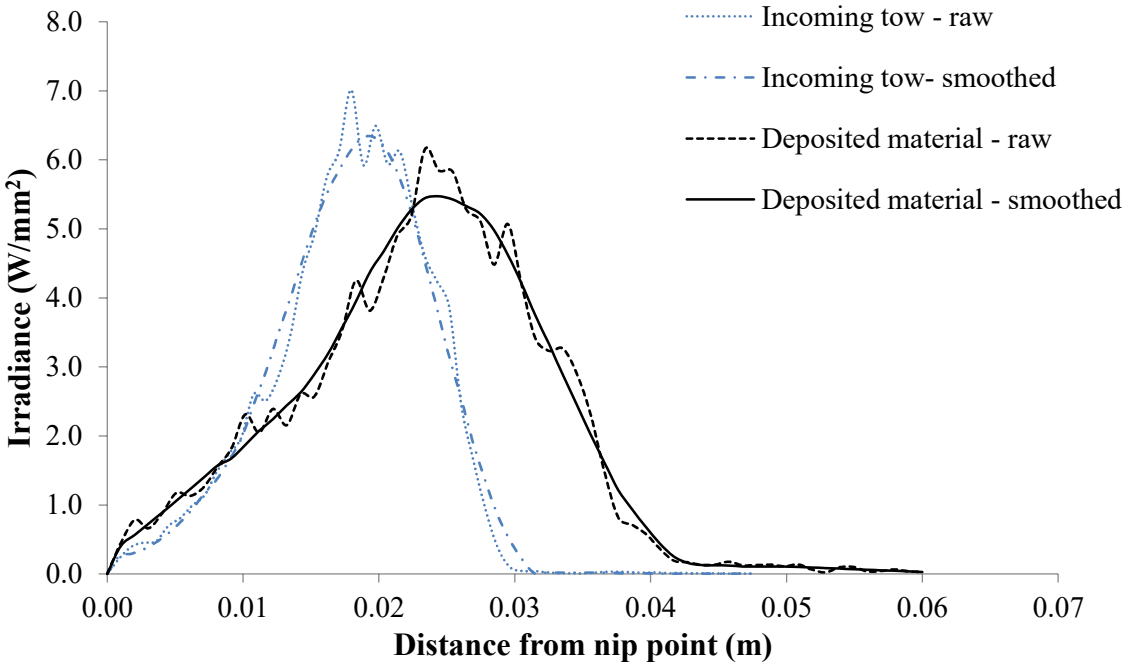

Figure 4.3 Irradiance profiles acting on the deposited material and tow surfaces.

4.4 Model predictions and validation

The temperature field predicted by the model for the 25 Hz/4.75 ms case and 50 mm/s are illustrated in Figure 4.4, 0.52 s and 2 s after the start of the analysis. As the process progresses, material moves throughout the analysis frame diffusing heat from the irradiated region to the consolidation and ambient parts of the process. Simultaneously, heat diffusion to deeper material levels takes place. The temperature field enters a periodic steady state after 2 s with a period corresponding to that of the flashlamp operation. Because of the fixed analysis frame, the model prediction provides the temperature field in a span of 0.12 m (total model length) in the movement direction, at a given time from the start of the layer deposition. Superimposing the thermal fields predicted for consecutive time steps composes the overall temperature history along the corresponding processed length of material.

The temperature profiles obtained during the manufacturing trials (section 3.3.2) and the corresponding model predictions are presented in Figure 4.5. The model profiles represent the temperature history of a single point which moves at 50 mm/s on the deposited material surface, or at one layer depth, across the analysis frame. A surface point enters the irradiation region of the process 1.2 s before the nip point which is reached at a time of 0 s (Figure 4.5a, c, e). The point is exposed to multiple irradiations since the time to cross the irradiation zone (1.2 s) is greater than the pulsing period (10- 40 ms). As a result, the point is subjected to a series of heating/cooling cycles with the repetition time of 40 ms, equal to the flashlamp operation period ($1 \, / \, F$), as observed in Figure 4.6. The heating phase duration of each cycle is equal to the duration of incoming energy pulses by the flashlamp, whilst cooling at ambient conditions occupies the remaining period. These effects are reproduced in detail by the model as a result of the fine time discretisation. Although Thermocouple 2 (Figure 4.5a, c, e) is located on the deposited material surface, it cannot capture these effects due to the short timescale compared to the sensor response time, approximately 0.05 s according to the manufacturer [214]. The recorded values are effectively an average of the surrounding temperature field on the composite surface. At the nip point region, a steep temperature increase occurs when the deposited material and hotter incoming tow, which reaches temperatures up to 600°C (Figure 4.4), come into contact and exchange heat rapidly. The interface is then consolidated underneath the roller for 0.28 s and subjected to ambient conditions for the

rest of the processing cycle. The irradiation is registered with a noticeable delay one layer below the surface (Figure 4.5b, d, f) due to the low transverse thermal conductivity of the composite. At this depth, the heat transfer between the composite parts is seen as a secondary temperature peak at a time of 0.05 s successfully reproduced by the model.

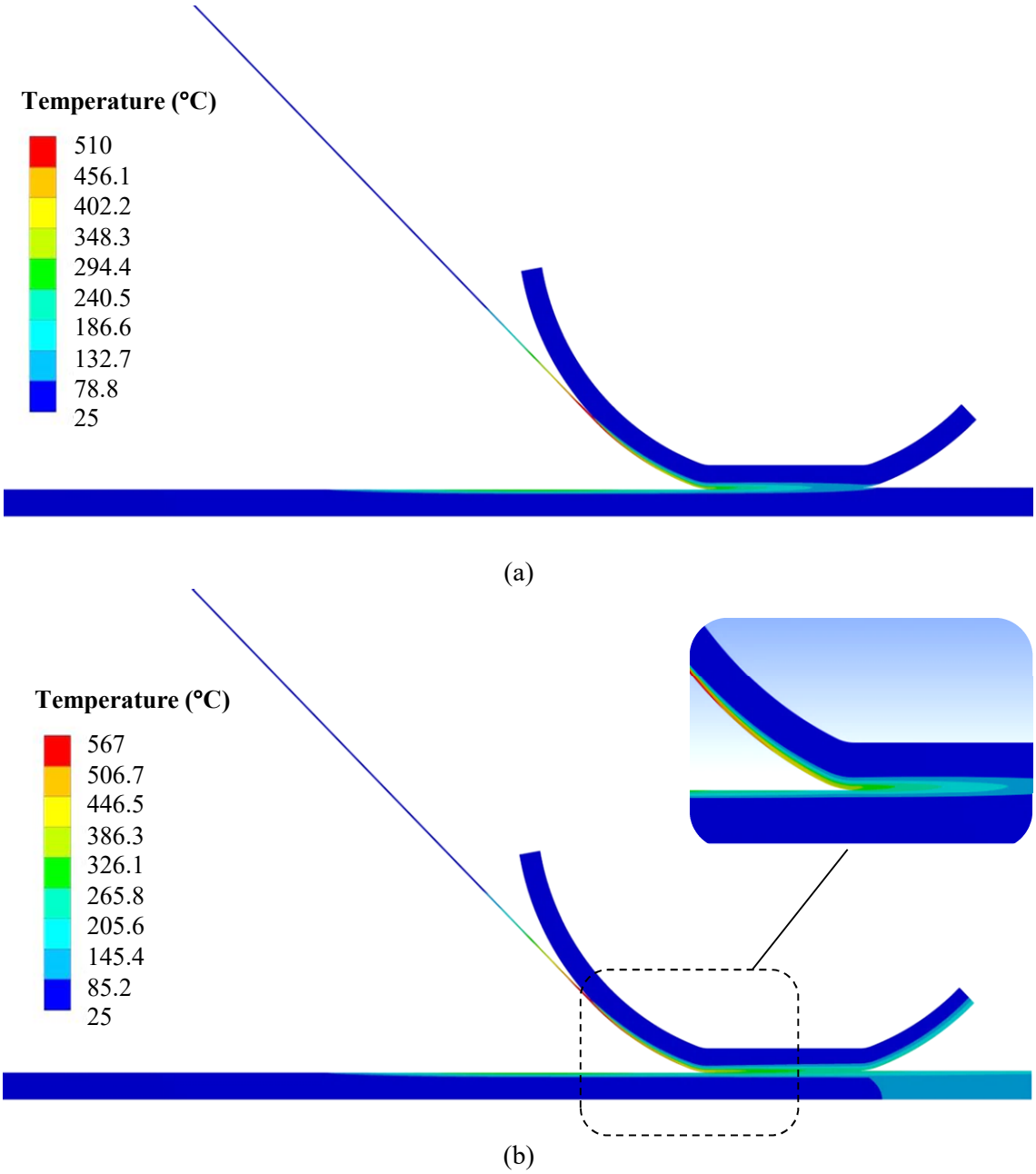

Figure 4.4 Colour maps of the predicted temperature field across the model for the 25 Hz/4.75 ms case: (a) 0.52 s and (b) 2 s after the start of the analysis.

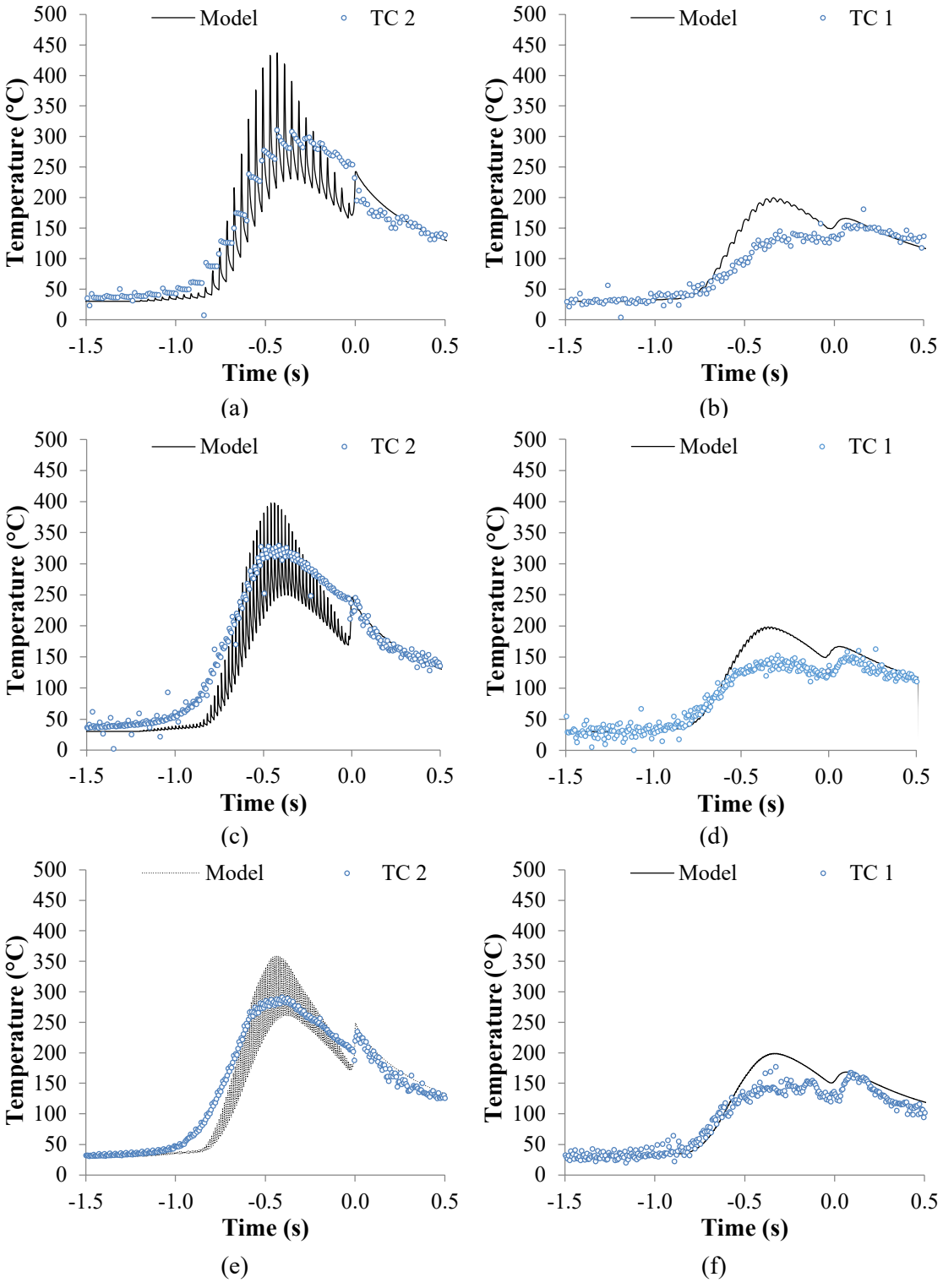

Figure 4.5 Validation of heat transfer model against experimental measurements at the locations of two thermocouples (TC1 and TC2) illustrated in Figure 3.6: (a) *25 Hz/4.75 ms* deposited material surface; (b) *25 Hz/4.75 ms* one layer depth; (c) *50 Hz/2.25 ms* deposited material surface; (d) *50 Hz/ 2.25 ms* one layer depth; (e) *100 Hz/1.1 ms* deposited material surface; (f) *100 Hz/1.1 ms* one layer depth.

The model predictions correlate well with the experimental data in terms of events timing and values. In the irradiation stage, the profile of Thermocouple 2 located on the composite surface (Figure 4.5a, c, e) is close to the mid-level of the temperature range the surface point experiences according to the model. The thermocouple is not irradiated directly in the consolidation and ambient parts of the process and the predictions present a maximum deviation of 20°C in all cases. The profiles predicted by the model at one layer depth are higher, up to 50°C, than the values captured by Thermocouple 1 at the equal depth. This is attributed to the poor consolidation, as a result of the processing temperatures being significantly lower than the melting point of PEEK at 340°C, which causes imperfect contact of the thermocouple with plies 2 and 3. The predictions show good agreement once the sensor enters the consolidation zone where the roller applies additional pressure to the plies.

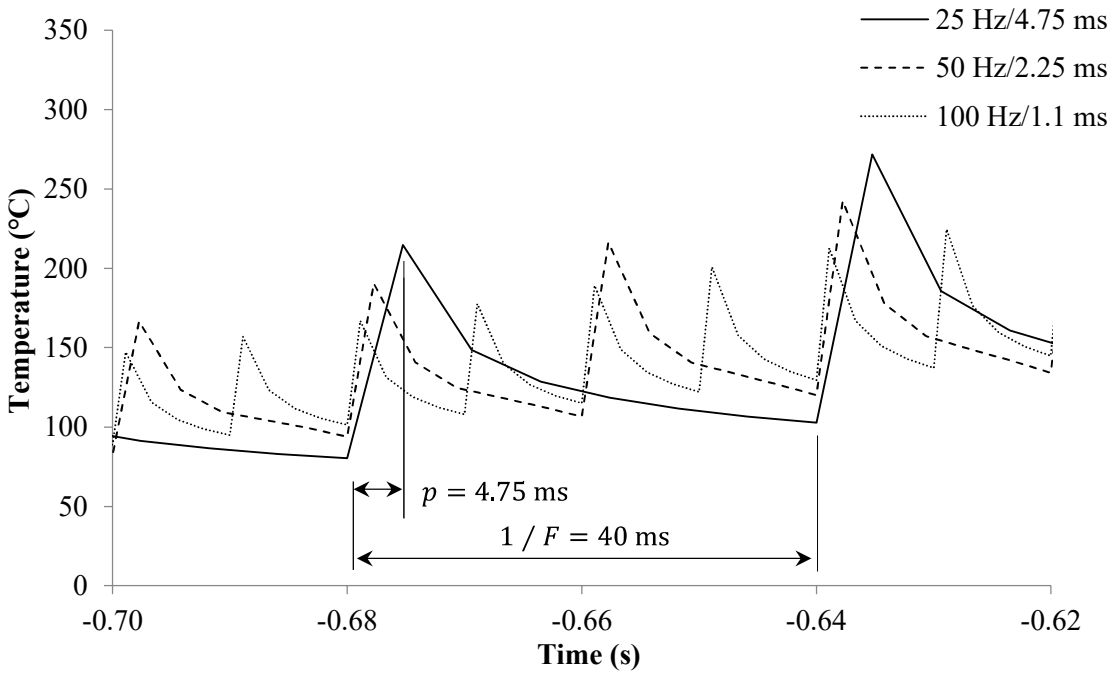

Figure 4.6 The heating/cooling cycles developed on the deposited material surface for different pulsing conditions. Relevant timings are noted for 25 Hz/4.75 ms operation.

4.5 Temperature field sensitivity to pulsing conditions

4.5.1 Surface profiles

The predicted temperature profiles of a surface point for the 25, 50 and 100 Hz operations are presented in Figure 4.7. Predictions for a continuous source of equivalent electrical power (4.4 kW), efficiency and irradiance profiles on the tape are also shown for

comparison. The flashlamp achieves significantly higher temperatures in the irradiation stage for the same average power. This is because the system delivers an order of magnitude higher power (39 kW) during each pulse, which is compensated by the remaining period to eventually result in equivalent average power to the continuous source (4.4 kW). The duration of the pulse plays a major role in the maximum values of temperature reached. A 4.75 ms pulse results in up to 50, 100 and 150°C higher peak temperatures compared to the 2.25 ms, 1.1 ms and the continuous cases respectively. At the end of each operation period, all pulsing scenarios drop below the results for continuous operation. The cooling of the surface appears greater at lower frequency due to the longer time intervals between consecutive irradiations. In addition, the flashlamp frequency determines the number of heating/cooling cycles a surface point is exposed to across the irradiation part of the process. The short operating period of the 100 Hz scenario leads to four times greater number of cycles in comparison to the 25 Hz case. In the irradiation region, the flashlamp profile converges to the continuous with increasing frequency. For the rest of the processing cycle, the profiles are nearly identical despite the significantly different operating conditions. In this region, the differences are lower than 10°C as a result of the use of equivalent average power. The effect of the pulse duration decoupled from frequency is presented in Figure 4.8 in which the frequency is kept constant at 25 Hz. In this case, changes in pulse duration affect the average power linearly with a sensitivity of 0.9 kW/ms. The surface temperature profiles are shifted to higher levels with increasing pulse duration, with a sensitivity of about 50°C/ms.

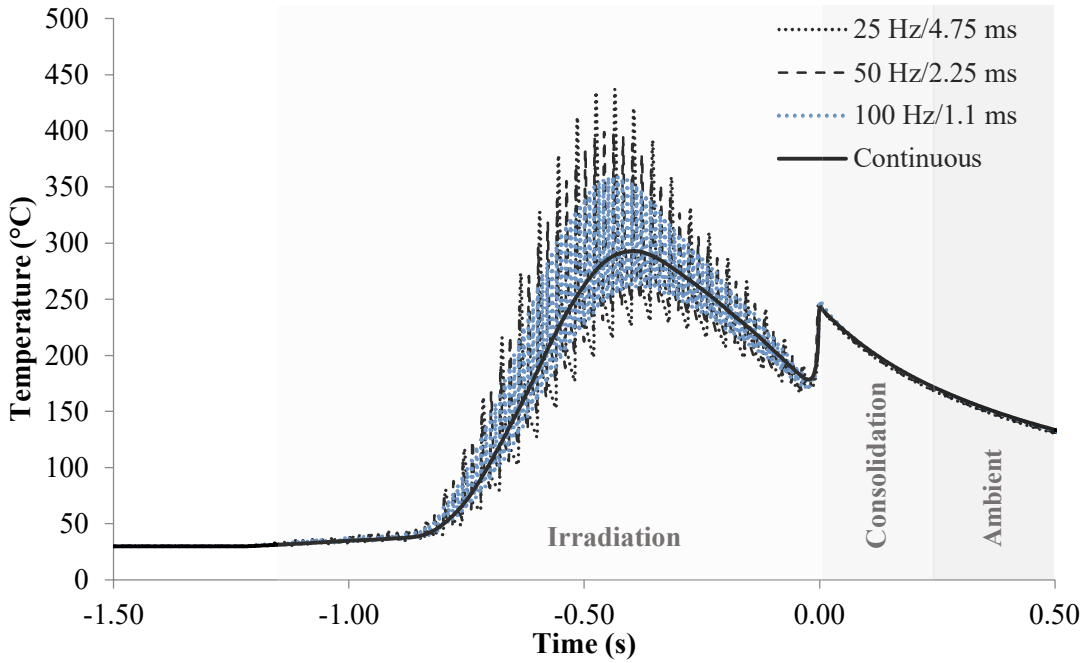

Figure 4.7 Comparison of surface temperature profiles across the process stages for the 25 Hz, 50 Hz and 100 Hz operations. The prediction for continuous source of equivalent average power (4.4 kW) is also shown.

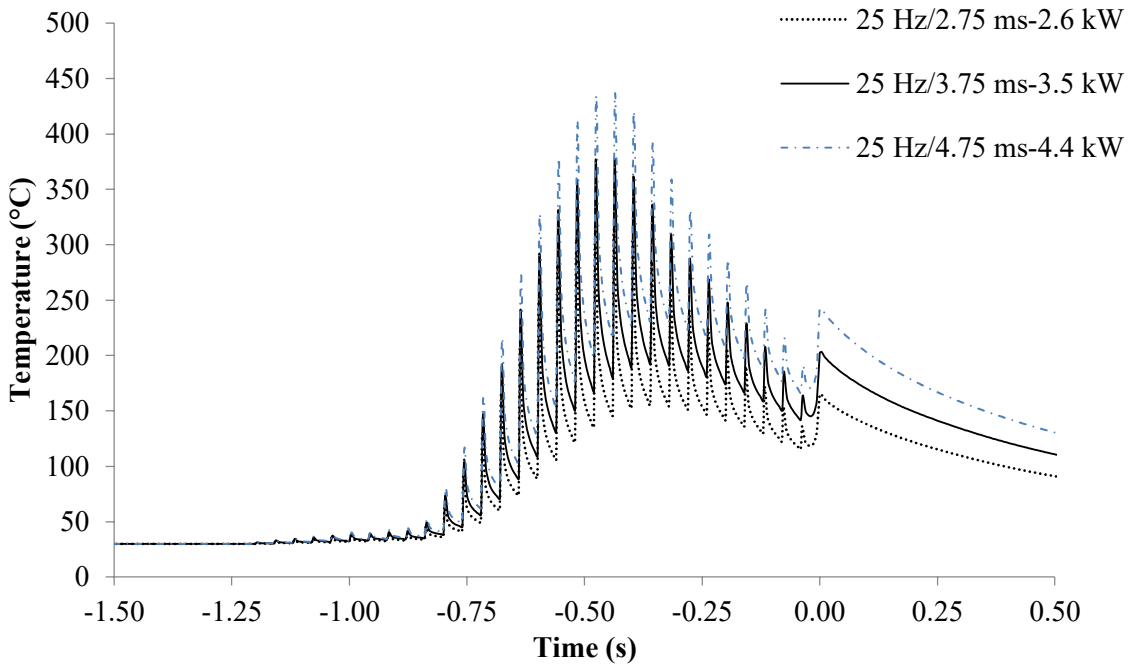

Figure 4.8 Effect of the pulse duration on the surface temperature profile and average power value under constant frequency of 25 Hz.

4.5.2 Through-thickness distribution

The temperature distribution in the substrate under irradiation for the 25 Hz, 100 Hz and continuous cases is given in Figure 4.9, at a location 25 mm before the nip point. Profiles at the end of the pulse event and the period are shown. An intermediate state is also reported for the 25 Hz case, 8.9 ms after the end of the pulse, to compare with the temperature distribution of the 100 Hz scenario at equal timings. The pulses result in an increase of the surface temperature with the profile decreasing significantly with depth compared to the continuous operation. At the end of the heating phase, the 25 Hz case reaches higher temperatures than the 100 Hz at a depth of approximately 100 μm. After 8.9 ms, significant heat diffusion towards the material bulk has occurred, especially for the 25 Hz scenario. At this point, the cycle of the 100 Hz case has been completed and the next energy pulse is delivered on the surface. On the other hand, the diffusion of the 25 Hz case continues for 26.35 ms and as a result the surface cools down further. Deeper material levels are affected in this stage. The two extreme temperature distributions of each heating/cooling cycle intersect at a depth level which represents the thermal penetration depth estimated by Eq. (3.14). In contrast, the profile of the continuous source does not present similar variations with time and the bulk temperatures can be influenced only by the heat flux applied on the surface for given material properties. The profiles of the pulsed and continuous cases almost coincide beyond a depth of 100 μm. Therefore, the flashlamp offers additional control over the maximum temperatures in the 0-100 μm depth range for the specific material and pulsed conditions tested. Operation scenarios of lower frequency and longer pulses result in higher surface and bulk temperatures, but these do not exist simultaneously, presenting time differences which are determined by the depth and the material conductivity in this direction. As frequency increases, lower depths are affected and the temperature range between the extreme states becomes narrower converging to the continuous operation.

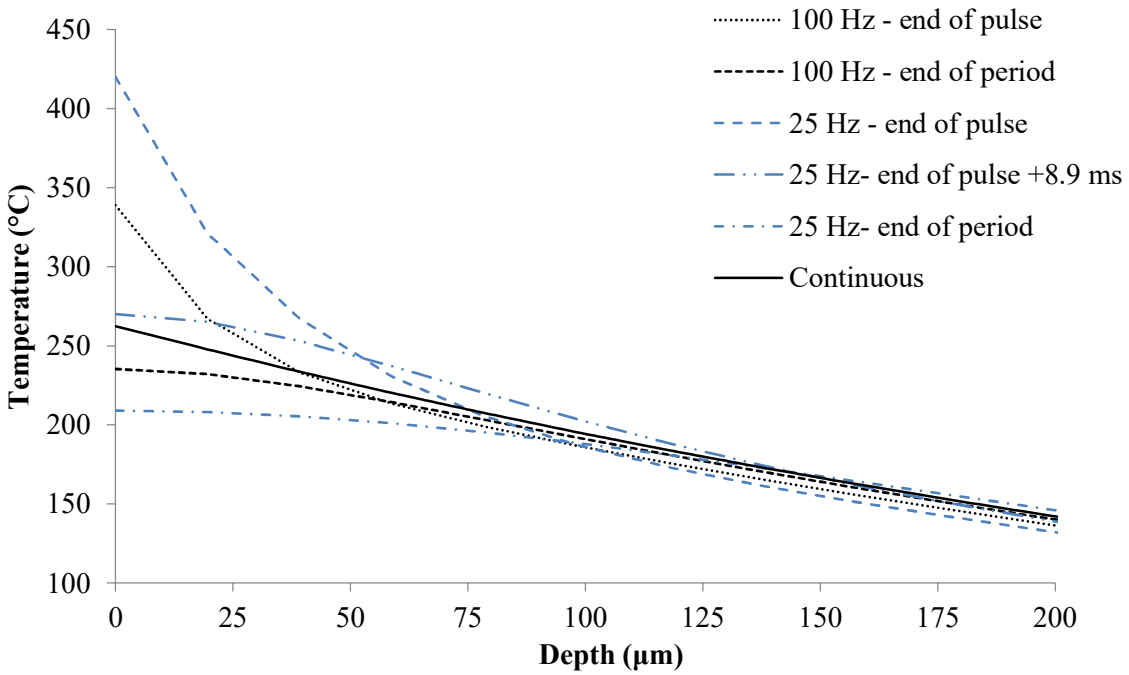

Figure 4.9 Evolution of through-thickness temperature profiles in the deposited material during a single operating period for the 25 and 100 Hz cases.

4.6 Temperature field sensitivity to processing rate

Figure 4.10 depicts the influence of processing rate on the nip point temperatures. As the velocity increases, the temperatures developed under the three pulsed cases and continuous irradiation diminishes in a non-linear manner. The values coincide for all examined operations as a result of the application of equivalent average power. The corresponding temperature maxima on the deposited material and incoming material are given in Figure 4.11. The flashlamp heating achieves significantly higher temperatures during the irradiation stage. Longer duration pulses, and consequently lower frequencies, lead to greater maxima for the whole range of velocities. The temperature on the tow surface (Figure 4.11b) is higher than on the substrate (Figure 4.11a) due to the greater irradiance applied (Figure 4.3), as well as the lower thickness. The sensitivity of the maximum temperatures to the processing rate is different for the deposited material and tow, with the latter experiencing higher temperature drops for equal velocity increments. In particular, the temperature decrease from 25 to 50 mm/s is approximately 300°C on the tow for all operations, but only 60°C for the deposited material.

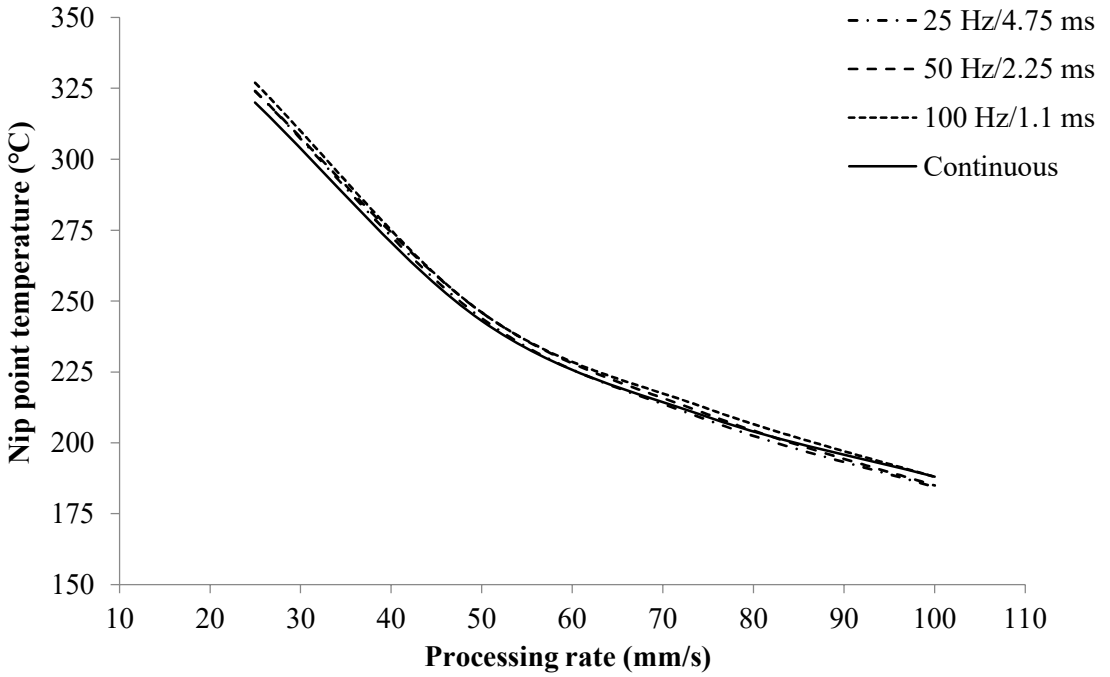

Figure 4.10 Nip-point temperature dependence on processing rate for the 25 Hz/4.75 ms, 50 Hz/2.25 ms, 100 Hz/1.1 ms and continuous operations.

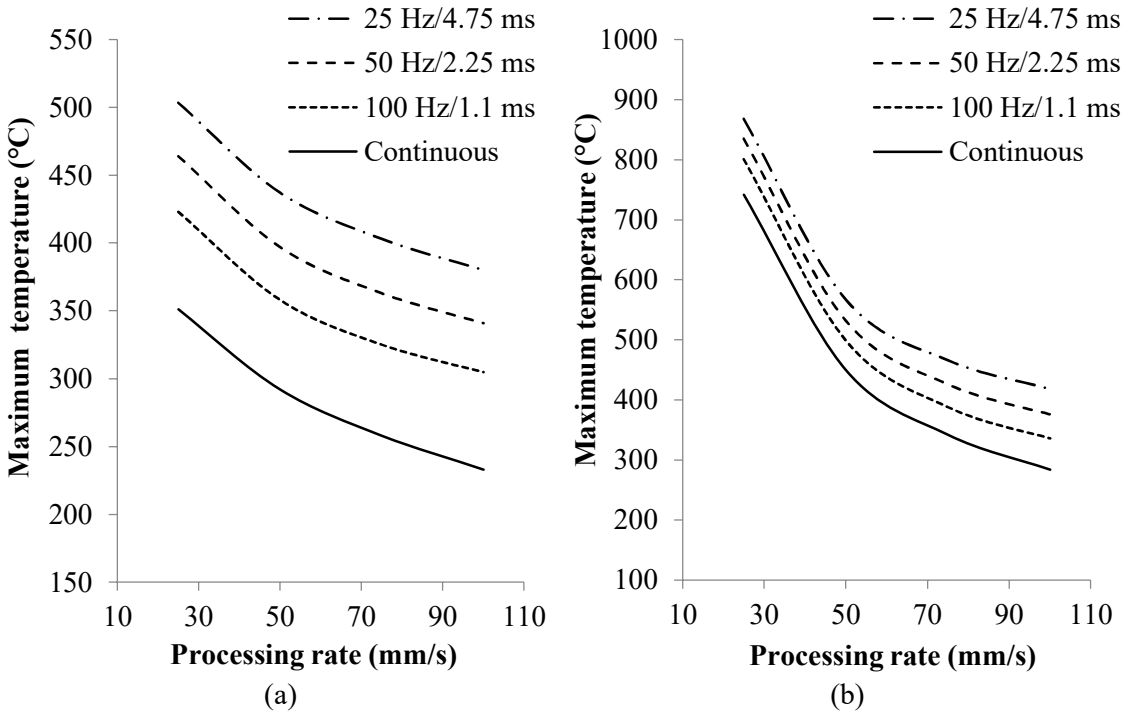

Figure 4.11 Effect of processing rate on: (a) deposited material and (b) tow maximum temperatures for 25 Hz/4.75 ms, 50 Hz/2.25 ms, 100 Hz/1.1 ms and continuous operations.

4.7 Process envelope for uniform heating

Under flashlamp heating, material points do not necessarily follow identical heating and temperature histories throughout the processing cycle. The magnitude of this effect depends on the combination of frequency and processing rate, which can cause consecutive pulses to be applied with a distance on the tape, with the effect intensifying at lower frequencies and greater velocities. Insufficient overlap of the energy pulses, in conjunction with the variable irradiance across the heated zone, creates variations in irradiation conditions. The bond line is indirectly affected since material regions with different temperature histories arrive at the nip point; however, this effect diminishes deeper into the consolidation region. The effect is negligible for the low processing rates presented in previous sections but becomes pronounced at higher ones.

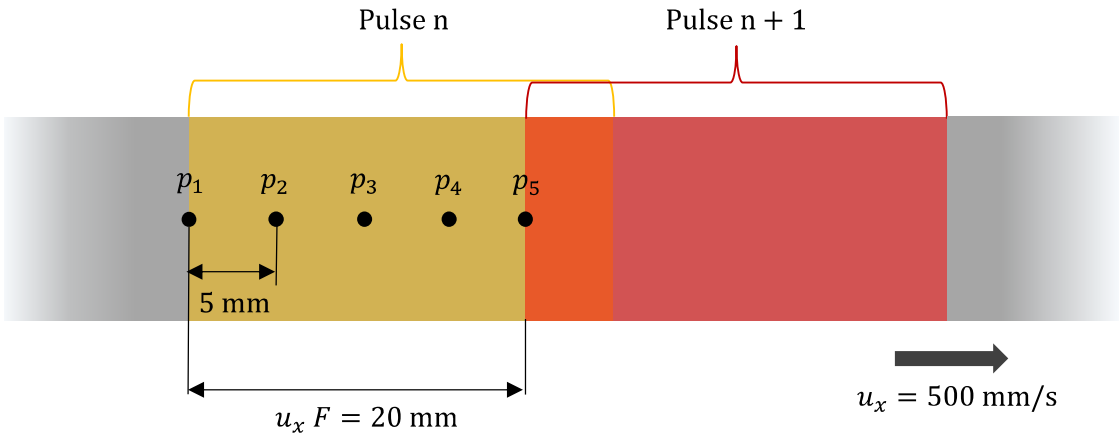

Figure 4.12 Examination of temperature history of five points on the composite tape under 25 Hz operation and 500 mm/s.

The temperature history of five points located 5 mm apart on the tape (Figure 4.12) is examined in Figure 4.13 under 25 Hz operation at 500 mm/s. In this case, the irradiation zone starts at a time of 0.12 s and the surface points are exposed to fewer irradiations than at 50 mm/s (Figure 4.8). The five points go through different temperature maxima, with differences up to 100°C, as well as different irradiation timings relative to the nip point. Furthermore, the bond line temperatures are not identical for all points but oscillate within a range of up to 15°C. Points 1 and 5 in Figure 4.12 are 20 mm apart, which corresponds to the distance covered between consecutive pulses, the product of 0.4 s operating period and 500 mm/s processing rate. These points go through similar heating conditions and

thus their temperature profiles coincide. The temperature profiles presented in Figure 4.13 repeat periodically on the substrate surface every 0.4 s or 20 mm in this case.

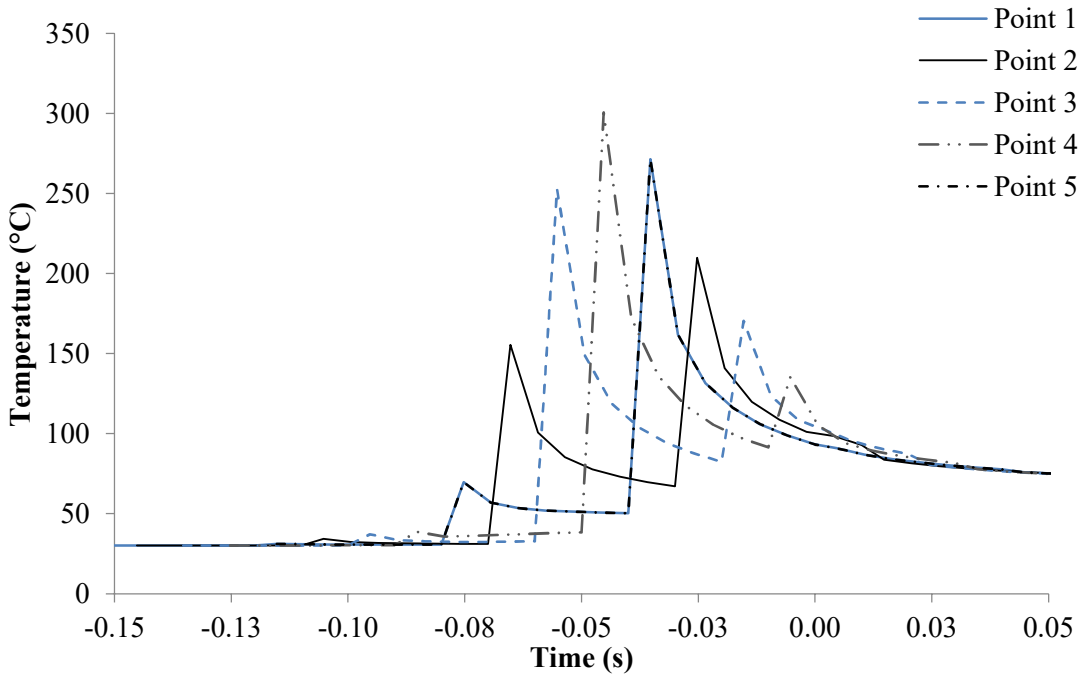

Figure 4.13 Temperature history of five surface points, 5 mm apart each, in the case of 25 Hz/4.75 ms and placement speed of 500 mm/s.

The differences in temperatures and irradiation times before the nip point can affect the melting/crystallisation of the composite matrix. Similarly, the oscillations of the bond line temperatures could lead to non-uniform bonding across the processed length (section 3.6.2). The process design space can be narrowed to eliminate these effects by defining the critical velocities - as a function of frequency - over which significant temperature variations occur. The velocity at which differences greater than 5, 10 and 20°C appear among surface points during the irradiation, or across the bond line, were determined for the 25, 50 and 100 Hz cases for the configuration of this study at 4.4 kW average power. The temperature history of 1000 points on the deposited material surface was examined in a span equal to the distance covered between consecutive pulses. The map of limit frequency and velocity conditions for 5, 10 and 20°C variations is illustrated in Figure 4.14. The map is valid for the specific ATP configuration, flashlamp system and average power. For each case, the points form a line in the frequency-speed space, which defines the feasible processing envelope in which the process conditions result in practically uniform heating across the material according to the acceptable temperature variations.

Combinations of operating frequency and velocity outside the shaded area result in greater variations. The use of such a map is necessary to select appropriate flashlamp settings and process conditions with the simulation offering an efficient way to obtain the underlying information.

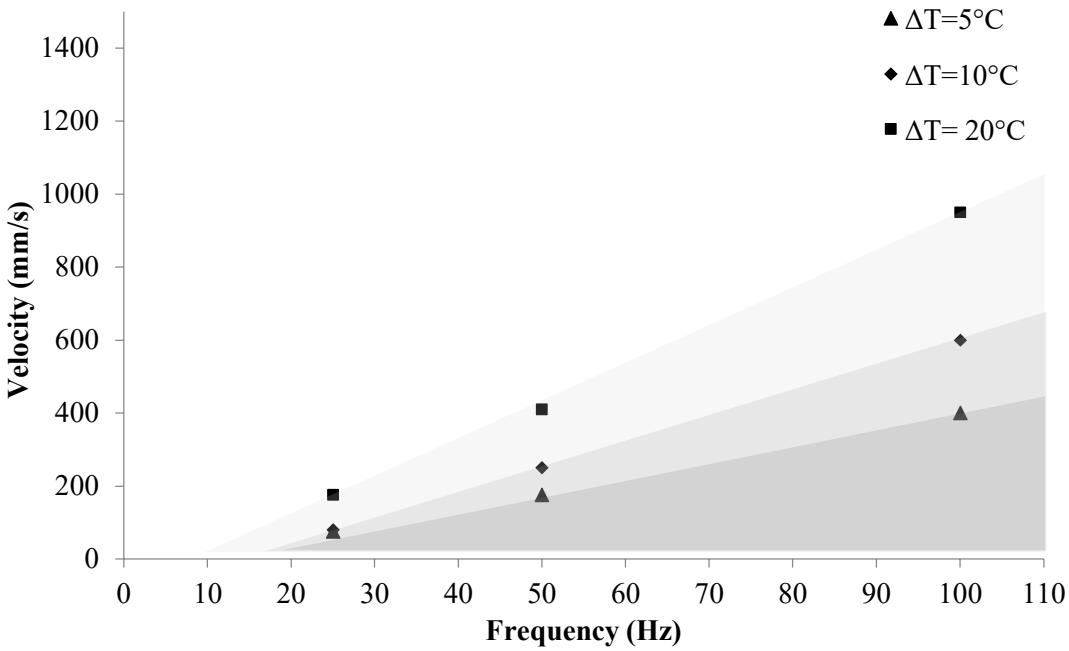

Figure 4.14 Frequency- deposition rate process map resulting in differences lower than 5, 10 and 20°C among surface points for the examined ATP configuration.

4.8 Concluding remarks

A modelling methodology combining a 2D heat transfer and 3D ray tracing model was developed. Good agreement was found between the predicted temperature profiles and experimental data, with maximum deviation of 20°C in the consolidation region. Parametric studies revealed that the effect of the operation parameters is significant on both the surface and bulk temperature, especially during the irradiation phase of the process. The results showed that flashlamp heating offers the potential of improved outcomes since the adjustable operation adds another layer of temperature control in the process. Conditions of velocity and frequency were found to potentially result in non-uniform heating, but these effects can be mitigated by deploying the models to produce operation maps and narrow the parameters space.

5. One-dimensional simplified simulation of ATP

5.1 Introduction

In this chapter, the 2D heat transfer simulation of Chapter 4 is simplified by decomposing the domain into three distinct one-dimensional FE models. These address the substrate heating, incoming tow heating and heat exchange across the consolidation stage, with appropriate transfer of temperature information to ensure field continuity. The approach is validated against predictions of the 2D model for a wide range of processing rates, material thicknesses and heater pulsing conditions. The improvements in computational efficiency are examined for a variety of processing scenarios.

5.2 Model strategy and assumptions

The 2D heat transfer of the ATP under flashlamp heating developed in Chapter 4 is expressed by Eq. (4.2):

$$\rho c_p \left(\frac{\partial T}{\partial t} + u_x \frac{\partial T}{\partial x}\right) = \frac{\partial}{\partial x}\left(k_x \frac{\partial T}{\partial x}\right) + \frac{\partial}{\partial y}\left(k_y \frac{\partial T}{\partial y}\right) \tag{5.1}$$

As discussed in section 3.4.2, the heat conduction in the composite in the placement direction is negligible when compared to the heat transport due to the rapid material advection, as indicated by the high values of Peclet number (Eq. (3.13)). As a result, the heat transport due to material advection dominates in the placement direction and Eq. (5.1) becomes:

$$\rho c_p \left(\frac{\partial T}{\partial t} + u_x \frac{\partial T}{\partial x}\right) = \frac{\partial}{\partial y}\left(k_y \frac{\partial T}{\partial y}\right) \tag{5.2}$$

This 2D energy balance can be transformed to a 1D transient state equation by applying the transformation $x' = x - u_x t$ to obtain:

$$\rho c_p \left(\frac{\partial T}{\partial t}\right) = \frac{\partial}{\partial y}\left(k_y \frac{\partial T}{\partial y}\right) \tag{5.3}$$

This transformation shifts the analysis reference frame from Eulerian to Lagrangian, in which the solution corresponds to a fixed material point, with the surface of the material subjected to a time-dependent heat flux input. Eq. (5.3) is a valid representation of heat transfer in ATP due to the negligible heat conduction in the placement direction, which renders the through-thickness conduction the dominant heat transfer mechanism.

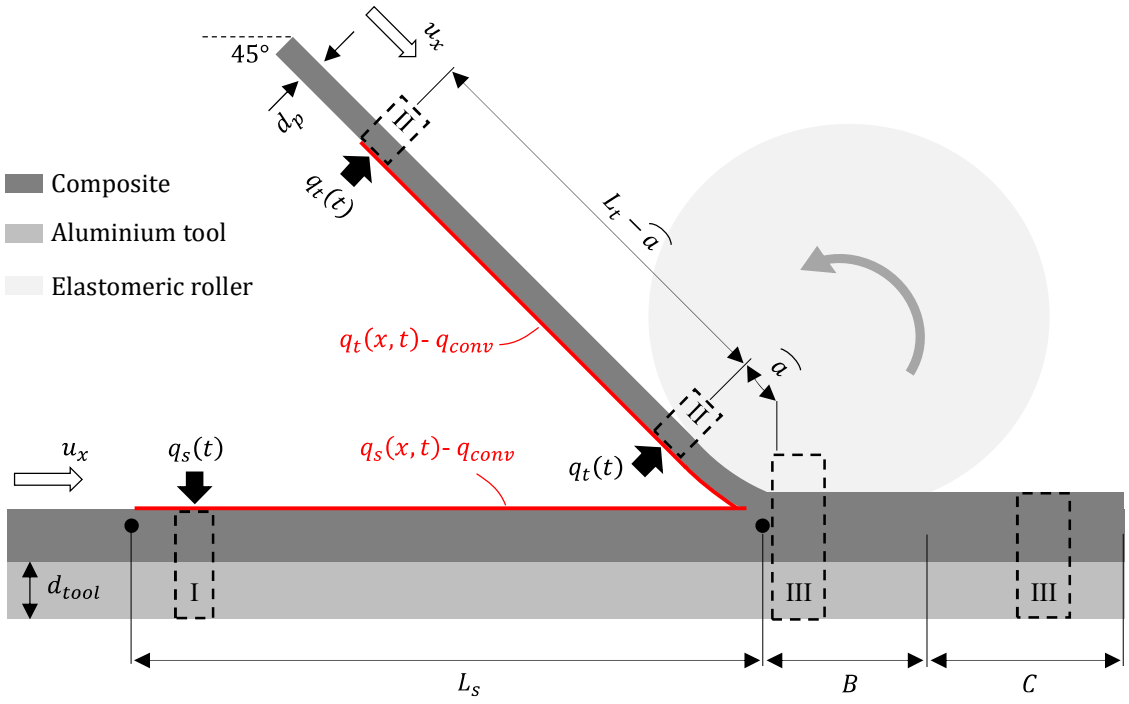

Figure 5.1 2D representation of heat transfer in ATP and identification of 1D submodels for the deposited material (Model I), incoming tow (Model II) and consolidation zone (Model III).

Application of the principle expressed by Eq. (5.3) to the 2D representation of ATP in Figure 5.1, results in three different submodels each addressing a different process region. Model I and Model II describe the temperature evolution in a material slice belonging to the deposited material and the incoming tow respectively, as they are irradiated prior to the nip point. Model III represents the heat transfer from the moment the deposited material and incoming tow come into contact underneath the compaction roller, until the end of the stage where the stack has been left to cool down at ambient conditions.

5.2.1 Model I – deposited material

Model I represents the deposited composite material consisting of n composite tape layers in perfect contact with the process tool. The submodel analysis time is equal to the distance covered from the irradiation start to the nip point, L_s as indicated in Figure 5.1, divided by the placement velocity. An overview of the applied boundary conditions is provided in Figure 5.2a.

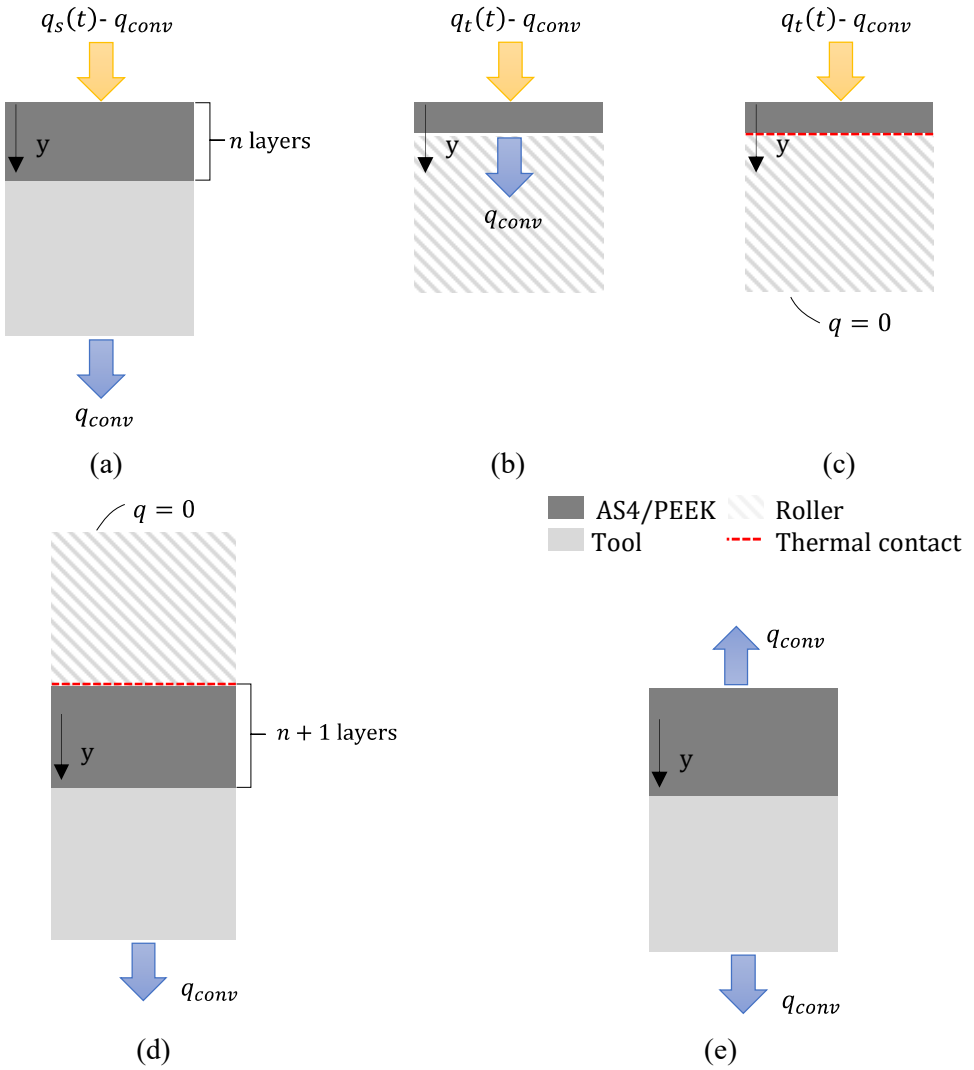

Figure 5.2 Materials and boundary conditions of 1D models: (a) Model I (deposited material); (b) Model II (tow) no thermal contact with roller, (c) Model II in contact with roller; (d) Model III (consolidation zone) underneath roller; (e) Model III outside the contact region.

The surface of the composite material is irradiated by the heating source and as a result it is subjected to a combined boundary of heat flux and convection to air, similarly to the 2D model (Eq. (4.5)):

$$k_y \frac{\partial T}{\partial t} = q_s(t) - h(T_{sur} - T_\infty) \tag{5.4}$$

It should be noted that the heat flux term $q_s(t)$ here represents the time-varying version of the spatial irradiance distribution applied in the 2D model ($q\,(x,t)$), after the transformation from a Eulerian to a Lagrangian system ($x' = x - u_x t$). The non-continuous operation of pulsed sources is accounted for in $q_s(t)$ by convoluting the

profile with a train of rectangular pulses of desired frequency and duration. The resulting heat flux is effectively the irradiation history of a single point moving across the irradiation zone under a non-continuous source. A schematic of this procedure is provided in Figure 5.3. Convection to ambient conditions is applied to the back surface of the tool, as expressed by Eq. (4.3).

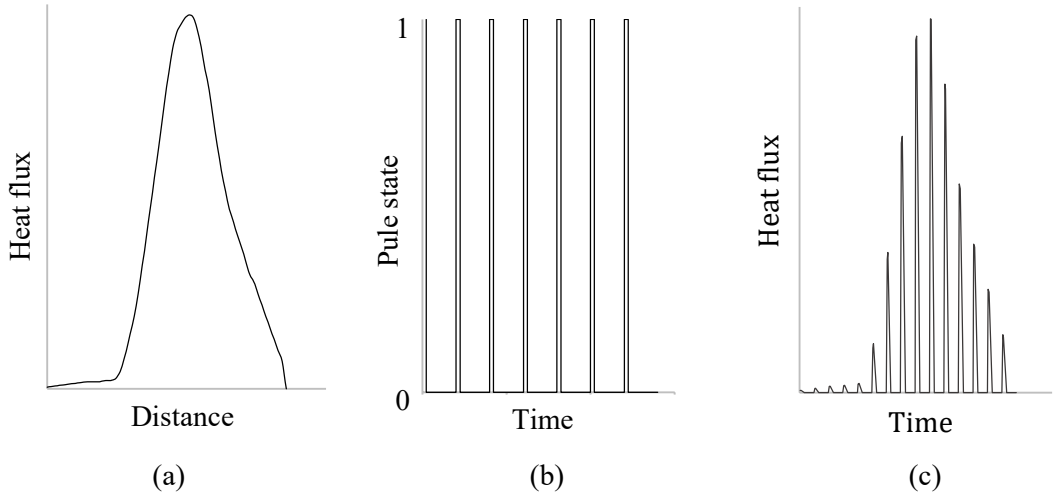

Figure 5.3 Determination of 1D simulation heat flux input: (a) spatial irradiance acting on tape surface; (b) pulse train of desired frequency and pulse duration; (c) corresponding heat flux for use in Model I and Model II for a given velocity.

5.2.2 Model II – incoming tow

Model II represents a single composite layer coming into contact with an elastomeric compaction roller which features a reduced geometry (Figure 5.2b, c). The submodel analysis time is equal to the distance covered from the irradiation zone entry to the nip point, L_t, as indicated in Figure 5.1, divided by the placement velocity. The irradiation path consists of a straight line and a curved part which follows the roller geometry and has an arc length equal to $\hat{a}$. In the transient analysis expressed by Eq. (5.3), heat conduction between the tape and the roller is not active throughout the whole analysis. Heat transfer between the two bodies is activated at a time which corresponds to the arrival time of a point moving from the irradiation start to the roller contact point, equal to $t = (L_t - \hat{a})/u_x$ (Figure 5.1). A thermal contact of negligible resistance between the nodes belonging to the tow-roller interface is created at this time.

Two sets of boundary conditions are applied in Model II (Figure 5.2b, c) as a result of the tow-roller contact established during the analysis. A combined boundary of heat flux and convection acts on the surface of the tow during both analysis stages:

$$k_y \frac{\partial T}{\partial t} = q_t(t) - h(T_{sur} - T_\infty) \tag{5.5}$$

where $q_t(t)$ in this case represents the converted spatial irradiance distribution on the tow surface, similarly to $q_s(t)$ in Eq. (5.4). During the analysis stage in which the contact with the roller is not active (Figure 5.2b), the tow back surface is subjected to air convection with a constant coefficient. Once the tow-roller thermal contact has been established, convection is no longer applied (Figure 5.2c). The roller is treated as a semi-infinite body due to its low conductivity (section 3.6.1) and short contact times with the tow, less than 1 s. The heat wave is not expected to reach the interior boundary of the roller under these conditions and thus it can be treated as insulated, represented by Eq. (4.6).

5.2.3 Model III – consolidation zone

Model III represents the resulting composite stack after the incoming tow and the deposited material come into contact at the nip point underneath the compaction roller (Figure 5.2d, e). The composite part then consists of $(n + 1)$ layers. The roller and tool have identical geometries as in Models I and II, whilst the interlayer resistance between plies is considered negligible. Unlike Model II, a thermal contact between the nodes at the composite-roller interface is active from the beginning of the analysis and it is deactivated at later steps, according to the contact patch length (B) and processing velocity (Figure 5.1). Two sets of boundary conditions are applied in Model III due to the loss of contact between the composite and the roller during the analysis. Similarly to Model II, the roller is treated as a semi-infinite body and thus an adiabatic boundary exists on its inner surface (Eq. (4.6)). After loss of contact, the stack is left to cool down at ambient conditions and thus natural air convection (Eq. (4.3)) is applied on its surface. Natural convection is applied to the tool back surface in both analysis stages (Figure 5.2d, e).

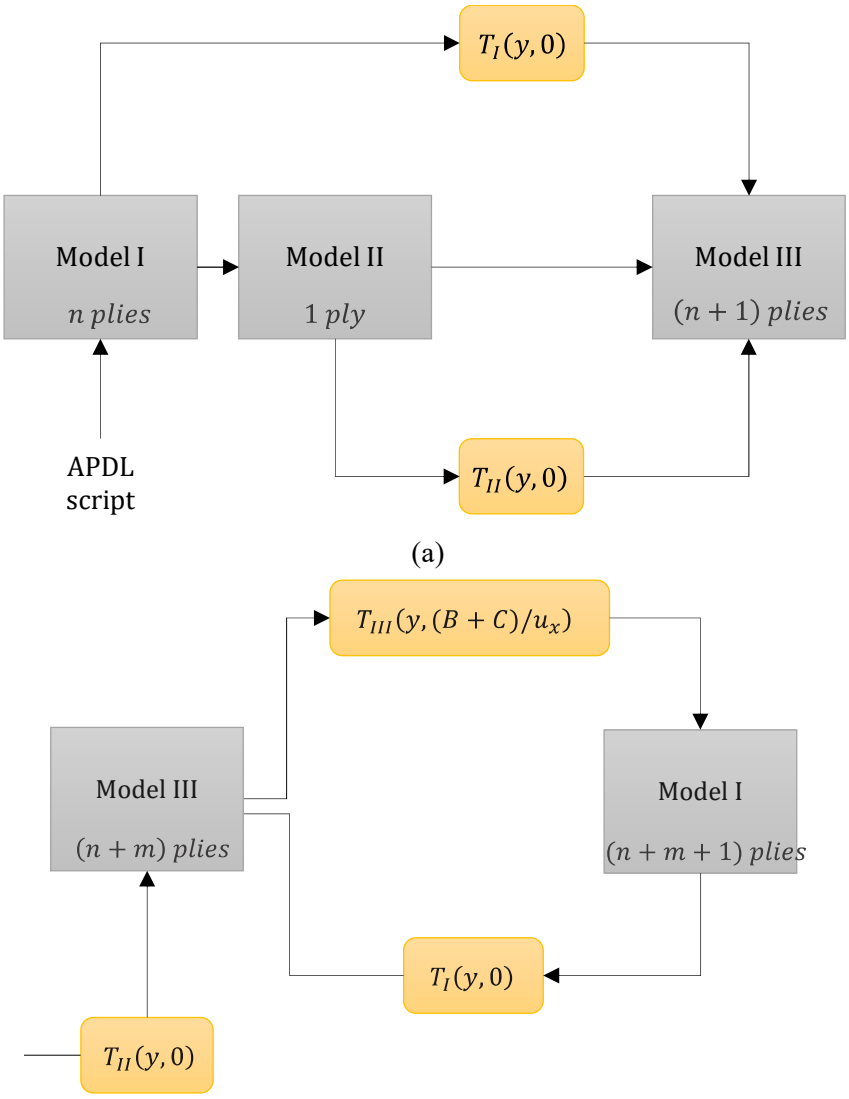

Figure 5.4 Operation of the integrated 1D simulation: (a) solution sequence and temperature data exchange among the submodels; (b) workflow for modelling multiple placement cycles including residual heating. $T_i(y,t)$ denotes temperature at position y across the thickness of submodel i at time t.

5.2.4 1D models integration

The analysis sequence and information flow between the 1D submodels is outlined in Figure 5.4. Once the solution of Models I and II has been completed at t=0 s, the resulting through-thickness temperature distributions are transferred as initial temperature conditions in Model III (Figure 5.4a), ensuring field continuity between the irradiation and consolidation zones. The temperature of the incoming tow-substrate interface at the nip point ($x = 0$) is set as the average value of the surface nodes in Models I and II. At

the end of the processing cycle, the temperature distribution across the thickness of Model III can be transferred to a new Model I (Figure 5.4b) with an additional layer. In this way, multiple placements are simulated incorporating the residual heating when complete cooling of the stack to ambient conditions has not been completed. Model II is solved once and used in the prediction of multiple placement cycles since the tow irradiation is independent of the increasing deposited material thickness. A heated tool or preheated tow can be simulated by fixing or initialising the temperature of the nodes belonging to the tool and tow respectively, to a constant value in the corresponding 1D models.

5.3 Solution comparison against 2D simulation

A comparison between the 1D simulation and the 2D FE model developed in Chapter 4 is carried out to establish the quality of the 1D approximation. An overview of the assumptions adopted by the two methodologies is presented in Table 5.1. The 2D model follows Eq. (5.1) and therefore the heat diffusion in the placement direction is included in the analysis. The composite and roller in the 2D analysis feature increased conductivities in this direction by a factor of 10, for meshing purposes as detailed in section 3.4.2. In contrast, the 1D simulation assumes these effects are negligible (Eq. (5.3)). The latent heat of matrix transformations is considered negligible in both methodologies, whilst the interlayer contact is perfect. The FE models use different type of elements, but in both cases the meshing follows the guidelines detailed in section 3.4.2 and utilised in section 4.2.

The ATP process examined for this comparison corresponds to the configuration used in the manufacturing trials (section 3.3.2) and modelled in Chapter 4. Key dimensions of the 2D geometry are provided in Table 5.2, in relation to Figure 5.1. The humm3® flashlamp system characterised in section 3.3.1 and modelled in Chapter 4 is the heater for this assessment. The irradiance profiles applied on the tapes in the 2D model are those of Figure 4.3. The corresponding heat flux profiles used in Model I and Model II are presented in Figures 5.5a and 5.5b respectively, at 50 mm/s. The procedure detailed in section 5.2.1 has been applied to transform the 2D profiles to suitable heat flux boundaries for the 1D simulation. Two extreme pulsing conditions of 25 Hz/4.75 ms and 100 Hz/1.1 ms are investigated. The convection coefficient is set at 5 $W/K/m^2$ in both models. The thermal properties of the materials used are reported in section 3.6.1.

Table 5.1 Overview of 1D and 2D model features and assumptions.

Model feature/assumption	1D FE modelling	2D FE model
Equation- Domain	Eq. (5.3) - 1D	Eq. (5.1) - 2D
Conduction in the placement direction	Negligible	Yes
Element type	2-node LINK33	4 -node PLANE55 (Mass transport effects)
Conduction in the thickness direction	Yes	
Conduction in the width direction	Negligible	
Latent heat of melting/crystallisation	Negligible	
Interlayer contact	Perfect	
Roller-tool	5 mm, 10 mm slices	

Table 5.2 Dimensions of ATP configuration for models' comparison in relation to Figure 5.1.

Dimension	Value (mm)
B	14
C	16
$\hat{a}$	12.16
R	25
L_s	50
L_t	35
d_p	0.18
d_{tool}	10

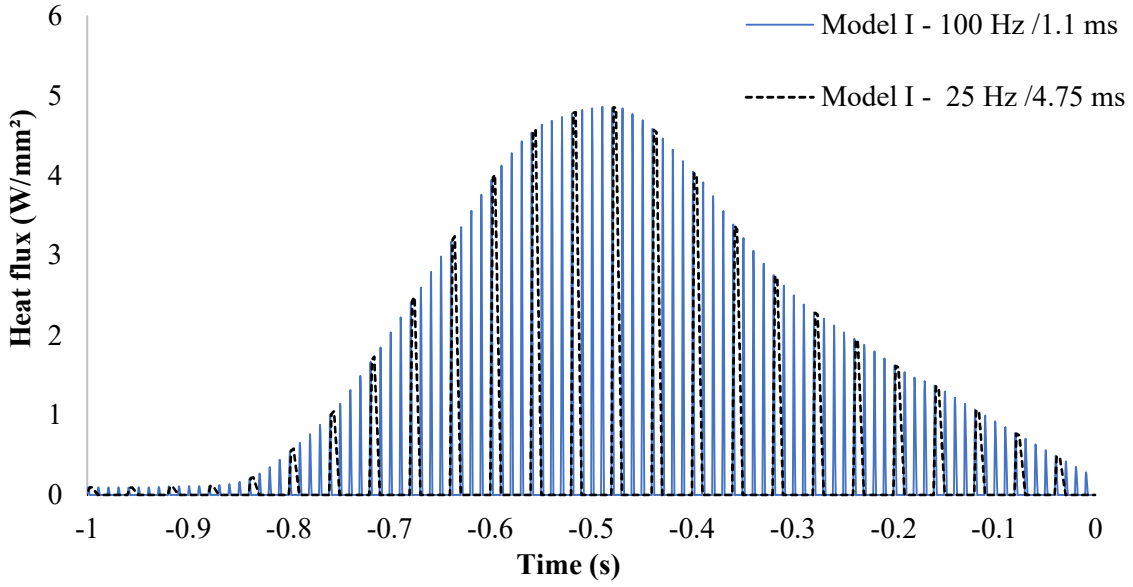

(a)

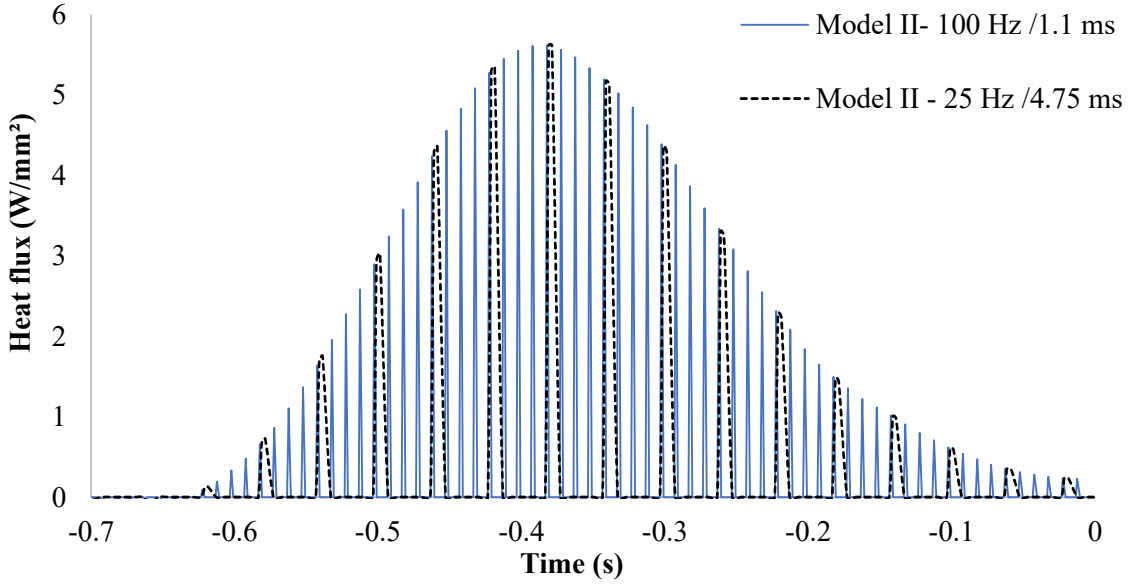

(b)

Figure 5.5 Heat flux input: (a) profile applied on the composite surface in Model I; (b) profile applied on the tow surface in Model II. Placement at 50 mm/s under two different pulsing conditions. Nip point reached at t=0 s.

The total analysis time corresponds to the analysis frame length divided by the processing speed. Each 1D submodel features a duration calculated using the length of the corresponding stage it describes and the placement velocity. For this comparison, the analysis time was discretised with five load steps per period: two for pulsing phase and three for the remaining period. Model III does not involve pulsed heating and therefore longer timesteps of 10 ms were used.

The computational effort needed by each model to provide solutions is also compared, as benchmarked by the FE solver for each run. Both models were implemented in Ansys APDL using the distributed memory parallel processing option within a single 4-core PC (i7- 4790). This solving mode decomposes the model into smaller domains, solves them simultaneously by assigning each to a single core, and then reconstructs the complete solution. This mode accelerates the solution compared to shared-memory parallel processing (SMP), especially for the 2D model, due to an overall larger domain. The default sparse direct solver was chosen which balances performance and accuracy.

5.3.1 Deposited material heating

A comparison of predicted temperatures by the 2D and 1D models for the deposited material surface (Model I) is illustrated in Figures 5.6 and 5.7. These are the highest temperatures expected in the substrate, due to the applied surface heat flux, and therefore important for material transformations. The nip point is reached at t=0 s. The irradiation of the deposited material is examined during the 2nd and 5th layer placement, under 25 Hz/4.75 ms (Figure 5.6) and 100 Hz/1.1 ms (Figure 5.7) pulsing conditions. The deposited material consists of one and four AS4/PEEK layers respectively. The predictions correspond to a velocity of 50 mm/s following the heat flux profiles of Figure 5.5a. The surface temperatures comprise consecutive heating/cooling cycles with timings dictated by the input heat flux (Figure 5.5a). A closer look at a pulse timescale is illustrated in Figure 5.8. The heating phase is as long as the pulse, whilst the repetition rate of the heating/cooling cycles is equal to the pulsing frequency. As a result, the material is subjected to more cycles at the higher frequency of 100 Hz. The longer pulses of the 25 Hz operation result in higher local maximum temperature; however, these decrease to lower values at the end of the period due to the longer cooling times before a new energy pulse is delivered (35.25 ms versus 8.9 ms). As the substrate thickness increases, greater temperatures are developed on the surface since the deposited layers, which have a low transverse conductivity, act as an insulating barrier to the heat diffusion towards the metallic tool.

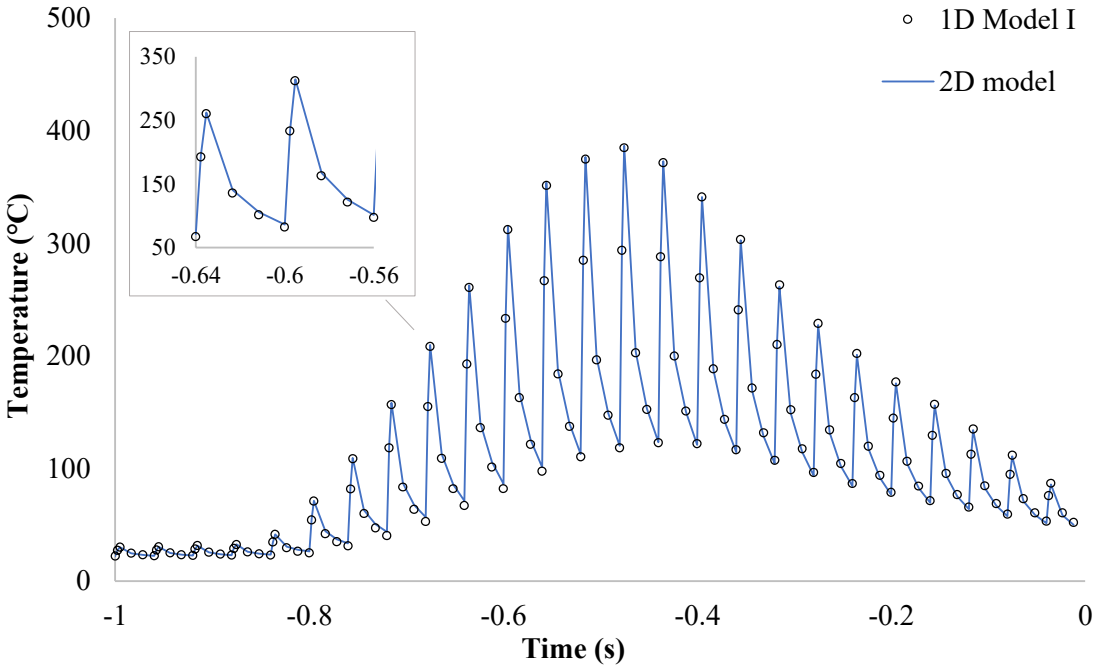

(a)

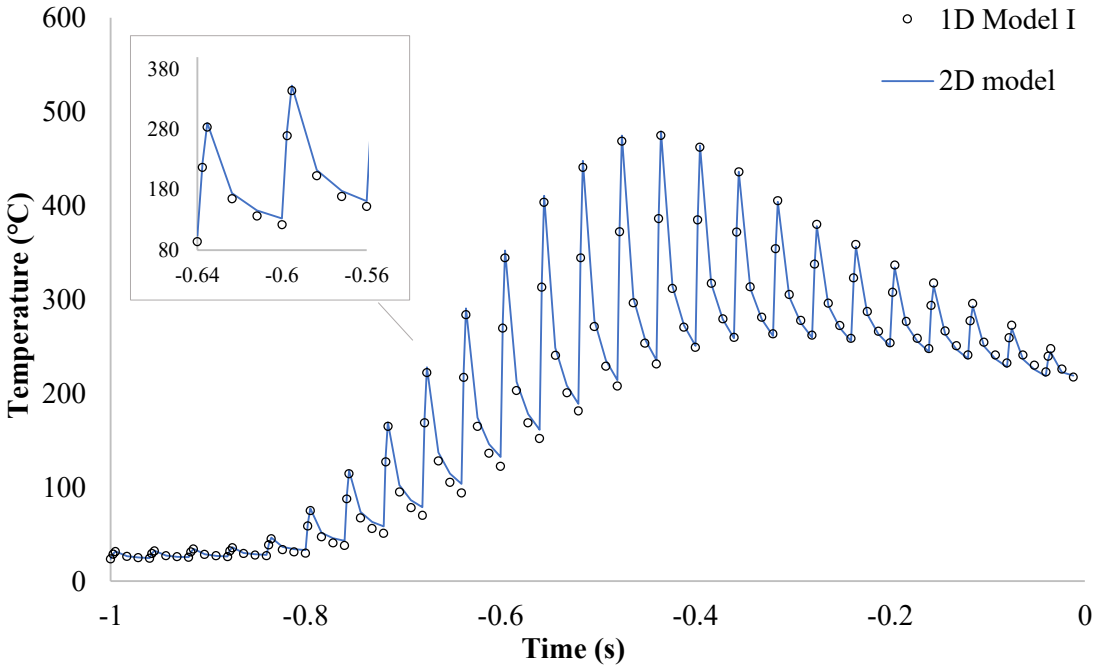

(b)

Figure 5.6 Comparison of predictions on the surface of the deposited material at 50 mm/s: (a) 2nd layer placement and (b) 5th layer placement under 25 Hz/4.75 ms operation. Nip point reached at t=0 s.

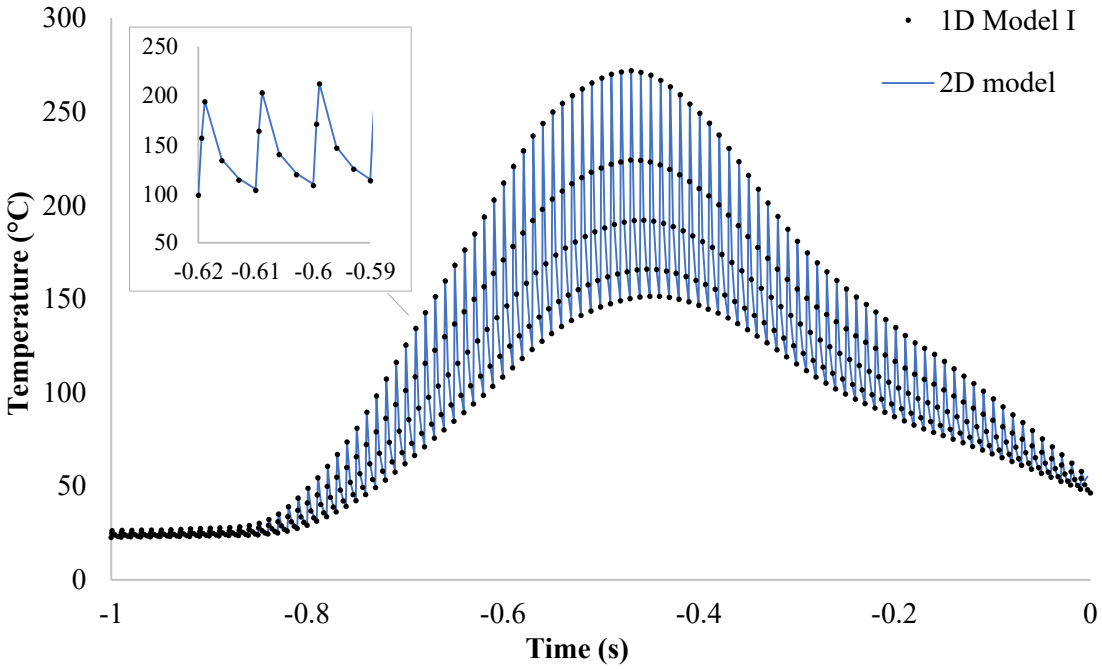

(a)

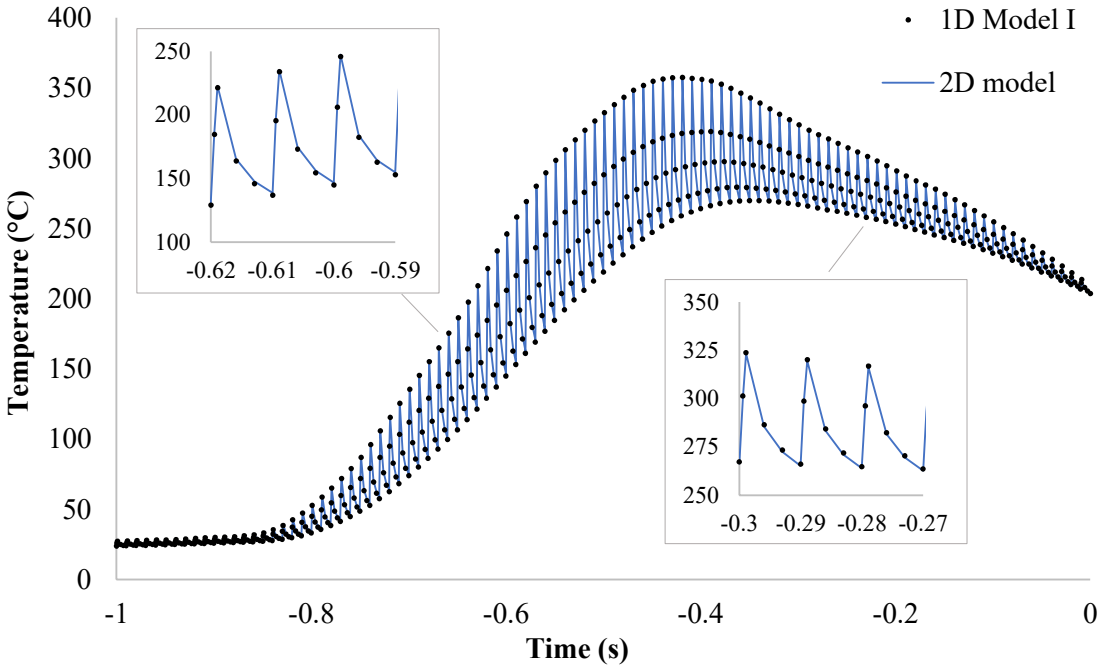

(b)

Figure 5.7 Comparison of predictions on the surface of the deposited material at 50 mm/s: (a) 2nd layer placement and (b) 5th layer placement under 100 Hz/1.1 ms operation. Nip point reached at t=0 s.

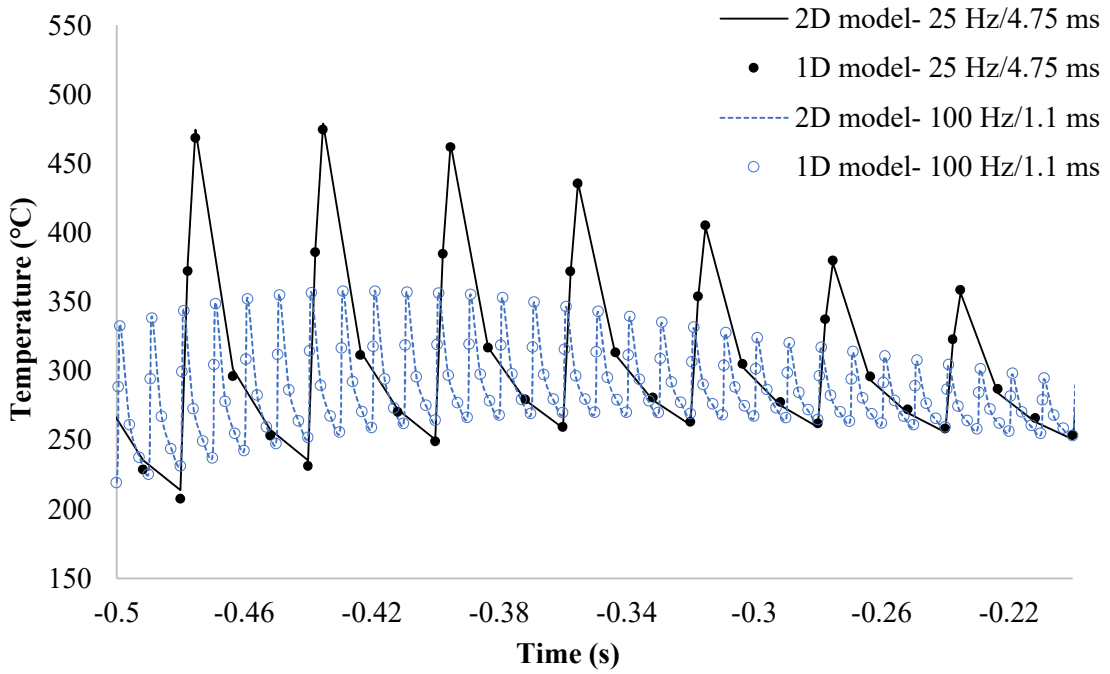

Figure 5.8 Heating/cooling cycles during pulsing on the surface of the deposited material under two different source operations. Placement of 5th layer at 50 mm/s.

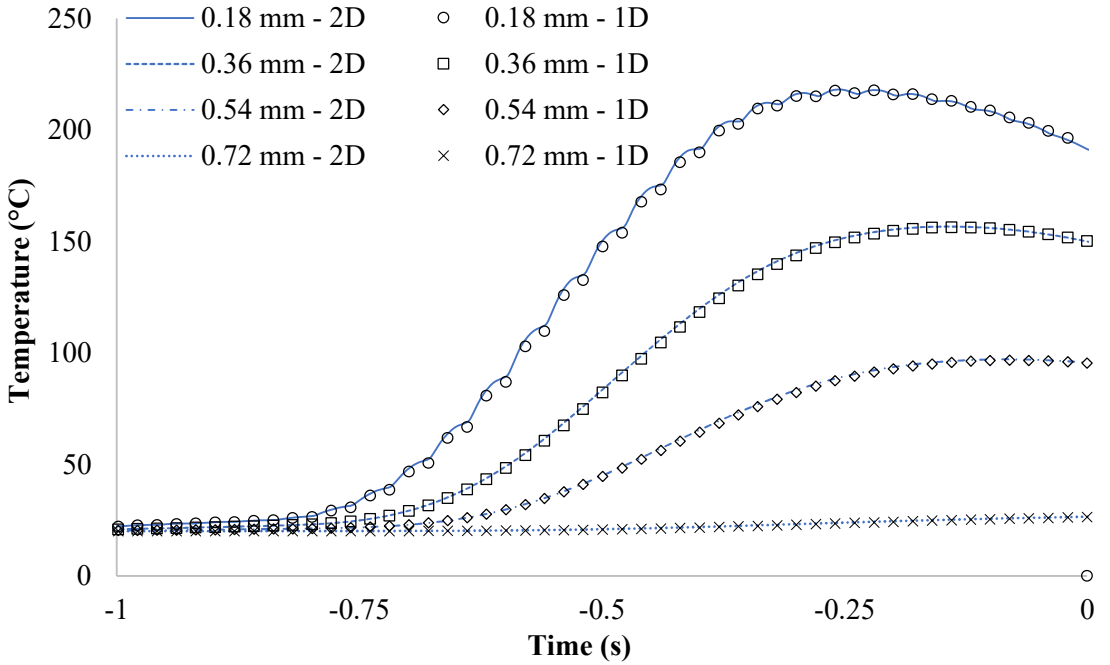

Figure 5.9 Comparison of bulk temperatures in the deposited material during the 5th placement at 50 mm/s. Operation is 25 Hz/4.75 ms. Depth measured from the composite surface. 1D data have been downsampled.

Model I predictions of surface temperature on the deposited material are in close agreement with the results of the 2D model (Figures 5.6 and 5.7), with errors of up to 10°C. An average error of 2°C is present across all examined scenarios. The timings of the heating/cooling cycles on the material surface are in full agreement (Figures 5.6 and 5.8) due to the exact time discretisation in steps. The greatest deviations occur at 25 Hz and for the 5th ply placement due to the greater temperatures developed (Figure 5.6). At 100 Hz, the maximum deviation for both placements is below 5°C (Figure 5.7). These minor deviations are attributed to the fact that the 1D simulation does not incorporate the heat conduction in the placement direction (Eq. (5.3)), in contrast to the 2D model (Eq. (5.1)). These effects have been assumed to be negligible due to the high Peclet number calculated; however, the specific tool examined features a very high conductivity which results in Peclet numbers corresponding to the conduction/advection of the tool being lower than unity. As a consequence, the reduction of the 2D domain to 1D for the tool introduces a discrepancy. However, this effect causes only small errors even at the low speed of 50 mm/s; it is expected that its influence is diminished at greater velocities where the Peclet number increases. Deviations of up to 5°C are observed inside the bulk of the substrate, as shown in Figure 5.9 for the 5th placement in the 25 Hz/4.75 ms scenario. The temperature oscillations created on the surface due to the pulsed operation are diminished even at one layer depth (0.18 mm). Lower temperatures are developed deeper in the material, whilst significant time lag is observed before these locations are affected by the incoming heat wave.

5.3.2 Tow heating

The predicted temperatures obtained by the 1D and 2D models for the incoming tow (Model II) surface are compared in Figure 5.10 for the two pulsing operations of 25 Hz/4.75 ms (Figure 5.10a) and 100 Hz/1.1 ms (Figure 5.10b). These are the highest temperatures expected for the tow and therefore important predictions for material transformations. The heat flux profiles presented in Figure 5.5b have been utilised. The heating conditions of the tow are independent of the substrate thickness in both methodologies, and thus tow temperatures are similar during the 2nd and 5th placement. Similarly to the profiles on the deposited material surface (Figures 5.6 and 5.7), the tow surface undergoes periodic heating cycles followed by cooling with timings dictated by the flashlamp operation. The higher frequency conditions (Figure 5.10b) lead to a greater

number of cycles whilst the 4.75 ms long pulses of the 25 Hz case cause higher local temperatures (Figure 5.10a). The tow temperature for both pulsing conditions presents a more pronounced cooling stage compared to that for the deposited material profiles (Figure 5.7), approximately after t= -0.25 s, when the tow comes into contact and dissipates heat to the roller. Predictions of Model II with ±10% shorter/longer roller arc length, compared to the actual length in the 2D model, are presented in Figure 5.10a. The arc length affects the contact activation time in Model II, and thus the heat exchange between the tow and the roller. The 1D predictions start deviating noticeably when the timing involved has an uncertainty of ±10%, indicating the strong heat transfer interaction between the two bodies.

Model II is in good agreement with the 2D model with an average error of 3°C and maximum of 12°C. Similarly to Model I, the deviations are attributed to the exclusion of longitudinal heat conduction as well as the 2D domain of the body in contact, the roller in this case. Differences are also introduced in this case due to the deformed mesh grid across the roller curved section in the 2D model. In addition, the linear velocity attributed to the elements which belong to this section follows their distance from the roller centre, ensuring they feature a common angular velocity as part of the same rotating body. Tow surface elements in the 2D model follow the same trajectory; however, elements towards the inner boundary of the roller have slightly lower linear velocity. The difference in velocities across the tow and roller thickness influences the thermal field evolution, but this effect is small.

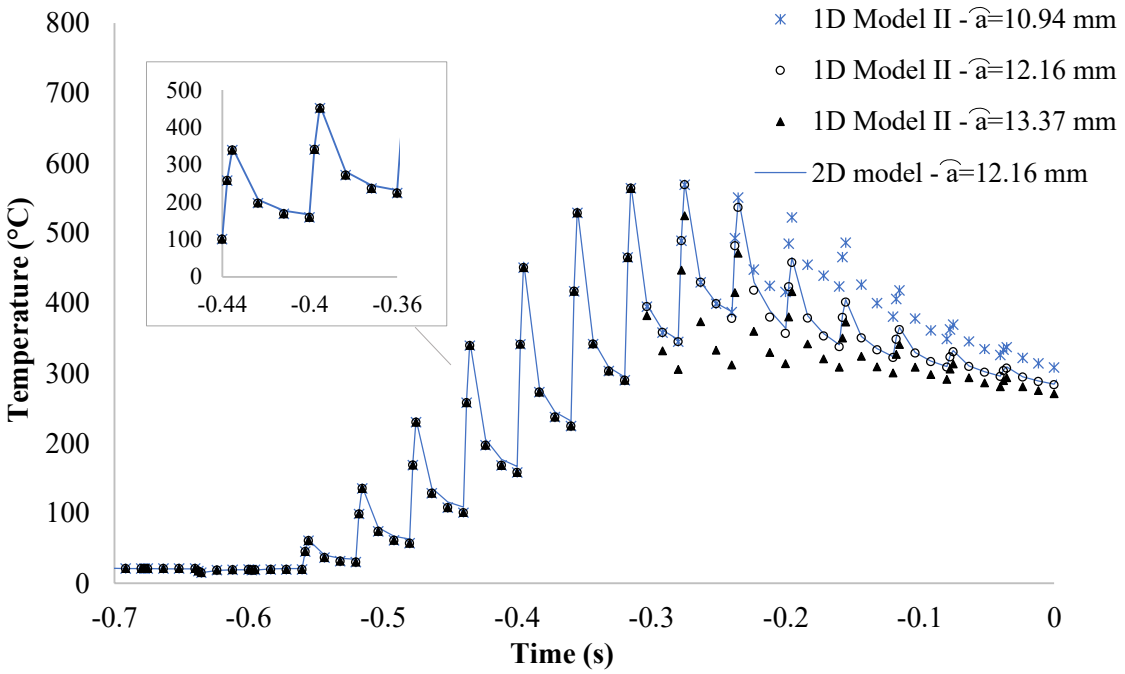

(a)

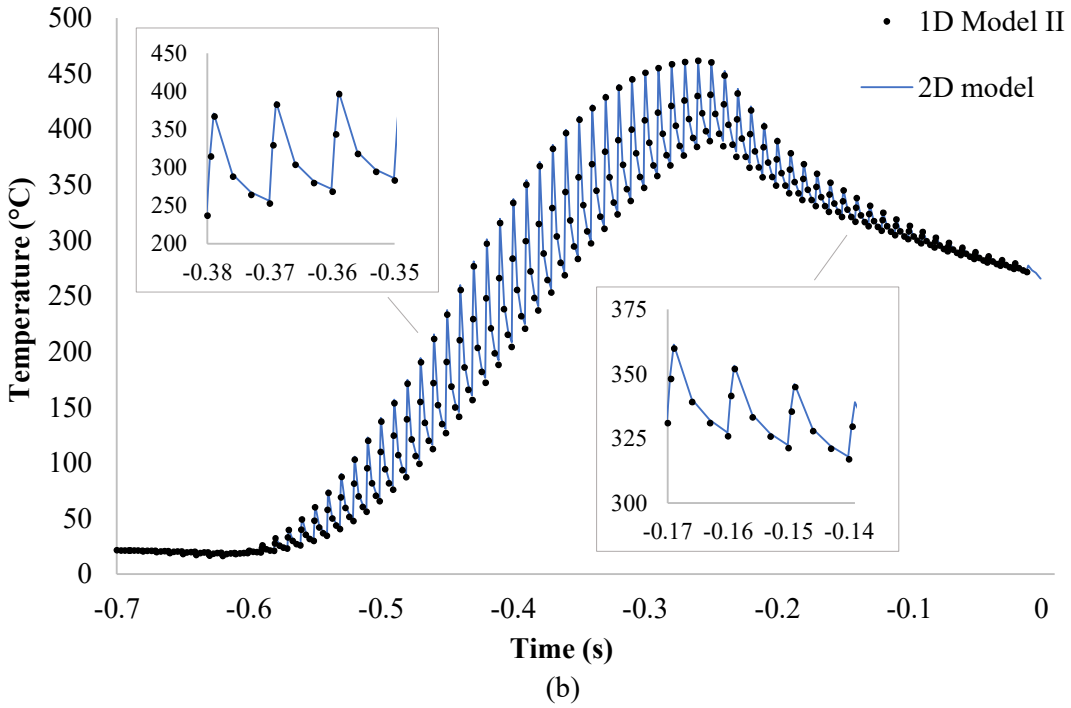

(b)

Figure 5.10 Comparison of tow surface predictions at 50 mm/s: (a) under 25 Hz/4.75 ms operation; (b) under 100 Hz/1.1 ms operation. Nip point reached at t=0 s.

5.3.3 Consolidation zone

A comparison of temperatures developed across the consolidation zone at 50 mm/s is provided in Figure 5.11 for different deposited material thicknesses, assuming ambient conditions at the start of each new placement. Profiles across different layer interfaces are examined, as this information is highly relevant for bond strength studies. Results of the 1D model have been downsampled to an interval of 0.03 s to facilitate visualisation. The developed temperature decreases away from the nip point due to heat losses to the roller, tool and environment. Lower values are encountered at deeper material levels, whilst as the thickness increases, higher temperatures are developed due to the insulating effect of deposited layers. Predictions for the 4^{th} and 10^{th} placement are reported in Figures 5.12 and 5.13, respectively, for a wider range of processing speeds. Five interfaces near the surface are examined for the thick substrate. The time span of the 30 mm long consolidation region is determined by the processing velocity in each case (Figures 5.12 and 5.13). The heat flux inputs used in Model I and Model II for these runs at 25 and 100 mm/s have been calculated similarly to the 50 mm/s case (Figure 5.5). Higher velocities lead to lower temperatures due to the shorter heating times of the deposited material and tow in the previous irradiation stage. The temperature oscillations created on the tape surfaces during irradiation have decayed in this region of the process.

Model III achieves good accuracy with an average error of 4°C and a maximum error of 14°C for all depositions and processing speeds. As in Model I and Model II predictions, these errors are attributed to the exclusion of longitudinal heat conduction effects, especially for the highly conductive tool, and the interaction of the stack with the roller body. As a result, both the tool and the roller representation as 1D bodies introduces errors in the 1D simulation. This effect is more noticeable for interfaces closer to the contact of the stack with the roller. The greatest deviations between the two methodologies in Figures 5.11- 5.13 are encountered for the 1^{st}- 2^{nd} layer interface predictions.

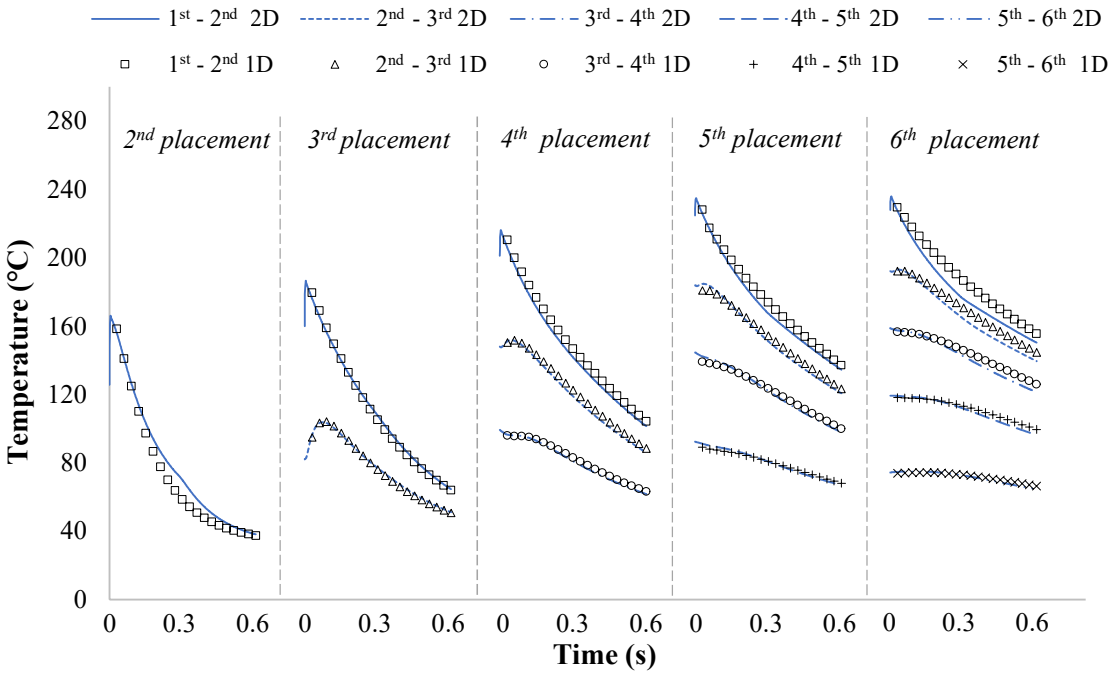

Figure 5.11 Predictions in the consolidation zone for consecutive placement assuming ambient initial conditions. Interface numbering is relative to the consolidated material surface. Velocity is 50 mm/s and operation is 100 Hz/1.1 ms. 1D data have been downsampled.

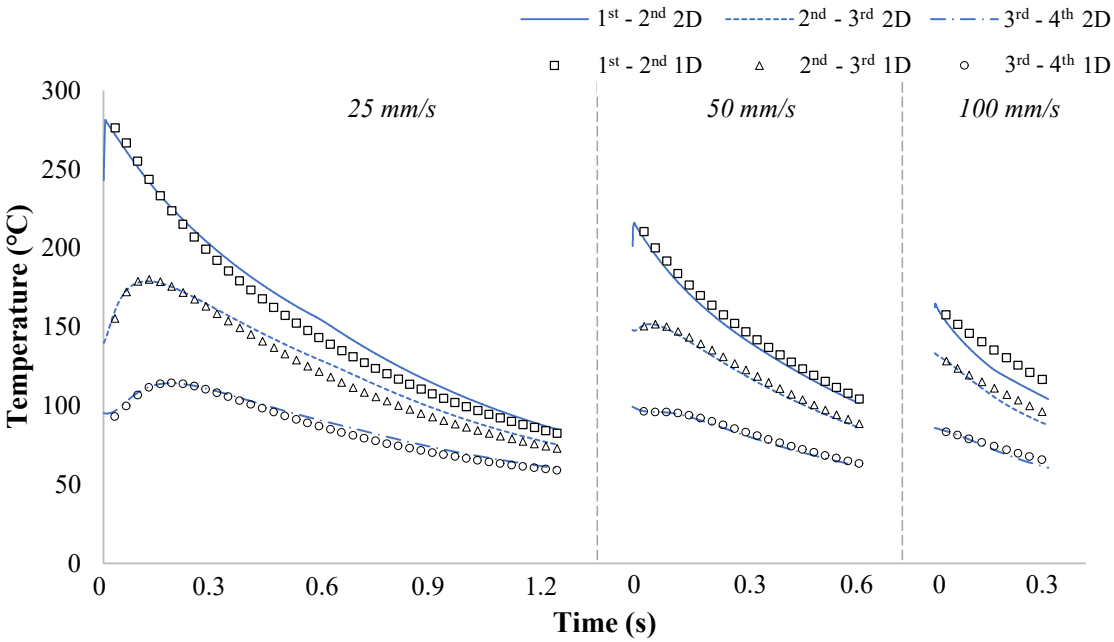

Figure 5.12 Predictions in the consolidation zone during the 4th placement at different velocities, assuming ambient initial conditions. Interface numbering is relative to the consolidated material surface. Operation is 100 Hz/1.1 ms. 1D data have been downsampled.

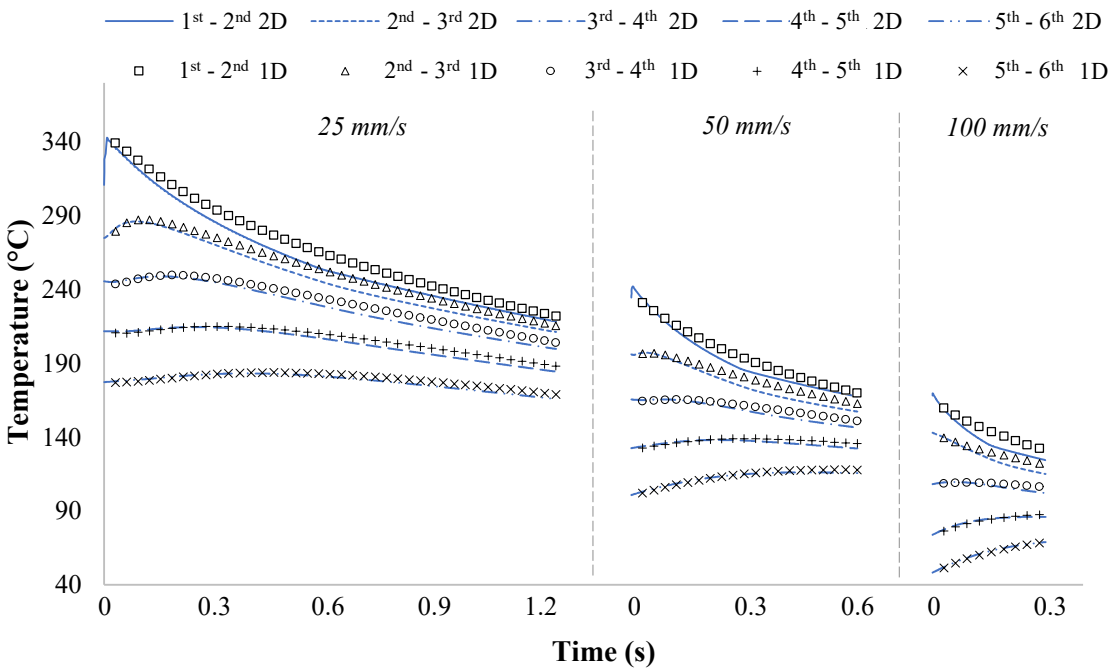

Figure 5.13 Predictions in consolidation zone during the 10th placement at different velocities. Interface numbering is relative to the consolidated material surface. Operation is 100 Hz/1.1 ms. 1D data have been downsampled.

5.4 Computational efficiency

The floating-point operations needed for the solution of the 1D and 2D models are presented in Figure 5.14, for different deposited material thicknesses and processing conditions. The reported values are calculated based on the CPU time and average computational rate, expressed as floating-point operations per second, provided by the finite element software (Ansys) in the analysis output file. For the 4-core PC (i7- 4790) used in this study, the average computational rates were in the 8-12 GFLOPS range.

The combined solution of the 1D models requires only 1-2% of the computational effort needed by the 2D analysis for the examined scenarios. The 1D model requires 0.2-1.5 TFLOP operations (20-150 s for the machine used) compared to 16-270 TFLOP (30-450 min for the machine used) for the solution of the 2D model. The thickness of the substrate has a more severe impact on the 2D analysis, with a 100% increase in computational effort between the thinner and thicker composite cases. The 2D solutions require 60 TFLOP and 130 TFLOP (104 and 220 min for the machine used) for a 0.18 and 1.62 mm thick deposited material at 50 mm/s respectively. The floating-point operations for the 1D simulation increase only by 25% between these two thicknesses and at 50 mm/s, from

0.67 to 0.77 TFLOP. This difference is because each layer introduces a larger number of elements in the 2D analysis due to the 0.09 m long geometry. Computational effort increases proportionally to the pulsing frequency but decreases with speed for both models due to the changes in the number of steps involved.

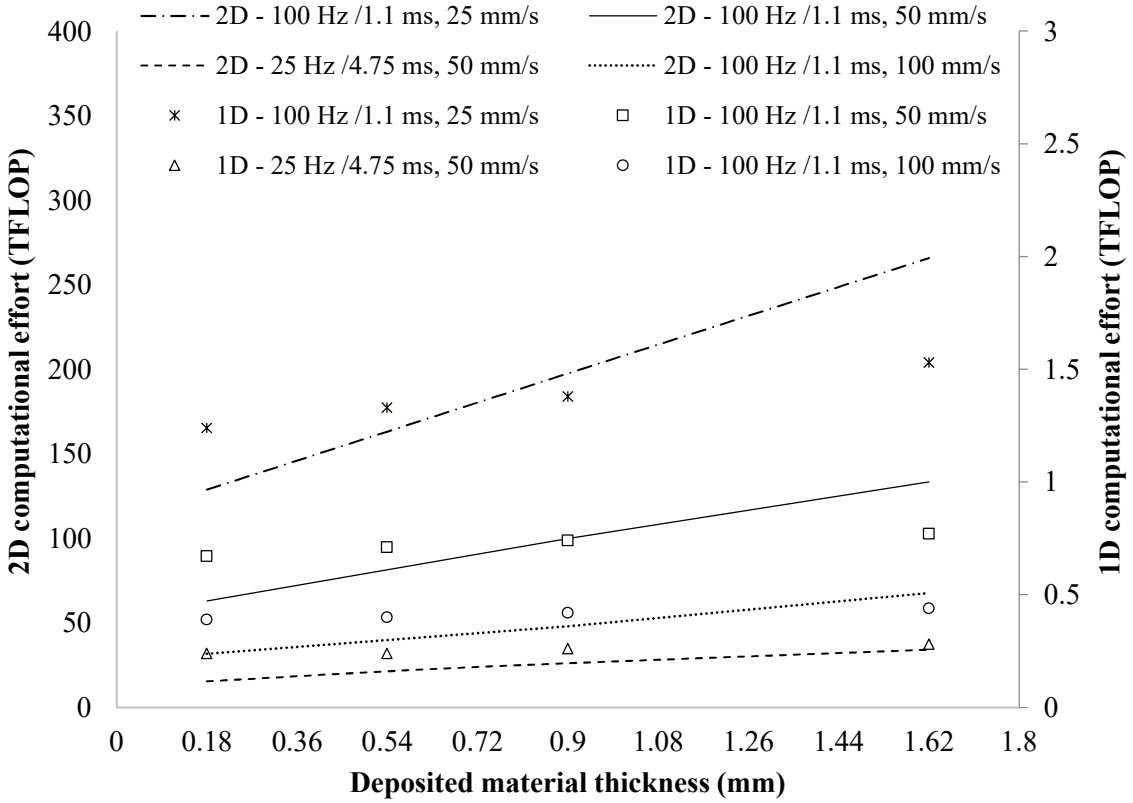

Figure 5.14 Computational effort needed by the two methodlogies for different processing scenarios of deposited material thickness, processing rate and pulsing conditions.

The 1D simulation requires significantly lower solution times due to the fewer elements in the analysis. Each submodel represents only a single 1D through-thickness section of the 2D model, thus the solution is carried out for only a small number of elements compared to the 2D version. In addition, the solution for the consolidation zone by Model III uses longer timesteps which contributes to the overall method efficiency. The decoupling of the time discretisation between the irradiation and consolidation zones is specifically advantageous in cases of residual heating effects during consecutive placements. Furthermore, the temperature evolution beyond the roller is critical in the prediction of material phenomena reflecting the final part quality, such as crystallinity and bonding strength development. Very high computational times are required by the

2D model even for the configuration of this study in which the geometry length outside the roller contact part is only 16 mm. Simulating a longer window would add a great number of elements and result in a severe computational penalty. The 1D simulation accomplishes the simulation of longer processing cycles by extending the analysis time of Model III, with no need of a larger geometry domain. Timesteps of 10 ms were used for Model III in this study; however, their duration can increase gradually away from the roller region, subject to analysis convergence and desirable time resolution. In addition, savings in computation times are expected during the simulation of consecutive layer placements since Model II predictions can be obtained once and used in the modelling of every processing cycle at equivalent conditions, reducing computational effort further.

5.5 Concluding remarks

A 1D heat transfer simulation of ATP was put forward in this chapter which represents the deposited material, incoming tow and resulting composite stack as distinct 1D through-thickness models. Appropriate transfer of temperature information ensures field continuity and inclusion of residual heating effects. The accuracy of the model was examined against the 2D model developed in Chapter 4. Deviations up to 14°C were found and attributed mainly to the exclusion of heat conduction in the placement direction in the metallic tool. The 1D simulation requires only 1-2% of the computational effort compared to the 2D analysis, indicating a significant gain in solution times for a minor trade off in accuracy. This exceptional efficiency is partially attributed to the decoupling of the irradiation and consolidation domains, a highly advantageous feature of the 1D simulation. Longer timesteps can be used across the consolidation and subsequent cooling stage allowing the investigation of temperatures throughout the process more efficiently.

6. Multi-objective optimisation of flashlamp-assisted ATP

6.1 Introduction

In this chapter, a multi-objective optimisation of the flashlamp-assisted ATP process is developed by coupling the 1D heat transfer simulation developed in Chapter 5, the constitutive models of interlaminar bonding and thermal degradation detailed in section 3.6, and a Genetic Algorithm implemented in MATLAB. The optimisation framework is employed to identify conditions of processing velocity, frequency and heater power which accomplish a desirable trade-off between production rate, maximum bonding strength, and suppression of thermal degradation effects during the manufacture of multi-layered thermoplastic composite parts.

6.2 Degradation model

6.2.1 TGA results

The results of dynamic TGA experiments at different heating rates are plotted in Figure 6.1. The methodology followed is detailed in section 3.6.3.Weight loss for the AS4/PEEK in air atmosphere commences at temperatures as low as 450°C (Figure 6.1a); however, this threshold shifts to higher temperatures with increasing heating rates, approximately to 600°C at 50°C/min. This is reflected in the derivative of weight loss with the curves shifting to higher temperatures with faster rates (Figure 6.1b). This is attributed to the fact the exposure time to oxidative high temperature conditions is longer than at slow rates, which promotes greater progress of decomposition reactions. The material is fully decomposed at approximately 620°C and 800°C for the slowest (2°C/min) and fastest (50°C/min) heating rates respectively.

Figure 6.2 presents the results of the five isothermal TGA tests conducted in the 530-610°C temperature range with an increment of 20°C. Overall, higher isothermal temperatures result in faster sample decomposition (Figure 6.2a) as the process is thermally activated. In this case, the derivative curves of weight loss shift to shorter times with increasing isothermal temperature (Figure 6.2b). The material fully decomposes at the end of the runs except the 530°C case for which the experiment time was not sufficient. Full decomposition occurs in 30 min at 610°C, whereas it requires more than 140 min at 530°C.

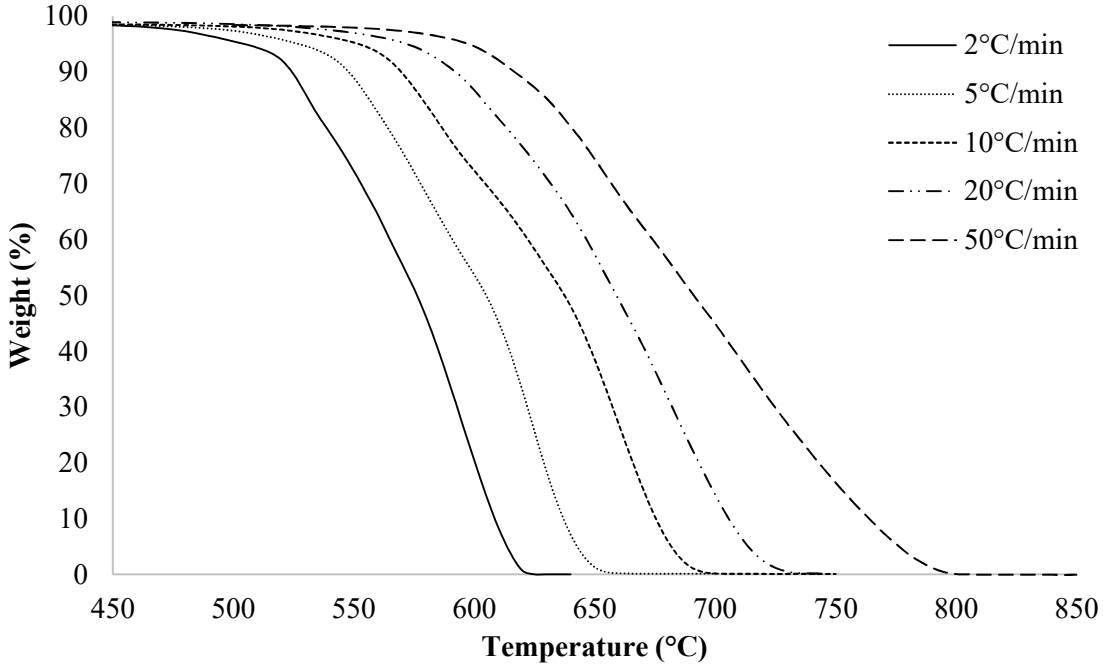

(a)

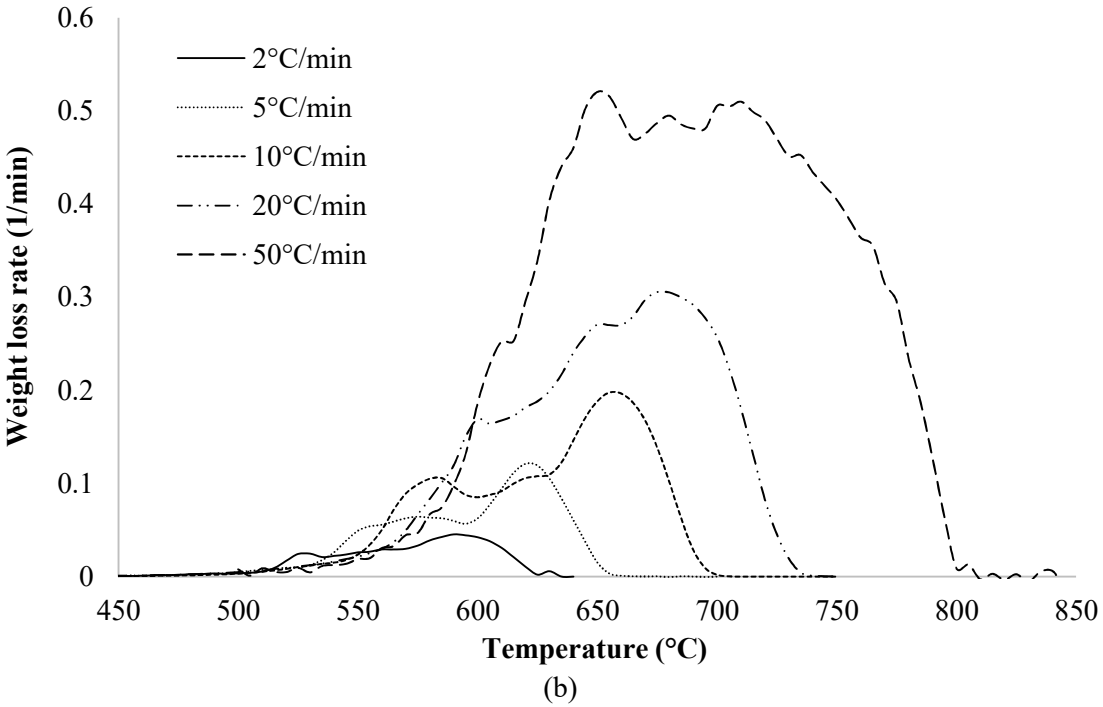

(b)

Figure 6.1 TGA results under dynamic conditions for the AS4/PEEK material in air: (a) sample weight loss and (b) weight loss rate.

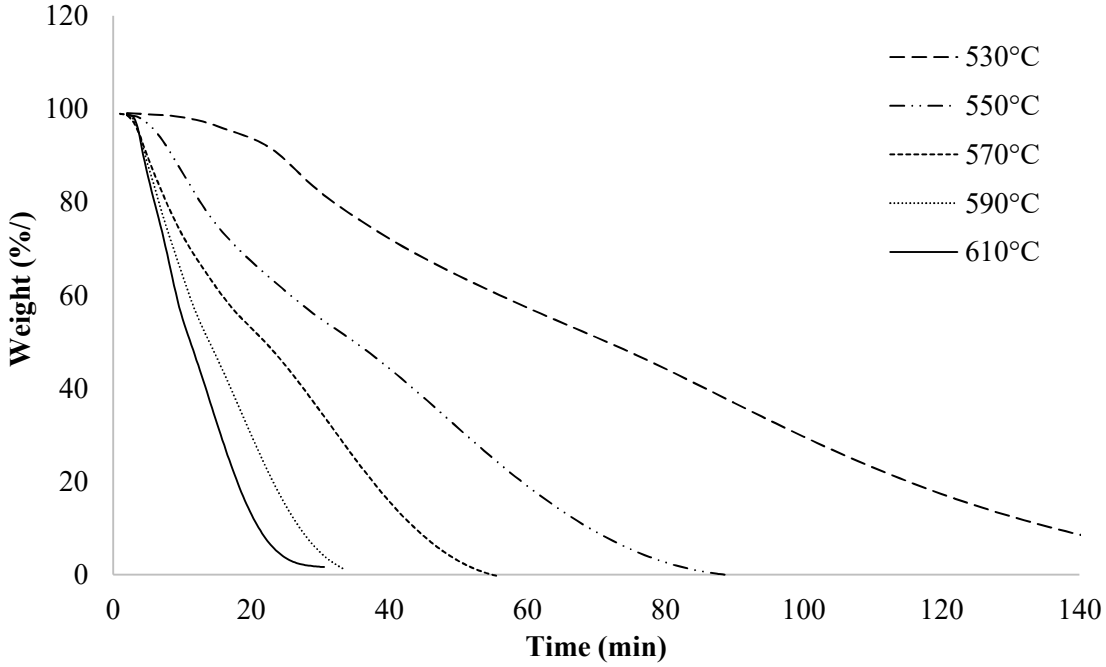

(a)

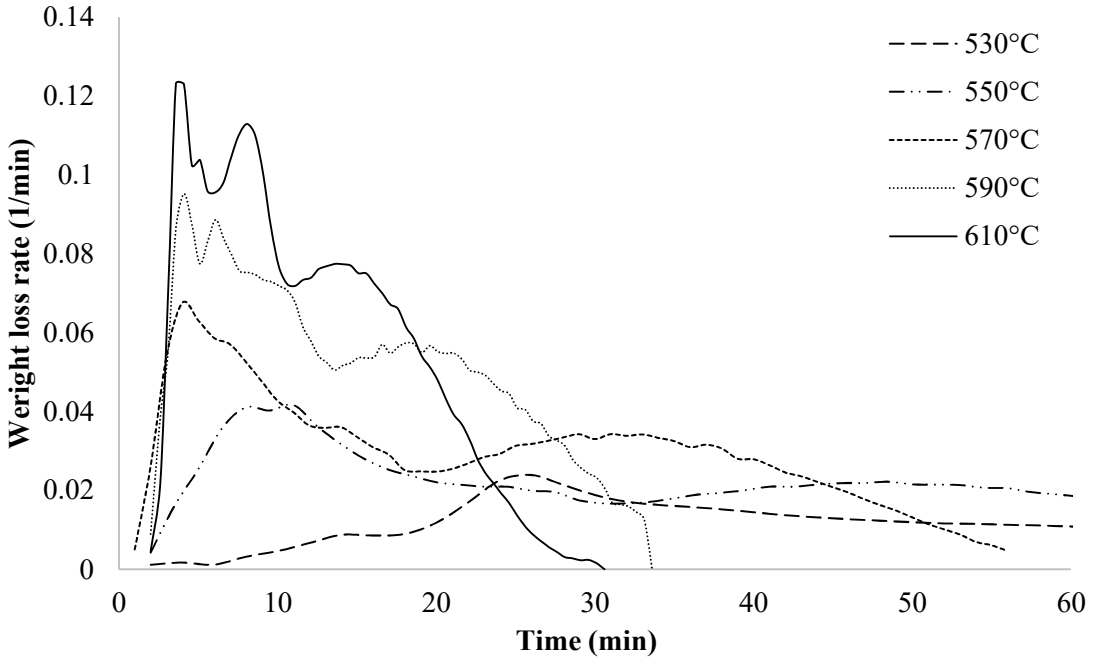

(b)

Figure 6.2 TGA results under isothermal conditions for the AS4/PEEK material in air: (a) sample weight loss and (b) weight loss rate.

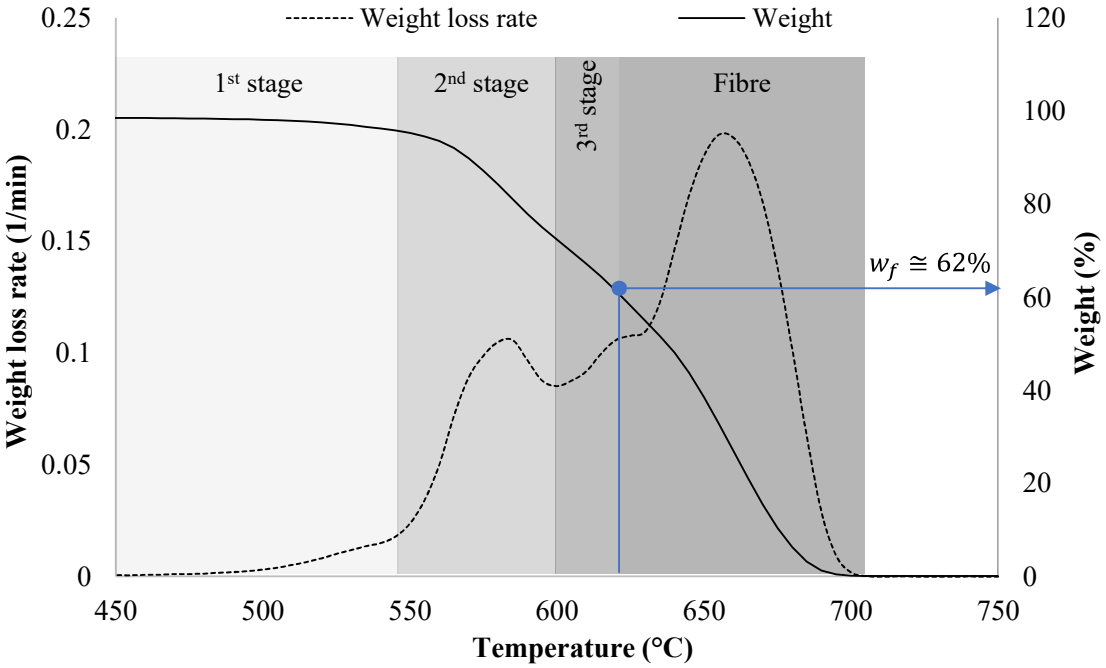

Figure 6.3 Decomposition stages for AS4/PEEK at 10°C/min in air.

The different decomposition stages of AS4/PEEK in air are identified in Figure 6.3 for the dynamic TGA trace at 10°C/min. In total, four processes are distinguished resulting in substantially different reaction rates. At this heating rate, PEEK degrades into char and gaseous products across the 500-630°C temperature range. The first decomposition mechanism starts at around 500°C. The second and third stage commence at approximately 550 and 600°C respectively. The sample weight is reduced by 4, 23 and 38% by the end of the first, second and third stage respectively. Decomposition of carbon fibres takes place over 630°C. As a result, the weight at the end of third stage (≅ 62%) coincides with the weight fraction of the carbon fibres in the sample (w_f). In this case, the estimated value corresponds to approximately 0.55 fibre volume fraction for representative density values, which is 0.05 lower than the nominal value of 0.6 (section 3.2). The exact fibre fraction is expected to vary around the nominal value due to the small size of the sample used in the TGA experiments.

6.2.2 Degradation kinetics model

The kinetics parameters determined based on the fitting procedure for the model represented by Eqs. (3.25) - (3.27) are reported in Table 6.1. The fitting was performed on both the dynamic and isothermal TGA data reported in section 6.2.1. The fibre weight fraction (w_f) determined for each experiment to represent the sampling variability is detailed in Table 6.2. These values are within the 0.6-0.7 range, as constrained during the fitting (section 3.6.3).

Table 6.1 Kinetic parameters for the four decomposition stages of the AS4/PEEK tape.

Stage	A_i (1/s)	E_i (J/mol)	n_i	m_{1i}
1st	4.747×10^{8}	2.1730×10^{5}	1.06×10^{-1}	1.48×10^{-1}
2nd	2.500×10^{9}	1.7786×10^{5}	1.05	7.09
3rd	2.432×10^{12}	2.5220×10^{5}	6.55×10^{-4}	1.05
Fibre	1.217×10^{5}	1.3638×10^{5}	7.32×10^{-2}	2.03×10^{-1}

Table 6.2 Fibre weight fraction fitted for each TGA run.

Dynamic tests		Isothermal tests	
2°C/min	0.70	530°C	0.70
5°C/min	0.60	550°C	0.60
10°C/min	0.70	570°C	0.70
20°C/min	0.62	590°C	0.70
50°C/min	0.60	610°C	0.70

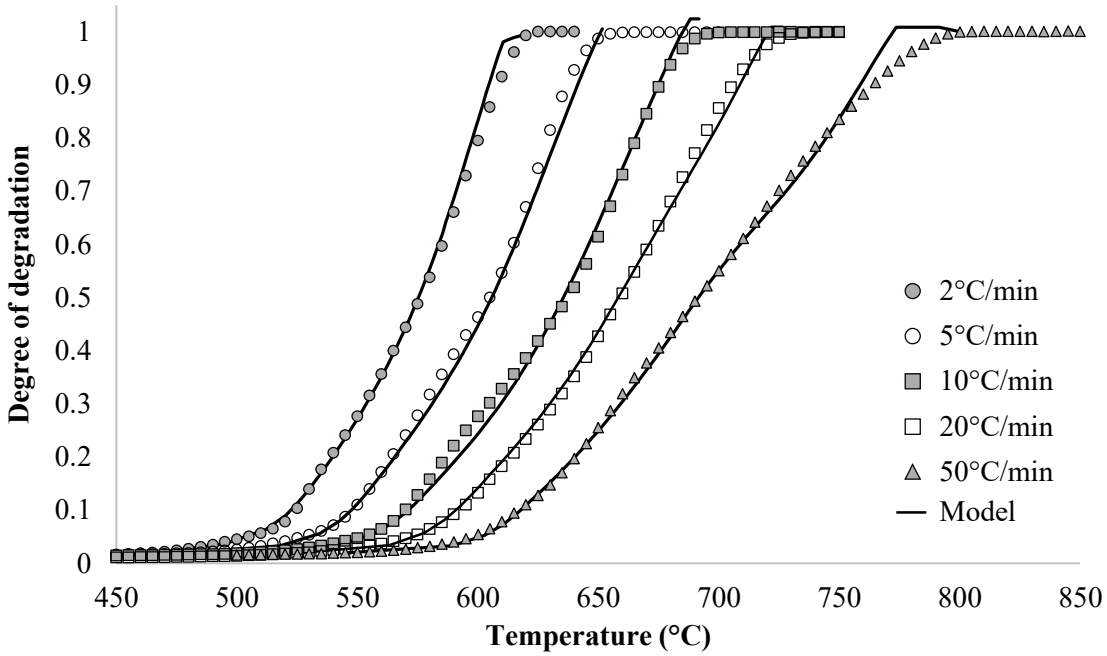

(a)

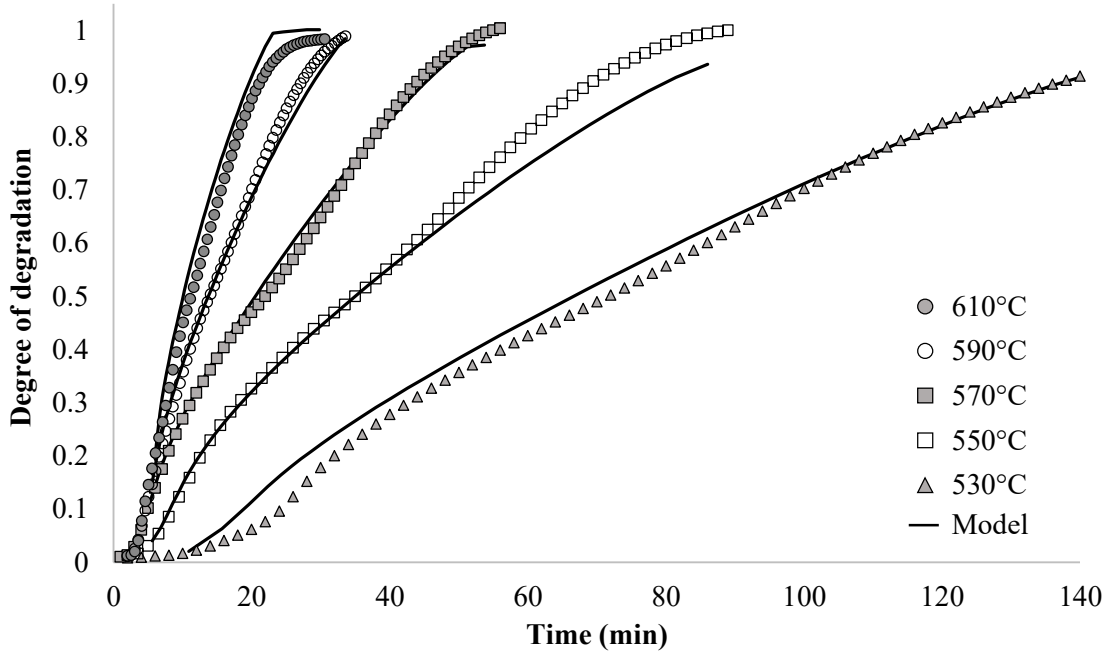

(b)

Figure 6.4 Comparison of the experimental and simulated degrees of conversion under (a) dynamic and (b) isothermal conditions for the AS4/PEEK tape in air.

A comparison of kinetics model and experimental TGA data for the AS4/PEEK in air is shown in Figure 6.4. The residual error between the two data sets averaged by the number of data points is shown in Figure 6.5 for the different heating conditions. The error is almost uniform across the different experiments ranging from 0.01 to 0.025; however, it is almost two times higher at 0.05 for the isothermal 610°C experiment. This is attributed to the fact that the decomposition has already started prior to reaching this temperature value and establishing isothermal conditions, which introduces an error during fitting.

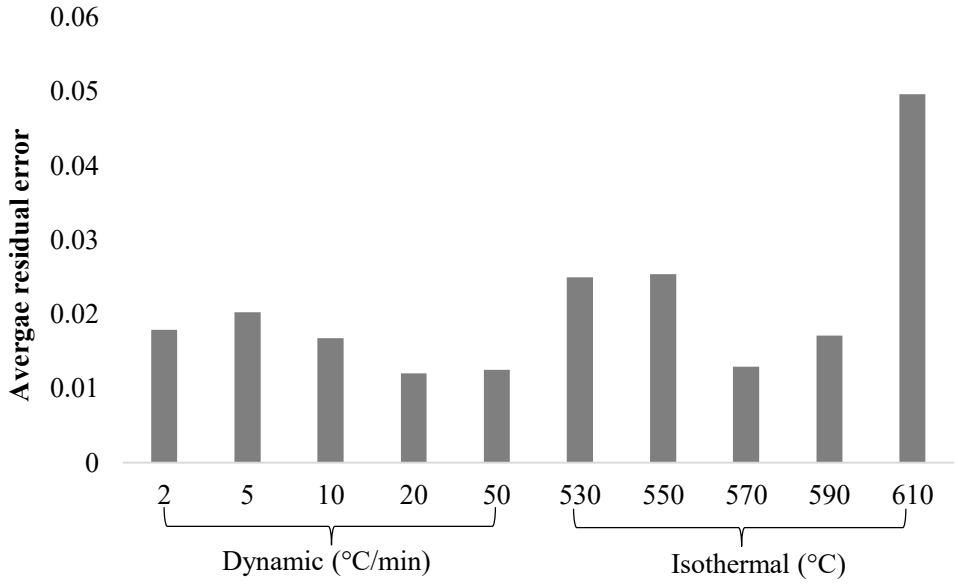

Figure 6.5 Average residual error in fractional degre of degradation between the kinetics model and experimental data for the different heating conditions.

6.3 Verification of bonding predictions

Calculations of intimate contact (D_{ic}), autohesion (D_h) and degree of bonding (D_b) were carried out based on thermocouple and pressure sensor data available in [124]. The profiles were captured during the manufacture of AS4/PEEK specimens at 100 and 333 mm/s [124]. Bonding predictions were performed in [124] using the same bonding models as the implementation described in section 3.6.2. As shown in Figure 6.6, predictions present minor deviations up to 8% attributed to the inaccuracies introduced due to the coarse sampling of values from the graphs and resampling to match the 0.001 s time increments used [124]. This assessment is carried out based on final values rather than the reaction profile due to lack of data. However, this is sufficient given that the objectives evaluation in this study is solely based on final values.

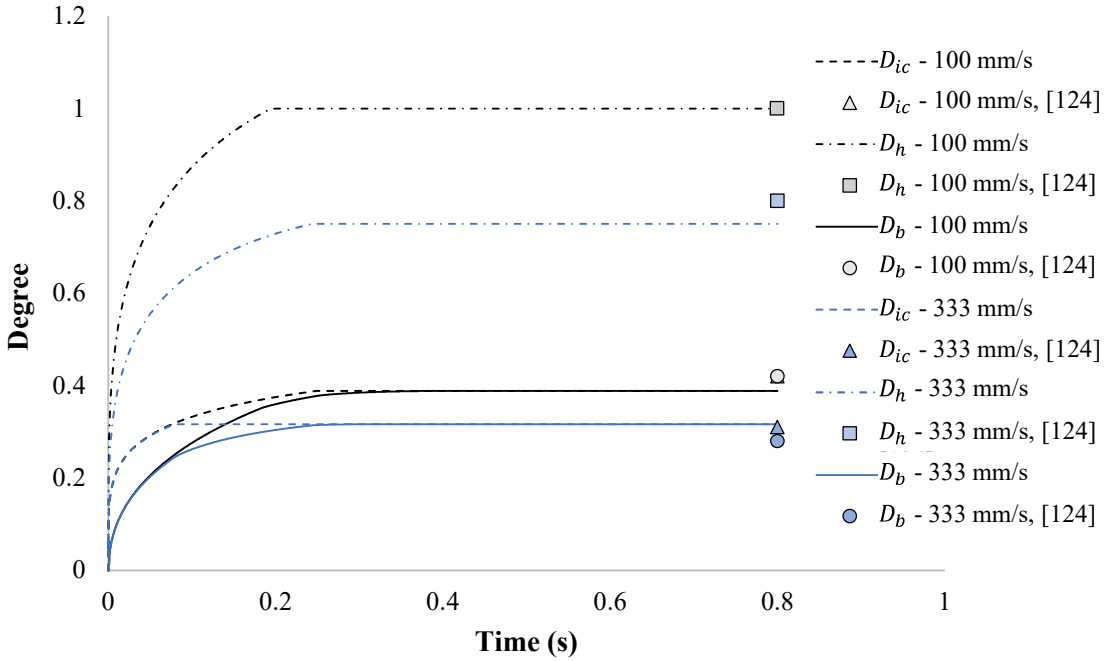

Figure 6.6 Verification of intimate contact (D_{ic}), autohesion (D_h) and bonding (D_b) estimations against values predicted in [124] for similar temperature and pressure profiles.

6.4 Optimisation scheme

A multi-objective optimisation scheme of ATP was developed by coupling the APDL solver with the GA available in MATLAB R2021 [215]. The overall scheme information flow is outlined in Figure 6.7. In each step, MATLAB exports an APDL input file containing a set of design variables as dictated by GA and triggers the execution of the FE solution. Once the heat transfer analysis has been completed, the temperature data are imported in MATLAB for the calculation of degree of bonding (Eqs. (3.17) - (3.21)) and thermal degradation (Eqs. (3.25) - (3.27)) across the stack with the parameters reported in Table 3.6 and Table 6.1 respectively. The objective function vector is evaluated, and a new APDL input file is created with the set of design variables for the next run. The following sections provides more information about the process model and the GA setup.

6.4.1 Process model

The process model utilised for the multi-objective optimisation of ATP integrates the 1D FE simulation developed in Chapter 5, the bonding development model described in section 3.6.2, and the degradation kinetics model of AS4/PEEK reported in section 6.2.2. The 1D simulation was favoured over the 2D version (Chapter 4) due to its significantly faster computation and minor trade-off in accuracy (section 5.4). Furthermore, the

simulation features a structure which allows efficient solutions of multiple layer placements incorporating residual heating and longer processing cycles, making full use of the capabilities of the simplified model presented in Chapter 5.

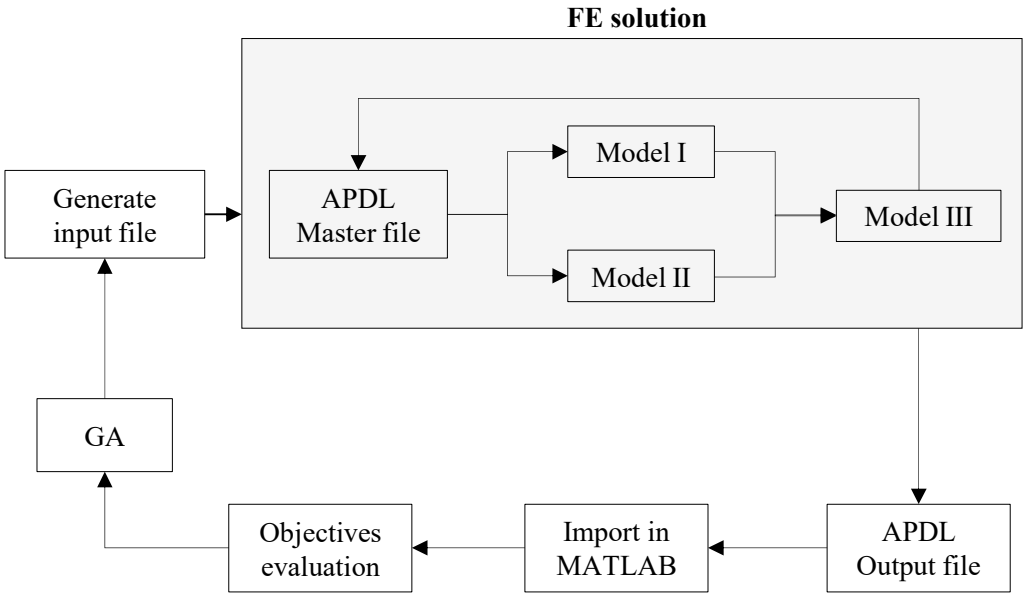

Figure 6.7 Flow of information between GA and FE solver.

The examined ATP setup features the geometry illustrated in Figure 5.1. For this optimisation, the ambient zone length (C) is adjusted for every speed so that the temperature field is monitored for 5 s in total after the roller contact patch. The heating source represents the humm3® system detailed in Chapters 4, 5 and section 3.3.1; however, its average power is considered in the 4.4 – 11 kW range to expand the process design/optimisation envelope. This power range is in line with the capabilities of humm3® systems. The duty cycle is independent of power following Eq. (3.2). A single parameter $Z \in [1, 2.5]$ is employed to control the power, with the lower and upper bounds corresponding to 4.4 kW and 11 kW of average power respectively. The irradiance distributions provided in section 4.3 act on the tapes, with their values scaled up linearly to match the pulsing power in each case. In addition, the profiles are transformed for use in the 1D simulation according to the pulsing conditions and processing speed, as described in Figure 5.3 and shown in Figure 5.5 for two pulsing conditions at 50 mm/s.

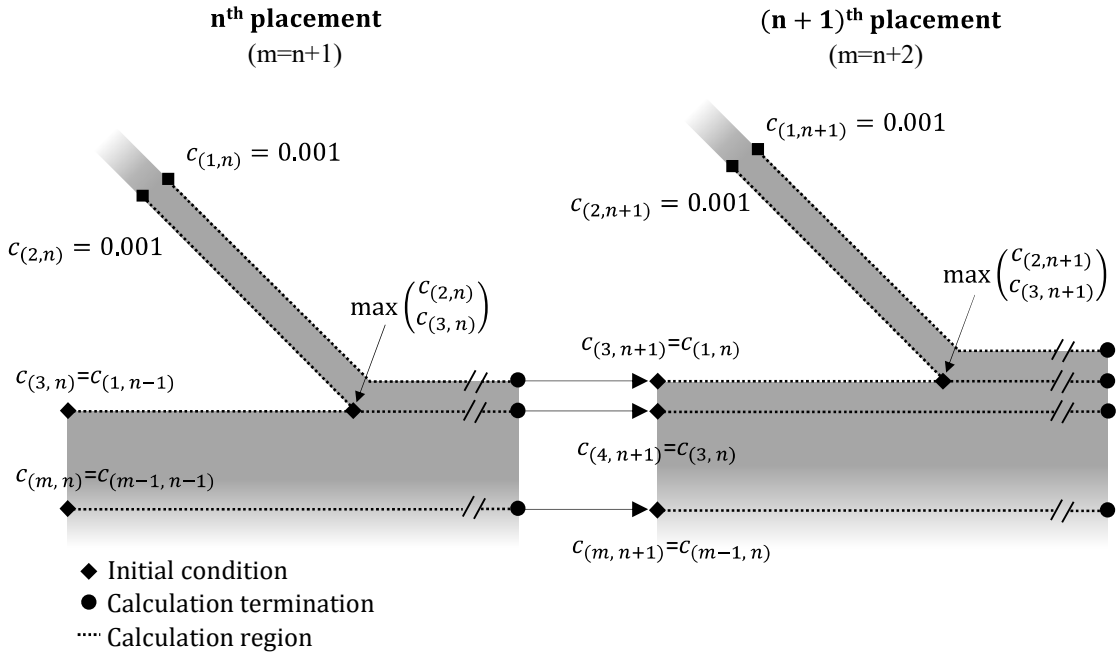

(a)

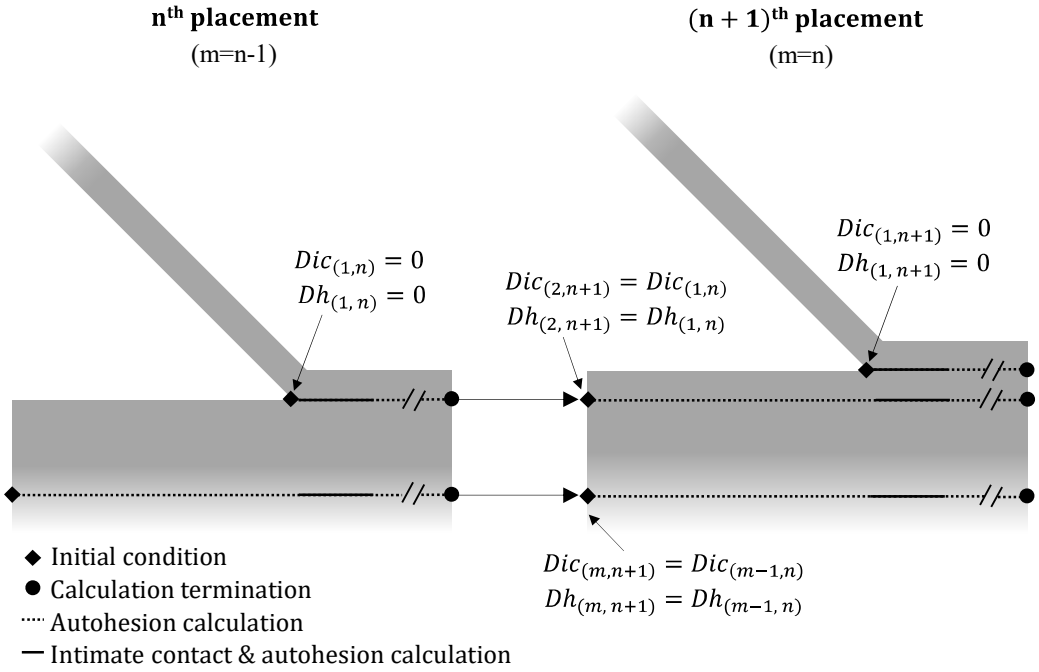

(b)

Figure 6.8 Computation of (a) degree of degradation and (b) degree of bonding for multiple placements. The regions each calculation takes place are represented with lines. m denotes region number and n placement number.

The solution of the constitutive models is outlined in Figure 6.8 for the manufacturing of multi-layered components. Overall, the implementation ensures that the history of the stack degradation and degree of bonding is maintained throughout multiple processing

cycles. Degradation calculations are performed across $m = n + 1$ regions during the n-th placement (Figure 6.8a). These regions include the tow $(m = 2)$ and deposited material $(m = 3)$ irradiation surfaces, which are expected to experience the highest temperatures during processing. These effects are also important on the tow back surface $(m = 1)$, which also develops high temperatures and acts as the deposited material surface for the next cycle. Degradation is also calculated across the layer interfaces in the deposited material. The incoming tow is assigned a very low initial degradation value of 0.001 since the material is assumed to be in pristine condition. On the other hand, the initial condition for the deposited material surface $(m = 3)$ is carried over from the previous placement. The incoming tow and substrate surfaces typically develop different temperatures and thus potentially different conversions. A single value is assigned to the newly formed interface commencing from the nip point, which is the highest of these two values, assuming that the contact between the tow-deposited material does not influence decomposition. Degradation calculation is then performed across the bondline and ambient region with that initial condition. Temperature and degradation are assumed to be the state variables of the kinetics model used (Eq. (3.25)) without any other effects induced by the dynamic character of the process, which is in line with previous studies. As a result, the model developed in section 6.2.2 is applicable to ATP conditions which involve substantially higher heating rates than those tested with TGA. Bonding calculations are carried out for $m = n - 1$ regions during the n-th placement, which is equal to the number of composite interfaces in the stack (Figure 6.8b). Autohesion development takes place across the whole process for all interfaces. On the other hand, intimate contact develops only across the roller contact patch for the newly formed interface $(m = 1)$, as well as the interfaces deeper inside the deposited material.

The pressure distribution ($P_{app}(t)$) under the compaction roller required for the intimate contact model is approximated by [216]:

$$\begin{cases} \varepsilon(x) = \dfrac{r - \sqrt{(r - \Delta d)^2 + (gx)^2}}{r - r_o} \\ P_{app}(x) = E_c \dfrac{\varepsilon(x)}{1 - \varepsilon(x)} \dfrac{r_o}{\sqrt{(r - \Delta d)^2 + (gx)^2}} \end{cases} \tag{6.1}$$

where $\Delta h = r - h_r$, h_r is the distance of the roller centre to the surface in contact at the deformed position, r_o is the roller inner diameter, E_c the effective compression modulus and g a scaling factor. The spatial x coordinate is with respect to the distance from the roller centre.

The solution expressed by Eq. (6.1) corresponds to a deformable roller pressed against a flat rigid surface. Therefore, the predicted pressure distribution corresponds to the roller-composite interface with no dependence on the composite thickness or temperature. Studies addressing the compaction problem in ATP have focused the analysis on the composite or the roller, treating the other body as rigid [67, 69, 107, 216]. This is necessary as the highly nonlinear behaviours of these materials lead to increased complexity. Here, the roller is assumed to be highly deformable so that a solution corresponding to a rigid composite-tool assembly applies. Furthermore, representative pressure profiles are adequate for the purposes of this study since processing outcomes sensitive to the roller-composite mechanical interaction such as the composite thickness, residual stresses and void dynamics are not included in the analysis. Optimising for these effects would require incorporation of additional physics in the simulation. As a result, the predicted pressure distribution acts on all interfaces in the deposited material.

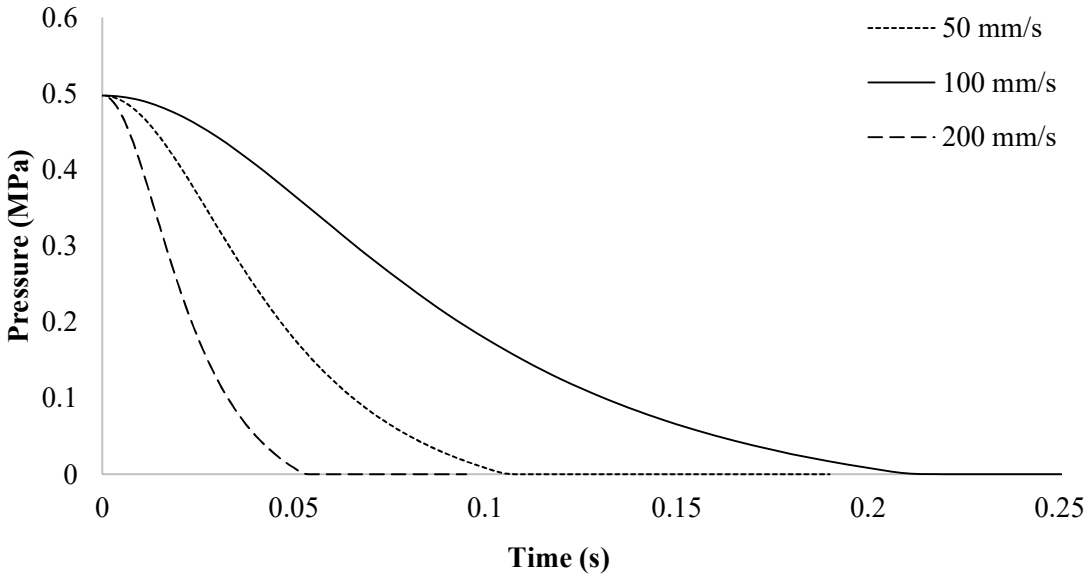

Figure 6.9 Symmetric pressure distribution applied to composite interfaces at different processing speeds. The roller centre is reached at t=0 s.

The model parameters (E_c, Δh and g) have been estimated empirically in [216] by fitting to FE analysis results under different compaction forces. The values extracted apply to the roller of this study. The roller external and internal radii were set at 25 and 10 mm respectively. The predicted pressure distribution at the roller-composite interface is illustrated in Figure 6.9 for different processing rates. The distribution is symmetrical around the roller centre and velocity influences the compaction time only. Equivalent pressure distributions have been measured [124] and predicted [216] for the combination of elastomeric rollers and AS4/PEEK composites.

6.4.2 Genetic algorithm setup

The GA employed for the multi-objective problem in MATLAB ($gamultiobj$) [215] is a variant of the Non-dominated Sorting Genetic Algorithm (NSGA-II) [208]. The algorithm favours design variable vectors (individuals) which result in better objective function vectors (fitness value). At the first step, the algorithm creates an initial random population of uniform distribution ($CreationFcn \rightarrow gacreationuniform$) and user defined size ($PopulationSize$). These sets of variables are created with respect to the upper (ub) and lower (lb) bounds defined for each design variable. The variables are converted to binary numbers with 0 or 1 digits ($Populationtype \rightarrow bitstring$). Each design variable can take 2^n discreet values in the $[lb, ub]$ range, where the value of n effectively controls the variable resolution. A fraction of 80% of the next generation individuals are created by crossover ($CrossoverFraction$), 5% by the current generation best performers ($EliteCount$) and the rest through a mutation procedure. The selection of parents for crossover is carried out by examining four random individuals and choosing the best as a parent though a tournament section process ($SelectionFnc \rightarrow selectiontournament$). The algorithm combines two parents to form a crossover offspring for the next generation. Uniform crossover is used in this implementation. A random binary vector, with a size equal to the design variable vector, is generated and the algorithm selects a gene from the first parent where the vector is 1, and one from the second parent where the vector is 0 ($CrossoverFcn \rightarrow crossoverscattered$). During the mutation, the algorithm makes small random changes in the population to ensure genetic diversity and achieve a broader search of the variables space. Here, the mutation function randomly generates changes in the population genes with respect to the last successful or unsuccessful generation ($MutationFcn \rightarrow mutationadaptfeasible$).

The iterative procedure for finding the best individuals, thus the Pareto front, continues until the maximum number of requested generations is exceeded ($MaxGenerations$), or if the average relative change of the Pareto solutions over a selected number of recent generations ($MaxStallGenerations$), 5 generations here, is lower than a tolerance ($FunctionTolerance$), set at 10^{-2} here. The spread of solutions is a measure of the movement of the Pareto set on the objectives space. Parameters of this implementation are summarised in Table 6.3. An extensive sensitivity study was performed to select these parameters examining the impact on the fitness value of the Pareto points in relation with the computational effort.

A penalty equal to ten times the original value is added to the objective function terms which do not satisfy the constrains. As a result, these individuals are assessed as inefficient by the algorithm and eliminated in subsequent generations by not being part of the crossover or carry over procedure. This penalty is introduced during the objective function evaluation without the use of integrated GA commands in MATLAB.

Table 6.3 GA configuration options used in MATLAB implementation.

GA input	Value
$PopulationSize$	100
$MaxGenerations$	30
$SelectionFcn \rightarrow Selectiontournament \rightarrow size$	4
$CrossoverFraction$	0.8
$EliteCount$	0.05
$FunctionTolerance$	10^{-2}
$MaxStallGenerations$	5

6.4.3 Optimisation objectives and variables

The design variables for the multi-objective optimisation of ATP are the processing rate (u_x), the flashlamp system frequency (F) and power scaling factor (Z) which controls

the system average power in the 4.4 kW - 11 kW range. As a consequence, the design variables vector is formed as $\boldsymbol{x} = [u_x, F, Z]^T$.

The system pulse duration for a given frequency is calculated using Eq. (3.2):

$$p = \frac{D}{F} \tag{6.2}$$

The range and discretisation of the optimisation variables are summarised in Table 6.4. Velocity has values in the 20 to 320 mm/s range with a uniform interval of 20 mm/s. The frequency is in the 25 - 100 Hz range, with increments of 5 Hz. The scaling factor (Z) is in the 1- 2.5 range, acquiring 16 possible values in total, with the lower bound representing the 4.4 kW power and the upper bound the maximum available power of 11 kW. These ranges and choice of discretisation result in 4096 (2^{12}) possible sets of processing parameters.

Table 6.4 Ranges of the optimisation design variables.

Variable	Range	Discreet values	Increments
u_x	[20, 320]	16	20 mm/s
F	[25, 100]	16	5 Hz
Z	[1, 2.5]	16	0.1

The optimisation scheme targets to maximise the production rate and bond quality of the part whilst suppressing thermal decomposition effects. The productivity objective is directly linked to u_x, assuming all placement steps during the component manufacture are carried out with a single constant processing rate. The bond quality is represented by a single value which is the average degree of bonding predicted across the stack interfaces after n placements, denoted as $\overline{D_b}$. The suppression of thermal degradation is ensured by minimising the maximum degree of degradation during manufacture.

A set of constrains is introduced for this optimisation. The minimum degree of bonding developed in the stack is constrained above a threshold value, equal to 0.10, to ensure sufficient interlaminar strength for part handling and integrity against gravitational and placement forces. On the other hand, the maximum degree of degradation should be kept

low to avoid deterioration of the part mechanical properties. This threshold has been set below 0.01 in previous studies [104, 107]. For this study, values up to 0.30 are allowed to elucidate the influence of processing conditions on decomposition. The conditions are restricted further in a second stage of analysis to consider this aspect.

At the end of the n-th placement, the objective function for $i \in (1, 2, \ldots, n)$ calculation regions (section 6.4.1) is defined as:

$$\boldsymbol{f}(u_x, F, Z) = \begin{cases} f_1 = 1 - \dfrac{\sum_{i=1}^{n-1} D_{b\ (i,n)}}{n-1} = 1 - \overline{D_b} \\ f_2 = 1 \,/ u_x \\ f_3 = \max\left(c_{(i+1,n)}\right) \end{cases} \tag{6.3}$$

under the constrains:

$$\min\left(D_{b\ (i,n)}\right) \geq 0.10 \ \text{ and } \ \max\left(c_{(i+1,n)}\right) \leq 0.30$$

where $D_{b\ (i,n)}$ and $c_{(i,n)}$ denote the degree of bonding and degradation developed across the i-th interface during the n-th placement (section 6.4.1). Objective f_1 is evaluated by subtracting $\overline{D_b}$ from unity, which leads to the maximisation of the quantity during the minimisation of the overall term. Similarly, objective f_2 is calculated as the inverse of processing rate, which translates to deposition time per unit length of processed tape.

6.5 Multi-objective optimisation

6.5.1 Pareto front and resulting trade-offs

The three-dimensional objective space of this optimisation is plotted in Figure 6.10. The results correspond to the placement of five layers on a single-layer deposited part, with the progression of material reactions being maintained throughout the manufacture as detailed in section 6.4.1. Each objectives triplet is coloured coded according to the average flashlamp power which ranges from 4.4 to 11 kW. Sixteen generations were executed by the GA before the stopping criterion concerning the average relative change of the Pareto solutions is met and the optimisation is terminated (section 6.4.2). As a result, the total number of variable sets tested is 1600 with 1405 of these satisfying the optimisation constrains (Eq. (6.3)). The eliminated cases correspond to objective values

which exceed the thresholds defined, and consequently receive a severe penalty (section 6.4.2).

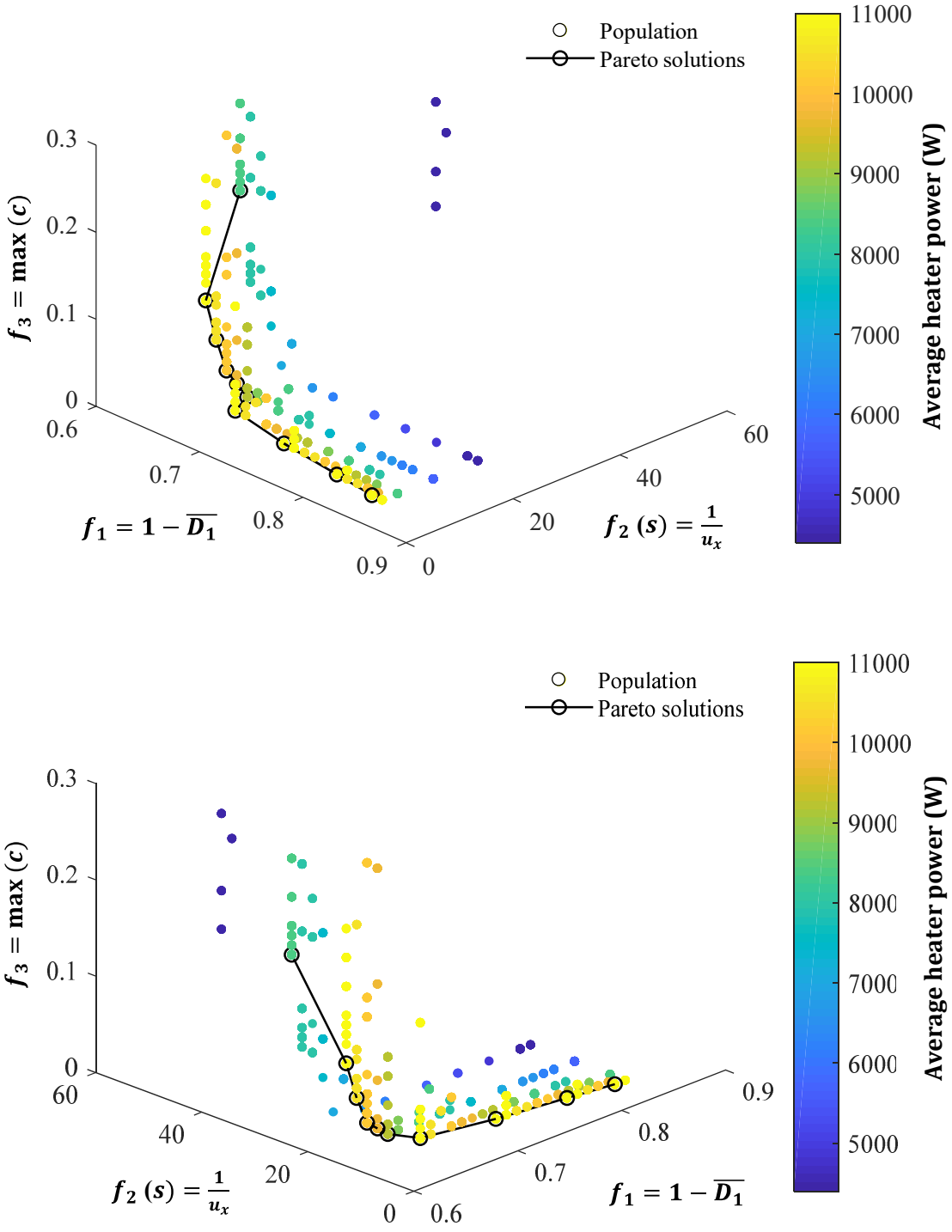

Figure 6.10 Two different views of the population and Pareto front of the three-objective optimisation of the ATP process.

The average degree of bonding ($\overline{D_b}$) achieved with the examined process configuration and variables selection (Table 6.4) varies from 0.15 to 0.39, with thermal degradation values up to 0.30 mainly developed on the tow surface (Figure 6.10). The lowest value of $\overline{D_b}$ and highest value for $\max(c)$ are in line with the constrains defined for this optimisation (Eq. (6.3)). The deposition time per unit length of tape (f_2) ranges from 7.14 to 50 s/m, which corresponds to velocities of 140 mm and 20 mm/s respectively. However, only a small number of cases feature at slow speeds such as 20 mm/s. These are present in the 1st generation in which the GA generates a uniform initial population, but are not selected as elite offspring and are soon eliminated as crossover parents for the next generations due to their inferior performance in all three objectives compared to other candidate solutions (Figure 6.10). As a result, the slowest velocity near the Pareto front is 40 mm/s. On the other hand, triplets featuring speeds greater than 140 mm/s receive a penalty for not achieving D_b values above the 0.10 threshold defined for this optimisation (Eq. (6.3)). As a consequence, only a narrow velocity range (40-140 mm/s) of the initially available range (20-320 mm/s) leads to minimisation of the problem objectives while satisfying the constraints defined.

The estimated Pareto front is presented in Figure 6.10, consisting of 10 points in the 3D objective space. The objective values of each Pareto point are detailed in Table 6.5. Pareto points score average bonding values in the 0.17-0.39 range, featuring processing times (f_2) within the 8.33-25 s/m range, and leading to degradation values (f_3) of up to 0.185. Projections of the 3D objective space on 2D surfaces are provided in Figure 6.11 to aid with the visualisation of the Pareto front and investigation of involved trade-offs. According to Figure 6.11a, interlaminar strength and productivity are in strong competition, as none of the points minimise objectives f_1 and f_2 simultaneously. High velocities improve production rates but result in low temperatures and shorter consolidation times, hindering the development of intimate contact and autohesion. High power levels generally improve $\overline{D_b}$ (Figure 6.11a) since bonding processes are thermally activated; however, low velocities have a stronger influence in achieving high degree of bonding. Specifically, Point 1 in Table 6.5 reaches a $\overline{D_b}$ value of only 0.17 at 140 mm/s although it utilises the full 11 kW average power. Reducing the velocity to 80 mm/s yields bonding values up to 0.33 for equivalent power levels (Point 4). This 75% increase of

production time translates to 94% improvement in bonding state. Further increase of $\overline{D_b}$ to 0.39 requires a velocity reduction to 40 mm/s (Point 10).

Table 6.5 Pareto front solutions and process variables after 16 generations.

Point	f_1	f_2 (s/m)	f_3	u_x (mm/s)	f (Hz)	$\overline{P}$ (W)
1	0.83	7.14	0	140	100	11000
2	0.79	8.33	0	120	70	11000
3	0.73	10.00	0	100	100	11000
4	0.67	12.5	0	80	90	11000
5	0.66	16.67	0	60	100	9240
6	0.65	16.67	0.010	60	100	9680
7	0.64	16.67	0.021	60	100	10120
8	0.63	16.67	0.045	60	100	10560
9	0.62	16.67	0.084	60	100	11000
10	0.61	25.00	0.185	40	100	8360

Point 5 in Table 6.5 scores a greater $\overline{D_b}$ than Point 4 due to the lower velocity at 60 mm/s; however, a marginal improvement of 0.01 in $\overline{D_b}$ is accomplished due to the simultaneous power decrease of approximately 2 kW. This behaviour is explained in Figure 6.11b which illustrates the objective space projected onto the f_1- f_3 plane. A strong trade-off between degree of bonding and thermal degradation is indicated. This is attributed to the fact that high temperatures facilitate fusion bonding but can trigger thermal decomposition under specific conditions. The conditions leading to thermal degradation correspond to points 5 to 10 in Table 6.5, with Point 5 representing the extreme case before thermal degradation effects progress above 0.01. The observed power drop is applied by the algorithm to maintain the degradation value of Point 5 at a minimum whilst achieving slightly higher $\overline{D_b}$ than Point 4. Without this adjustment, Point 5 would score a 0.19 degradation value matching Point 9 since both feature the same velocity (Table 6.5). Points 6 to 9 utilise increasing power almost in a linear way since this leads to improved $\overline{D_b}$ values, despite the fact that the values for objectives f_1 and f_3 are equivalent or inferior to Point 5. Minimising the thermal degradation at 40 mm/s whilst yielding the highest

interlaminar strength in the population necessitates a further reduction of power down to 8.3 kW (Point 10).

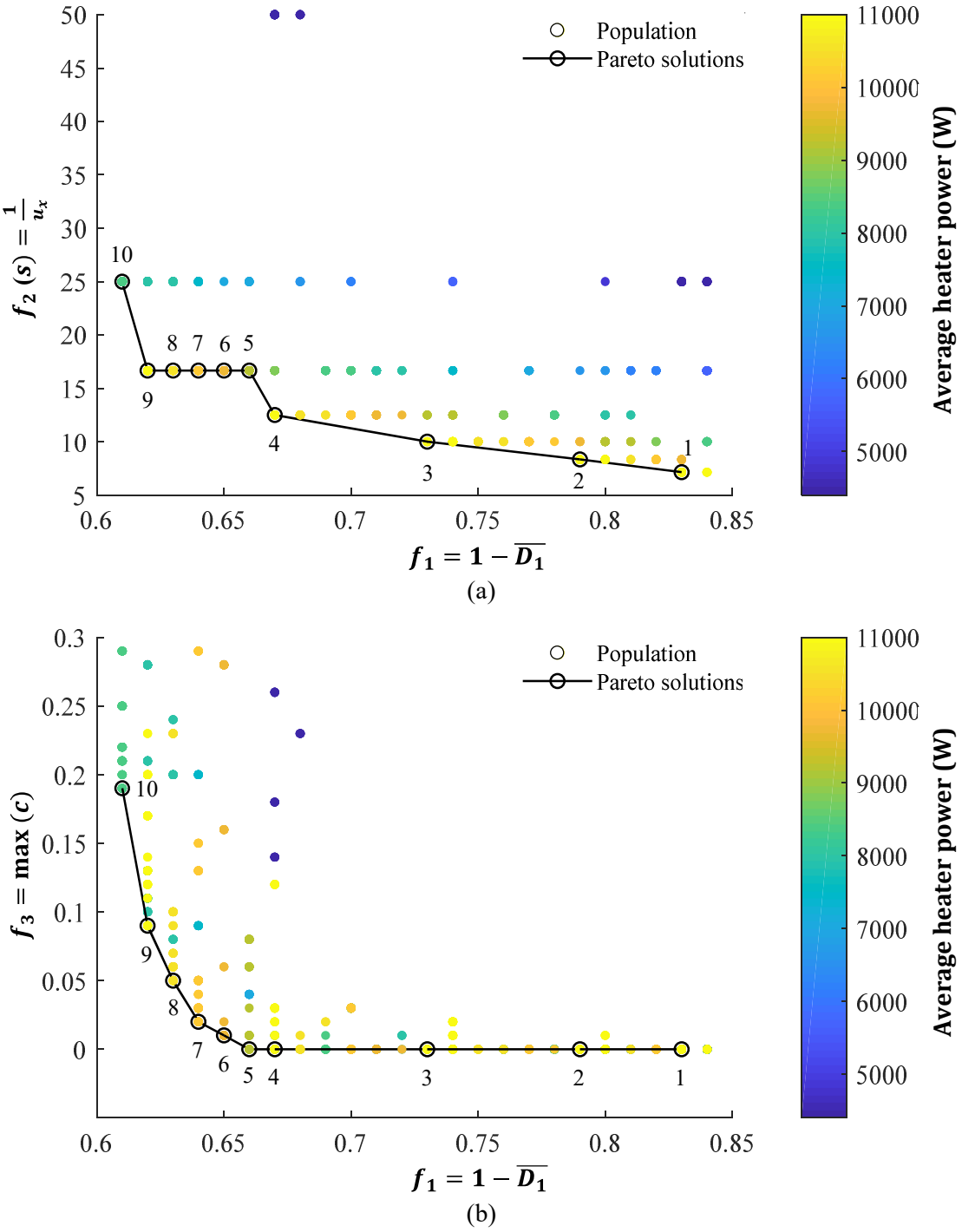

Figure 6.11 2D representation of the population and Pareto solutions as projected on: (a) f_1-f_2 and (b) f_1-f_3 objective surfaces.

According to the design variable values of the Pareto solutions (Table 6.5), this optimisation favours high frequency operations with 80% of points utilising a frequency of 100 Hz. Point 2 features a frequency below 90 Hz; however, this outlier value is attributed to incomplete convergence under the GA termination criteria selected, as determined by the inputs of $MaxStallGenerations$ and $FunctionTolerance$ (Table 6.3). The utilisation of high frequencies near the Pareto front is also displayed in Figure 6.12, in which the solutions are colour-coded based on the frequency of the heating source. Several low frequency points are present in this 2D projection, especially between Points 1 to 4, but these are located deeper along the f_2 axis. The overall trend for high frequencies is attributed to the relationship between frequency and pulse duration as set by Eq. (6.2). Lower frequency operations require longer energy pulses to yield equivalent average system power, leading to greater surface temperature maxima on the tapes during the irradiation phase (Figure 4.7), which in turn increases the potential of decomposition. On the other hand, longer pulses lead to higher bulk temperatures (Figure 4.9) which can aid bonding of interfaces located near the surface. Nevertheless, the influence of longer pulses on thermal degradation is stronger in this optimisation. Consequently, high frequency operations achieve the lowest thermal degradation for a given degree of bonding value. Indicative of this effect is the minimisation of the thermal degradation scores with increasing frequency as illustrated in Figure 6.12 for Pareto solutions 4 to 10.

The maximum $\overline{D_b}$ possible with the examined process configuration is 0.35 (Point 5 in Table 6.4) before thermal degradation is triggered severely and exceeds the 0.01 threshold commonly considered in aerospace applications. Pareto solutions suppressing thermal degradation represent different compromises between interlaminar strength and processing time, allowing the designer to balance these according to the requirements of a given application. However, quality is key for in-situ consolidation and therefore Point 5 represents the conditions of highest bond strength achievable with minor thermal decomposition. Two-stage manufacturing programs combining ATP layup with post-consolidation in autoclave or a press could boost throughput by selecting process setups among Points 1 to 4.

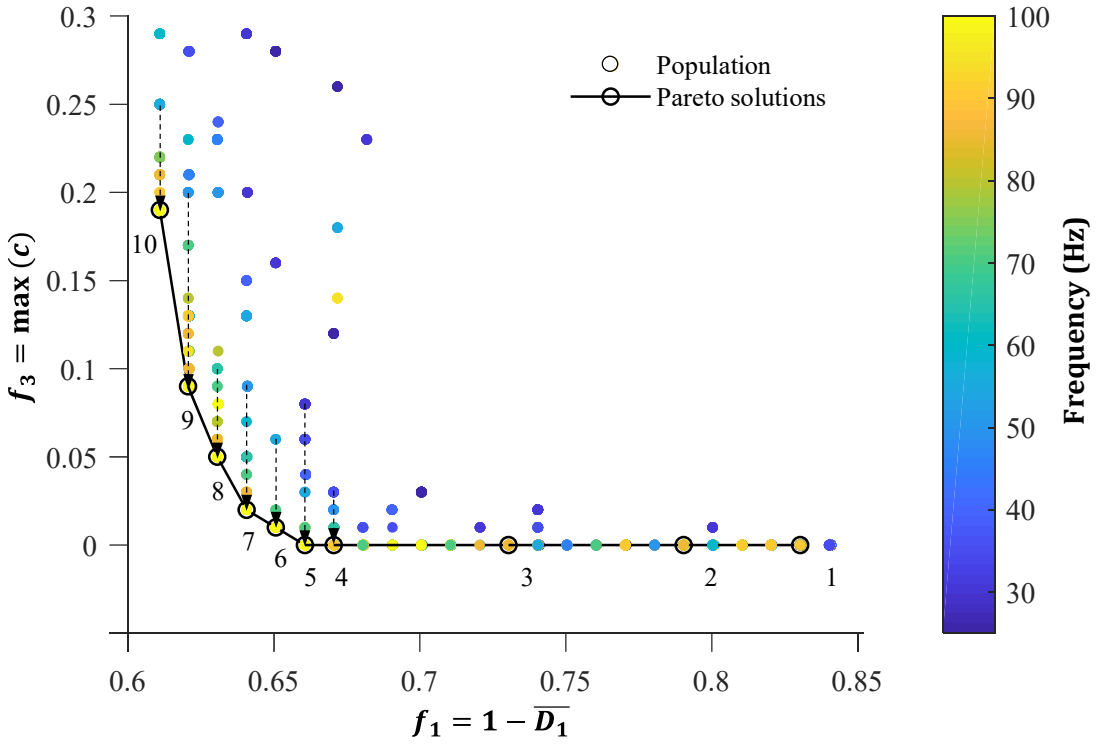

Figure 6.12 The f_1-f_3 objective surface with the population with colour coded representing the flashlamp pulsing frequency.

6.5.2 Computational efficiency

Three design variables were utilised in this optimisation each acquiring 16 potential values (Table 6.4), resulting in 4094 potential sets of variables. However, the use of the GA algorithm led to the determination of the Pareto front after 16 generations, each consisting of 100 solutions. This corresponds to 40% of the total runs required for an exhaustive reach, which in turn translates to approximately 60% faster computation. The evolution of the Pareto front throughout the generations is presented in Figure 6.13. Substantial differences of the Pareto front are observed during the 10 first generations. However, only a marginal improvement, below 2% of the value for each objective, is accomplished during the last 6 generations. Therefore, the algorithm has yielded a satisfactory estimation of the Pareto front by the end of the 10th generation, requiring only 25% of the computational effort of the exhaustive search. The GA inputs of $MaxStallGenerations$, $FunctionTolerance$ and $MaxGenerations$ can be tailored to increase the computational efficiency of this scheme further, with only a minor trade-off in accuracy. This is crucial for the application of the method to the manufacture of

components requiring multiple optimisation runs, as a result of complex geometry, varying process inputs and higher number of layers than the scenario examined here.

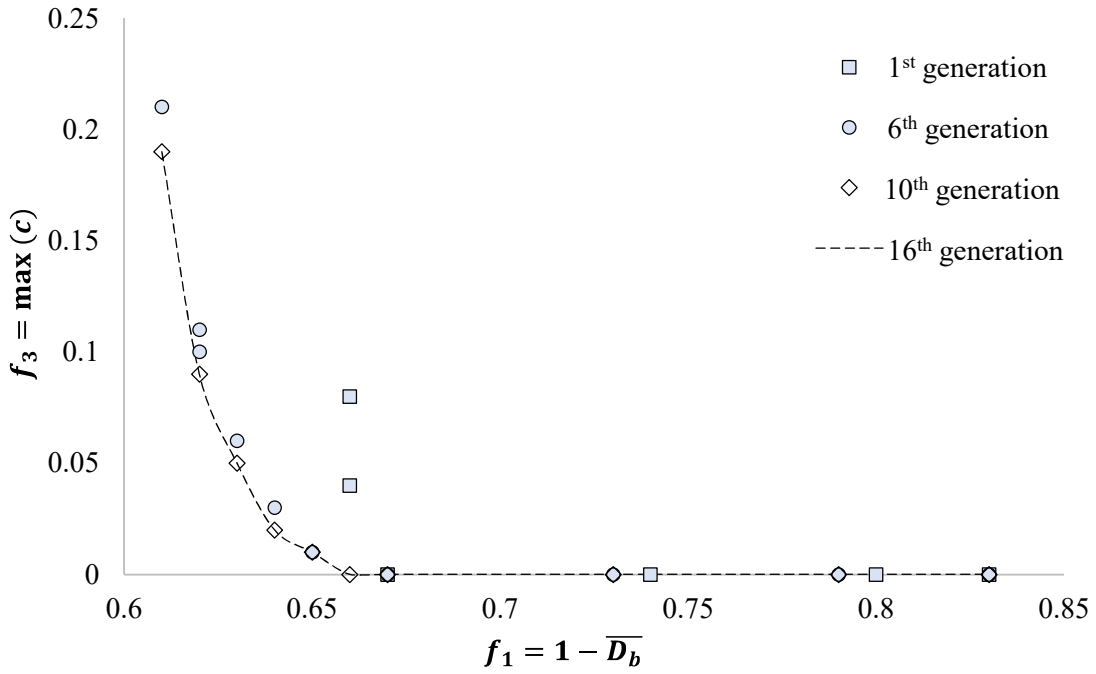

Figure 6.13 Evolution of population as viewed in the f_1-f_3 2D projection.

6.6 Concluding remarks

A multi-optimisation scheme of the ATP process was developed by coupling the 1D simulation presented in Chapter 5 with a GA in MATLAB. The constitutive models of interlaminar strength (section 3.6.2) and thermal degradation (section 6.2.2) were integrated in order to calculate values of degree of bonding and thermal degradation across the produced part. Design variables of processing rate, flashlamp frequency and system average power were investigated in order to maximise bond strength and production throughput whilst avoiding thermal degradation effects. The results show strong trade-offs between bond strength and productivity, as well as between bond strength and thermal degradation. The highest value of average degree of bonding possible with the examined configuration is 0.35, before degradation exceeds the 0.01 threshold. High frequency pulsing conditions are more suitable for this minimisation problem. The estimated Pareto front provides a set of optimal solutions with significantly compromises among the three objectives, with the determination of these achieved by testing only the 25% of the available set of variables due to the use of GA.

7. Real time remote estimation of nip point temperatures in ATP

7.1 Introduction

In this chapter, a monitoring strategy for ATP is put forward based on a combination of analytical solutions and temperature data acquired on the tool surface, in contact with the composite substrate, allowing the estimation of nip point temperature in real time. The method integrates an inverse solution to determine the heater power input from the temperature data and enhance the accuracy of nip point estimation. The accuracy of the scheme is assessed against the outputs of the 2D FE model (Chapter 4) for a wide range of process rates, number of substrate layers and tool materials. A virtual processing scenario is studied to showcase the scheme ability to identify condition changes and highlight the benefits of ATP process monitoring.

7.2 Analytical approximation of heat transfer in ATP

The analytical approximation combines two analytical 1D solutions describing the two different regimes of heat transfer in ATP. As the part is built up and the thickness increases, the heat transfer shifts from that of a material slab with finite thickness to a semi-infinite body. The transition between the two behaviours is indicated by the Fourier number [76] which expresses the ratio between conductive heat transport and power storage, with conductive transport being dominant for thin stacks whilst power storage governing heat conduction at high thickness. The Fourier number is:

$$F_o = \frac{a_y t}{{d_s}^2} \tag{7.1}$$

where t is time - in the ATP case the time needed for the tape to reach the nip point after entering the irradiation heating zone - and d_s is the thickness, which in ATP corresponds to the thickness of material already deposited on the tool.

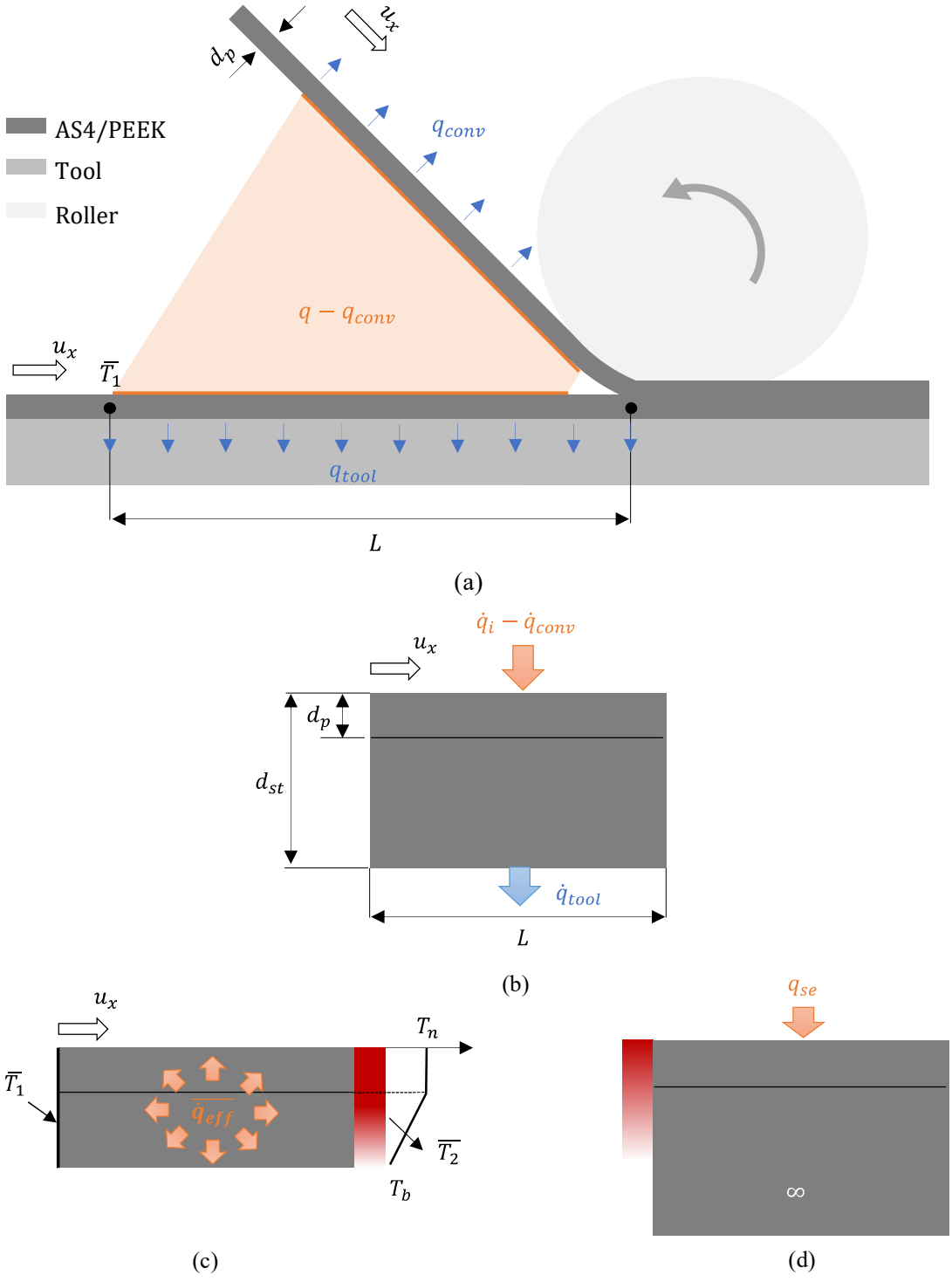

Figure 7.1 Heat transfer in ATP: (a) 2D representation; (b) simplification of geometry to a single material slab; (c) finite slab behaviour with averaged volumetric heating for $F_o > 1$; (d) semi-infinite body behaviour under surface heating at greater thickness ($F_o < 1$).

In tape placement terms, a high Fourier number means that the material thickness is low and/or the process slow enough for a temperature gradient to be established across the thickness direction, whilst a low value implies the deposited material is too thick and/or the process too fast for a significant material depth to be affected by the incoming energy prior to the nip point. The existence of these two heat transfer regimes necessitates two different solutions to approximate conduction effects and a strategy for the transition from one behaviour to the other.

The energy balance of the 2D heat transfer problem was reduced in section 5.2 (Eq. (5.2)) assuming the heat conduction in the placement direction is negligible, based on high Peclet number values, and material motion aligned with the x-axis:

$$\rho c_p \left(\frac{\partial T}{\partial t} + u_x \frac{\partial T}{\partial x} \right) = \dot{q} + \frac{\partial}{\partial y} \left(k_y \frac{\partial T}{\partial y} \right) \tag{7.2}$$

The next step of the approximation is to represent the deposited material and the incoming tow as a single slab which corresponds to the geometry at the nip point section, as seen in Figure 7.1. This material slab is heated at its surface, has a thickness (d_{st}) equal to the total thickness the composite parts and length (L) equal to the irradiation zone prior to the nip point. The thermal contact resistance between the two composites is assumed to be negligible although its effect has been found to be relevant [37].

7.2.1 Finite slab approximation

For the finite slab behaviour, assuming the material has a uniform temperature at the start of the irradiation zone and at the nip point, $\overline{T_1}$ and $\overline{T_2}$, Eq. (7.2) can be approximated by:

$$\rho c_p u_x \frac{\partial T}{\partial x} - \dot{q}_{eff} = 0 \tag{7.3}$$

where $\dot{q}_{eff}$ is the heat rate per unit volume across the path of the tape. Eq. (7.3) can be integrated in the $[0, L]$ range to obtain:

$$\overline{T_2} = \overline{T_1} + \frac{L \, \overline{\dot{q}_{eff}}}{\rho c_p u_x} \tag{7.4}$$

where $\overline{\dot{q}_{eff}}$ is the average volumetric heat rate across the tape path $\left(\overline{\dot{q}_{eff}} = \int_0^L \dot{q}_{eff} \, dx \right)$ from entry to the nip point.

Eq. (7.4) links the material temperature at the start of the irradiation and at the process nip point. Although the entry temperature in ATP is typically ambient and thus uniform, this is not true for the nip point section where steep through-thickness profiles are developed as a result of the energy delivered on the surface and the low transverse thermal conductivity of the material. To account for this, the temperature profile at the nip point location is assumed to have a bilinear shape as shown in Figure 7.1c. The temperature of the first ply is assumed to be constant (T_n). In the rest of the material section, temperature decreases linearly to T_b - the temperature of the tool surface. The nip point is at the interface between the incoming tow and substate at one ply depth (d_p) having a temperature T_n. Calculating the average of the assumed profile yields:

$$\overline{T_2} = T_n \left(\frac{d_p + d_{st}}{2\, d_{st}}\right) + T_b \left(\frac{d_{st} - d_p}{2\, d_{st}}\right) \tag{7.5}$$

In the approximation expressed by Eqs. (7.3) - (7.5), the energy balance operates using the average temperature of the deposited material through the thickness, while surface heat flux becomes part of the heat rate term $(\dot{q}_{eff})$. The total heat rate per unit volume incorporates contributions from the heating source irradiation ($\dot{q}_i$), latent heat due to matrix transformations ($\dot{q}$), natural convection ($\dot{q}_{conv}$), and conduction losses to the tool ($\dot{q}_{tool}$). Expressing these as average heat rates yields:

$$\overline{\dot{q}_{eff}} = \overline{\dot{q}_i} + \overline{\dot{q}_{tool}} + \overline{\dot{q}_{conv}} \tag{7.6}$$

The latent heat term is assumed to be negligible compared to the power input of the heating source.

The average power losses per unit volume of material due to contact with the tool can be approximated as the average heat transfer by conduction between the lower surface of the first ply and the lower surface of the material slab, assuming a linear increase of T_n and T_b across the irradiation length:

$$\overline{\dot{q}_{tool}} = -k_y \left(\frac{T_n - T_b}{d_{st} - d_p}\right) \frac{1}{2\, d_{st}} \tag{7.7}$$

Similarly, the power losses to air per unit volume due to convection can be approximated by:

$$\overline{\dot{q}_{conv}} = -h\left(\frac{\overline{T_1} + T_n}{2} - T_\infty\right)\frac{2}{d_{st}} \tag{7.8}$$

A factor of two is used to account for the two surfaces (deposited material and incoming tow) exposed to air convection.

The average volumetric power input due to radiative heating is:

$$\overline{\dot{q}_i} = \bar{E}_i \frac{1}{d_{st}} \tag{7.9}$$

where $\bar{E}_i$ denotes the average irradiance over the surface of material exposed to radiation.

Combining Eqs. (7.6) - (7.9), the total heat rate per unit volume of material is:

$$\overline{\dot{q}_{eff}} = \bar{E}_i \frac{1}{d_{st}} - k_y \frac{T_n - T_b}{d_{st} - d_p} \frac{1}{2\, d_{st}} - h\left(\frac{\overline{T_1} + T_n}{2} - T_\infty\right)\frac{2}{d_{st}} \tag{7.10}$$

Combination of Eqs. (7.4), (7.5) and (7.10) yields:

$$T_n = \frac{2d_{st}\rho c_p u_x \overline{T_1} + 2\bar{E}_i L + hL(4\,T_\infty - 2\overline{T_1}) + \left[\frac{k_y\, L}{d_{st} - d_p} - \rho c_p u_x\left(d_{st} - d_p\right)\right] T_b}{\rho c_p u_x\left(d_{st} + d_p\right) + \frac{k_y\, L}{d_{st} - d_p} + 2hL} \tag{7.11}$$

which expresses an approximation of the nip point temperature (T_n) based on the measured tool temperature (T_b), the power input ($\bar{E}_i$) and the thermal/geometrical properties of the deposited material.

7.2.2 Semi-infinite body approximation

As the substrate thickness increases the heat transfer phenomena approach the behaviour of a semi-infinite solid with a heat flux ($\dot{q}_{se}$) applied to its surface (Figure 7.1d). In this regime, the temperature at the tool surface is not affected by the irradiation on the surface of the deposited substrate, as the times involved are too short for the heating to propagate through the thickness of the low conductivity material. Eq. (7.2) was transformed from Eulerian to Lagrangian analysis reference frame in section 5.2 using the transformation $x' = x - u_x\, t$ to obtain:

$$\rho c_p \frac{\partial T}{\partial t} = \frac{\partial}{\partial y}\left(k_y \frac{\partial T}{\partial y}\right) \tag{7.12}$$

which for a prescribed surface heat flux has the following established transient semi-infinite body solution [217]:

$$T(y,t) = \overline{T_1} + 2\frac{q_{se}}{k_y}\sqrt{\frac{k_y\, t}{\pi\rho c_p}}e^{\frac{-y^2\rho c_p}{4k_y t}} + \frac{q_{se}}{k_y}y\left(erf\left(\frac{y\sqrt{\rho c_p}}{2\sqrt{k_y t}}\right) - 1\right) \tag{7.13}$$

Here erf is the error function and the average surface flux is:

$$q_{se} = \bar{E}_i - 2h\left(\frac{\overline{T_1} + T_n}{2} - T_\infty\right) \tag{7.14}$$

obtained similarly to Eq. (7.10) for a surface flux instead of volume heating rate.

Combining Eqs (7.12) - (7.14) for the nip point position ($y = d_p$) and time equal to the travelling across the heating zone (L/u_x) results in:

$$T_n = \frac{\overline{T_1} + \frac{(\bar{E}_i + 2hT_\infty - h\overline{T_1})}{k_y}\left[2\sqrt{\frac{k_y L}{\pi\rho c_p u_x}}e^{\frac{-d_p{}^2\rho\, c_p u_x}{4k_y L}} + d_p\left(erf\left(\frac{d_p\sqrt{\rho c_p u_x}}{2\sqrt{k_y L}}\right) - 1\right)\right]}{1 + h\left[2\sqrt{\frac{k_y L}{\pi\rho c_p u_x}}e^{\frac{-d_p{}^2\rho\, c_p u_x}{4k_y L}} + d_p\left(erf\left(\frac{d_p\sqrt{\rho c_p u_x}}{2\sqrt{k_y L}}\right) - 1\right)\right]} \tag{7.15}$$

7.2.3 Transition between regimes

The approximations represented by Eqs. (7.11) and (7.15) are effective for the case of thin and thick composite substrates respectively. The transition between the two behaviours is governed by the instantaneous Fourier number (Eq. (7.1)). Switching between these two behaviours can be done predictively by using the Fourier number and setting a threshold value of 1 for the transition. To ensure the transition in behaviour does not cause a discontinuity, a smooth step using the logistic function is selected between the two solutions:

$$T_n = T_n^o + \frac{T_n^\infty - T_n^o}{1 + e^{G(Fo-1)}} \tag{7.16}$$

where T_n^o is the approximation corresponding to the thin stack of material calculated using Eq. (7.11) and T_n^∞ the approximation corresponding to a semi-infinite stack using Eq. (7.15). The breadth of the transition is controlled by the empirical parameter G, with a large G corresponding to a discontinuous transition and a value of zero corresponding to the average of the two approximations.

7.3 Inverse estimation of irradiance from temperature measurements

A value of average irradiance ($\bar{E}_i$) acting on the ATP cavity is required for the analytical solutions of Eq. (7.11) and Eq. (7.15). An initial estimate on each tape can be made:

$$\bar{E}_i = \frac{\bar{P}\, e}{v\, L} \tag{7.17}$$

where e the conversion factor from electrical to optical power for the heater and v the width of the irradiated area, typically 10-15% wider than the tape.

The irradiance estimated by Eq. (7.17) can deviate significantly from the actual value because the conversion factor and irradiation area have high uncertainty. In addition, effective irradiance may vary across regions where the tool geometry alters the angle or distance of the source to the target surface. It is important for the accuracy of the analytical scheme to identify this input power during the process. An inverse calculation scheme is introduced here, using temperature measurements at the tool surface, based on the direct 1D analytical solution of a two-layered body with a semi-infinite substrate, in the case here representing the tool, under a power-law varying surface flux [218]:

$$q(y=0,t) = q_o \left(\frac{t}{t_o}\right)^n \tag{7.18}$$

Using the same transformation and assumptions as those utilised to obtain Eq. (7.12), but for the case of the tool incorporated in the model as a semi-infinite body, the temperature at the interface between the composite and the tool, which coincides with the sensor location during the 2nd deposition at $y = d_p$ relative to the substrate surface, is [218]:

$$T(d_p,t) = \overline{T_1} + \frac{q_o L}{k_y}\sqrt{\frac{4\,k_y\,t}{\rho\, c_p\, {d_p}^2}}\,\Gamma\left(1+\frac{n}{2}\right)\left(\frac{4t}{t_o}\right)^{\frac{n}{2}}(H+1)\left[i^{n+1}erfc\left(\sqrt{\frac{\rho\, c_p\, {d_p}^2}{4\,k_y\,t}}\right) + \sum_{j=1}^{\infty} H^j i^{n+1} erfc\left(\frac{(2j+1)\sqrt{\rho\, c_p\, {d_p}^2}}{\sqrt{4\,k_y\,t}}\right)\right] \tag{7.19}$$

where $H = \frac{\theta-1}{\theta+1}$ and $\theta = \sqrt{\frac{\rho\, c_p k_y}{\rho' {c_p}' {k_y}'}}$ with ρ', ${c_p}'$ and ${k_y}'$ denoting the density, specific heat capacity and transverse conductivity of the tool material respectively.

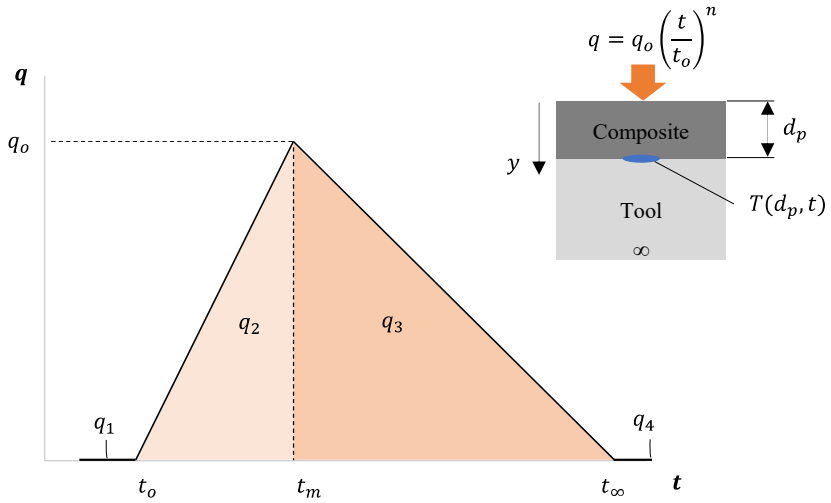

Figure 7.2 Schematic of the triangular irradiance with the function segments expressed by Eq. (7.18), and the configuration of the 1D solution deployed for the inverse scheme.

In general, the irradiance acting on the tapes follows an asymmetric bell shape, as predicted in section 4.3 and previous studies [40]. This can be approximated by a time-varying triangular profile as illustrated in Figure 7.2, expressed by:

$$q(t,0) = \begin{cases} 0 & t < t_o \\ q_o \dfrac{t - t_o}{t_m - t_o} & t_o \le t \le t_m \\ q_o \dfrac{t_\infty - t}{t_\infty - t_m} & t_m < t \le t_\infty \\ 0 & t \ge t_\infty \end{cases} \tag{7.20}$$

with q_o representing the peak flux value applied at $t = t_m$, whilst t_o and t_∞ determine the time span of irradiation. Each segment of this heat flux function can be derived from Eq. (7.18) with appropriate choice of parameters, and therefore used with Eq. (7.19). The interface temperature is the result of the superposition of these segments acting for their corresponding timings. The contribution of each segment is calculated using Eq. (7.19) and then the contributions are superimposed to estimate the interface temperature. An initial set of $[q_o, t_o, t_m, t_\infty\ ]$ is needed with an Evolutionary Algorithm in the Solver of Microsoft Excel, which offers a versatile and more efficient implementation compared to other accessible platforms [205], deployed to identify the optimal set of parameters which satisfies:

$$[q_o, t_o, t_m, t_\infty\ ] = argmin\ \sum_i [T(q_o, t_o, t_m, t_\infty, t_i) - T_m(t_i)]^2 \tag{7.21}$$

where the summation is over all the measured temperature (T_m) acquired at times t_i.

The average irradiance acting on the composites inside the ATP cavity is:

$$\overline{E_i} = U \frac{1}{t_\infty - t_o} \int_{t_o}^{t_\infty} q(0,t)\, dt \tag{7.22}$$

where parameter U accounts for the fact that $\overline{E_i}$ is the average incident irradiance on the substrate and incoming tow, whilst the method identifies only the portion delivered to the substrate. For an equal power distribution between the substrate and incoming material the value of U is 2.

The irradiance acting on the tapes is expected to scale linearly with the total power of the heating source whilst changes to the processing rate only rescale the time variable of the distribution. In addition, the irradiance distribution is independent of the inlet temperature and deposited material thickness. Therefore, the distribution retrieved with this method corresponds to a placement path and can be used during future depositions across the same path regardless of the changes to these parameters. This method cannot be applied during the 1st ply deposition as the tool optical properties are different from the tapes, leading to an irradiance distribution not applicable to subsequent processing cycles with a composite substrate.

7.4 Strategy of nip point temperature online monitoring

An overview of the proposed strategy for in-process estimation of nip point temperatures in ATP is illustrated in Figure 7.3. The manufacturing of the composite part takes place on a tool with a number of sensors strategically placed. The sensors record and feed the controller continuously. Each sensor captures the tool surface temperature (T_b) during the placement of a new layer, which is then used to approximate the nip point temperature at that location using Eq. (7.16). The working algorithm uses the position of the placement head to identify the sensor involved and post-process the data. The irradiance value ($\overline{E_i}$) and irradiation length (L) needed are identified during the second ply deposition across the tool geometry via the inverse solution developed in section 7.3. The rest of the inputs for the remote calculation include the composite thermal properties (c_p, k_y, ρ), processing velocity (u_x), ambient temperature before irradiation ($\overline{T_1}$), thickness of the stack (d_{st}) and convection coefficient (h).

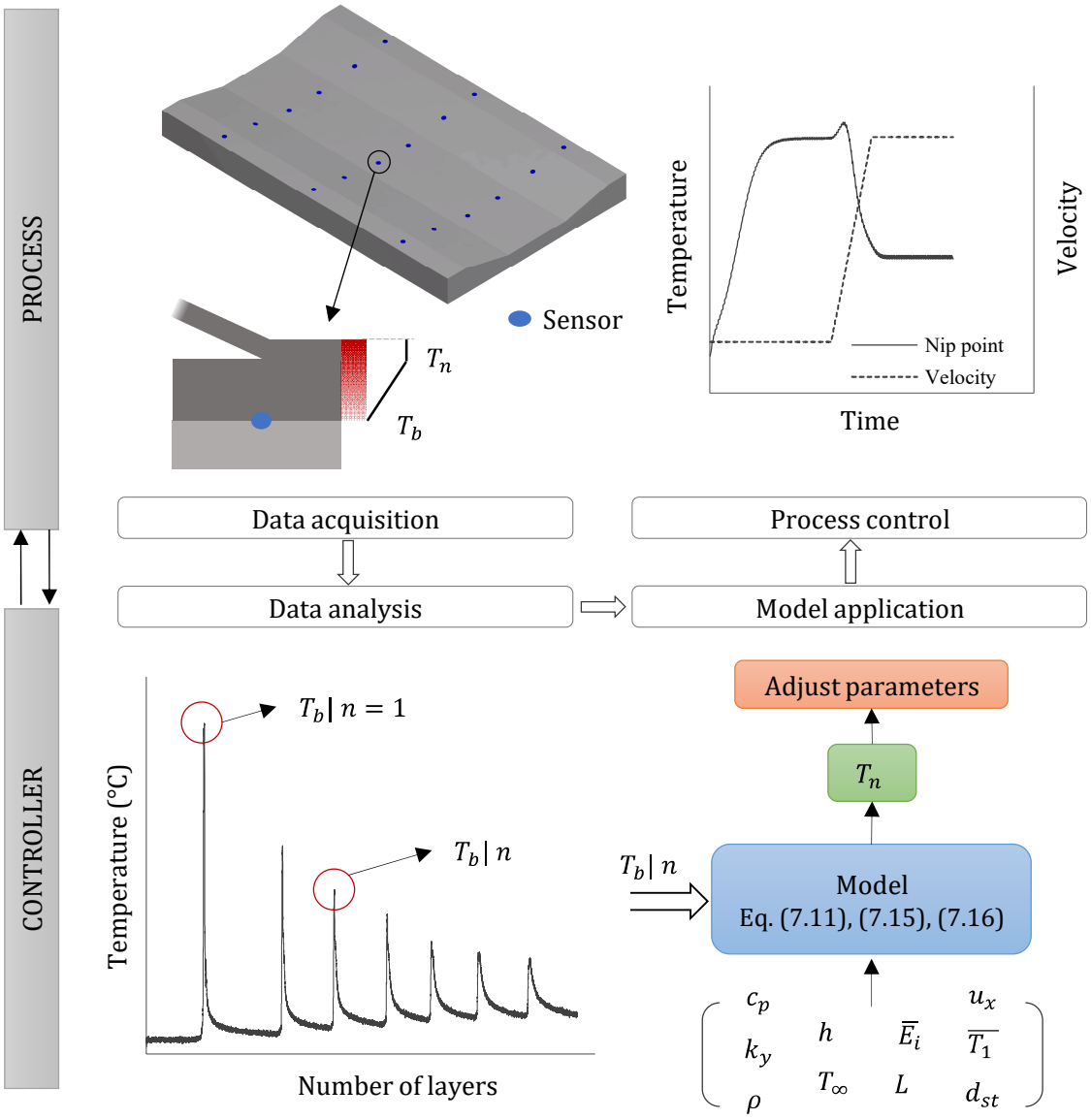

Figure 7.3 Overview of the strategy for in-process nip point temperature estimation in ATP and utilisation of the modelling estimates for process control.

Knowledge of the nip point temperature obtained using the approach presented here can allow adjustment of the process conditions through on-line control to maintain its value within an optimal envelope. The processing velocity and heat source power can be adjusted according to the sensitivity of the nip point temperature to these variables. This strategy allows conditions to be adapted as the process progresses and the build-up of thickness alters the heat transfer conditions. Furthermore, potential variability resulting in changes in heat transfer conditions around the part manufactured can be addressed.

7.5 Assessment of method performance against 2D model data

The performance of the proposed scheme was assessed utilising predictions of the 2D finite element model developed in Chapter 4. The tool temperature input (T_b) required for the analytical calculations, as well the profiles at one layer below the surface for the inverse solution, were provided by the FE model for each examined set of processing conditions. The FE model predictions correspond to the configuration modelled in Chapter 4, with the humm3® flashlamp system characterised in section 3.3.1 acting as the heater. The convection coefficient was set at 5 W/ m^2/K whilst the entry temperature of the composite tapes and tool in the analysis frame was set at 20°C.

A metallic tool and one made from insulating material are tested to challenge the application of the analytical scheme over a wide range of setups. The properties of representative metallic and insulating tool are reported in Table 3.5 and Table 7.1 respectively. The tool thickness is 15 mm which is sufficient for semi-infinite body behaviour in both cases at the lowest velocity of 25 mm/s and a representative irradiation length of 50 mm (Eq. (7.1)). The analytical scheme and inverse solution use an average of the AS4/PEEK thermal properties over the 0-400°C range (section 3.6.1), which are reported in Table 7.1. The analytical calculations do not utilise the longitudinal thermal conductivity of the composite and roller, which in the 2D model feature artificially increased values by 10 times to accommodate meshing efficiency (section 3.6.1).

Table 7.1 Average thermal properties of AS4/PEEK, elastomer and tool used in the analytical solutions.

Material	Specific heat capacity (J/kg/K)	Transverse thermal conductivity (W/m/K)	Density (kg/m^3)
AS4/PEEK	1290	0.6	1570
Insulating tool	1500	0.25	1500

An overview of the 1D analytical and FE models is given in Table 7.2. The latent heat of melting/crystallisation and heat conduction in the width direction is negligible in both analyses, whilst the interlayer and composite - tool contacts are considered perfect. On the other hand, the FE model uses temperature dependent thermal properties and spatial

distributions by ray tracing (section 4.3). The heater input for the analytical scheme is determined through the inverse solution presented in the following section.

Table 7.2 Overview of the analytical and FE model comparison.

Model feature/assumption	**Analytical scheme**		**2D FE model**
	Finite slab	*Semi-infinite*	
Equation-Domain	Eq. (7.11) - 1D	Eq. (7.15) - 1D	Eq. (7.2) - 2D
Conduction in the thickness direction	Bilinear profile (Figure 7.1c)	Yes	Yes
Conduction in the placement direction	Negligible		Yes
Conduction in the width direction	Negligible		Negligible
Latent heat of melting/crystallisation	Negligible		Negligible
AS4/PEEK thermal properties	Constant		Temperature-dependent
Interlayer contact	Perfect		Perfect
Composite/tool contact	Perfect		Perfect
Radiative heating	Averaged by inverse estimation (section 7.3)		Spatial distributions by ray tracing (section 4.3)

7.5.1 Inverse estimation of irradiance

The temperature profiles on the tool surface predicted by the FE model during the 2nd ply deposition at 100 mm/s are plotted in Figure 7.4 for the metallic and insulating tooling. The profiles correspond to the temperature history of a material point which moves across the 110 mm long analysis frame at the interface between the first ply and the tool. The point enters the irradiation region at 0.2 s at a temperature of 20°C and reaches the nip point at 0.8 s after which a secondary temperature peak occurs due to the additional

energy the substrate gains in this case when it comes into contact with the hot incoming tow underneath the roller (0.8-0.94 s). Significantly higher temperatures develop on the surface of the insulating tool during deposition due to its low conductivity which reduces the dissipation of energy. In order to simulate typical noisy temperature sensor data, a Gaussian noise of zero mean value was added to the FE profiles (Figure 7.4). The standard deviation was set at 2°C for the metallic tool and 20°C for the insulating one, representing approximately 10% of the maximum temperature reached in each case.

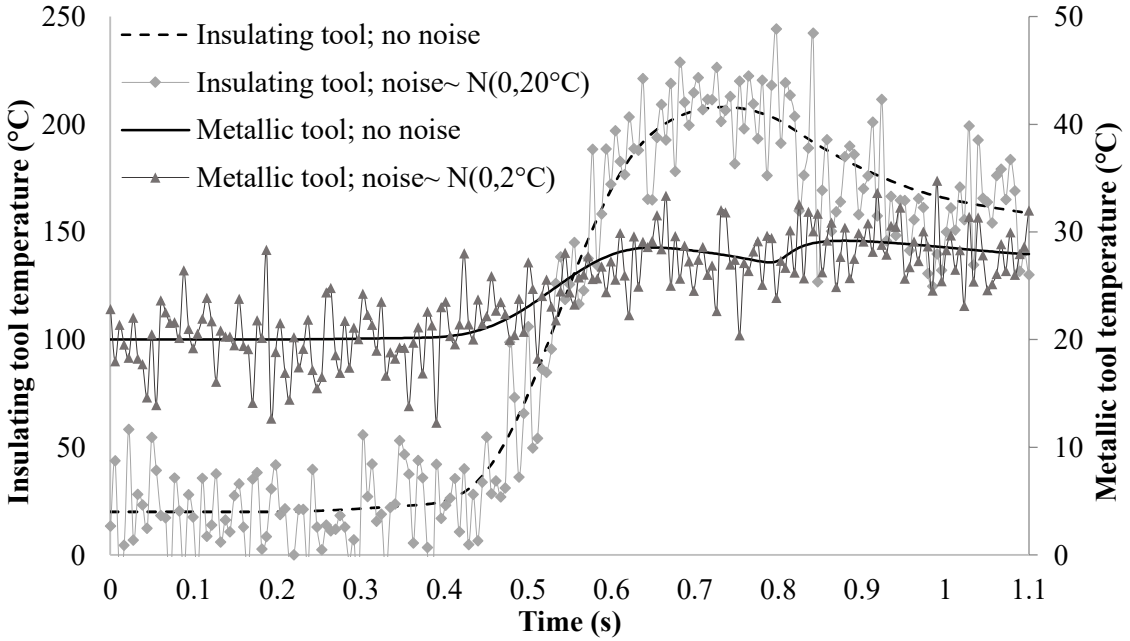

Figure 7.4 Temperature profiles (FE model) on the tool surface during the 2nd ply deposition at 100 mm/s used for the inverse calculation of irradiance on the substrate surface, before and after the addition of Gaussian noise.

The inverse scheme introduced in section 7.3 was applied to determine the irradiance input ($\bar{E}_i$). For the parameter estimation in Eq. (7.21), an initial value of q_o equal to 8.8×10^5 W/m^2 was used based on Eq. (7.17). This value corresponds to half of the available optical power (1.1 kW) delivered to the substrate, assuming equal distribution with the tow and a conversion factor from electrical to optical energy of 0.5, a tape width of 0.025 m and irradiation length of 0.05 m. The selection of initial values for the timing parameters relies on the synchronisation of the robotic head position and sensor data in the process. Here, in order to test the performance of the inverse method under realistic variability, an uncertainty of the temperature sensor position of ±10 mm was assumed

which translates to ±0.1 s in the temperature-time data at 100 mm/s. As a result, the inverse scheme uses temperature data spanning from 0.1 to 0.9 s with the actual time window in the FE model being 0.2- 0.8 s. Consequently, t_o=0.1 s, t_∞=0.9 s and t_m was selected as their mean value at 0.5 s. The value of q_o was constrained in the 10^5- 10^6 range whilst the time parameters were constrained to satisfy the inequalities in Eq. (7.20).

The values of the triangular profile parameters determined by the inverse solution are reported in Table 7.3 for the two tool scenarios. For the metallic tool, results based on the original noiseless FE data and for t_∞ fixed at 0.8 s are added to examine the effect of noise and location uncertainty, as well as to showcase the capability of the inverse method to cope with noise in the data. The inversion yields an error of 12% for the metallic tool data with noise and location uncertainty. The contribution of noise to this deviation is about 3%, whilst in the absence of position uncertainty and the same noise levels as previously, an error of 2% over the FE values is accomplished. Consequently, the uncertainty of the nip point timing in the captured temperature profiles has a strong effect on accuracy. Significantly better correlation of the profiles is observed close to the nip point region when t_∞ is known as demonstrated in Figure 7.5a. The cases in which t_∞ was assumed equal to 0.9 s and included in the inversion do not follow the FE profile near the nip point accurately. This deviation is caused by the inclusion of temperature data after the nip point in the inversion, as a result of the uncertainty of its exact location. Eq. (7.19) does not describe the behaviour of the secondary temperature peak, which is a result of the heat exchange with the incoming tow, and thus the temperatures calculated are lower in that region with the fitting algorithm compensating with increased irradiance. Changes in the tool material do not affect the accuracy of the inverse solution. The inversion for the insulating tool leads to slightly higher error of 16%, which is attributed to the significant noise introduced. The effect of the Gaussian noise on the profile estimation is illustrated in Figure 7.5b for the metallic tool and different realisations of noise using a random number generator and t_∞=0.8 s. The identified irradiance distribution presents limited variations for the different noise realisations with an average irradiance variability lower than 5%.

Table 7.3 Parameters of the inverse triangular irradiance distribution and comparison of the average with the value applied in the FE model. N(μ, σ) denotes a normal distribution with mean μ and standard deviation σ.

Tool	Noise	t_∞ (s)	q_o (W/m^2)	t_o (s)	t_m (s)	t_∞ (s)	$\overline{E_\iota}$ (W/m^2)	Error
Insulating	N(0, 20°C)	0.9	4.98×10^5	0.341	0.505	0.858	1.52×10^5	16%
Metallic	N(0, 2°C)	0.9	4.41×10^5	0.318	0.572	0.858	1.49×10^5	12%
Metallic	N(0, 0°C)	0.9	4.57×10^5	0.351	0.535	0.858	1.45×10^5	9%
Metallic	N(0, 2°C)	0.8	4.57×10^5	0.351	0.535	0.8	1.29×10^5	2%

Overall, the inverse solution yields satisfactory results even when significant noise is incorporated in the temperature data and sensor position uncertainty exists. The problem of identifying a boundary heat flow based on temperature measured at a depth within the domain is ill-posed [219]. The use of a strong function specification through the triangular profile has a regularising effect on the estimation problem resulting in a robust inversion. Furthermore, the triangular profile is the simplest shape representing the irradiance distribution in ATP and can be expressed in the form of Eq. (7.18); and therefore, used in the direct solution of Eq. (7.19). The method put forward here obtains an estimate of the irradiance distribution by experimental means with inaccuracy similar to more complicated and time-consuming off-line studies such as optical modelling, whilst also including effects of variability which cannot be considered in off-line computations. The influence of parameters that are either difficult to determine or subject to significant variability, such as the heater efficiency or optical absorptivity, is included in the data captured in real time during the process, and therefore is directly incorporated in the inverse prediction, making the proposed method advantageous compared to off-line predictive strategies.

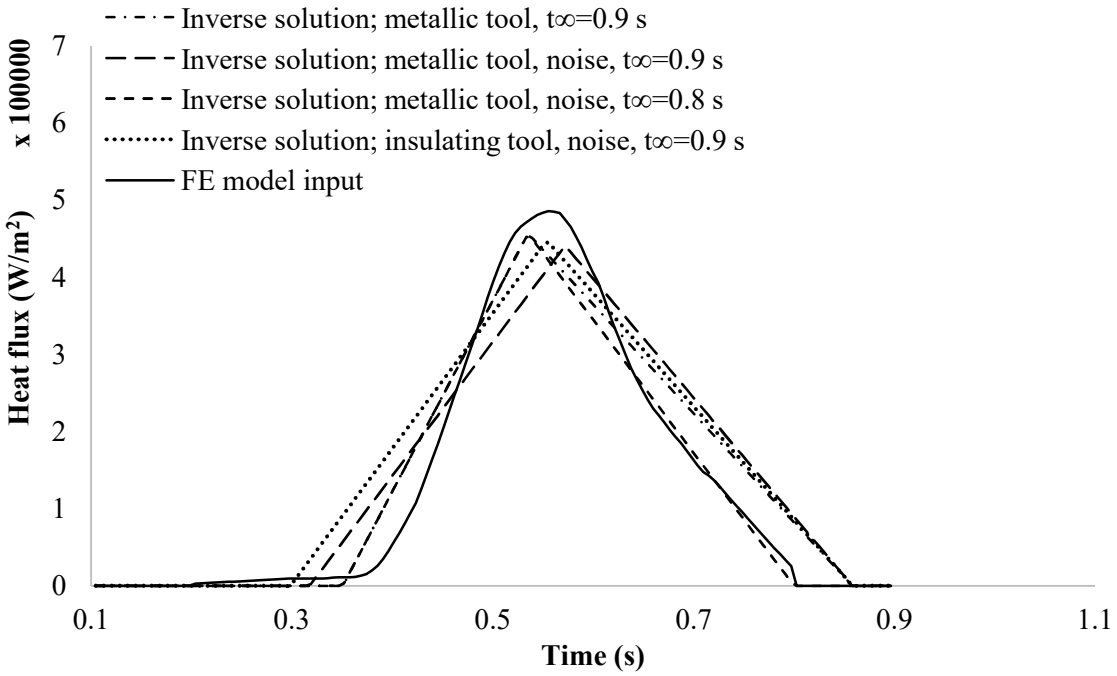

(a)

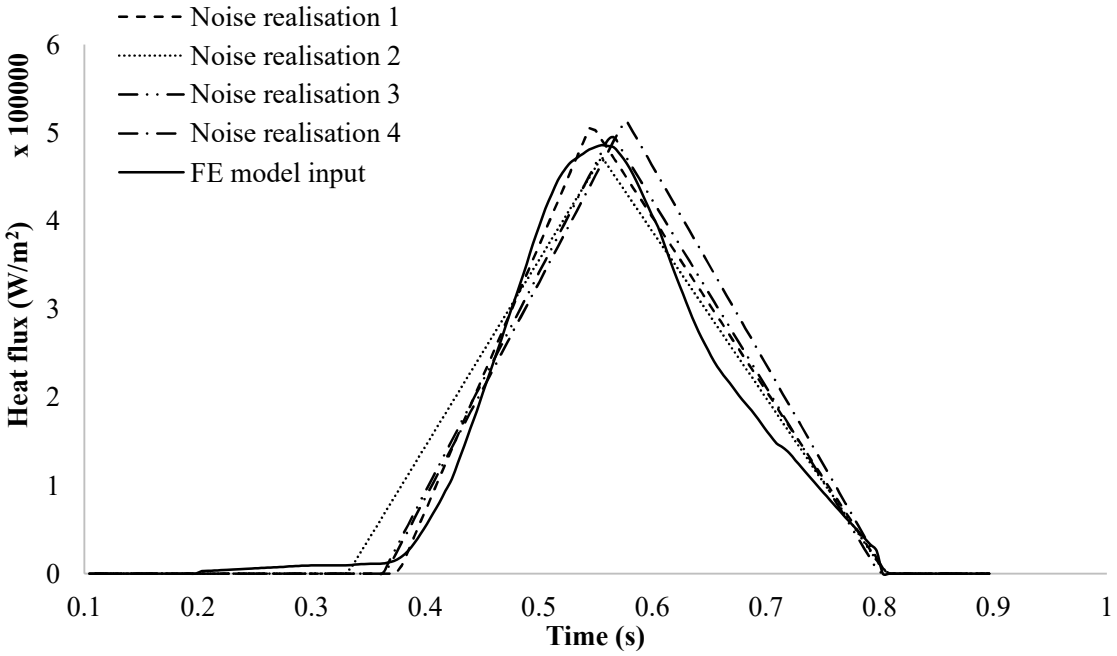

(b)

Figure 7.5 Inverse calculation of irradiance distribution: (a) profiles recovered and the profile applied on the FE model; (b) estimation for different noise realisations for the case of metallic tool, noise of 2°C standard deviation and t_∞ fixed at 0.8 s.

7.5.2 Nip point temperature estimation

A comparison of the FE and analytical predictions of the nip point temperature is presented in Figure 7.6 for a wide range of process velocities, number of plies and different tool materials, whilst Figure 7.7 shows a regression plot of the approximate model versus the FE results. The total irradiance used for all analytical calculations corresponds to the case of metallic tooling with 2°C standard deviation noise and t_∞= 0.8 s (Table 7.3) and was set to 2.58×10^5 W/m^2 assuming an even distribution between substrate and tow $(U = 2)$ and 0.08 m irradiation zone length. The average thermal properties of the composite used are reported in Table 7.1 and the empirical parameter (G) for the transition to semi-infinite physics in Eq. (7.16) was set to 5.

Figure 7.6 shows that the nip point temperature decreases with increasing rate whilst for a given velocity the temperature evolves as the process progresses in a way which depends on the tool material. For the conductive metallic tool (Figure 7.6a), the nip point temperature increases for several layers at the start of the process until it reaches a plateau at which subsequent layer depositions result in similar values. This is caused by the low conductivity of the composite, which reduces heat losses to the tool as its thickness increases, resulting in higher temperature near the surface. The influence of conduction losses towards the tool becomes negligible after a number of layers, depending on the placement velocity. In contrast, the nip point temperature for the insulating tool (Figure 7.6b) decreases for several layers until it converges to the same plateau value as for the metallic tool. The nip point temperatures reached at low thickness are significantly higher compared to the case of highly conductive metallic tooling. In this case, the tool acts as a thermal barrier to heat diffusion resulting in higher nip point values. For the given data, the plateau is reached approximately after the 4th ply at 200 mm/s and the 10th ply at 25 mm/s. This plateau indicates the transition of the heat transfer physics to that of a semi-infinite solid for which an increase of thickness or changes in the tooling material properties do not affect the temperature field. This transition coincides with the reduction of the Fourier number below 1; therefore, it can be predicted, and it is taken in account automatically in the approximation through Eq. (7.16). As a result, the predictions for the plateau rely on the semi-infinite solution expressed by Eq. (7.15). This transition is also reflected in the tool temperature (T_b) achieved during the deposition and reported in Figure 7.8. For a given velocity, the tool temperature drops with the number of layers

until it becomes virtually equal to ambient for thicknesses similar to those at which the plateau occurs in Figure 7.6. Only a part of the material near the surface is affected by heating at these thicknesses, indicating conditions of conduction in a semi-infinite solid.

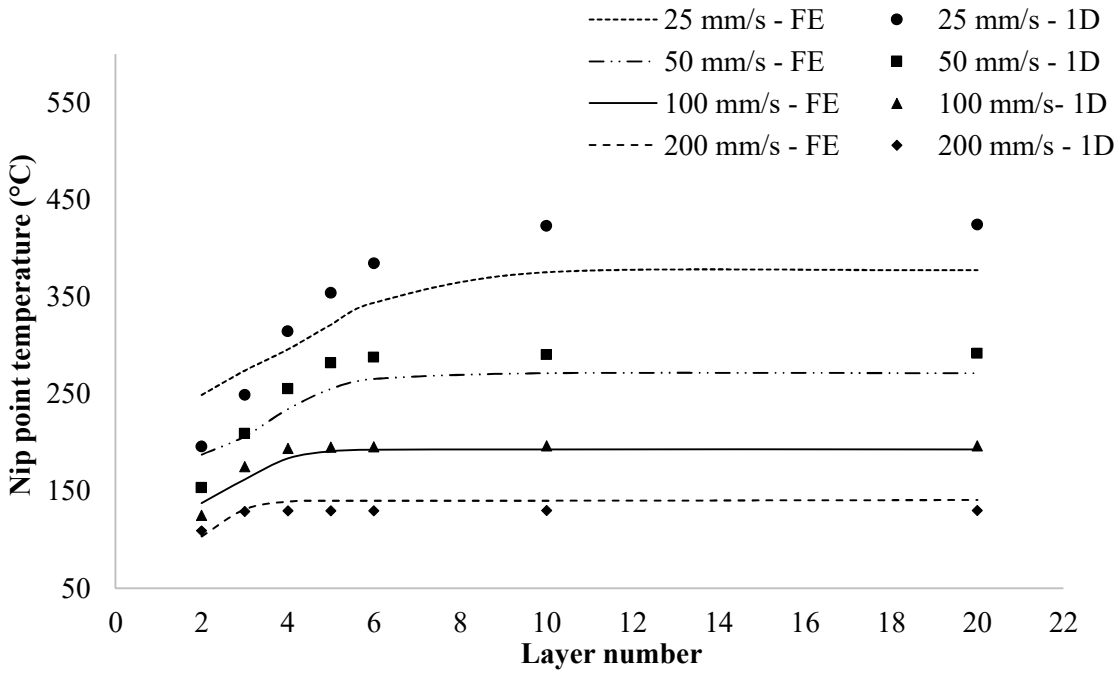

(a)

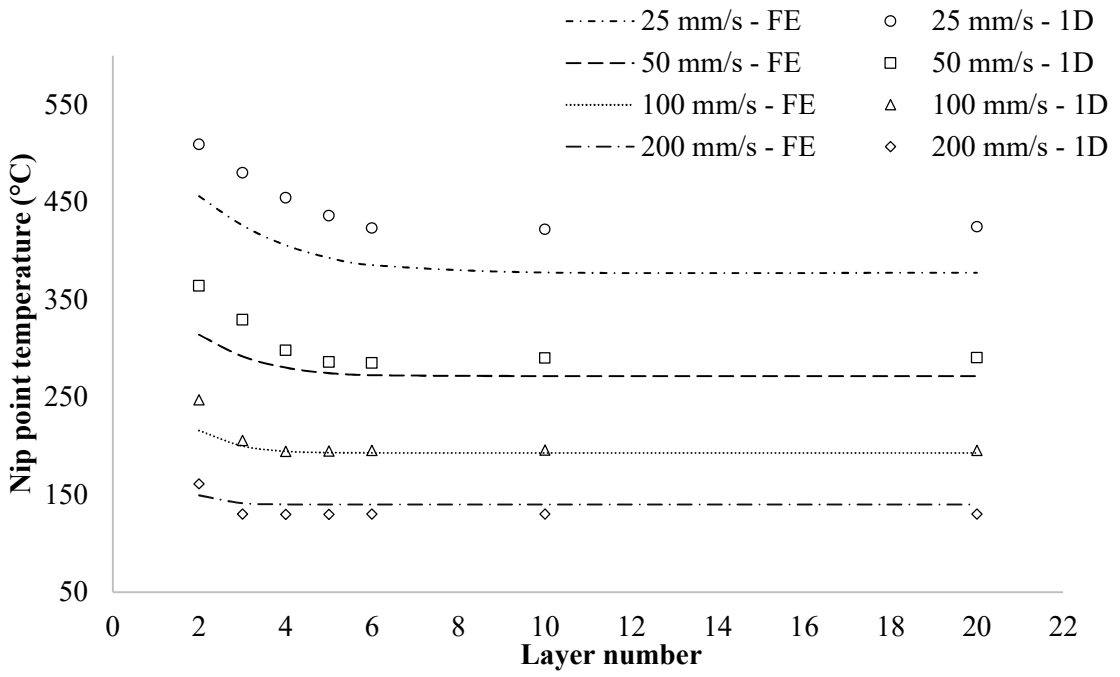

(b)

Figure 7.6 Comparison of the FE and analytical model predictions for a range of velocities, number of layers and: (a) metallic tool; (b) insulating tool.

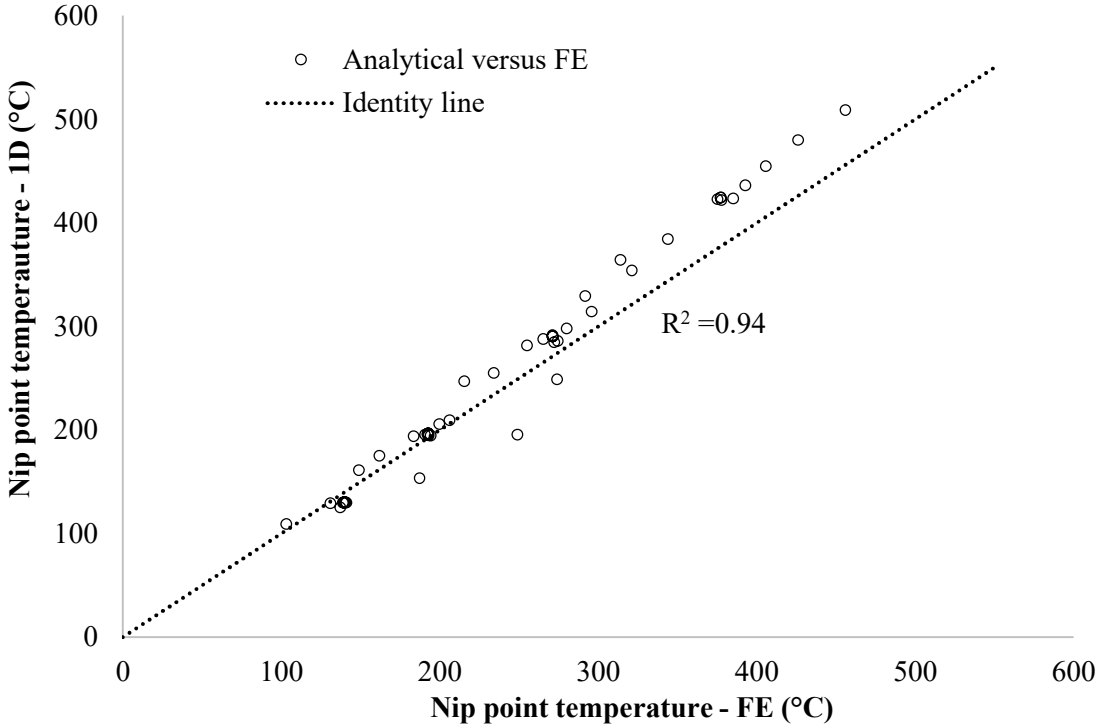

Figure 7.7 Regression plot of the analytical and FE model predictions indicating good agreement between the two data sets.

The approximation is in good agreement with the FE results as shown in Figure 7.7. A linear relation exists between the two sets of predictions which can be approximated by the identity line shown, with a coefficient of determination (R^2) of 0.94. Approximately 85% of the scenarios present an error lower than 30°C whilst 45% of the total data present deviations of less than 10°C. The maximum deviation across all cases is 50°C, encountered in only 4 cases at the lowest speed of 25 mm/s for both tool materials. The deviations at 25 mm/s are high, ranging from 30-50°C, with the analytical scheme mainly overestimating the temperature. This is attributed to the constant thermal properties in the analytical calculations in contrast to the temperature dependence in the FE model. The average conductivity used in the approximation is 0.6 W/m/K for all scenarios, which is applied at a temperature of 180°C (section 3.6.1) in the FE model. The temperatures achieved at 25 and 200 mm/s are up to 400 and 120°C respectively, which correspond to conductivities of 0.65 and 0.52 W/m/K in the FE model. As a result, the analytical predictions correlate well at temperature levels around the value of the average thermal properties and deviate at temperatures away from the average point used. Predictions at 25 mm/s are overestimates whilst predictions at 200 mm/s are underestimates, due to the

lower and higher conductivity values used respectively. It can be seen also in Figure 7.7 where the predictions are in very good agreement below 200°C but gradually start deviating at higher temperatures. The 2nd layer predictions have the highest error. This is attributed to the greater effect of energy losses to the tool.

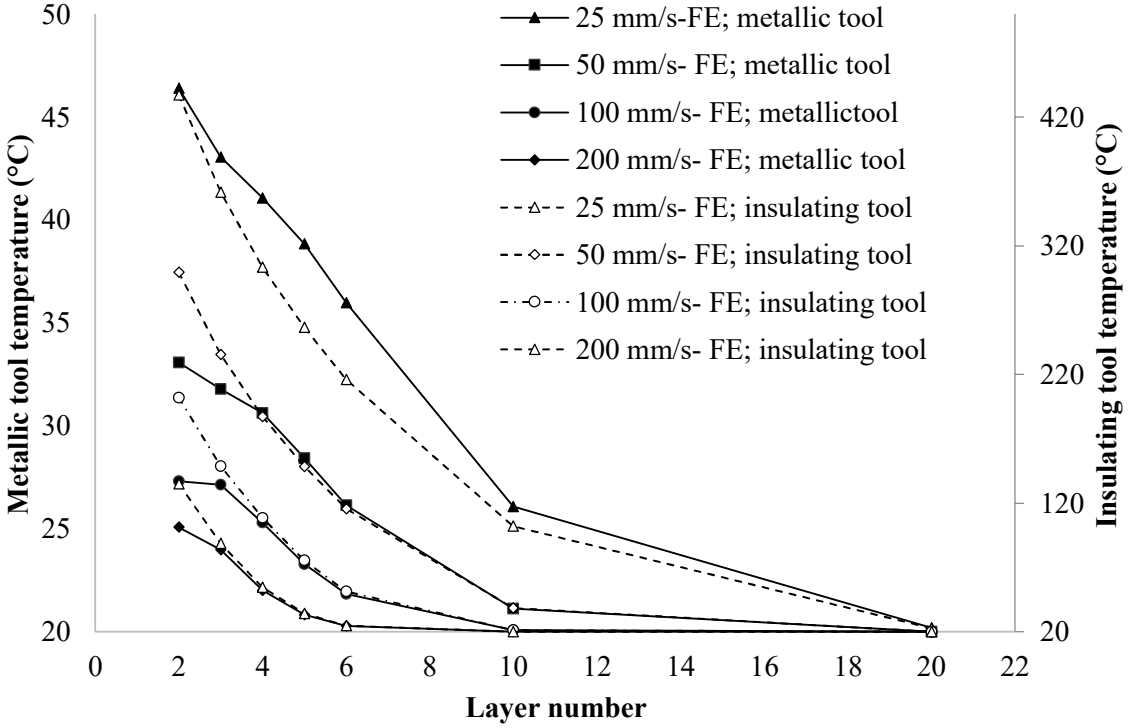

Figure 7.8 Tool temperature at the nip point section (T_b) given by the FE model used for the analytical calculations.

Despite the simplification of the ATP geometry and heat transfer phenomena, the analytical scheme presents good predictive capability for a wide range of process conditions. It can describe the process and follow the nip point temperature evolution regardless of tool material. This is due to the use of a monitoring input in the form of tool temperature (T_b) which compensates for the approximations made. It can also account for increased temperature of the composite prior to the irradiation via the $\overline{T_1}$ input, which in this study was set equal to ambient for all cases. These features make the methodology appealing for application in a manufacturing environment since changes to processing conditions and materials are reflected in the monitoring signals and included in the solution indirectly. This capability offers significant advantages over fully predictive FE analysis which requires a large number of inputs and operates under ideal conditions, whilst it also unlocks the potential for process control. The 15°C average error achieved

during the extensive validation of the method is in line with, or an improvement over, thermal imaging which can only capture temperatures outside the consolidation zone. The location of these measurements and the actual nip point are in close distance along the longitudinal direction; however, rapid temperature changes occur in this region as a result of the reduced heater energy reaching deep in the ATP cavity and the abrupt heat exchange when tow and substrate come into contact. Furthermore, a constant emissivity value is typically used which can introduce errors when measurements are conducted for the broad temperature range (20-600°C) encountered in ATP.

7.6 Sensitivity of nip point estimations to input parameters

The sensitivity of nip point estimations to the model parameter inputs is presented in Figure 7.9. The effect of a 10% increase in each variable individually is examined for the baseline scenario of a metallic tool at 50 mm/s process speed. For $\overline{T_1}$ and T_b, a 10°C increment is tested. The convection coefficient and ambient temperature have been excluded due to weak influence. Positive values of sensitivity indicate an increase of nip point temperature under the parameter change examined. Overall, the analytical predictions are highly sensitive to the average irradiance input ($\bar{E}_i$), which increases with the number of layers, reaching a maximum of 27°C temperature increase at high thicknesses. Irradiance is followed in sensitivity by the irradiation length, deposition rate and volumetric heat capacity (ρc_p). Sensitivity to these parameters increases as the process progresses. Tape thickness (d_p) and conductivity (k_y) present an intermediate sensitivity of 10°C which decreases with the placement of new layers. The effect of conductivity becomes weaker as the heat transfer moves towards a semi-infinite state. The sensitivity to inlet temperature ($\overline{T_1}$) increases with the number of plies, whereas that of tool temperature (T_b) decreases towards a zero value. The influence of the latter is strong for only a few layers since the levels of thickness and speed allow heat to diffuse to the tool and becomes weak near the transition to a semi-infinite state.

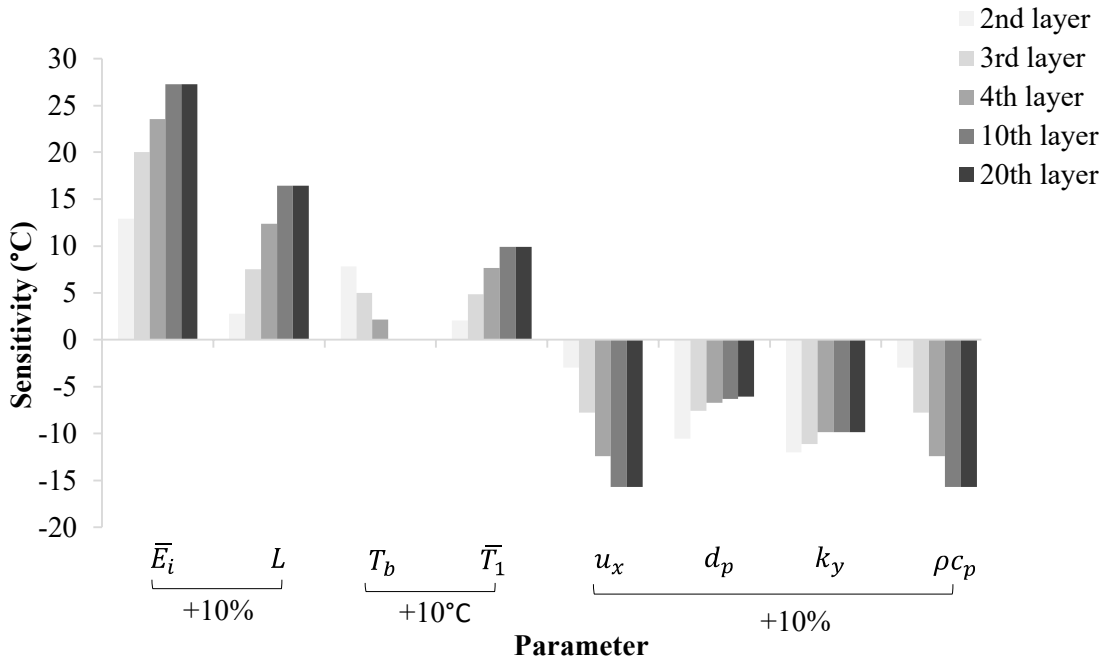

Figure 7.9 Sensitivity of the analytical scheme inputs to the predicted nip point temperatures for 10%, or 10°C, increase at different layers. Positive sensitivity denotes increase of the nip point value.

7.7 Example application under varying heater power

The in-process strategy proposed is demonstrated here in a virtual experiment simulated using the FE model. In this scenario, the deposition takes place on an insulating tool, with the properties reported in Table 7.1 at a speed of 50 mm/s. The tool features four temperature sensors placed 50 mm apart. The irradiance distribution on the tapes is constant across this straight placement path and equivalent to that of Figure 7.5, with a total irradiance value of 2.58×10^5 W/m^2. During the manufacture, the heater power is reduced to 75% of the initial value, linearly over the span of 1 s as shown in Figure 7.10a. Three scenarios are examined that may take place during ATP manufacture: (i) the analytical nip point approximation is carried out knowing a priori the irradiance drop as part of process design; (ii) the power drop is unexpected and needs to be identified by the analytical scheme; (iii) no sensors are used in this tooling region progressing with predictions obtained away from this power variation.

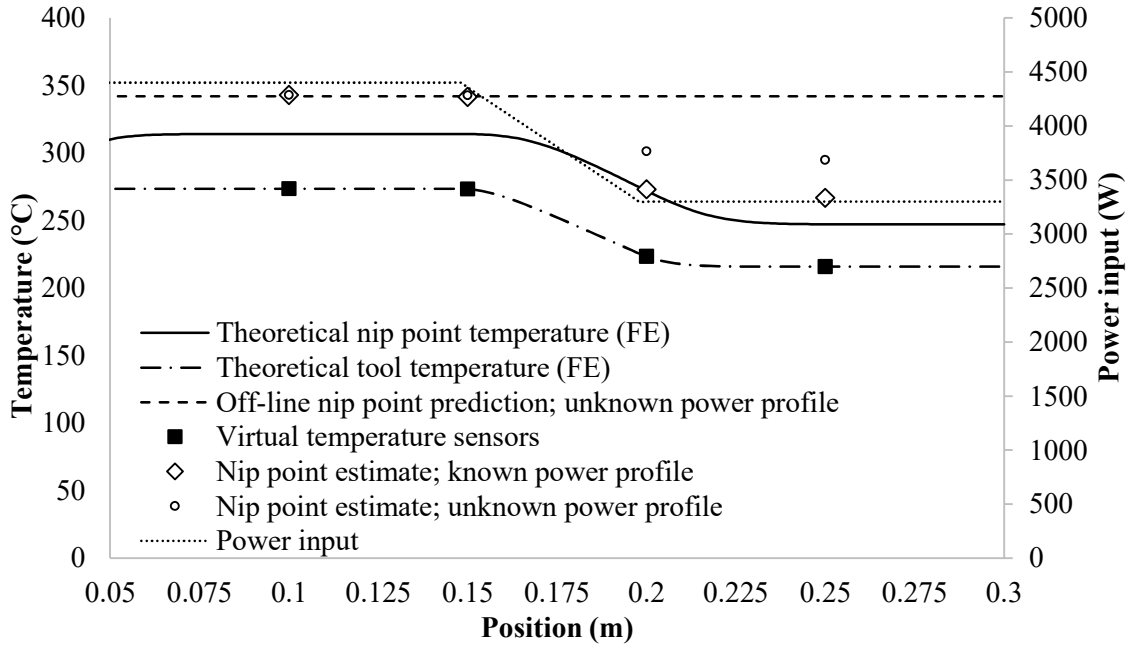

(a)

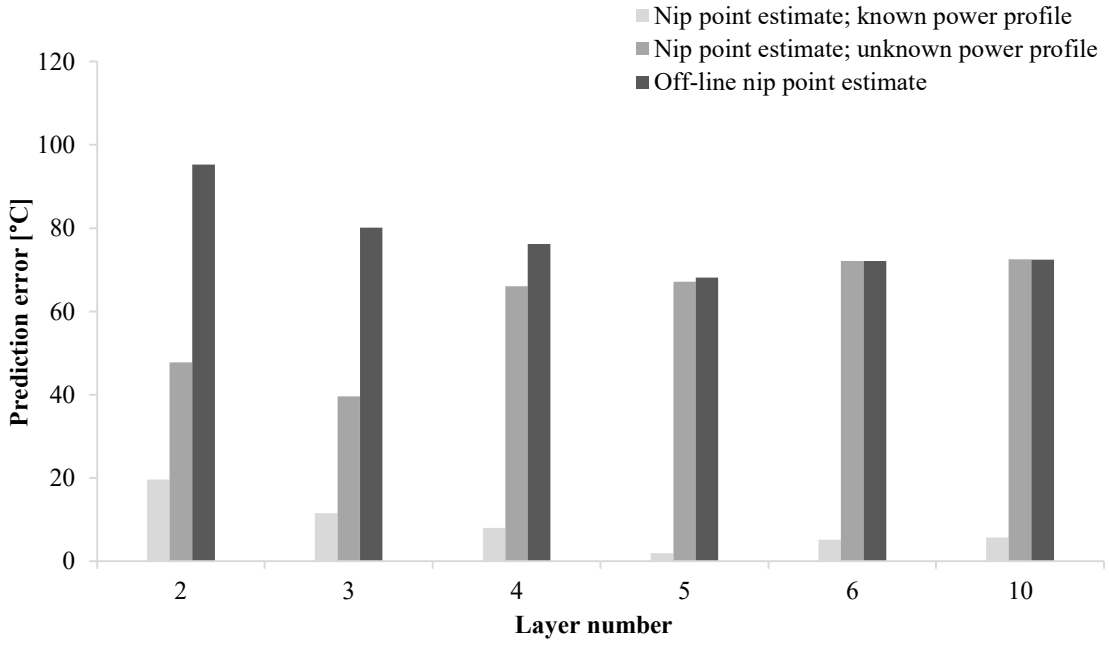

(b)

Figure 7.10 Processing at 50 mm/s with heater power drop: (a) FE profiles and analytical predicitions based on the available information for 2nd ply deposition; (b) errors of nip point temperature inside the reduced power region for different number of layers.

The nip point and tool profiles across the deposited length are plotted in Figure 7.10a for the 2nd layer deposition alongside readings of the virtual sensors. When the power variation is known beforehand, the analytical prediction follows the nip point profile

across the processed length satisfactorily, even in the transient region of decreasing power. In the case in which the power variation is not expected, the analytical predictions continue to follow the FE profile closely but with slightly greater error, up to 45°C. The estimation scheme acts in a monitoring sense, identifying the condition changes and potentially allowing their correction in future steps. In the case of solely off-line estimation, the change of nip point temperature is not measured, and predictions are almost 100°C off the theoretical.

The ability of the scheme to follow changes in conditions is also assessed in Figure 7.10b for different number of deposited layers. The analytical predictions inside the reduced-power region are within a 20°C error when the power variations are known. The potential to describe the resulting profile without this knowledge (case of unknown power variation) is good for the first four layers in which the estimation errors are lower than those of off-line studies. However, this capability is lost for thicker substrates due to the low sensitivity of tool temperature, as the heat transfer is shifted to conduction in a semi-infinite solid. The highest errors are obtained in the absence of process monitoring with an error of about 70 to 100°C.

This example highlights the role monitoring can play in ATP. The scheme allows identification of variations and translates them to changes in nip point temperature. The loss of monitoring capability as the thickness of the component is built up can be partially compensated for by information about the actual power profile obtained during the deposition of the first few layers, using the inverse calculation, which can then be used in a predictive way when the estimation operates in the semi-infinite solid regime.

7.8 Concluding remarks

An analytical approximation consisting of two 1D solutions was developed for estimating the nip point temperatures in ATP based on tool temperature measurements. The solutions address the two heat transfer regimes present in additive processes: heat conduction across a material interface while the deposited material has not reached large thicknesses and heat conduction in a semi-infinite solid governing the behaviour once substantial thickness of material has been built. The scheme is capable of utilising real-time temperature sensor data to estimate the power input profile of the heating source using an inverse solution that has regularisation behaviour in the presence of significant noise in

the temperature signals achieved through function specification of the profile. The nip point predictions assessed against data from the 2D FE model show good correlation with an average error of 15°C, with the simplification of constant thermal properties and tool losses having the highest impact. A virtual experiment of varying heater power across a placement path was conducted and highlighted the advantages of the monitoring scheme against solely offline studies in controlling the nip point temperatures under unexpected changes in conditions.

8. Overall discussion

8.1 Progress with respect to objectives

A 2D heat transfer model of the flashlamp-assisted ATP process was developed as part of this work. The model was coupled with a ray tracing analysis to obtain accurate estimates of incident irradiance on the composite tapes considering material properties, heat source position and characteristics. The combined methodology was utilised to gain an in-depth understanding of how the pulsing conditions influence the temperature field in the process. The results showed that the temperature distribution and thermal penetration depth in the irradiation phase can be tailored through the flashlamp parameters, demonstrating the flexibility and improved control pulsed heating introduces to composites processing. Such tailoring capabilities are not available with established continuous heating technologies. The interdependence of operating frequency and velocity when targeting uniform heating was uncovered, and the simulation was used to define an envelope of process conditions that supress these effects. This detailed assessment would not be possible through experimental means, as highlighted during the instrumented manufacturing trials. The use of miniature thermocouples yields only a coarse description of the temperature maxima/minima developed on the material surface, limiting the effectiveness of solely experimental process design. Thermal imaging is widely employed for temperature measurements in ATP; however, the short high-power pulses introduce additional challenges. Capturing enough data points to describe the non-linear heating curves during a 2 ms pulse requires a frame rate of at least 1500 Hz, which exceeds the capabilities of commercially available systems. Furthermore, the view on the ATP cavity can be restricted or blocked, especially when processing complex geometries such as concave ramps. As a result, the developed combined modelling offers an effective way to obtain the underlying information for process design purposes. Previous investigations have been limited to uncovering the relationship of processing rate and nip point temperatures, applying semi-empirical schemes originally developed for continuous sources. Nevertheless, the fidelity of this fully predictive methodology is highly dependent on a high number of inputs, which can present strong uncertainties during processing. Satisfactory agreement with experimental data was achieved using representative material properties and power conversion factor for the flashlamp system,

but additional characterisation of materials and the heat source is expected to improve accuracy further.

The 2D methodology elucidated the role of process parameters on the temperature field on a basis of parametric studies. However, performing a high number of runs for optimisation purposes requires faster solutions. The ability to model long processing cycles is also crucial for ATP processing, since the relevant material phenomena continue progressing away from the nip point region on which the 2D model focuses. To address these, a simplified 1D simulation for the flashlamp-assisted ATP was developed. Despite being capable of modelling pulsed sources with resolution equivalent to that of the 2D analysis, the 1D simulation requires only 1-2% of the computational effort representing a significant improvement in efficiency. The simulation features a structure which allows the modelling of consecutive depositions seamlessly, accounting for residual heating effects. Modelling of long processing cycles is facilitated by decoupling the irradiation and consolidation domains, with the simulation of the latter using considerably longer time steps. The simulation is also an improvement over existing 1D methodologies which oversimplify the heat exchange between the composite and roller, or between the substrate and incoming material. The 1D simulation presented can be readily incorporated into the combined thermal-optical framework substituting the 2D heat transfer model of ATP. The adaptation of the ray tracing results to the 1D simulation requires straightforward transformations. The speed of the 1D model enables the investigation of a wide range of process parameters and materials in a feasible timeframe, whilst the ability to simulate both continuous and pulsed sources ensures that different improvement routes can be explored. Large data sets produced by a high number of runs can be the basis of training AI approaches, as well as of stochastic simulation. This increased efficiency comes with a trade-off in accuracy which was shown to be minor for the configurations investigated; however, this might not be the case for different ATP setups. The 2D model can be utilised as the standard to assess the 1D simulation suitability for a given process configuration before utilisation.

The investigations of this study involving the 2D and 1D models were performed for straight placement paths under a constant velocity. However, both the 2D and 1D simulations are fully transient allowing the modelling of processes involving varying velocities. This requires the adjustment of material advection velocity at each time step

in the 2D model, or the adjustment of timings and heat flux profile in the 1D model. On the other hand, the simulation of complex geometries can be achieved by decomposing the domain into a finite number of intervals and solving using the previous state as initial condition. The 1D simulation is considered to be more suitable for this approach. For each interval, the heater distribution can be updated to incorporate potential deviations induced by the robotic movements which can influence the heater position relatively to the materials. Irradiance predictions over these intervals can be acquired using ray tracing. Furthermore, non-unidirectional laminates can be modelled as well as the deposition on substrates featuring off-axis fibre orientation. In the case of the 1D simulation, the heat conduction in the placement direction is considered negligible which assumption becomes even stronger as the fibre orientation deviates from this axis.

The 1D and 2D methodologies provide a detailed approximation of the temperature field in the flashlamp-assisted ATP. However, effective process design and optimisation necessitate the translation of temperature information to quality metrics. For this reason, the 1D heat transfer model was coupled with material constitutive models relating temperature evolution to interlaminar bond development and thermal degradation. A degradation kinetics model was developed based on TGA results able to describe the decomposition stages of the polymer matrix and carbon fibres, presenting good correlation with previous studies although these have mainly focused on the degradation of the polymer. The developed process model of ATP provides fast estimates of degree of bonding and thermal degradation for the manufacture of multi-layered composites, maintaining the reaction history throughout the process. Extensive characterisation campaigns are typically required to obtain the necessary information for developing these constitutive models. Literature data can be used for representative estimates as it was the case here for the bonding development model, but differences can be observed between similar material systems due to variations in chemical composition or quality aspects, such as tape roughness which affects intimate contact development directly.

A multi-objective optimisation scheme was developed based on the ATP process model and a GA algorithm. The framework allows the investigation of the trade-offs among the different objectives, as well as the identification of processing conditions which offer the most efficient compromise. The Pareto front of the multi-objective problem can be approximated by the GA by evaluating only a small fraction of the wide design space,

offering a computationally efficient method to optimise ATP compared to an exhaustive search carried by previous studies. The framework incorporates three objectives whilst it can optimise the flashlamp pulsing parameters. The results indicate a strong trade-off between quality and productivity, with the thermal degradation effects playing a key role in defining the potential processing window. The multi-objective scheme identifies the threshold conditions at which a further decrease of velocity and/or increase of power results in decomposition levels above acceptable values typically set for composite components. The balance between quality and productivity can then be selected depending on the process requirements, which could be significantly different for in-situ or autoclave consolidation. The inclusion of other relevant quality related aspects for thermoplastics processing into the optimisation, such as crystallinity and void dynamics, is expected to narrow the processing window even further. These effects could be incorporated into the scheme through material constitutive models and the necessary assumptions to reduce the computational penalty. Both productivity and quality could be improved by tailoring the velocity for each deposition individually, since heat transfer effects vary significantly as a function of part thickness.

The predictive simulation developed yields results corresponding to ideal process conditions and material properties, whilst producing zero defect parts with ATP can be facilitated by online monitoring and control to account for process variations. To address this, a monitoring strategy for ATP was put forward based on analytical heat transfer solutions and temperature data acquired on the composite back surface, allowing the estimation of nip point temperature in real time. A similar concept has been outlined involving simplified process models and thermal imaging measurements on the tow back surface, but its implementation has not been carried out. In this study, an inverse solution was also integrated to determine the heater power input from the temperature data and enhance the accuracy of nip point estimation. Such inverse methods have not been for ATP previously. This methodology puts forward a new approach to the heat transfer optimisation of ATP, which uses process data and simplified solutions instead of comprehensive models requiring numerous high-uncertainty inputs. The potential to access approximate values of the nip point temperature during the process generates the opportunity to control its value, therefore tuning the process to follow temperature profiles optimal in terms of layer bonding and material degradation. The approximation

of power input has been addressed here through an inverse solution; however, improvements on other critical parameters such as the material thermal properties and stack thickness are necessary, potentially accounting for the effects of partial consolidation on both the local thickness and effective conductivity. The utilisation of analytical solutions ensures fast and accurate results compared to numerical approaches.

8.2 Potential impact

The methodological contribution of this study is on the heat transfer analysis, monitoring and optimisation of automated composites manufacture under pulsed heating. The potential impact of this study on research and industrial applications is discussed here.

In terms of research, this study has established the use of pulsed heat sources for the automated processing of composites. The increased capabilities of these heating systems in terms of temperature control have also been showcased. The findings of this work are expected to drive further research in the field of composites manufacture aiming to investigate potential improvements offered over conventional heating methods. Studies could also focus on the influence of pulsed heating on material transformations, given the fundamentally different temperature profiles developed and lack of relevant established knowledge. The heat transfer analysis of ATP uses a set of simplifications which yield substantially improved computational efficiency with only minor trade-offs in accuracy. These principles could be adopted by studies on processes which share common characteristics with ATP, such as FW and pultrusion. Furthermore, a computationally efficient method for optimising ATP has been introduced, enabling the selection of process parameters to achieve the desired process outcomes. Studies could extend this framework with additional process variables and quality metrics in a form of objectives aiming to overcome existing challenges related to process complexity. In addition, this study introduced a process monitoring/control strategy for automated processes which utilises real-time process data and analytical solutions, coupled with an inverse technique to recover critical process parameters from the temperature data. Further studies are expected to follow improving over these approaches for ATP as well as similar manufacturing methods. The developments of this study focused on flashlamp-assisted ATP of thermoplastic composites; however, the majority of these could be applied to continuous heating and deposition of thermosetting composites. The flexibility of the tools developed strengthens the potential for increased impact on composites research.

Related to industrial advancements, the modelling and optimisation developments can drastically reduce the duration and cost of experimental campaigns which have been the basis for process design in recent years. The transition to modelling practices is crucial for the competitiveness of ATP against other processes, given the cost and time required for extensive experimental campaigns. The continuous effort to offer computationally efficient methodologies throughout this work ensures the provided tools are appealing to industrial applications, enabling complex studies within tight timeframes to meet the increased market demand. Furthermore, the optimisation scheme uncovers the trade-offs and interdependencies involved with the least solution effort, providing an effective way to adjust the compromise between quality and productivity for a given application. Such capability can be crucial for flexible production where the output is adjusted in response to short-term market fluctuations or component design changes. The monitoring and control strategy can be integrated into production lines to improve consistency in terms of part quality, maximising the production throughput whilst minimising the number of ineligible components according to certification standards. The outcomes of this work could also be used for further development of the flashlamp-based heating systems as well as the expansion to other applications, targeting for integration into the production of the next generation composite structures. These developments could also be used for customer support and consultancy to aid with knowledge and technology dissemination, as commonly required for innovations which differ significantly from established solutions.

9. Conclusions

The main conclusions of this work are:

- The optical-thermal 2D model of the flashlamp-assisted ATP presents deviations up to 20°C from experimental temperature measurements in the consolidation zone of the process; however, the slow response of temperature sensors yielded an average profile of the surface temperature maxima/minima developed in the irradiation phase due to pulsing, with the mid-level line of model predictions converging satisfactorily.
- The influence of flashlamp parameters is critical for the surface and bulk temperature developed in the irradiation stage of the ATP process, whereas consolidation temperatures are identical for pulsing scenarios of equivalent average power including continuous operation.
- Flashlamp operations of low frequency and long pulses (25 Hz/4.75 ms) result in up to 150°C higher irradiation temperatures and increased thermal penetration depth, 100 over 50 μm, compared to high frequency and short pulses (100 Hz/1.1 ms) and continuous operation.
- Combinations of low flashlamp frequency and rapid velocities result in nonuniform heating due to insufficient overlapping of the energy pulses on the material, with differences up to 100°C in the temperature maxima of surface points for processing at 25 Hz and 500 mm/s; however, the simulation can yield process maps to suppress these effects under a desired temperature difference threshold.
- The simplified 1D simulation of the flashlamp-assisted ATP requires only 1-2% of the computational effort required by the 2D model, with only a minor trade off in accuracy of up to 14°C.
- The estimated Pareto front for the multi-objective optimisation of ATP consists of points in the 3D space, with moderate bonding values in the 0.17-0.39 range, deposition times per meter of tape of 8.33-25 s/m which are on par with the state-of-the-art, and degradation values of up to 0.19 mainly on the tow surface which far exceed the acceptable levels for aerospace applications.

- The Pareto optimal solutions utilise velocities in the 40-140 mm/s range and average system power in the 8-11 kW range; however, 80% of the solutions feature the highest frequency (100 Hz) and as a result the shortest pulse duration (1.1 ms), showing a preference of these heating conditions over low frequency-long pulses scenarios.
- A strong trade-off exists between the degree of bonding, thermal degradation and productivity achieved in ATP, limiting the maximum average bonding in the stack to 0.35 for the configuration examined before thermal degradation exceeds the 0.01 threshold typically set for aerospace applications.
- The GA optimisation scheme of the flashlamp-assisted ATP identifies the Pareto front of the multi-objective problem requiring only 25% of the effort of an exhaustive research (1000 over 4094 runs).
- The in-process monitoring scheme of nip point temperatures in ATP presents good accuracy for a wide range of velocities, substrate thickness and tooling material tested, with an average error of 15°C.
- The accuracy of the inverse solution for heater input determination is highly dependent on the uncertainty of nip point position followed by measurement noise, presenting deviations up to 15% for high uncertainty and noise scenarios, but only 2% in the absence of these.

10. Suggestions for further investigation

Further work that could expand the outcomes of this study and enhance industrial applications is as follows:

- Further validation of heat transfer surface predictions in the irradiation zone of the process can be achieved with the use of special thermal imaging equipment capable of capturing the rapid temperature changes due to the short high-energy pulses. Extensive calibration of emissivity value is needed in this case due to the wide range of temperatures developed. Confidence can be also established by placing a higher number of thermocouples in thicker laminates validating predictions across more depth levels.
- The fidelity of the thermal-optical simulation can be improved by characterising the modelled flashlamp system further. Integrated sphere equipment can be utilised to capture the total light energy emitted from the source and compare with the electrical power to estimate the system conversion factor. The influence of pulsing conditions and average power to system efficiency can be examined and included in the simulation to increase the accuracy of incident irradiance on the materials. This factor is applied during the thermal model setup, scaling the optical predictions linearly, and thus only a single ray tracing run is needed for parametric studies. Further improvements are expected with the inclusion of interlayer thermal resistance effects which have been assumed negligible in the thermal simulation but have been found significant for laminates under imperfect consolidation in previous studies.
- The multi-objective GA scheme could be extended to tailor the processing rate for each layer deposition, which is expected to result in improved outcomes given that the heat transfer effects vary significantly as a function of part thickness. However, adding a velocity variable for each deposition would pose a high computational penalty for multi-layered components. As shown, temperature levels shift monotonically with increasing part thickness depending on the tool thermal properties. A simple relationship for velocity evolution with number of layers, for instance a linear or exponential, would introduce the least number of variables in the optimisation framework.

- The multi-objective optimisation could incorporate the ray tracing modelling developed, which would allow the tailoring of heater position/angle relatively to composites. This development could lead to improvements in quality and productivity given the strong influence of these on the irradiance distributions. The ray tracing simulation could provide irradiance predictions based on the inputs dictated by the GA and then the thermal analysis and objectives evaluation would be executed as in this study. This optimisation could be also used for product development, determining the design and materials for key components, such as the reflector and quartz block, to achieve desirable outcomes.
- The inverse scheme could be extended to provide a finer description of the bell-shaped irradiance acting on materials. This could be achieved by superimposing the direct solution used in this study for a finite number of linear profiles, beyond the triangular representation, which is not expected to impact computation times. The recovery of the irradiance profile could be used for validation of optical modelling and could enable the thermal analysis based on process data. In this way, high uncertainty parameters such as heater efficiency or optical absorptivity would be incorporated in the results, providing a more accurate input to thermal modelling than offline studies.
- The online monitoring scheme could be integrated in an industrial environment to enable the real time estimation of nip point temperatures. The industrial implementation is expected to necessitate further developments concerning the inputs required for the calculations. The power input has been addressed in this study through the inverse solution, but advancements for other critical variables such as material thermal properties and stack thickness are necessary. Instead of using estimated values, additional sensors and inverse solutions could be integrated into the strategy. This could result in more accurate temperature estimates based on instantaneous conditions, which opens the way for controlling the process parameters directly to ensure temperatures are within the desired window. The controller decisions for these adjustments could be based on AI approaches utilising offline simulation and/or experimental data.
- The industrial use of the developed simulation tools would be strongly facilitated by creating a software package which incorporates the different models and codes,

potentially in the form of an add-on to existing commercial solutions. The tools of this study have been implemented in commercially available software; however, further developments towards a user-friendly interface are required. In cases such as the multi-objective optimisation scheme, additional visualisation tools are required to aid with results interpretation and actual utilisation in an industrial environment. Furthermore, the inclusion of representative material databases with the involved properties is necessary.

11. References

[1] Slayton R, Spinardi G. Radical innovation in scaling up: Boeing's Dreamliner and the challenge of socio-technical transitions. Technovation 2016; 47: 47-58.

[2] Airbus. A350 less weight, less fuel, more sustainable. Available at: https://aircraft.airbus.com/en/aircraft/a350/a350-less-weight-less-fuel-more-sustainable (Accessed: 5 November 2022).

[3] Airbus. Airbus delivers its 500th A350. Available at: https://www.airbus.com/en/newsroom/stories/2022-09-airbus-delivers-its-500th-a350 (Accessed: 5 November 2022).

[4] The Boeing Company. Orders and deliveries. Available at: https://www.boeing.com/commercial/#/orders-deliveries (Accessed: 5 November 2022).

[5] Airbus. Global market forecast 2022-2041. Available at: https://www.airbus.com/aircraft/market/global-market-forecast.html (Accessed: 5 November 2022).

[6] The Boeing Company. Commercial market outlook 2022–2041. Available at: https://www.boeing.com/commercial/market/commercial-market-outlook/index.page (Accessed: 5 November 2022).

[7] Lucaszewicz DHJA, Ward C, Potter KD. The engineering aspects of automated prepreg layup: History, present and future. Compos B Eng 2012; 43 (3): 997–1009.

[8] Brasington A, Sacco C, Halbritter J, Wehbe R, Harik R. Automated fiber placement: A review of history, current technologies, and future paths forward. Compos C Open Access 2021; 6: 100182.

[9] CompositesWorld. Plant tour: Spirit AeroSystems, Wichita, KS. Available at: https://www.compositesworld.com/articles/the-first-composite-fuselage-section-for-the-first-composite-commercial-jet (Accessed: 5 November 2022).

[10] Hosseini SMA, Baran I, Drongelen M, Akkerman R. On the temperature evolution during continuous laser-assisted tape winding of multiple C/PEEK layers: The effect of roller deformation. Int J Mater Form 2021; 14: 203-221.

[11] Donough MJ, Shafaq, John NA, Philips AW, Prusty BG. Process modelling of in-situ consolidated thermoplastic composite by automated fibre placement – A review. Compos A Appl Sci Manuf 2022; 163: 107179.

[12] Yassin K, Hojjati M. Processing of thermoplastic matrix composites through automated fiber placement and tape laying methods: A review. J Thermoplast Compos Mater 2017; 31(12): 1676-1725.

[13] Schledjewski R, Latrille M. Processing of unidirectional fiber reinforced tapes—fundamentals on the way to a process simulation tool (ProSimFRT). Compos Sci Technol 2003; 63(14): 2111–2118.

[14] Guan X, Pitchumani R. Modeling of spherulitic crystallization in thermoplastic tow placement process: Heat transfer analysis. Compos Sci Technol 2004; 64(9): 1123–1134.

[15] Beyeler EP, Güçeri SI. Thermal analysis of laser-assisted thermoplastic-matrix composite tape consolidation. J Heat Transfer 1988; 110 (2): 424–430.

[16] Stokes-Griffin CM, Kollmannsberger A, Ehard S, Compston P, Drechsler K. Manufacture of steel–CF/PA6 hybrids in a laser tape placement process: Effect of first-ply placement rate on thermal history and lap shear strength. Compos A Appl Sci Manuf 2018; 111: 42–53.

[17] Chinesta F, Leygue A, Bognet B, Ghnatios Ch, Poulhaon F, Bordeu F, Barasinski A, Poitou A, Chatel S, Maison-Le-Poec S. First steps towards an advanced simulation of composites manufacturing by automated tape placement. Int J Mater Form 2014; 7(1): 81–92.

[18] Toso YMP, Ermanni P, Poulikakos D. Thermal phenomena in fiber-reinforced thermoplastic tape winding process: Computational simulations and experimental validations. J Compos Mater 2016; 38(2): 107–135.

[19] Zaami A, Baran I, Bor TC, Akkerman R. 3D numerical modeling of laser assisted tape winding process of composite pressure vessels and pipes-effect of winding angle, mandrel curvature and tape width. Materials 2020; 13(11): 2449-2470.

[20] Hassan N, Thompson JE, Batra RC, Hulcher AB, Song X, Loos AC. A heat transfer analysis of the fiber placement composite manufacturing process. J Reinf Plast Compos 2005; 24(8): 869–888.

[21] Chern BC, Moon TJ, Howell JR. Thermal analysis of in-situ curing for thermoset, hoop-wound structures using infrared heating: Part I- Predictions assuming independent scattering. J Heat Transfer 1995; 117(3): 681–686.

[22] Skandali M, Jansen KMB, Koussios S, Sinke J, Benedictus R. Two-dimensional and transient thermal model of the continuous tape laying process. In: 20th International Conference on Composite Materials, Copenhagen, 2015.

[23] Orth T, Krahl M, Parlevliet P, Modler N. Optical thermal model for LED heating in thermoset-automated fiber placement. Adv Manuf Polym Compos Sci 2018; 4(3): 73–82.

[24] Lichtinger R, Hörmann P, Stelzl D, Hinterhölzl R. The effects of heat input on adjacent paths during Automated Fibre Placement. Compos A Appl Sci Manuf 2015; 68: 387–397.

[25] Hörmann P, Stelzl D, Lichtinger R, Nieuwenhove S, Carro GM, Drechsler K. On the numerical prediction of radiative heat transfer for thermoset automated fiber placement. Compos A Appl Sci Manuf 2014; 67: 282–288.

[26] Ghasemi Nejhad MG, Cope RD, Güçeri SI. Thermal analysis of in-situ thermoplastic-matrix composite filament winding. J Heat Transfer 1991; 113(2): 304–313.

[27] Zaami A, Schäkel M, Baran I, Bor TC, Janssen H, Akkerman R. A fully coupled local and global optical-thermal model for continuous adjacent laser-assisted tape winding process of type-IV pressure vessels. J Compos Mater 2020; 55(8): 1073-1090.

[28] Zaami A, Baran I, Bor TC, Akkerman R. New process optimization framework for laser assisted tape winding of composite pressure vessels: Controlling the unsteady bonding temperature. Mater Des 2020; 196: 109130.

[29] James DL, Black WZ. Thermal analysis of continuous filament-wound composites. J Thermoplast Compos Mater 1996; 9(1): 54–75.

[30] Hosseini SMA, Schäkel M, Baran I, Janssen H, Martin D, Akkerman R. A new global kinematic-optical-thermal process model for laser-assisted tape winding with an application to helical-wound pressure vessel. Mater Des 2020; 193: 108854.

[31] Zacherl L, Shadmehri F, Rother K. Determination of convective heat transfer coefficient for hot gas torch (HGT)-assisted automated fiber placement (AFP) for thermoplastic composites. J Thermoplast Compos Mater 2021; 36(1): 1-23.

[32] Agarwal V, Güçeri SI, McCullough RL, Schultz JM. Thermal characterization of the laser-assisted consolidation process. J Thermoplast Compos Mater 1992; 5(2): 115–135.

[33] Chern BC, Moon TJ, Howell JR. On-line processing of unidirectional fiber composites using radiative heating: I. Model. J Compos Mater 2002; 36 (16): 1905-1934.

[34] Sonmez FO, Hahn HT. Modeling of heat transfer and crystallization in thermoplastic composite tape placement process. J Thermoplast Compos Mater 1997; 10(3): 198–240.

[35] Mantell SC, Springer GS. Manufacturing process models for thermoplastic composites. J Compos Mater 1992; 26(16): 2348–2377.

[36] Grove SM. Thermal modelling of tape laying with continuous carbon fibre-reinforced thermoplastic. Compos 1988; 19(5): 367–375.

[37] Levy A, Tierney J, Heider D, Gillespie JW, Lefébure P, Lang D. Modelling of inter-layer thermal contact resistance during thermoplastic tape placement. In: SAMPE, Baltimore, 2012.

[38] Kim HJ, Kim SK, Lee WI. Flow and heat transfer analysis during tape layup process of APC-2 prepregs. J Thermoplast Compos Mater 2004; 17(1): 5–12.

[39] Stokes-Griffin CM, Compston P, Matuszyk TI, Cardew-Hall MJ. Thermal modelling of the laser-assisted thermoplastic tape placement process. J Thermoplast Compos Mater 2013; 28(10): 1445–1462.

[40] Stokes-Griffin CM, Compston P. A combined optical-thermal model for near-infrared laser heating of thermoplastic composites in an automated tape placement process. Compos A Appl Sci Manuf 2015; 75: 104–115.

[41] Maurer D, Mitschang P. Laser-powered tape placement process–simulation and optimization. Adv Manuf Polym Compos Sci 2015; 1(3): 129–137.

[42] Baho O, Ausias G, Grohens Y, Barile M, Lecce L, Férec K. Automated fibre placement process for a new hybrid material: A numerical tool for predicting an efficient heating law. Compos A Appl Sci Manuf 2020; 144: 106360.

[43] Baho O, Ausias G, Grohens Y, Férec J. Simulation of laser heating distribution for a thermoplastic composite: effects of AFP head parameters. Int J Adv Manuf Technol 2020; 110: 2105–2017.

[44] Dedieu C, Chinesta F, Barasinski A, Leygue A, Lorente B, Dupillier JM. Advanced simulation of the laser-assisted tape placement process. In: 16th European Conference on Composite Materials, Seville, 2014.

[45] Barasinski A, Leygue A, Soccard E, Poitou A. Identification of non-uniform thermal contact resistance in automated tape placement process. Int J Mater Form 2014; 7: 479–486.

[46] Dai SC, Ye L. Characteristics of CF/PEI tape winding process with on-line consolidation. Compos A Appl Sci Manuf 2002; 33(9): 1227–1238.

[47] Kim HJ, Kim SK, Lee WI. A study on heat transfer during thermoplastic composite tape lay-up process. Exp Therm Fluid Sci 1996; 13(4): 408–418.

[48] Han Z, Cao Z, Shao Z, Shao Z, Fu H. Parametric study on heat transfer for tow placement process of thermoplastic composite. Polym Polym Compos 2014; 22(8): 713-722.

[49] Kollmannsberger A, Lichtinger R, Hohenester F, Ebel C, Drechsler K. Numerical analysis of the temperature profile during the laser-assisted automated fiber placement of CFRP tapes with thermoplastic matrix. J Thermoplast Compos Mater 2018; 31(12): 1563–1586.

[50] Tumkor S, Turkmen N, Chassapis C, Manoochehri S. Modeling of heat transfer in thermoplastic composite tape lay-up manufacturing. Int Commun Heat Mass Transf 2001; 28(1): 49–58.

[51] Ghasemi Nejhad MN, Cope RD, Güçeri SI. Thermal analysis of in-situ thermoplastic composite tape laying. J Thermoplast Compos Mater 1991; 4(1): 20–45.

[52] Kim J, Moon TJ, Howell JR. Transient thermal modeling of in-situ curing during tape winding of composite cylinders. J Heat Transfer 2003; 125(1): 137-146.

[53] Sarrazin H, Springer GS. Thermochemical and mechanical aspects of composite tape laying. J Compos Mater 1995; 29(14): 1908–1943.

[54] Zhao Q, Hoa SV, Gao ZJ. Thermal stresses in rings of thermoplastic composites made by automated fiber placement process. Sci Eng Compos Mater 2011; 18: 35–49.

[55] Shih PJ, Loos AC. Heat transfer analysis of the thermoplastic filament winding process. J Reinf Plast Compos 1999; 18: 1103–1112.

[56] Tafreshi OA, Hoa SV, Shadmehri F, Hoang DM, Rosca D. Heat transfer analysis of automated fiber placement of thermoplastic composites using a hot gas torch. Adv Manuf Polym Compos Sci 2019; 5(4): 206–223.

[57] Lionetto F, Dell'Anna R, Montagna F, Maffezzoli A. Modeling of continuous ultrasonic impregnation and consolidation of thermoplastic matrix composites. Compos A Appl Sci Manuf 2016; 82: 119–129.

[58] Cao Z, Dong M, Liu K, Fu H. Temperature field in the heat transfer process of PEEK thermoplastic composite fiber placement. Materials 2020; 13(9): 4417-4433.

[59] Saliba TE, Anderson DP, Servais RA. Process modeling of heat transfer and crystallization in complex shapes thermoplastic composites. J Thermoplast Compos Mater 1989; 2(2): 91–104.

[60] Hosseini SMA, Baran I, Akkerman R. Thermal modeling strategies for laser assisted tape winding (LATW) process. In: 21st International Conference on Composite Materials, Xi'an, 2017.

[61] Pitchumani R, Gillespie JW, Lamontia MA. Design and optimization of a thermoplastic tow-placement process with in-situ consolidation. J Compos Mater 1997; 31(3): 244–275.

[62] Lionetto F, Dell'Anna R, Montagna F, Maffezzoli A. Ultrasonic assisted consolidation of commingled thermoplastic/glass fiber rovings. Front Mater 2015; 2(1): 1-9.

[63] Moghadamazad M, Hoa SV. Models for heat transfer in thermoplastic composites made by automated fiber placement using hot gas torch. Compos C Open Access 2022; 7: 100214.

[64] Colton J, Leach D. Processing parameters for filament winding thick-section PEEK/carbon fiber composites. Polym Compos 1992; 13(6): 427–434.

[65] Schlottermuller M, Lu H, Roth Y, Himmel N, Schledjewski R, Mitschang P. Thermal residual stress simulation in thermoplastic filament winding process. J Thermoplast Compos Mater 2003; 16(6): 497–519.

[66] Grouve WJB, Warnet LL, Akkerman R. Towards a process simulation tool for the laser assisted tape placement process. In: 14th European Conference on Composite Materials, Budapest, 2010.

[67] Khan MA, Mitschang P, Schledjewski R. Tracing the void content development and identification of its effecting parameters during in situ consolidation of thermoplastic tape material. Polym Polym Compos 2010; 18(1): 1–15.

[68] Khan MA, Mitschang P, Schledjewski R. Parametric study on processing parameters and resulting part quality through thermoplastic tape placement process. J Compos Mater 2013; 47(4): 485–499.

[69] Tierney J, Gillespie JW. Modeling of in situ strength development for the thermoplastic composite tow placement process. J Compos Mater 2006; 40(16): 1487–1506.

[70] Tierney J, Gillespie JW. Modeling of heat transfer and void dynamics for the thermoplastic composite tow-placement process. J Compos Mater 2003; 37(19): 1745–1768.

[71] Grouve WJB. Weld strength of laser-assisted tape-placed thermoplastic composites. PhD Thesis, University of Twente, 2012.

[72] Weiler T. Thermal skin effect in laser-assisted tape placement of thermoplastic composites. PhD Thesis, RWTH Aachen University, 2019.

[73] de Sá Rodrigues J, Gonçalves PT, Pina L, de Almeida FG. Modelling the heating process in the transient and steady state of an in situ tape-laying machine head. J Manuf Mater Process 2022; 6(1): 8-38.

[74] Hajiloo A, Xie W, Hoa SV, Khan S. Thermal control design for an automated fiber placement machine. Sci Eng Compos Mater 2013; 21(3): 427-434.

[75] Sun WC, Mantell SC, Stelson KA. Modeling and control of the in-situ thermoplastic composite tape-laying process. J Dyn Syst Meas Control 1998; 120 (4): 507-515.

[76] Weiler T, Emonts M, Wollenburg L, Janseen H. Transient thermal analysis of laser-assisted thermoplastic tape placement at high process speeds by use of analytical solutions. J Thermoplast Compos Mater 2017; 31(3): 311-338.

[77] Rizzolo RH, Walczyk DF. Ultrasonic consolidation of thermoplastic composite prepreg for automated fiber placement. J Thermoplast Compos Mater 2016; 29(11): 1480–1497.

[78] Li Z, Yang T, Du Y. Dynamic finite element simulation and transient temperature field analysis in thermoplastic composite tape lay-up process. J Thermoplast Compos Mater 2013; 28(4): 558–573.

[79] Dai SC, Ye L. GF/PP tape winding with on-line consolidation. J Reinf Plast Compos 2002; 21(1): 71–90.

[80] Di Francesco M, Veldenz L, Dell'Anno G, Potter K. Heater power control for multi-material, variable speed automated fibre placement. Compos A Appl Sci Manuf 2017; 101: 408–421.

[81] Levy A, Heider D, Tierney J, Gillespie JW. Interlayer thermal contact resistance evolution with the degree of intimate contact in the processing of thermoplastic composite laminates. J Compos Mater 2014: 48(4): 491-503.

[82] Weiler T, Striet P, Voell A, Emonts M, Janssen H, Stollenwerk J. Tailored irradiation by VCSEL for controlled thermal states in thermoplastic tape placement. In: SPIE Photonics West Conference, San Francisco, 2018.

[83] Esselink FS, Hosseini SMA, Baran I, Akkerman R. Optimization of laser-assisted tape winding/placement process using inverse optical model. Procedia Manuf 2020; 47(7): 182–189.

[84] Stokes-Griffin CM, Compston P. An inverse model for optimisation of laser heat flux distributions in an automated laser tape placement process for carbon-fibre/PEEK. Compos A Appl Sci Manuf 2016; 88: 190–197.

[85] Levy A, Corre LS, Poitou A, Soccard E. Ultrasonic welding of thermoplastic composites: modeling of the process using time homogenization. Int J Multiscale Comput Eng 2011; 9(1): 53–72.

[86] Nonhof CJ, Luiten GA. Estimates for process conditions during the ultrasonic welding of thermoplastics. Polym Eng Sci 1996; 36(9): 1177–1183.

[87] Levy A, Corre LS, Chevaugeon N, Poitou A. A level set based approach for the finite element simulation of a forming process involving multiphysics coupling: Ultrasonic welding of thermoplastic composites. Eur J Mech A Solids 2011; 30(4): 501–509.

[88] O'Shaughnessey PG, Dube´ M, Villegas IF. Modeling and experimental investigation of induction welding of thermoplastic composites and comparison with other welding processes. J Compos Mater 2015; 50(21): 2895-2910.

[89] Brandt L, Deden D, Fischer FJC, Dreher PN, Williams D, Engelschall M, Nieberl D, Nowotny S. Xenon flashlamp based in-situ automated fibre placement of thermoplastic composites. In: 22nd International Conference on Composite Materials, Melbourne, 2019.

[90] Monnot P, Williams D, Francesco M. Power control of a flashlamp-based heating solution for automated dry fibre placement. In: 18th European Conference on Composite Materials, Athens, 2018.

[91] Reichardt J, Baran I, Akkerman R. New analytical and numerical optical model for the laser assisted tape winding process. Compos A Appl Sci Manuf 2018; 107: 647-656.

[92] Chern BC, Moon TJ, Howell JR. On-line processing of unidirectional fiber composites using radiative heating: II. Radiative properties, experimental validation and process parameter selection. J Compos Mater 2002; 36 (16): 1935-1964.

[93] Stokes-Griffin C.M, Compston P. Optical characterisation and modelling for oblique near-infrared laser heating of carbon fibre reinforced thermoplastic composites. Opt Lasers Eng 2015; 72: 1-11.

[94] Xu H, Hu J, Yu Z. Absorption behavior analysis of carbon fiber reinforced polymer in laser processing. Opt Mater Express 2015; 5(10): 2330-2336.

[95] Meister S, Kolbe A, Groves RM. Reflectivity and emissivity analysis of thermoplastic CFRP for optimising Xenon heating and thermographic measurements. Compos A Appl Sci Manuf 2018; 158: 106972.

[96] Louët V, Rousseau B, Corre LS, Boyard N, Tardif X, Delmas J, Delaunay D. Directional spectral reflectivity measurements of a carbon fibre reinforced composite up to 450°C. Int J Heat Mass Transf 2017; 112: 882–890.

[97] Schaefer PM, Gierszewski D, Kollmannsberger A, Zaremba S, Drechsler K. Analysis and improved process response prediction of laser-assisted automated tape placement with PA-6/carbon tapes using Design of Experiments and numerical simulations. Compos A Appl Sci Manuf 2017; 96: 137–146.

[98] Lichtenwalner PF. Neural network-based control for the fiber placement composite manufacturing process. J Mater Eng Perform 1993; 2(5): 687-691.

[99] Pagano RL, Calado VMA, Bezerra de Souza M, Biscaia EC. Proposal of an optimum cure cycle for filament winding process using a hybrid neural network-first principles model. Polym Compos 2013; 35:1377–1387.

[100] Heider D, Piovoso MJ, Gillespie JW. Application of a neural network to improve an automated thermoplastic tow-placement process. J Process Control 2002; 12(1): 101–111.

[101] Heider D, Piovoso MJ, Gillespie JW. A neural network model-based open-loop optimization for the automated thermoplastic composite tow-placement system. Compos A Appl Sci Manuf 2003; 34(8): 791–799.

[102] Heider D, Piovoso MJ, Gillespie JW. Intelligent control of the thermoplastic composite tow-placement process. J Thermoplast Compos Mater 1998; 11(6): 573–595.

[103] Yu T, Shi Y, He X, Kang C, Deng B. Modeling and optimization of interlaminar bond strength for composite tape winding process. J Reinf Plast Compos 2017; 36(8): 579–592.

[104] Sonmez FO, Akbulut M. Process optimization of tape placement for thermoplastic composites. Compos A Appl Sci Manuf 2007; 38(9): 2013–2023.

[105] Khan MA, Mitschang P, Schledjewski R. Identification of some optimal parameters to achieve higher laminate quality through tape placement process. Adv Polym Technol 2010; 29(2): 98–111.

[106] Sonmez FO, Hahn HT. Analysis of the on-line consolidation process in thermoplastic composite tape placement. J Thermoplast Compos Mater 1997; 10(6): 543–572.

[107] Levy A, Heider D, Tierney J, Gillespie JW, Lefebure P, Lang D. Simulation and optimization of the thermoplastic automated tape placement (ATP) process. In: SAMPE, Baltimore, 2012.

[108] Sonmez FO, Hahn HT. Thermoviscoelastic analysis of the thermoplastic composite tape placement process. J Thermoplast Compos Mater 1997; 10(4): 381–414.

[109] Sonmez FO, Hahn HT, Akbulut M. Analysis of process-induced residual stresses in tape placement. J Thermoplast Compos Mater 2002; 15(6): 525–544.

[110] Tzeng JT, Pipes RB. Thermal residual stress analysis for in situ and post consolidated composite rings. Compos Manuf 1992; 3(4): 273–279.

[111] Pitchumani R, Ranganathan S, Don RC, Gillespie JW, Lamontia MA. Analysis of transport phenomena governing interfacial bonding and void dynamics during thermoplastic tow-placement. Intl J Heat Mass Transf 1996; 39(9): 1883–1897.

[112] Ranganathan S, Advani SG, Lamontia MA. A non-isothermal process model for consolidation and void reduction during in-situ tow placement of thermoplastic composites. J Compos Mater 1995; 29(8): 1040–1062.

[113] Comer AJ, Ray D, Obande W, Jones D, Lyons J, Rosca I, O'Higgins RM, McCarthy MA. Mechanical characterisation of carbon fibre-PEEK manufactured by laser-assisted automated-tape-placement and autoclave. Compos A Appl Sci Manuf 2015; 69: 10–20.

[114] Qureshi Z, Swait T, Scaife R, El-Dessouky HM. In situ consolidation of thermoplastic prepreg tape using automated tape placement technology: potential and possibilities. Compos B Eng 2014; 66: 255–267.

[115] Chu Q, Li Y, Xiao J, Huan D, Zhang X, Chen X. Processing and characterization of the thermoplastic composites manufactured by ultrasonic vibration–assisted automated fiber placement. J Thermoplast Compos Mater 2017; 31(3): 339-358.

[116] Ray D, Comer AJ, Lyons J, Obande W, Jones D, O'Higgins RM, McCarthy MA. Fracture toughness of carbon fiber/polyether ether ketone composites manufactured by autoclave and laser-assisted automated tape placement. J Appl Polym Sci 2015; 132(11): 41643.

[117] Rosselli F, Santare MH, Güçeri SI. Effects of processing on laser assisted thermoplastic tape consolidation. Compos A Appl Sci Manuf 1997; 28(12): 1023–1033.

[118] Chen J, Fu K, Li Y. Understanding processing parameter effects for carbon fibre reinforced thermoplastic composites manufactured by laser-assisted automated fibre placement (AFP). Compos A Appl Sci Manuf 2021; 140: 106160.

[119] Pistor CM, Yardimci MA, Güçeri SI. On-line consolidation of thermoplastic composites using laser scanning. Compos A Appl Sci Manuf 1999; 30(10): 1149–1157.

[120] Hoa SV, Hoang DM, Simpson J. Manufacturing procedure to make flat thermoplastic composite laminates by automated fibre placement and their mechanical properties. J Thermoplast Compos Mater 2017; 30(12): 1693-1712.

[121] Saenz-Castillo D, Martín MI, Calvo S, Rodriguez-Lence F, Güemes A. Effect of processing parameters and void content on mechanical properties and NDI of thermoplastic composites. Compos A Appl Sci Manuf 2019; 121: 308–320.

[122] Saenz-Castillo D, Martín MI, García-Martínez V, Ramesh A, Battley M, Güemes A. A comparison of mechanical properties and X-ray tomography analysis of different out-of-autoclave manufactured thermoplastic composites. J Reinf Plast Compos 2020; 39(19-20): 703–720.

[123] Ghasemi Nejhad MN. Issues related to processability during the manufacture of thermoplastic composites using on-line consolidation technique. J Thermoplast Compos Mater 1993; 6(2): 130-146.

[124] Stokes-Griffin CM, Compston P. Investigation of sub-melt temperature bonding of carbon-fibre/PEEK in an automated laser tape placement process. Compos A Appl Sci Manuf 2016; 84: 17–25.

[125] Hosseini SMA, Esselink F, Baran I, Drongelen M, Akkerman R. Optimization of the laser-assisted tape winding process using an inverse kinematic-optical-thermal model. Adv Manuf Polym Compos Sci 2020; 6(4): 226–244.

[126] Bur N, Joyot P, Villon P. Reduced-order model of optimal temperature control for the automated fibre placement process. CR Mecanique 2018; 346(7): 556–570.

[127] Druiff P, King M, Visrolia A, Arruda M, Palardy-Sim M, Bolduc S, Dell'Anno G, Ward C. A smart interface for machine learning based data-driven automated fibre placement. In: The Composites and Advanced Materials Expo, Dallas, 2021.

[128] Struzziero G, Skordos AA. Multi-objective optimisation of the cure of thick components. Compos A Appl Sci Manuf 2017; 93: 126-136.

[129] Oromiehie E, Gain AK, Prusty BG. Processing parameter optimisation for automated fibre placement (AFP) manufactured thermoplastic composites. Compos Struct 2021; 272: 114223.

[130] Oromiehie E, Garbe U, Prusty BG. Porosity analysis of carbon fibre-reinforced polymer laminates manufactured using automated fibre placement. J Compos Mater; 54(9): 1217-1231.

[131] Comer AJ, Hammond PE, Ray D, Lyons J, Obande W, Jones D, O'Higgins R, McCarthy MA. Wedge peel interlaminar toughness of carbon-fibre/ PEEK thermoplastic laminates manufactured by laser-assisted automated-tape-placement (LATP). In: 9th SAMPE Europe Technical Conference, Tampere, 2014.

[132] Grouve WJB, Warnet LL, Rietman B, Visser HA, Akkerman R. Optimization of the tape placement process parameters for carbon–PPS composites. Compos A Appl Sci Manuf 2013; 50: 44-53.

[133] Grouve WJB, Warnet LL, Akkerman R, Wijskamp S, Kok JSM. Weld strength assessment for tape placement. Int J Mater Form 2010; 3: 707-710.

[134] Mantell SC, Qiuling W, Springer GS. Processing Thermoplastic Composites in a press and by tape laying—Experimental Results. J Compos Mater 1992; 26(16): 2378–2401.

[135] Pistor CM, Güçeri SI. Crystallinity of on-line consolidated thermoplastic composites. J Compos Mater 1999; 33(4): 306–324.

[136] Shadmehri F, Hoa SV, Fortin-Simpson J, Ghayoor H. Effect of in situ treatment on the quality of flat thermoplastic composite plates made by automated fiber placement (AFP). Adv Manuf Polym Compos Sci 2018; 4(2): 41–47.

[137] Agarwal V, McCullough RL, Schultz JM. The thermoplastic laser-assisted consolidation process-mechanical and microstructure characterization. J Thermoplast Compos Mater 1996; 9(4): 365–380.

[138] Mazumdar SK, Hoa SV. Determination of manufacturing conditions for hot-gas-aided thermoplastic tape winding. J Thermoplast Compos Mater 1996; 9(1): 35-53.

[139] Beyeler E, Phillips W, Güçeri SI. Experimental investigation of laser-assisted thermoplastic tape consolidation. J Thermoplast Compos Mater 1988; 1(1): 107–121.

[140] Clancy G, Peeters D, Oliveri V, Jones D, O'Higgins RM, Weaver PM. A study of the influence of processing parameters on steering of carbon fibre/PEEK tapes using laser-assisted tape placement. Compos B Eng 2019; 163: 243–251.

[141] Oromiehie E, Prusty BG, Compston P, Rajan G. The influence of consolidation force on the performance of AFP manufactured laminates. In: 21st International Conference of Composite Materials, Xi'an, 2017.

[142] Hoang VT, Kwon BS, Sung JW, Choe HS, Oh SW, Lee SM, Kweon JH, Nam YW. Postprocessing method-induced mechanical properties of carbon fiber-reinforced thermoplastic composites. J Thermoplast Compos Mater 2020: 36(1): 432-447.

[143] Stokes-Griffin CM, Compston P. The effect of processing temperature and placement rate on the short beam strength of carbon fibre–PEEK manufactured using a laser tape placement process. Compos A Appl Sci Manuf 2015; 78: 274–283.

[144] Chanteli A, Bandaru AK, Peeters D, O'Higgins RM, Weaver PM. Influence of repass treatment on carbon fibre-reinforced PEEK composites manufactured using laser-assisted automatic tape placement. Compos Struct 2020; 248: 112539.

[145] Arhant M, Briançon C, Burtin C, Davies P. Carbon/polyamide 6 thermoplastic composite cylinders for deep sea applications. Compos Struct 2019; 212: 535–546.

[146] Schiel I, Raps L, Chadwick AR, Schmidt I, Simone M, Nowotny S. An investigation of in-situ AFP process parameters using CF/LM-PAEK. Adv Manuf Polym Compos Sci 2020; 6(4):191–197.

[147] Samak S, Risteska S, Dukovski V, Trajkoski S. Some experimental investigation of products from thermoplastic composite materials manufactured with Robot and LAFP. Int J Eng Res Technol 2020; 9(9): 1083–1088.

[148] Croft K, Lessard L, Pasini D, Hojjati M, Chen J, Yousefpour A. Experimental study of the effect of automated fiber placement induced defects on performance of composite laminates. Compos A Appl Sci Manuf 2011; 42(5): 484–491.

[149] Andersen BJ, Colton JS. Automation of thermoplastic composite processing. J Compos Mater 1990; 24(2): 150–174.

[150] Dobrzanski LA, Domagala J, Silva JF. Application of Taguchi method in the optimisation of filament winding of thermoplastic composites. Arch Mater Sci Eng 2007; 28(3): 133–140.

[151] Nath NK. Optimization of tape winding process parameters to enhance the performance of solid rocket nozzle throat back up liners using Taguchi's robust design methodology. J Inst Eng India Ser C 2017; 98(4): 479-484.

[152] Schulz M, Janssen H, Brecher C. A digital shadow for the infrared-based tape laying process of tailored blanks out of thermoplastic unidirectional tape. Procedia CIRP 2019: 85: 224-229.

[153] Mazumdar SK, Hoa SV. Application of Taguchi method for process enhancement of online consolidation technique. Compos 1995; 26(9): 669–673.

[154] Kang C, Shi Y, He X, Yu T, Deng B, Zhang H, Sun P, Zhang W. Multi-response optimization of T300/epoxy prepreg tape-wound cylinder by grey relational analysis coupled with the response surface method. Mater Res Express 2017; 4(9): 095301.

[155] Wanigasekara C, Oromiehie E, Swain A, Prusty BG, Nguang SK. Machine learning Based predictive model for AFP-based unidirectional composite laminates. IEEE Trans Ind Inf 2020; 16(4): 2315-2324.

[156] Wanigasekara C, Oromiehie E, Swain A, Prusty BG, Nguang SK. Machine learning-based inverse predictive model for AFP based thermoplastic composites. J Ind Inf Integr 2021; 22: 100197.

[157] Islam F, Wanigasekara C, Rajan G, Swain A, Prusty GB. An approach for process optimisation of the Automated Fibre Placement (AFP) based thermoplastic composites manufacturing using Machine Learning, photonic sensing, and thermo-mechanics modelling. Manuf Lett 2022; 32: 10-14.

[158] Deng B, Shi Y, Yu T, Kang C, Zhao P. Multi-response parameter interval sensitivity and optimization for the composite tape winding process. Materials 2018; 11(2): 220-240.

[159] Aized T, Shirinzadeh B. Robotic fiber placement process analysis and optimization using response surface method. Int J Adv Manuf Technol 2011; 55: 393–404.

[160] Shi Y, Yu T, He X, Kang C, Zhang X, Zhang J. Mechanism and optimization of process parameters coupling for composite tape winding. Acta Mater Compos Sin 2015; 32: 831–839.

[161] Sun S, Han Z, Fu H, Jin H, Dhupia JS, Wang Y. Defect characteristics and online detection techniques during manufacturing of FRPs using automated fiber placement: A review. Polymers 2020; 12(6): 1337-1359.

[162] Juarez PD, Gregory ED. In situ thermal inspection of automated fiber placement for manufacturing induced defects. Compos B Eng 2021; 220: 109002.

[163] Yadav N, Tranta BO, Schledjewski R, Wachtarczyk K. Ply-by-ply inline thermography inspection for thermoplastic automated tape layup. Adv Manuf Polym Compos Sci 2021; 7: 49-59.

[164] Schmidt C, Denkena B, Völtzer K, Hocke T. Thermal Image-based monitoring for the automated fiber placement process. Procedia CIRP 2017; 62: 27–32.

[165] Gregory E, Juarez P. In situ thermal non-destructive evaluation for assessing part quality during composite automated fiber placement. J Nondestruct Eval 2018; 1(4): 10.

[166] Schmidt C, Denkena B, Hocke T, Völtzer K. Influence of AFP process parameters on the temperature distribution used for thermal in-process monitoring. Procedia CIRP. 2017; 66: 68–73.

[167] Denkena B, Schmidt C, Völtzer K, Hocke T. Thermographic online monitoring system for automated fiber placement processes. Compos B Eng 2016; 97: 239–243.

[168] Brüning J, Denkena B, Dittrich MA, Hocke T. Machine learning approach for optimisation of automated fiber placement processes. Prodecia CIRP 2017; 66: 74-78.

[169] Oromiehie E, Prusty BG, Compston P, Rajan G. Characterisation of process-induced defects in automated tape placement (ATP) manufacturing of composites using fiber Bragg grating sensors. Struct Health Monit 2016; 17(1): 108-117.

[170] Han AZ, Sun S, Li W, Zhao Z, Shao Z. Experimental study of the effect of internal defects on stress waves during automated fiber placement. Polymers 2018; 10(4): 413-427.

[171] Shadmehri F, Hoa VS. Digital image correlation applications in composite automated manufacturing, inspection, and testing. Appl Sci 2019; 9(13): 2719-2727.

[172] Shadmehri F, Ioachim O, Pahud O, Brunel JE, Landry A, Hoa SV, Hojjati M. Laser-vision inspection system for automated fiber placement (AFP) process. In: 20th International Conference on Composite Materials, Copenhagen, 2015.

[173] Krombholz C, Perner M, Bock M, Röstermundt D. Improving the production quality of the advanced automated fiber placement process by means of online path correction. In: 28th International Congress of the Aeronautical Science, Brisbane, 2012.

[174] Oromiehie E, Prusty BG, Compston P, Rajan G. In-situ simultaneous measurement of strain and temperature in automated fibre placement (AFP) using optical fibre Bragg grating (FBG) sensors. Adv Manuf Polym Compos Sci 2017; 3(2): 52–61.

[175] Tifkitsis KI, Skordos AA. Real-time inverse solution of the composites' cure heat transfer problem under uncertainty. Inverse Probl Sci Eng 2020; 28(7): 1011-1030.

[176] Humfeld KD, Gu D, Butler GA, Nelson K, Zobeiry N. A machine learning framework for real-time inverse modeling and multi-objective process optimization of composites for active manufacturing control. Compos B Eng 2021; 223: 109150.

[177] Solvay. APC-2(PEEK)/AS4. Available at: https://www.solvay.com/en/product/apc-2-peekas4#product-documents (Accessed: 18 July 2022).

[178] MBK MaschinenBau Kieler. Available at: http://www.maschinenbau-kieler.de/ (Accessed: 18 July 2022).

[179] Heraeus Noblelight. humm3® - intelligent heat for composites. https://www.heraeus.com/en/hng/products_and_solutions/arc_and_flash_lamps/humm3/humm3_1/humm3.html (Accessed: 18 July 2022).

[180] Pico technology. 70 MHz 7000 V differential oscilloscope probe 100:1/1000:1. Available at: www.picotech.com/accessories/active-differential-high-voltage/70-mhz-7000-v-differential-probe (Accessed: 18 July 2022).

[181] Pico technology. 200 A / 2000 A AC/DC current probe, BNC connector. Available at: www.picotech.com/accessories/current-probes/200a-2000a-current-probe-bnc (Accessed: 18 July 2022).

[182] Tektronix. MDO3000 Series Datasheet. Available at: www.tek.com/en/datasheet/mixed-domain-oscilloscopes (Accessed: 18 July 2022).

[183] Omega Engineering. Portable USB thermocouple/voltage input data acquisition module. Available at: www.omega.co.uk/pptst/OM-DAQ-USB-2400.html (Accessed: 18 July 2022).

[184] Lewis RW, Morgan K, Thomas HR, Seetharamu KN. The finite element method in heat transfer analysis. New York: John Wiley & Sons Ltd, 1996.

[185] Ansys Inc. Ansys® Mechanical Enterprise, Release 2021 R1. Available at: www.ansys.com. (Accessed: 15 May 2022).

[186] Ansys Inc, Ansys® Mechanical Enterprise, Release 2021 R1, Thermal Analysis Guide, 2022.

[187] Gresho PM, Lee RL. Don't suppress the wiggles-They're telling you something. Comput Fluids 1981; 9(2): 223–53.

[188] Parker WJ, Jenkins RJ, Butler CP, Abbott GL. Flash Method of determining thermal diffusivity, heat capacity, and thermal conductivity. J Appl Phys 1961; 32(9): 1679-1684.

[189] Lau SK, Almond DP, PM Patel. Transient thermal wave techniques for the evaluation of surface coatings. J Phys D Appl Phys 1991; 24: 428-436.

[190] Lamba Research Corporation. TracePro®. Available at: www.lambdares.com/tracepro (Accessed: 18 July 2022).

[191] Hale GM, Query MR. Optical constants of water in the 200-nm to 200-µm wavelength region. Appl Optics 1973; 12(3): 555–563.

[192] Rakić AD, Djurisic AB, Elazar JM, Majewski ML. Optical properties of metallic films for vertical-cavity optoelectronic devices. Appl Optics 1998; 37(22): 5722-5783.

[193] Kim SK, Jung BS, Kim HJ, Lee WL. Inverse estimation of thermophysical properties for anisotropic composite. Exp Therm Fluid Sci 2003; 27(6): 697–704.

[194] Cogswell FN. Thermoplastic aromatic polymer composites: A study of the structure, processing, and properties of carbon fibre reinforced polyetheretherketone and related materials. Oxford: Butterworth Heinemann; 1992.

[195] Yang F, Pitchumani R. Nonisothermal healing and interlaminar bond strength evolution during thermoplastic matrix processing. Polym Compos 2003; 24(2): 3213–24.

[196] Yang F, Pitchumani R. A fractal cantor set based description of interlaminar contact evolution during thermoplastic composites processing. J Mater Sci 2001; 36(19): 4661–4671.

[197] Yang F, Pitchumani R. Healing of thermoplastic polymers at an interface under nonisothermal conditions. Macromolecules 2002; 35(8): 3213–3224.

[198] Lamèthe JF, Beauchêne P, Léger L. Polymer dynamics applied to PEEK matrix composite welding. 2002; 35(8): 3213–24. Aerosp Sci Technol 2005; 9(3): 233-40.

[199] Patel P, Hull TR, McCabe RW, Flath D, Grasmeder J, Percy M. Mechanism of thermal decomposition of poly (ether ether ketone) (PEEK) for a review of decomposition studies. Polym Degrad Stab 2010; 95(5): 709–718.

[200] Martin MI, Rodríguez-Lence F, Güemes A, Fernández-López A, Pérez-Maqueda LA, Perejón A. On the determination of thermal degradation effects and detection techniques for thermoplastic composites obtained by automatic lamination. Compos A Appl Sci Manuf 2018; 111: 23–32.

[201] Phillips R, Glauser T, Manson JAE. Thermal stability of peek/carbon fiber in air and its influence on consolidation. Polym Compos 1997; 18(4): 500-508.

[202] Day M, Cooney JD, Wiles DM. The kinetics of the oxidative degradation of poly (aryl-ether-ether-ketone) (PEEK). Thermochim Acta 1989; 147:189–197.

[203] Vasconcelos GC, Mazur RL, Ribiero B, Botelho EC, Costa ML. Evaluation of decomposition kinetics of poly (ether-ether-ketone) by thermogravimetric analysis. Mater Res 2013; 17: 227–235.

[204] Nam JD, Seferis JC. Generalized composite degradation kinetics for polymeric systems under isothermal and nonisothermal conditions. J Polym Sci B Polym Phys 1992; 30(5): 455–463.

[205] Gizynski M, Romelczyk-Baishya B. Investigation of carbon fiber–reinforced thermoplastic polymers using thermogravimetric analysis. J Thermoplast Compos Mater 2021; 34(1): 126-140.

[206] Dasović B, Klanšek U. Comparison of spreadsheet-based optimization tools applied to construction site layout problem. IOP Conf Ser Mat Sci Eng 2021; 1209: 012010.

[207] TA Instruments. TGA 550. Available at: https://www.tainstruments.com/tga-550/ (Accessed: 18 July 2022).

[208] Branke J, Deb K, Miettinen K, Słowiński R. Multi-objective optimisation: Interactive and evolutionary approaches. Berlin: Springer; 2008.

[209] Incropera FP, Dewitt DP, Bergman TL, Lavine AS. Fundamentals of Heat and Mass Transfer- 6th edition, New York: John Wiley and Sons; 2006.

[210] Savitzky A, Golay M, Smoothing and differentiation of data by simplified least squares procedures. Anal Chem. 1964; 36: 1627-38.

[211] Orfanidis SJ. Introduction to Signal Processing. New Jersey: Prentice Hall; 2010.

[212] Iffländer R. Solid state lasers for materials processing: Fundamental relations and technical realizations. Berlin: Springer; 2001.

[213] Koechner W. Solid state laser engineering- 6th edition. New York: Springer; 2006.

[214] Omega Engineering. Thermocouple response time. Available at: https://www.omega.co.uk/temperature/z/thermocoupleresponsetime.html (Accessed: 18 July 2022).

[215] MathWorks. Global optimisation tool. Available at: https://uk.mathworks.com/products/global-optimization.html (Accessed: 18 July 2022).

[216] Jiang J, He Y, Wang H, Ke Y. Modeling and experimental validation of compaction pressure distribution for automated fiber placement. Compos Struct 2021; 256: 113101.

[217] Azad H, Mustafa MT, Arif A. Analytic solutions of initial-boundary-value problems of transient conduction using symmetries. Appl Math Comput 2009; 215 (12): 4132-40.

[218] Cole KB, Beck JV, Woodbury KA, Monte F. Intrinsic verification and a heat conduction database. Int J Therm Sci 2014; 78 :36-47.

[219] Weber CF. Analysis and solution of the ill-posed inverse heat conduction problem. Int J Heat and Mass Transf 1981; 24 (11): 1783-1792.